Electrochemical properties of phosphorus compounds in fluoride melts

by
Elke Willam Thisted

Thesis submitted in partial fulfilment of the
requirements for the degree
Doktoringeniør

Norwegian University of Science and Technology
Department of Materials Technology

Trondheim, August 2003

URN:NBN:no-6427

URN:NBN:no-6427

Summary

In the present work the behaviour of phosphorus species in fluoride-based melts was investigated. The motivation for the study was based on the deleterious effect of phosphorus on the aluminium production process. It is "known" that for each 100 ppm phosphorus (P) in the bath the current efficiency is reduced by 1%. In addition, the properties of cast alloys are influenced by the phosphorus content.

The thesis contains a literature review on the chemistry of phosphorus with focus on its behaviour in molten salts.

The solubility of aluminium orthophosphate in cryolite melt was studied. Part of the phase diagram of the system Na_3AlF_6-$AlPO_4$ was investigated. The eutectic point was determined to be at (57.21 ± 0.02) mole% $AlPO_4$ and (695.9 ± 1.0) ºC. It was found that the orthophosphate dissociates partly into a metaphosphate species and an oxide ion in pure cryolite melts:

$$PO_4^{34} \lozenge \quad PO_3^4 \; 2\, O^{24}$$

The degree of dissociation depends on the oxide concentration in the melt and decreases with increasing amount of orthophosphate added.

Electrochemical measurements were performed in the systems Na_3AlF_6-$AlPO_4$, Na_3AlF_6-Al_2O_3-$AlPO_4$, Na_3AlF_6-Al_2O_3-Na_3PO_4 and NaF-Na_3PO_4. By means of cyclic voltammetry, chronoamperometry, chronopotentiometry and square wave voltammetry the behaviour of the P(V) species were studied. The most suitable electrode materials were found to be tungsten and copper. With a tungsten working electrode the number of electrons transferred when reducing P(V) in an alumina-saturated cryolite melt was found to be two. The diffusion coefficient for the PO_4^{3-} added as Na_3PO_4 at 1000 ºC was calculated to be $(9.2 \pm 1.0)\cdot10^{-6}$ cm^2/s with cyclic voltammetry and $(6.8 \pm 0.7)\cdot10^{-6}$ cm^2/s with chronopotentiometry. When adding $AlPO_4$ the diffusion coefficients of the P(V) species at 1000 ºC seem to vary from $1.2\cdot10^{-5}$ to $2.1\cdot10^{-5}$ cm^2/s for cyclic voltammetry, while for chronopotentiometry and chronoamperometry the values were between $1.9\cdot10^{-5}$ and $2.5\cdot10^{-5}$ cm^2/s. The reduced phosphorus species seemed to adhere on the tungsten working electrode.

URN:NBN:no-6427

In the pure cryolite system the reduction of P(V) on a copper electrode at 1020 ºC seemed to involve three electrons. However, the number of electrons transferred when using the tungsten electrode at 1020 ºC was found to be 2 as for the alumina-saturated system. For both electrode materials the system under study was found to be soluble-soluble. The diffusion coefficients for the P(V) species determined with the copper electrode was found to be between $1.6 \cdot 10^{-5}$ and $1.8 \cdot 10^{-5}$ cm^2/s. In the case of the tungsten working electrode, they were found to be about $1.9 \cdot 10^{-5}$ to $2.2 \cdot 10^{-5}$ cm^2/s.

At low contents of aluminium orthophosphate in pure molten cryolite, two peak couples were observed. Two possible mechanisms were proposed. One of them included reduction of P(V) to P(III) and further to P(I), while in the other the reduction of two different P(V) species (PO_4^{3-} and PO_3^-) to P(III) species was suggested.

Since the deposition of aluminium might hide further reduction steps of phosphorus, electrochemical studies in the pure sodium fluoride system with addition of Na_3PO_4 were performed at 1002 ºC and 1005 ºC with a tungsten working electrode. The investigation indicated that the orthophosphate ion dissociates into an oxide ion and a phosphorus containing species. The number of electrons transferred when reducing the phosphorus compounds was determined to be 2. The oxide ion seemed to oxidize the tungsten working electrode forming tungsten oxide compounds. The number of electrons transferred in this reaction was found to be 1. The diffusion coefficient of the O^{2-} species was determined to be between and $3.2 \cdot 10^{-5}$ to $7.4 \cdot 10^{-5}$ cm^2/s.

Additions of Na_3PO_4 to industrial cells (prebake, 230 - 250 kA) were performed and the variation of the concentration in both bath and metal was followed over time. Phosphorus seemed to have a longer retention time in the bath than metallic impurities e.g. silicon or titanium. Variations in the anode-cathode distance and interruption of the cell current seemed to influence the phosphorus level in the cell temporarily. Since carbon particles in the electrolyte act as a nucleation site for impurities, additions of carbon dust to the electrolyte were made. The carbon dust addition did not appear to have an influence on the phosphorus in the bath or metal, however a small increase in the phosphorus concentration in the bath was observed after addition. A model for the behaviour of phosphorus and other impurities was established including the distribution in the electrolyte and the mass transfer to the metal. The distribution times for a SBS prebake cell

operating at 230 to 250 kA (30 anodes) were found to be between 2.5 and 3 hours. From industrial data trends could be observed where the amount of phosphorus in the cell decreases with increasing temperature.

Mass balances for phosphorus for both prebake cells (fed with secondary alumina) and Søderberg cells (fed with primary alumina) are presented. For the Søderberg cells it was found that only about 10% of the phosphorus entering with the raw material ends up in the metal. In case of the prebake cells apparently up to 80%. of the phosphorus entering with the raw materials leaves the cell with the metal.

A laboratory study on the behaviour of phosphorus during electrolysis was performed. The results confirmed that approximately 1% of current efficiency is lost for each 100 ppm P present in the electrolyte. It turned out that the phosphorus concentration found in the bath remained almost constant throughout the period of electrolysis. Several electrolysis experiments were performed at temperatures between 940 ºC to 1020 ºC to investigate the effect of temperature on the bath/metal ratio concerning phosphorus. For some experiments carbon dust was added or the current interrupted for a certain period of time to observe how this influences the concentration of phosphorus in bath and metal. A tentative mechanism for the behaviour of phosphorus impurities in the Hall-Héroult process was proposed.

URN:NBN:no-6427

Melk er mer enn kalsium!

Fosfor – viktig for skjelettet.
Mange av stoffene som kroppen trenger for å fungere, er ukjente for de fleste av oss. Fosfor er ett av dem. Dette mineralstoffet er nødvendig for bein og tenner. Hele 80 % av fosforet er bundet sammen med kalsium. Fosfor har også andre viktige oppgaver. Stoffet er for eksempel nødvendig for at vitaminene B1 og B6 skal virke i kroppen. Det er rikelig med fosfor i norsk kosthold. Melkeprodukter er den matvaregruppen som inneholder mest. To glass melk og noen skiver brunost og hvitost er nok til å dekke den mengden fosfor som en voksen kropp trenger daglig. Andre matvarer som er rike på fosfor, er grove brød- og kornvarer, erter, fisk, kjøtt, lever og egg.

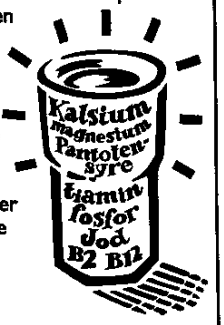

*" **Milk is more than calcium!***

<u>Phosphorus</u> – important for the skeleton.

Many of the substances, which the body needs to function, are unknown to most of us. One of them is phosphorus.
This mineral is necessary for bones and teeth. About 80% of phosphorus is bound together with calcium. Phosphorus has also other important tasks. The substance is e.g. necessary for the vitamines B1 and B6 to function in the body. In norwegian nutrition there is plenty of phosphorus. Diary products are one of the food groups, which contain the most. Two glasses of milk and some slices of cheese are enough to supply the body of an adult with the daily amount.
Other food groups, which are rich in phosphorus are wholemeal bread and corn products, peas, fish, meat, lever and eggs."

(information on norwegian milk carton)

Acknowledgements

This work was carried out under the supervision of Professor emeritus Dr. Jomar Thonstad and Professor Dr. Geir Martin Haarberg at the Institute for Materials Technology (IMT) at the NTNU Trondheim. I am very grateful for their guidance throughout this period and the growing interest in my work.

I would like to express my sincere thanks to Ana Maria Martinez, who was a great support when it came to questions regarding electrochemical methods. Her patience with me is highly appreciated.

For practical guidance, discussions on theoretical matters and good times in the "coffee corner" I would like to thank Lisbeth Støen, Karen Sende Osen, Sverre Rolseth, Henrik Gudbrandsen, Espen Olsen, Egil Skybakmoen and Asbjørn Solheim from SINTEF Materials Technology, Electrochemistry and Ceramics. Social events as the Baccalau parties or the "Bondefest" will be dearly remembered.

From the staff at the IMT, I would like to thank Martha Bjerknes and Kjell Røkke for their helpfulness throughout the years of this thesis.

The industrial measurements were carried out at the Hydro Aluminium plant in Årdal. I am grateful for the support and help I obtained from Elin Haugland, Trond Støre, Trond Eirik Jentoftsen and Rune Hovland.

I would like to express my thanks to Professor Lars Arnberg (NTNU) Ernest W. Dewing (Kingston, Canada) and Odd-Arne Lorentsen, who took the time to read through parts of my thesis. Their comments and advices are highly appreciated. Gro Soleng and Marthe Folstad are gratefully acknowledged for their help in the laboratory studies.

I would like to thank Professor Vladimir Danək and Martha Chrenkova for fruitful discussions and their hospitality during my stay in Bratislava (Slovakia). For interesting conversations and financial support in connection with a visit to KUBAL in Sundsvall (Sweden) I would like to express my gratitude to Stig Handå.

I would also like to thank my former "hall"-colleagues Niels Peter, Odd-Arne, Trond Eirik and Gro for memorable years. I am also very grateful for

the cheerful talks late in the night or at the weekends with Espen Sandnes, especially in the last period of this thesis. Thanks to all friends and colleagues at the institute, who made the time enjoyable.

The Research Council of Norway and the Norwegian aluminium industry are gratefully acknowledged for their financial support of this work in connection of the PROSMAT Primary Aluminium Programme.

Furthermore, I would like to thank my husband Ulrik for his specialist support regarding my thesis and the moral support throughout the last years. My mother's support and encouragement during the last years is deeply acknowledged. Even though the subject might be beyond her comprehension, this work would not have been accomplished without her.

Finally, I would like to thank my two sons, Martin and Lars, who made it clear that there is more to life than just this thesis.

Elke Willam Thisted

August 2003

Table of content

List of symbols and abbreviations

Symbol	Meaning	Units
a_i	activity of species i	
Ŭ	degree of dissociation of the cryolite	
ɓ	degree of dissociation of the orthophosphate	
c_{added}	amount added to cell	ppm
$c_{bath}(t)$	concentration in bath at time t	ppm
c_{bc}	background concentration	ppm
$c_{boundary}$	concentration at boundary interface	ppm
C_d	capacitance of the double layer	$F \cdot cm^{-2}$
c^o	bulk concentration	$mol \cdot cm^{-3}$
$\subseteq c_o$	concentration gradient for species O	
c_O	concentration for species O	$mol \cdot cm^{-3}$
$c_O(x,t)$	concentration of species O at position x and time t	$mol \cdot cm^{-3}$
qpc_p	specific heat	
$c_R(x,t)$	concentration of species R at position x and time t	$mol \cdot cm^{-3}$
d	distance between lattice plane	Å
D_O	Diffusionscoefficient for species O	$cm^2 \cdot s^{-1}$
D_R	Diffusionscoefficient for species R	$cm^2 \cdot s^{-1}$
qpE	square wave potential in SQWV	V
E°	standard potential	V
E_d°	standard decomposition potential	V
E_d	decomposition potential	V
E_p	peak potential	V
E_p^a	peak potential of anodic peak	V
E_p^c	peak potential of cathodic peak	V
$E_{1/2}$	half wave potential	V
$E_{1/2}^c$	half wave potential of cathodic peak	V
$E_{p/2}^c$	half peak potential of cathodic peak	V
E^{rev}	reversible potential	V
E_{start}	starting potential	V
E_{Step}	staircase potential in square wave voltammetry	V
$E(t)$	potential at time t	V
$E_{ϑ4}$	quarter-wave potential in chronopotentiometry	V
q	(1) viscosity	mPa Ţs
	(2) overvoltage	V
f	frequency	s^{-1}
F	Faraday constant (96487)	$C \cdot mole^{-1}$
qpG°	standard Gibbs reaction energy	$kJ\ mole^{-1}$

Symbol	Meaning	Units
$\div G_{f(T)}$	Gibbs energy of fusion	kJ mole^{-1}
$\div \overline{G}_i$	partial molar Gibbs energy of species i	kJ mole^{-1}
qpG^{rx}	Gibbs energy of reaction	kJ mole^{-1}
$\div H_{f(T)}$	Gibbs enthalpy of fusion	kJ mole^{-1}
$\div \overline{H}_i$	partial molar Gibbs enthalpy of species i	kJ mole^{-1}
$\div H^o_{tot}$	total standard Gibbs enthalpy	kJ mole^{-1}
I	current	A
i	current density	A·cm^{-2}
i_b	background current density	A·cm^{-2}
i_c	capacity current density	A·cm^{-2}
i_l	limiting current density	A·cm^{-2}
i_p	peak current density	A·cm^{-2}
i_p^a	peak current density of anodic peak	A·cm^{-2}
i_p^c	peak current density of cathodic peak	A·cm^{-2}
ŭi_p	differential peak current density	A·cm^{-2}
i_r	residual current density	A·cm^{-2}
$J_{(}$	flux of species i	mol·cm^{-2}·s^{-1}
k	rate constant	m·s^{-1}
k_{bath}	mass transfer coefficient from bath into metal	m·s^{-1}
k_B	Boltzmann constant (1.38066·10^{-23})	J·K^{-1}
k_m	mass transfer coefficient	m·s^{-1}
k_1	Distribution coefficient	s^{-1}
k_2	mass transfer coefficient	s^{-1}
K	equilibrium constant	
ə	(1) time of change in potential direction	s
	(2) wavelength in XRD measurements	Å
m	weight	kg
M	molar weight	g·mole^{-1}
n	(1) number of electrons	
	(2) number of moles	
з	(1) sweep rate	V·s^{-1}
	(2) amount of new species in cryoscopy	
p_i	pressure of gaseous species i	
P	specific electric energy consumption	kWh/kg
Q	reaction constant	
R	(1) universal gas constant (8.31443)	J·K^{-1}·mole^{-1}
	(2) resistance	q
r_i	radius of ion i	pm
rpm	rounds per min	min^{-1}
$\div S_{f(T)}$	Gibbs entropy of fusion	J mole^{-1} K^{-1}

Symbol	Meaning	Units
$\div\overline{S}_i$	partial molar Gibbs entropy of species i	J mole^{-1} K^{-1}
Ű	(1) transistion time in chronopotentiometry	s
	(2) time of pulse in square wave voltammetry	s
T	temperature	˚C or K
d	scattering angle in XRD measurements	radians
T_f	temperature of fusion	˚C or K
U	cell voltage	V
V	Volume	m^3
$W_{1/2}$	half-height width of the peak in square wave voltammetry	V
x_i,	weight fraction of species i	
x_i	mole fraction of species i	
$\mathfrak{I}_i$	activity coefficient of species i	

Abbreviation	Meaning
ACD	anode cathode distance
CA	chronoamperometry
CE	current efficiency (%)
CP	chronopotentiometry
CR	cryolite ratio (mole NaF/mole AlF_3)
CV	cyclic voltammetry
CWPB	center worked prebake
DS	dry scrubber
ETE	end-to-end
HSS	Horizontal Stud Søderberg
ICP-AES	inductively coupled plasma – atomic emission spectrometry
OCP	open circuit potential
PFPB	point fed prebake
ppm	part per million of weight
ref.	Reference
SBS	side-by-side
SEM	Scanning electron microscope
SHE	Standard hydrogen electrode (1 atm, 25 ˚C)
SQWV	square wave voltammetry
VSS	Vertical Stud Søderberg
XRF	X-ray fluorescence spectroscopy
XRD	Powder X-ray Diffraction

1. Introduction

The interest for phosphorus in aluminium production has increased significantly since the cell design changed to more closed systems and dry scrubbers with recycling of alumina were introduced. The current efficiency for aluminium in modern cells is typically in the range from 92-96%. Further increase of the current efficiency depends on improving factors that contribute only marginally. One of these factors is the behaviour of impurities in the cells, especially for phosphorus. For each 100 ppm phosphorus in the electrolyte, the current efficiency is reduced by about 1% [1]. Furthermore, there is a limit on the phosphorus content in aluminium, especially for cast alloys. To avoid future problems due to phosphorus, it is necessary to improve the understanding of the behaviour of phosphorus in industrial cells.

1.1. History of the production of primary aluminium

In nature it is not common to find aluminium in its elemental state [2]. Due to its chemical activity, aluminium occurs usually in an oxidized state, as oxide, silicate or in compounds with both calcium and silicon. The electrolytic production of aluminium from these raw materials in aqueous solutions is not possible since hydrogen is more noble than aluminium. Therefore, it was a demanding task to develop a process where aluminium compounds were sufficiently soluble in a non-aqueous solvent, so that electrochemical reduction was possible.

In 1808 H. Davy was the first person to isolate small amounts of Al-Fe-alloy by an electrothermic-electrochemical method. The product was named aluminium. Several attempts were made since then to produce aluminium commercially. In 1854 the electrolysis of sodium tetrachloroaluminate as a process to produce aluminium was studied independently by Bunsen and Deville [1]. This was the first process used for commercial production of aluminium. However, the aluminium content was only about 96% and the manufacturing costs were high.

A major contribution to the rapid commercialization of electro-metallurgy was the invention of new steam-engine driven dynamos from Siemens and Tesla [3, 4]. While Siemens managed to commercialize his invention by himself, “Westinghouse bought the patent rights to Tesla’s polyphase

system of alternating–current dynamos" and started large-scale production [5-7].

Charles Martin Hall in the USA and Paul Louis Touissaint Héroult in France independently developed and patented another process in 1886, based on electrolysis of alumina, Al_2O_3, dissolved in molten cryolite, Na_3AlF_6. The Hall's cell from the patent of the process and the cell of Héroult are shown in Figure 1-1 and 1-2 [8].

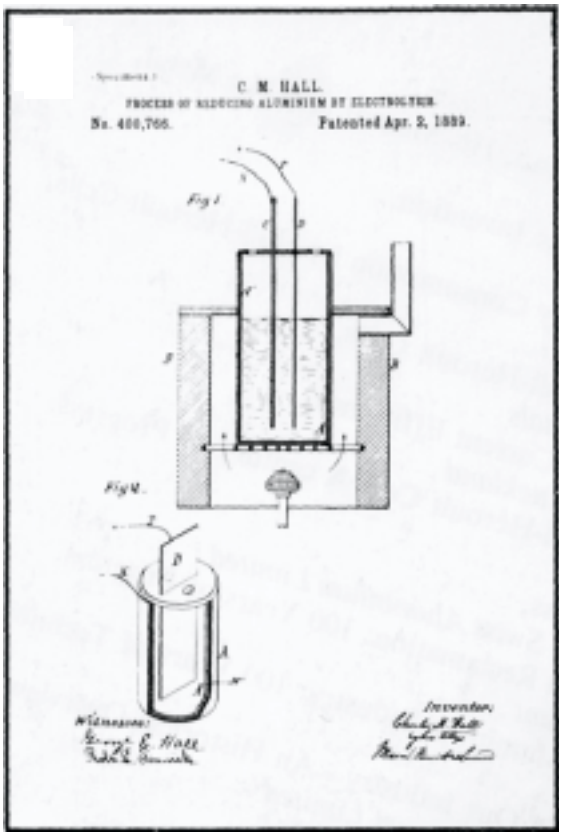

Fig. 1-1: *Hall's cell in the patent from 1889.*

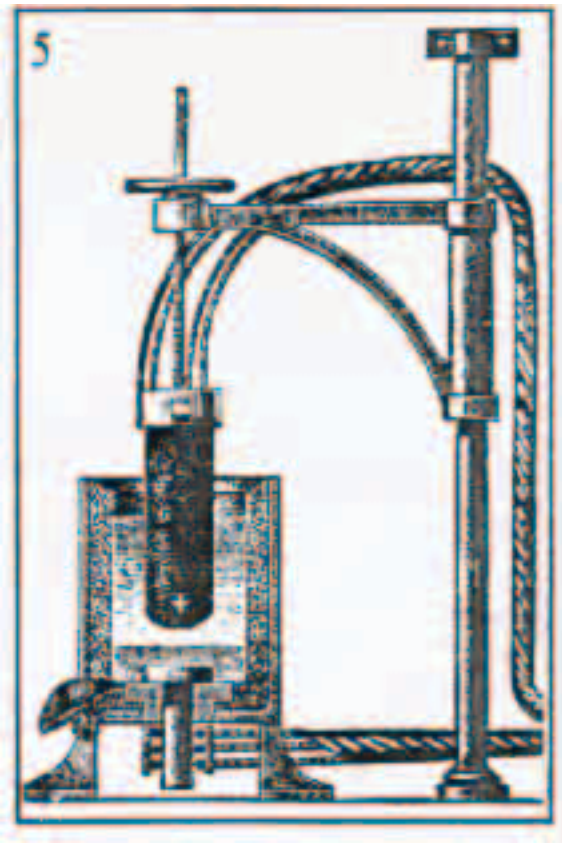

Fig. 1-2: *Héroult's cell for production of aluminium 1892.*

The development of this method led to the only commercial process by which aluminium is produced today – the Hall-Héroult process.

1.2. The Hall-Héroult process

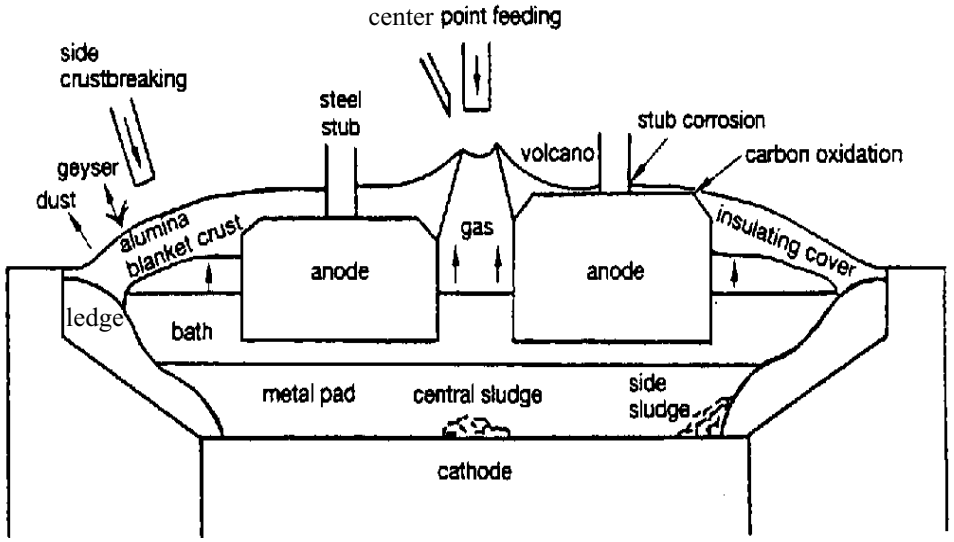

Fig. 1-3: *Schematic view of an alumina reduction cell [9]. Both side crustbreaking and centre point feeding are shown.*

A schematic view of an alumina reduction cell with two possible alumina feeding mechanisms, center point feeding and side crustbreaking, is illustrated in Figure 1-3. When alumina dissolves in the electrolyte, the oxide ions will be discharged at a carbon anode, forming carbon dioxide, CO_2, thereby consuming the anode, while the aluminium ions will be reduced at the metal pool. The actual cathode is the liquid aluminium metal, but it became common to describe the carbon lining of the cell as cathode as well. The overall chemical reaction, by which aluminium is produced, can be written as [10]:

$$2\,Al_2O_{3|dissolved}0\;2\;3\,C_{(s)}\;|\;4\,Al_{(l)}\;2\;3\,CO_{2(g)} \qquad (1.1)$$

Cryolite is the main component of the electrolyte, with an alumina content of 2 - 4 wt%. The bath has some additional constituents as excess aluminium fluoride, AlF_3, (6 - 13 wt%) and calcium fluoride, CaF_2, (4 - 6 wt%). Sometimes lithium fluoride, LiF, or magnesium fluoride, MgF_2, (2 - 4 wt%) are added as well, while the content of aluminium fluoride then has to be reduced correspondingly (6 - 7 wt%) [10]. The bath temperature is normally in the region from 940 ºC to 970 ºC.

Besides being the reactant for producing aluminium, alumina has to serve as cell cover to decrease the heat and vapour losses of the cell as well as

avoiding air-burn of the anodes. Thirdly, alumina is used in the so-called dry-scrubber system, which reduces emissions from the cells by anode gas cleaning. Alumina powder is used to adsorb the hydrogen fluoride gas and other vapours, which are mainly sodium tetrafluoroaluminate, $NaAlF_4$. The fluoride-rich alumina, also called secondary alumina, rejoins the bath as feeding material.

The alumina feeding rhythm of the cells is very important for a stable cell operation. Too low alumina concentration will lead to a so-called anode effect, where carbon fluorides instead of carbon oxides form as the anode products and the cell voltage increases up to 40 - 50 V. If too large quantities of alumina are added at once or the solubility limit of the aluminium oxide in the bath is exceeded, the formation of so-called muck or sludge is possible. Sludge is a viscous mixture of solid alumina particles and bath. It can be found either on the surface of the metal pad or underneath it forming so-called bottom sludge. Lying on top of the metal pad or along the ledges, the dissolution of sludge can be fairly rapid, while bottom sludge dissolves rather slowly, especially when it converts into corundum. Larger pieces of crust might break off, for example when changing an anode, and sink through the bath and the metal phase to form sludge or muck as well [11].

Earlier systems, where alumina was added by side- or centre-breaking the crust of the cell at long time intervals, caused a large variation in the alumina concentration of the bath. In modern cells automated point-feeders, which usually are mounted in the center channel of the cell, Figure 1-4, supply the bath with small amounts of alumina every three to four minutes [10], which leads to a more stable alumina concentration and better cell operation.

With regard to anode design there are two main types, which involve either pre-manufactured anodes as shown in Figure 1-4 or self-baking anodes, see Figure 1-5.

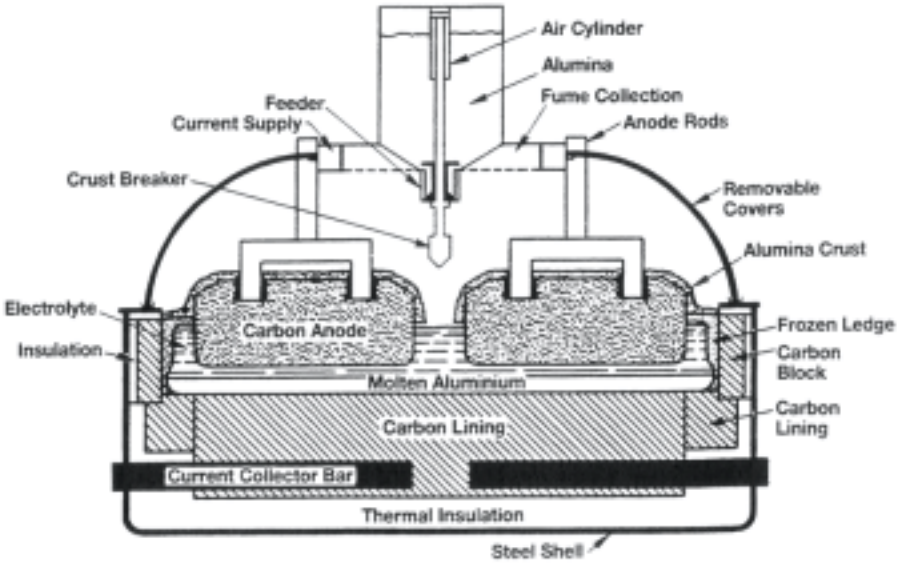

Fig. 1-4: *Cell with prebaked anodes.*

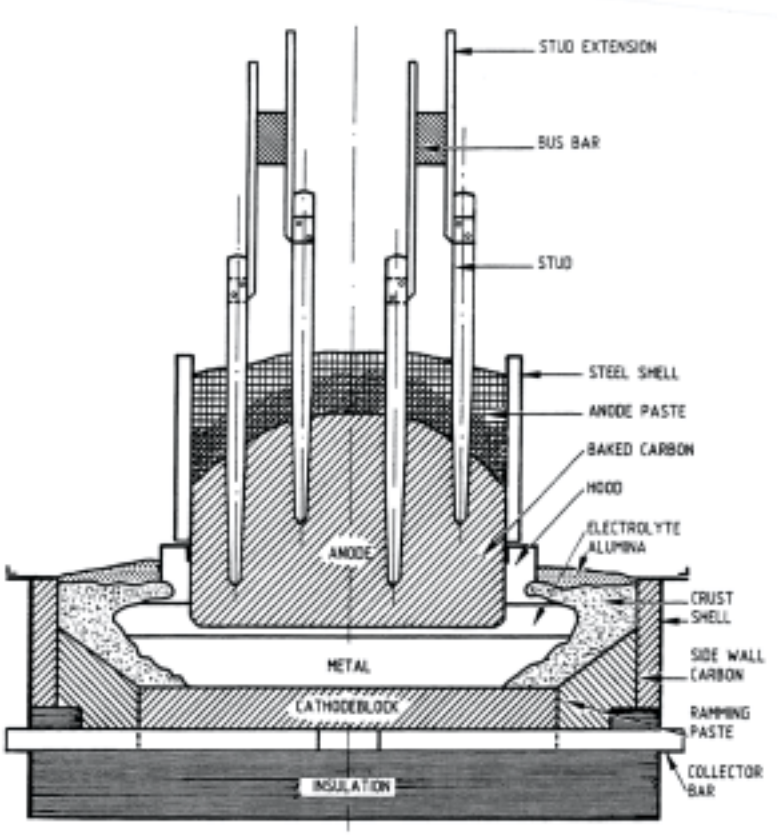

Fig. 1-5: *Cell with Søderberg anode.*

The cell shown in Figure 1-4 is called a prebake cell, while the cell in Figure 1-5 with self-baking anodes is called a Søderberg cell after the inventor of this type of anodes. Both cell types are currently used in the aluminium industry. The advantages when using a prebake type of cell are a lower carbon consumption compared to the Søderberg type and the gas collection hoods, which gives a better heat balance for the cell as well as a better working environment. When an anode in a prebake cell is consumed after 22 - 26 days to one-third to one-fourth of its original size, it has to be replaced. This operation causes disturbances in cell operation, local temperature changes in the bath and varying local current densities.

For a Søderberg cell with its continuous, self-baking anode, this operation is not necessary. However, the spikes or studs, which supply the cell/anode with electric current, are pulled and reset at a higher level when they approach the bottom surface of the anode. The studs can either be mounted vertically (VSS), as shown in Figure 1-5, or horizontally (HSS) in the case of older Søderberg cells [10]. A disadvantage of the Søderberg technology is the poor ability to dissolve and distribute alumina in the bath due to its cell design.

Modern prebake cells (PFPB) have an almost continuous feed of alumina with the help of typically four point feeders at the center channel, which allow an even distribution of alumina in the bath. Søderberg cells, both HSS and VSS, as well as older, center-worked prebake cells (CWPB) are crust fed cells, where the time interval between each alumina addition is rather long, and the additions are correspondingly larger. This technological disadvantage of Søderberg cells is compensated by higher cell temperatures and a lower acidity of the bath, which allows the alumina to dissolve faster.
It should be mentioned, that a new Søderberg technology has been developed, where the anode top is hooded, emissions of the cells are led to the dry scrubber system and the addition of the alumina is done by point feeders [12].

Looking at the bath chemistry, it is generally agreed that molten cryolite dissociates into sodium ions, Na^+, and hexafluoroaluminate ions, AlF_6^{3-}.
The equilibrium for dissociation concerning hexafluoroaluminate was up to 1980 believed to be

$$AlF_6^{34} \mid AlF_4^4\ 2\ \ 2\,F^4 \qquad (1.2)$$

Several authors like Dewing [13], Feng et al. [14] and Gilbert et al. [15] questioned the existing dissociation model by introducing a new possible ion, AlF_5^{2-}. The hexafluoroaluminate could therefore also dissociate into smaller complex ions by the following equilibria.

$$AlF_6^{34} \mid AlF_5^{24} \; 2\,F^4 \tag{1.2a}$$

$$AlF_5^{24} \mid AlF_4^4 \; 2\,F^4 \tag{1.2b}$$

The existence of AlF_6^{3-}, AlF_4^- and especially AlF_5^{2-} has been indicated by both Raman spectroscopy [15] and NMR studies [16], while the distribution concerning the equilibria is clearly depending on the cryolite ratio (CR).

With alumina present, there exist oxyfluoroaluminate complexes, such as $Al_2OF_x^{(4-x)}$ and $Al_2O_2F_y^{(2-y)}$, where x may be 8 or 6 and y may be 6 or 4. While species of the type $Al_2OF_x^{(4-x)}$ have been suggested for low alumina concentration in the bath, the species $Al_2O_2F_y^{(2-y)}$ will prevail at high alumina concentrations. These oxyfluoroaluminates transport the oxide ions to the anode, where they will be discharged.
Even though there are several ions existing in the bath, it is the sodium ion, Na^+, which is carrying about 95 to 99% of the electric current through the bath. The residual current is carried by the fluoride ions [17].

The improvements made on the Hall-Héroult process over the last two decades made it possible that modern cells with prebake technology are able to reach current efficiencies (CE) of 96% [18]. The loss of the last percentages is mainly due to the back reaction of aluminium with carbon dioxide, both dissolved in the electrolyte,

$$2\,Al_{(dissolved)} \; 2\,3\,CO_{2(g)} \mid Al_2O_{3(dissolved)} \; 2\,3\,CO_{(g)} \tag{1.3}$$

as well as being due to the presence of impurities in the electrolyte. Furthermore, electronic conduction, short circuits or parallel current paths lower the CE. To a lesser extent metal absorption into the cell lining or losses by tapping contribute to decreased CE [10].

Since the invention of the Hall-Héroult process the energy consumption was one main factor to be kept as close as possible to the minimum needed.

From thermodynamic data the minimal required energy can be calculated with x = CE/100 and a temperature of 977 ºC [10]:

$$\div H^{o}_{tot} \mid \left(\frac{1.43}{x} 2\ 4.91\right) kWh \left(kg\ Al\right)^{41} \qquad (1.4)$$

With a current efficiency of 94% the minimum energy requirement is calculated to be 6.43 kWh/(kg Al).

Including the cell voltage (U), the specific electric energy consumption (P) can be calculated as well by using equation (1.5) [18]:

$$P \mid \frac{2.980 \left(U\right.}{CE} \qquad (1.5)$$

With a typical cell voltage of 4.2 V and a CE of 94%, the specific electric energy consumption is 13.3 kWh/(kg Al).
In modern alumina reduction plants the usual energy consumption is in the range from 13 - 14 kWh/(kg Al). A forecast for the next 20 years shows that the energy consumption will reach 12 – 12.5 kWh/(kg Al) due to an increase in CE and a decrease in cell voltage [18].

1.3. Impurities in the process

1.3.1. Nature and type of impurities

It was known for a long time that impurities in the aluminium production process disturb the cell performance and lower the metal quality. Already in the 19th century, Hall described in his patent [19] the importance of the purity of alumina and suggested methods of cleaning this raw material. The impurities focused on in those days were silicon, iron and titanium.
Modern analysis techniques have made it possible to detect more impurities in the process and have helped to elucidate their importance. According to Grjotheim et al. [1] “all impurities are – to a varying extent – deleterious to aluminium electrolysis. They may take part in the electrochemical process and, depending on their character, may influence the electrolysis in several ways”. As such should be mentioned:

1) Impurities and components of the electrolyte may react and thereby change its chemical composition.

2) Carbon in the anode and in the bath or the carbon lining may react with impurities.
3) Impurities with a lower decomposition potential than alumina may react electrochemically.

Impurities enter the process mainly by the raw materials, which are fed to the cells. These are alumina, carbon anodes and bath components, in particular aluminium fluoride. Nevertheless, it should be mentioned that some impurities originate from tools used for cell maintenance (iron) as well as from the cell lining (silicon) [18].
Depending on their behaviour in the electrolyte, Grjotheim et al. [1] have divided the impurities into several categories:

1) water
2) metal oxides with higher decomposition potential than alumina
3) metal oxides with lower decomposition potential than alumina
4) non-metal oxides
5) sulphurous compounds

In this work the main interest lies at non-metal oxides, where the two main examples are boron and phosphorus oxide. Other important non-metal compounds are sulphurous species.

1.3.2. Behaviour and reactions of impurities

Impurities, which are more noble than aluminium, will tend to end up in the metal, while impurities which are less noble, will tend to accumulate in the electrolyte. A more noble impurity should theoretically deposit entirely into the metal, but in reality the transfer to the metal phase is never complete.
Assuming that the major part of the impurities that enter the process, are present as oxides and react with the bath, the dissolution might take place as follows:

$$M_xO_y + 2\frac{2y}{3}AlF_3 \rightarrow xMF_{2y/x} + 2\frac{y}{3}Al_2O_3 \qquad (1.6)$$

Usually the saturation concentration for an impurity species will not be reached in the electrolyte, and therefore, all impurities are present in their dissolved form. In some cases aluminates, for example MAl_2O_4, can be formed as the stable solid phase, when the pure oxide is not the stable form at high alumina concentrations:

$$MO + Al_2O_3 = MAl_2O_4 \quad (1.7)$$

If M is more noble than aluminium, it will be reduced into the metal, as shown in reaction (1.8):

$$MF_{2y/x} + \frac{2y}{3x} Al = M_{in\ Al} + \frac{2y}{3x} AlF_3 \quad (1.8)$$

From a thermodynamic point of view the reaction behaviour of different impurities can be expressed by their decomposition potential in comparison to that of alumina (see Section 2.2.2.). Phosphorus oxide compounds are found to be more noble than alumina. The deposition of phosphorus pentoxide can be expressed as followed:

$$2\,P_2O_{5(l)} + 5\,C = 5\,CO_{2(g)} + 2\,P_{2(g)} \quad (1.9)$$

According to thermodynamical calculations $E^o(P_2O_5)$ = +0.1 V at 1020 ºC, while the deposition potential of alumina when reacting with carbon is –1.16 V at the same temperature. Therefore it is expected that phosphorus pentoxide should react according to the following scheme [1]:

$$3P_2O_{5(l)} + 10Al_{(l)} = 5Al_2O_{3(l)} + 3P_{2(g)} \quad (1.10)$$

At temperatures around 950 ºC elemental phosphorus will be in its gaseous state, as indicated in reaction (1.10). Therefore, contrary to metal oxides, which are more noble than alumina, only a small amount of phosphorus will alloy with the aluminium metal. Beer [20] investigated the solution of aluminium phosphide, AlP, in aluminium in the temperature range of 900 ºC to 1200 ºC and found, that at e.g. 980 ºC about 0.194 wt% P is soluble in liquid aluminium. The major part of the phosphorus might therefore escape from the metal pad when reduced and thereby return to the bath, where it can be reoxidized by the anode or CO_2. Some phosphorus will escape with the off-gas from the cell in form of $P_{2(g)}$ or as the oxide, $P_2O_{5(g)}$, or an oxyfluoride compound, $POF_{3(g)}$ [1, 16], or adsorbed on particles leaving the cell with the gas flow [21].

The off-gas from the cell contains CO_2, CO and some fluorides in the form of HF and particulates. To reduce fluoride losses from the cell, these fluorides in the off-gas are collected in a gas-cleaning facility called dry scrubber as mentioned earlier, where they will be adsorbed on primary

alumina. Not only the fluorides will be adsorbed, but also volatile impurities like phosphorus compounds, which will be returned to the cell as well.

Therefore, it is important to keep the phosphorus level in the raw materials as low as possible. Thonstad et al. [18] reported a typical phosphorus concentration (P_2O_5) in primary alumina of around 0.0004 - 0.0011 wt%, while for aluminium fluoride it is 0.015 - 0.020 wt%. Even though the phosphorus content in the aluminium fluoride is higher than in the primary alumina, the main source of phosphorus in the alumina reduction process is the alumina. This is due to the feeding frequencies of alumina in comparison to aluminium fluoride. The consumption of alumina is several times higher than that of aluminium fluoride, and therefore the amount of AlF_3 added is very small compared to the alumina addition during one day.

A certain amount of phosphorus is introduced through the anode carbon, which normally contains 0.0007 wt% phosphorus (P) [22]. The inclusion of phosphorus impurities in the carbon matrix may result in a reduced oxidation rate [1]. By addition of P_2O_5 the combustion rate of the anode can be reduced, or the combustion can be inhibited by converting active catalysts to less active phosphates. However, addition of P_2O_5 in the anode carbon cannot be tolerated due to its detrimental effect on the current efficiency.

Another possible phosphorus source might be the phosphate binders of the cell lining. Phosphoric acid or phosphates are the most common binders for refractory materials, since the thermal and mechanical resistance will be much higher than for pure high-alumina bricks. The usage of these high-alumina bricks instead of the traditional chamotte bricks in electrolysis cells and alloying furnaces of the aluminium industry has become more common in recent years [23]. Since the lining of the cell is covered by both carbon blocks and frozen bath, a possible diffusion of phosphorus from the side- and bottom lining into the electrolyte should be negligible. In addition, it should be mentioned, that usually the mass transport takes place from the bath to the metal and further into the bottom lining. Therefore, transport of phosphorus in the opposite direction seems rather unlikely.

Due to the use of dry scrubbers, phosphorus, among other impurities, is recycled, thereby reentering the process. But this is not the only cycle phosphorus is believed to go through. It is assumed that phosphorus cycles between reduction at the metal pad and oxidation at the anode or by CO_2.

This redox cycle is probably the main reason why phosphorus is the most harmful impurity when it comes to current efficiency losses. As stated in the literature [1] the current efficiency decreases by 1% when 100 ppm of phosphorus, P, is present in the bath. On a laboratory scale, Solli [24] showed that the current efficiency was reduced by 0.68% per 100 ppm P present in the bath.

1.3.3 Effect of phosphorus on the metal quality

Although phosphorus is present only to a minor extent with aluminium, even a small amount of P can increase the brittleness of the metal and lower the corrosion resistance according to Grjotheim et al. [1]. The solubility in molten aluminium is around 0.01% P at 660 ºC [25].
The effect of phosphorus on aluminium metal concerns mainly its alloys with silicon, Si. The Al-Si system is a simple binary system, and has a eutectic point at around 12.7 wt% Si [26]. Based on the eutectic point the system can be divided into hypo- and hypereutectic alloys.

Hypoeutectic alloys with up to 12.7 wt% Si are the most important alloy group of the Al-Si system. A very coarse microstructure of an unmodified alloy with 12 wt% Si is shown in Figure 1-6 where plates or needles of silicon are embedded in a continuous aluminium matrix.

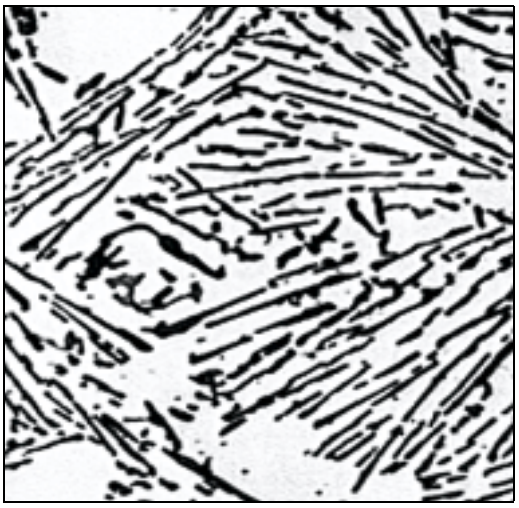

Fig. 1-6: *unmodified Al-Si alloy with 12 wt% Si, SEM-magnification Δ 400, [26].*

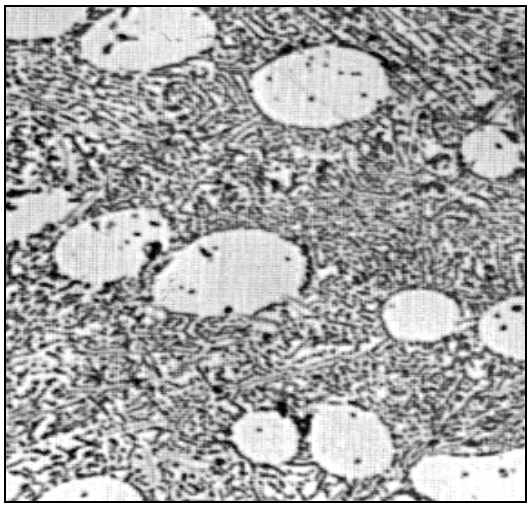

Fig. 1-7: *Al-Si alloy (12 wt% Si) modified with sodium, SEM-magnification Δ 400, [26].*

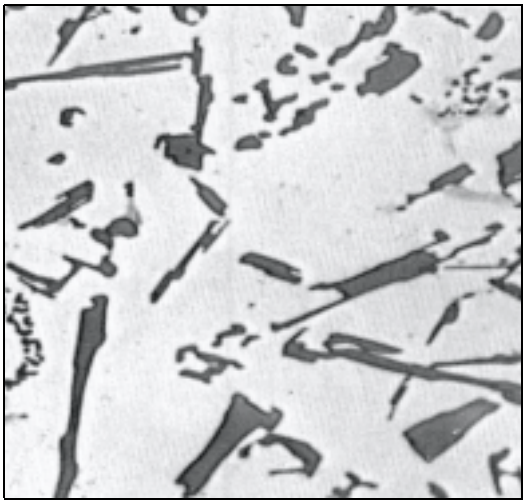

Fig. 1-8: *Al-Si alloy (12 wt% Si) with excess phosphorus, SEM-magnification Δ 400, [26].*

Additions of strontium or sodium will modify and refine the microstructure (see Figure 1-7). The eutectic temperature may be depressed by as much as 12 ºC through adding strontium or sodium. The growth mechanism of the aluminium-silicon eutectic is changed [26] due to the adsorption of the modifying elements (strontium or sodium) on the silicon crystals. This results in a finer microstructure. The compound AlP formed by a reaction of aluminium with impurity amounts of phosphorus, will serve as nucleation sites for silicon and thereby counteract the effect of strontium or sodium. If phosphorus is present in an excessive level, it will again produce a coarse microstructure, like in Figure 1-8. The effect of phosphorus on the microstructure of the alloy can be eliminated to a certain degree by adding more strontium or sodium as well.

Fig. 1-9: *hypereutectic alloy without phosphorus, SEM-magnifcation Δ100, [27].*

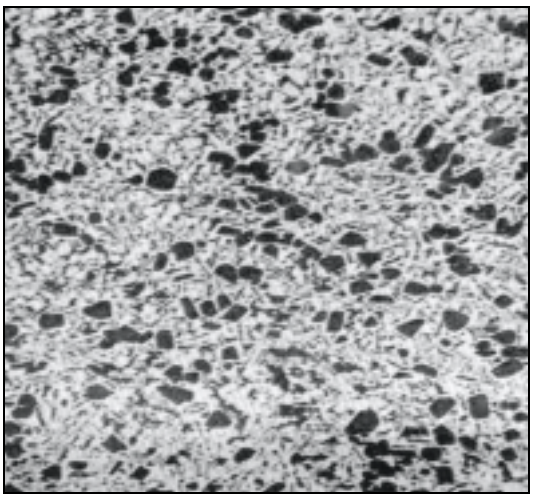

Fig. 1-10: *hypereutectic alloy with small phosphorus additions, SEM-magnification Δ100, [27].*

Hypereutectic alloys represent all alloys with a silicon content higher than 12.7 wt%. In these alloys silicon particles are distributed in the eutectic (see Figure 1-9). The hard primary silicon particles provide a high wear resistance of the alloy. Since it is desirable, for improved ductility, to have well refined primary silicon crystals, 0.01 to 0.03 wt% phosphorus is added in form of $AlCu_{19}P_{1.4}$ or CuP_{15} . The expression well refined means that silicon has reached a fine, homogeneous distribution in the metal phase. As explained for the hypoeutectic alloys, insoluble particles of AlP will form, which serve as nuclei on which silicon can grow in more dispersed ways (see Figure 1-10).

Consequently, depending on the alloy group (hypo- or hypereutectic), phosphorus can be both undesirable or desirable. Additions of modifiers like strontium or sodium can diminish the effect of phosphorus.

The corrosion resistance of aluminium is apparently reduced by phosphorus as it is in the case of iron. It is assumed that the polarisation (overvoltage) for both hydrogen reduction and anodic dissolution of aluminium is reduced, when phosphorus is present [28].

1.4. Scope of the work

The objective of the present work is to achieve a general understanding of the behaviour of phosphorus species in fluoride melts.

The solubility of $AlPO_4$ in cryolite melts was measured by cryoscopy. The reduction of five-valent phosphorus in cryolite-based melts was investigated by means of electrochemical methods like cyclic voltammetry, chronopotentiometry, chronoamperometry and square wave voltammetry.

Industrial measurements were performed in prebake alumina reduction cells. Sodium phosphate, Na_3PO_4, was added, and samples of bath and metal were taken and analyzed to see variation of the phosphorus over time. Different parameters like the carbon powder (dust) content in the electrolyte or the distance between anode and cathode (ACD) were changed to see if there was any effect on the concentration of phosphorus. A mass balance of a prebake line and a Søderberg line was established.

In a laboratory scale cell, electrolysis was performed while adding phosphate to the bath. A continuous sampling every 30 minutes should show if there is a similar trend in the laboratory cell as in the industrial one. Only one parameter, which was assumed to influence the phosphorus content in the cell, was changed at a time, i. e. temperature, carbon content and current interruption for a certain time period. These experiments should elucidate the relationship between phosphorus in bath and in metal and how this relationship is affected by changing parameters in the cell.

The goal of the work was to get a quantitative understanding of phosphorus as an impurity in the aluminium electrolysis process by determining its electrochemical behaviour, transport properties, mass balance and distribution coefficients.

References to Chapter 1:

[1] K. Grjotheim, C. Krohn, M. Malinovsky, K. Matiasovsky, J. Thonstad, *Aluminium Electrolysis – Fundamentals of the Hall-Héroult Process*, 2nd edition, Aluminium-Verlag GmbH, Düsseldorf, Germany, 1982.

[2] Q. Zhuxian, K. Grjotheim, H. Kvande, *Naturally occuring aluminium?*, Aluminium, 75. Jahrgang, **7/8**, 619-625, 1999.

[3] http://www.ideafinder.com/history/inventors/tesla.htm.

[4] http://www.bartelby.net/65/si/SiemensE.htm.

[5] http://www.neuronet.pitt.edu/~bogdan/tesla/bio.htm.

[6] http://www.etimotors.com/history.htm.

[7] N.C. Craig, "*Charles Martin Hall – the young man, his mentor, and his metal"*, J chem. education, **63**(7), 557-559, 1986.

[8] W.S. Peterson, *Hall-Héroult Centennial 1886-1986*, Light Metals, 1-2, 1986.

[9] Y. Bertaud, A. Lectard, *Aluminium Pechiney specifications for optimising the aluminas,* Light Metals, 667-686, 1984.

[10] K. Grjotheim, H. Kvande, *"Introduction to aluminium electrolysis"*, Aluminium-Verlag GmbH, Düsseldorf, Germany, 1993.

[11] N.E. Richards, *Alumina in smelting*, 19th international course on process metallurgy of aluminium, Trondheim, Norway, 2000.

[12] M. Sørlie, *Søderberg technology*, 19th international course on process metallurgy of aluminium, Trondheim, Norway, 2000.

[13] E.W. Dewing, *Models of Halo-Aluminate Melts*, The Electrochem. Soc., Proc. 86-1, 675-677, 1986.

[14] N.X. Feng, H. Kvande, *Dissociation Equilibria in Molten Cryolite: The presence of AlF_5^{2-} Ions*, Acta Chem. Scand. A40, 622-630, 1986.

[15] B. Gilbert, T. Materne, *Reinvestigation of molten fluoroaluminate raman spectra: the question of the existence of AlF_5^{2-} ions*, Appl. Spectrosc., **44**, 299-305, 1990.

[16] V. Lacassagne, C. Bessada, P. Florian, S. Bouvet, B. Ollivier, J.-P. Coutures, D. Massot, *Structure of high-temperature NaF-AlF_3-Al_2O_3 melts: a multinuclear NMR study*, Journal of Physical Chemistry B, **106**(8), 1862-1868, 2000.

[17] J. Brynestad, K. Grjotheim, S. Urnes, *Structural interpretation of molten cryolite and of cryolite melts containing aluminium oxide,* Metal. Ital. **52**, 495-502, 1960.

[18] J. Thonstad, P. Fellner, G.M. Haarberg J. Híveš, H. Kvande, Å. Sterten, *Aluminium Electrolysis – Fundamentals of the Hall-Héroult Process*, 3rd edition, Aluminium-Verlag GmbH, Düsseldorf, Germany, 2001.

[19] C.M. Hall, *"Method of making alumina"*, US Patent 663, 167; filed May 26, 1900; pat. Dec. 4, 1900, copy at http://pmeiers.bei.t-online.de/p-aluminum.htm.

[20] S.Z. Beer, *The solution of aluminum phosphide in aluminium*, J. Electrochem. Soc., **116**(2), 263-265, 1969.

[21] J. Thonstad, *The Behaviour of impurities in Aluminium Cells*, Proceedings of the 10th international Aluminium Symposium, Stara, Lesna, Slovakia, 5, 1999.

[22] Industrial data from Norsk Hydro Aluminium, 2002.

[23] A. Seltveit, *Ildfaste Materialer*, 2nd edition, Tapir Trondheim, 255, 1992.

[24] P.A. Solli, *Current efficiency in aluminium electrolysis cells*, Dr.ing. thesis, NTNU Trondheim, Norway, 1993.

[25] J.E. Hatch, *Aluminium – Properties and Physical Metallurgy*, American Society for Metals, Chapter 6, 235-236, 1984.

[26] I.J. Plomear, *Light Alloys – Metallurgy of the Light Metals*, 3rd edition, 147-160, 1995.

[27] J.L. Jorstad, *Hypereutectic aluminum-silicon alloys 390 and A390,* Met. Soc. AIME, 242(7), pp. 1217-1222, 1968.

[28] E. Bardal, *Korrosjon og korrosjonsvern*, 2nd edition, Tapir Trondheim, Norway, 209, 1994.

2. Literature review and theoretical considerations

2.1. Literature review

In 1669 the alchemist Hennig Brand discovered phosphorus when searching for a way to transform silver into gold. Among several attempts to reach his goal, he dried out a "gold"-coloured urine sample by heating it. Afterwards he glowed the residue of the urine sample in an oxygen-free vessel. By doing so, he obtained a substance, which was glowing in the dark. This substance was white phosphorus, P_4, which was originally from a phosphorus salt, $NaNH_4HPO_4$ that urine contains. Because of the chemiluminescent behaviour, the substance got the name phosphorus, which in Greek [:phosphoros:] means light bearing [1]. In this context it is worthwhile mentioning that in ancient times the planet Venus was named Phosphorus as well when appearing before sunrise [2].

2.1.1. Overview of the general chemistry of phosphorus

2.1.1.1. Natural occurrence and production of phosphorus

In today's lithosphere there is about 0.4 atoms of phosphorus for every 100 atoms of silicon [3], where silicon is the second-most abundant element in the earth's crust, with 26.3 wt% after oxygen with 48.9 wt% [1]. In extraterrestrial materials like iron meteorites phosphorus exists mainly as iron-nickel phosphide, while the phosphorus content of igneous rocks on earth is mostly present in the form of apatites, $CaX_2 \cdot 3Ca_3(PO_4)_2$ (X = F, Cl or OH). Apatites can also be found in some marine sediments. In soils, a variety of phosphates can be found, which not necessarily has to be orthophosphates. Nevertheless, phosphorus found on earth, is mainly in its five-valent state, and the geochemical cycle involving this element is one of the most important in the biosphere [3]. In difference to the homologous nitrogen, phosphorus is not found in its elemental state in nature, but in the form of derivates of phosphoric acid, H_3PO_4, as for examples apatites, because of its high affinity towards oxygen.

The production of elemental phosphorus is based on carbothermal reduction of calcium phosphate, $Ca_3(PO_4)_2$, with silicon oxide, SiO_2, at

1400 ºC to 1500 ºC. Besides phosphorus, calcium silicate in the form of $CaSiO_3$ and carbon monoxide are formed:

$$Ca_3(PO_4)_2 + 3\,SiO_2 + 5\,C \Rightarrow P_2 + 3\,CaSiO_3 + 5\,CO \qquad (2.1)$$

Phosphorus will dimerize upon cooling and form white phosphorus, P_4, which sometimes also appears yellow. The product is purified by distillation [1]. It should be mentioned that besides white phosphorus there exist other modifications such as red, violet and black phosphorus, which are stable under different conditions, concerning temperature and pressure, and which differ from each other by structure.

When heating white solid phosphorus from room temperature in an oxygen-free atmosphere, the substance will melt at 44.3 ºC. At its boiling point of 280.5 ºC gaseous P_4 molecules form, which are in a temperature dependent equilibrium with other modifications of phosphorus,

$$P_4 \rightleftarrows 2\,P_2 \rightleftarrows 4P \qquad (2.2)$$

Looking at equilibrium (2.2), P_4 molecules will dissociate by 1% into P_2 molecules at 800 ºC. When reaching 1200 ºC, about 50% P_2 have been formed. Above 2000 ºC the P_2 molecules will dissociate into P atoms.

At the usual working temperature of 950 ºC in an alumina reduction cell, any gaseous elemental phosphorus should, therefore, be present in the form of P_4 and P_2 molecules.

2.1.1.2. Compounds of phosphorus with oxygen

If oxygen is present together with phosphorus, the following reaction will occur, even at room temperature:

$$P_4 + 5\,O_2 \Rightarrow P_4O_{10} \qquad (2.3)$$

Reaction (2.3) is a strongly exothermic reaction where tetraphosphorus decaoxide, P_4O_{10}, is formed. Phosphorus is able to form five monomolecular oxides with the composition P_4O_n with n = 6, 7, 8, 9 and 10 and one highmolecular oxide with the formula $(P_2O_5)_x$. For historical reasons the monomolecular oxide, P_4O_{10}, is often called phosphorus pentoxide, P_2O_5, as well, which is understandable when looking at the molecular formulas. Lower oxides like P_2O_3 can be formed when

controlling the oxygen pressure in the atmosphere when heating elemental phosphorus.

Besides being the starting material in the production of phosphoric acid, phosphorus pentoxide is one of the most effective dehydration agents known. The hydration reaction of phosphorus pentoxide is shown in reaction (2.4):

$$2\,P_2O_5 \xrightarrow{+2\,H_2O} H_4P_4O_{12} \xrightarrow{+2\,H_2O} 2\,H_4P_2O_7 \xrightarrow{+2\,H_2O} 4\,H_3PO_4 \qquad (2.4)$$

Because of its extraordinary ability to take up water, it seems unlikely that phosphorus can be existent as P_2O_5 in an atmosphere like ambient air that has a certain humidity.
As mentioned in Chapter 1, most of the phosphorus entering the aluminium production process originates from the alumina. In analysis reports concerning alumina, phosphorus is given as P_2O_5, but it seems unlikely that P_2O_5 is actually present in alumina. Considering the humidity in the atmosphere and the duration of the alumina transport to the aluminium plant, it can be assumed that phosphorus is either present in hydrated form as H_3PO_4 or as aluminium phosphate.

Phosphorus has a strong tendency to achieve its highest oxidation state, preferably in the form of phosphates. Therefore, phosphates have a small oxidative effect in nature in comparison with its periodic neighbours C, N, O or S. The natural cycle of phosphorus does not involve any redox processes, and it takes place in the form of phosphate regarding both the inorganic and biological cycles. There are no volatile phosphorus compounds either formed at low temperatures, which means that the atmosphere does not take part in any of the phosphorus cycles. The inorganic phosphate cycle consists of weathering of vulcanic and sedimental rocks by which phosphate is released. The phosphate dissolves in water and is transported to the oceans where it forms deposits, so-called sediments, and takes part in the formation of new land. The time range of this process is millions of years. On the other hand, the biological cycle of phosphate repeats itself after some years, and it takes place on land. Phosphate comes with plants and micro-organisms into the food of humans and animals. By decay of excrements or bodies, the phosphate is led back to the soil. Therefore, the phosphate anion can be considered to be a stable species.

If we compare the homologous nitrogen pentoxide, N_2O_5, with P_2O_5, the difference between the two compounds with regard to redox behaviour is striking. While N_2O_5 is a very oxidative oxide as for example,

$$N_2O_5 \quad 2 \quad I_2 \Downarrow \quad I_2O_5 \; 2 \quad N_2 \tag{2.5}$$

a similar reaction with P_2O_5 will not proceed, since the high affinity of phosphorus towards oxygen favours the stability of the pentoxide. By heating phosphorus pentoxide, it will react with metal oxides like Na_2O to form phosphates like Na_3PO_4.

$$3\,Na_2O \quad 2 \quad P_2O_5 \Downarrow \quad 2\,Na_3PO_4 \tag{2.6}$$

In literature [1] it can be found that metal fluorides, such as CaF_2, do react with phosphorus pentoxide at higher temperatures to form phosphorus pentafluoride,

$$5\,CaF_2 \quad 2 \quad P_2O_5 \Downarrow \quad 2\,PF_5 \; 2 \; 5\,CaO \tag{2.7}$$

Based on monophosphoric acids there are several oxyanions and one anion of phosphorus. Nevertheless, in water the phosphate anion is the only stable species among all ions present in Figure 2-1. The free electron pairs at the phosphorus atom will form bonds with hydrogen ions from water, forming new compounds, see Figure 2-2.

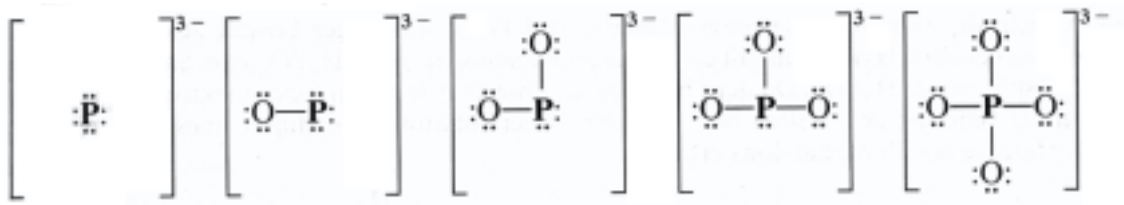

Fig. 2-1: *Different anions of phosphorus with oxygen [1].*

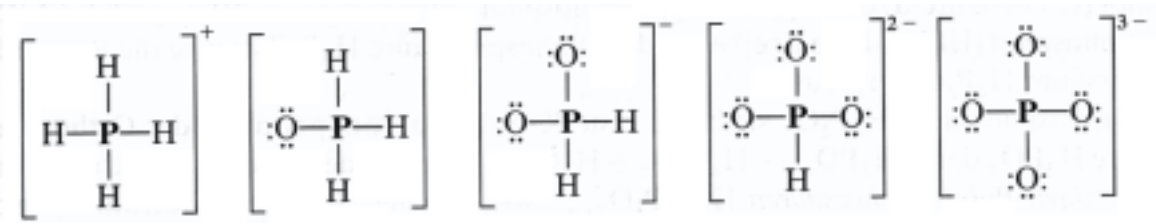

Fig. 2-2: *Different anions of phosphorus with oxygen where the free electron pairs of the phosphorus have formed bonds with hydrogen ions [1].*

Besides the monophosphoric acids, there are peroxophosphoric acids, diphosphoric acids, chainlike polyphosphoric acid and ringforming metaphosphoric acids [1]. As can be seen, the chemistry of phosphorus and its compounds with oxygen is rich in variety concerning structure and composition. Looking at the oxygen/phosphorus ratio, it is obvious that it decreases from monoorthophosphate towards phosphorus pentoxide with 4 to 2.5 respectively [1].

Type:	Mono-phosphate	Diphosphate	Oligo-phosphate	High-molecular phosphate
example:	PO_4^{34}	$P_2O_7^{44}$	$P_3O_9^{34}, P_4O_{12}^{44}$	$(P_2O_5)_x$
O/P ratio:	4 ⟶	3.5 ⟶	3 ⟶	2.5

This is typical for phosphates when they form chains, rings or networks. A similar trend can be seen in melts with phosphates forming polymeric ions or groups, as can be seen in Figure 2-3.

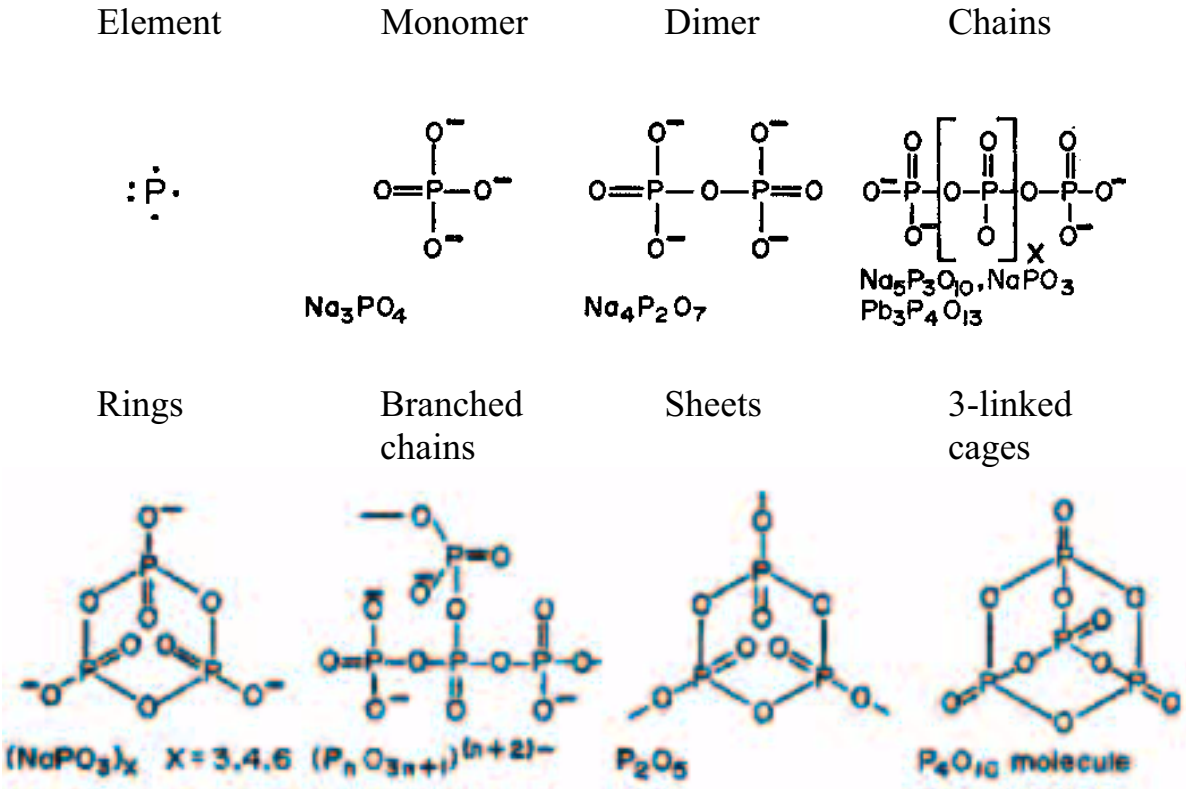

Fig. 2-3: *Different ions of phosphorus in phosphate melts [4].*

2.1.1.3. Phosphorus and its compounds with fluorine

When looking at the alumina reduction process, species of phosphorus with fluorine should also be taken into consideration. The phosphorus halogenides can be divided into the following types: phosphorus trifluoride PF_3, phosphorus pentafluoride PF_5, diphosphorus tetrafluoride P_2F_4 and tetraphosphorus hexafluoride P_4F_6. All phosphorus fluorides apart from P_4F_6 are gaseous at room temperature (see Table 2-2). The structure of these fluorophosphoric compounds can be described as follows:

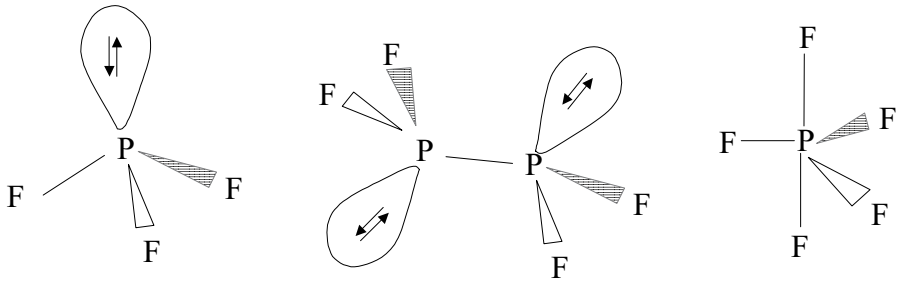

Fig. 2-4: *Chemical structures of the phosphorus fluoride compounds PF_3, P_2F_4 and PF_5 [1]. The free electron pairs are shown as well.*

Phosphorus trifluoride is an odeurless, poisonous gas, like carbon monooxide, CO, and like CO it can block the oxygen anchorspace on the haemoglobin in the human blood. As can be seen, CO and PF_3 are isoelectronic and have a similar reaction behaviour as for example the complex $Fe(CO)_5$, which also exists with PF_3 as ligand, $Fe(PF_3)_5$. The decomposition temperature for the $Fe(PF_3)_5$ complex is around 270 ºC. In terms of acidity, phosphorus trifluoride is a rather weak Lewis acid, but a very strong Lewis base due to its free electron pair on the phosphorus atom.

P_2F_4 is a stable, colourless gas, the structure of which can be seen in Figure 2-4. When heating above 900 ºC, it will decay into PF_3, $P(PF_2)_3$ and a yellow unidentified decomposition product.

Another phosphorus fluoride is phosphorus pentafluoride, PF_5, which is a strong Lewis acid. By addition of another fluoride ion, PF_6^- will form, which is isoelectronic to AlF_6^{3-}.

2.1.1.4. Phosphorus and its compounds with both oxygen and fluorine

Compounds of oxyfluorides can be found both as molecules or ions. The existence of POF_3, phosphorylfluoride, and $P_2O_3F_4$, pyrophosphoryl-fluoride is known. Looking at anhydrous polyphosphoric acids, exchange of hydroxyl-groups with fluoride ions will enlarge the variety of possible oxyfluorophoshorus compounds, as for example $F_2P\text{-}O\text{-}PF_2$, a derivate of the anhydrous diphosphorus acid. Ionic compounds of oxygen and fluorine with phosphorus exist as well, as can be seen in Figure 2-5.

Tetrafluoro phosphonium ion | *Phosphorus oxyfluoride* | *Difluoro phosphate* | *Fluoro phosphate* | *Phosphate*

Fig. 2-5: *Different compounds of oxygen and fluorine with phosphorus [1].*

The PO_3F^{2-} and $PO_2F_2^-$ ions correspond in structure and charge to the sulphate, SO_4^{2-}, and perchlorate ions, ClO_4^-, respectively. Therefore, their reaction behaviour can be assumed to be somewhat similar.

2.1.1.5. Phosphorus as an anion

Phosphorus has a strong tendency to form elemental chains, rings or networks. In fact, after carbon phosphorus is the element with the strongest distinctive ability to form element-element bonds. Until today there are no compounds with cationic phosphorus, P_n^{m+}, known. On the other hand, there are a large number of anionic phosphorus compounds, which can be divided into three major groups: saltlike, highmolecular covalent and metallic phosphides. Typical saltlike phosphides are compounds with strong electropositive metal ions like alkali, earth alkali or lanthanoid ions. A variety of compositions is known where phosphorus can be found in such anionic compounds, P_n^{m-}, as for example,

$$P^{3-} \quad P_2^{4-} \quad P_5^{7-} \quad P_6^{4-} \quad P_7^{3-} \quad P_{11}^{3-} \quad P_{21}^{3-} \quad [P^-]_x \quad [P_5^-]_x \quad [P_7^-]_x$$

Low-molecular anions hydrolyse fast to form phosphine, PH_3, whereas the compounds with high-molecular phosphorus anions are stable in water [1]. Most of them can be assigned to the so-called Zintl phases [5].

Examples of covalent forms are compounds with boron, BP or $B_{12}P_n$, or silicon, SiP_2. The metallic phosphides can again be divided into metal-rich, metal-poor and metal-monophosphides. Examples of all three groups can be found in the following Table 2-1:

Table 2-1: *Different metallic phosphides, general formula and examples [1].*

metal-rich phosphides	metal-monophosphides	metal-poor phosphides
$M_{>1}P$	MP	$M_{<1}P$
Fe_3P, Fe_2P, Ni_2P	CrP, MnP, MoP, AlP	FeP_2, NiP_2, NiP_3

The four subsequent sections are intended to give an overview about the diverse nature of phosphorus concerning its chemistry. The following table will sum up all mentioned compounds of phosphorus with fluoride and/or oxygen, which may be of some importance regarding the aluminium production process.

As can be seen from Table 2-2, most phosphorus compounds are gaseous at the usual working temperature of an alumina reduction cell. Only the phosphates seem to be in either liquid or solid state, which is valid for the aluminium phosphide as well.

Table 2-2: *Names and transition temperatures of different compounds with phosphorus [1, 6, 7].*

Compound	**$T_{m.p.}$ [°C]**	**$T_{b.p.}$ [°C]**	**Name**
P_4	44.1	280	Phosphorus
P_2O_4	>100	-	Diphosphorus tetraoxide
P_2O_3 (P_4O_6)	23.8	175.4	(Di-)phosphorus trioxide (Tetraphosphorus hexaoxide)
P_2O_5 (P_4O_{10})	580-585	subl. at 300	(Di-)phosphorus pentoxide (Tetraphosphorus decaoxide)
PF_3	-151.5	-101.5	Phosphorus trifluoride
P_2F_4	-86.5	-6.2	Diphosphorus tetrafluoride
PF_5	-83	-75	Phosphorus pentafluoride
P_4F_6	-68	-	Tetraphosphorus hexafluoride
POF_3	-68	-39.8	Phosphorus oxyfluoride
$P_2O_3F_4$	0.1	72	Pyrophosphoryl fluoride
PH_3	-133	-87.7	Phosphorus trihydride (Phosphine)
AlP	2000	-	Aluminium phosphide
$AlPO_4$	>1500	-	Aluminium orthophosphate
$NaPO_3$	627	-	Sodium metaphosphate
Na_3PO_4	1340	-	Sodium orthophosphate
$Na_4P_2O_7$	880	-	Sodium pyrophosphate
H_3PO_4	42.35	-	orthophosphoric acid

2.1.2. Phosphorus compounds in the molten state

In the literature phosphorus pentoxide is well known as a glass-forming oxide. Besides oxides like SiO_2, B_2O_3 and Al_2O_3, P_2O_5 will form a three-dimensional network upon heating. When adding oxides of sodium, potassium, magnesium, calcium, lead or zinc, the network will break up into smaller pieces, due to the additional oxide ions added with for example Na_2O. The more the network is broken up, the lower the melting point of the glass will be [1]. A typical phosphate glass like $CaO{\cdot}P_2O_5$ consists primarily of PO_4 tetrahedra linked together by P-O-P bridges [4].

One would assume that a melt of pyrophosphate should consist solely of the $P_2O_7^{4-}$ anion. But there is evidence that polymeric melts consist of a

wide distribution of anions of different sizes and chain lengths. For the phosphate glass $CaO{\cdot}P_2O_5$, a mean chain length of 2 phosphorus atoms per chain was calculated at 577 ºC, indicating the major anion to be $P_2O_7^{4-}$. Temperature and the type of metal oxide added to the phosphorus pentoxide seem to influence the chain length that is prevailing. Depending upon the ratio R of M_2O/P_2O_5, alkali metal phosphates form two main polymeric structure types, chains and rings. The general formula for chains is $M_{n+2}P_nO_{3n+1}$. Ring phosphates can be obtained if the ratio R = 1 and their general formula is $M_nP_nO_{3n}$. For linear polymers the average chain length n' can be estimated by

$$n' = 2/(R-1) \tag{2.8}$$

In a phosphate glass with the composition $5Na_2O{\cdot}3P_2O_5$ the only anion expected should, therefore, be $P_3O_{10}^{5-}$. Investigations reveal that chains both longer and shorter than with 3 phosphorus atoms have been found in the glass, and this implies that they were present in the melt as well [4].
According to Julsrud [8] pure, molten sodium pyrophosphate is expected to dissociate to some degree according to reaction (2.9).

$$2\,P_2O_7^{44} \;\ddot{Y}\!\!\leftarrow\; PO_4^{34} \;2\; P_3O_{10}^{54} \tag{2.9}$$

When adding sodium fluoride to molten sodium pyrophosphate, he suggested that an additional equilibrium reaction (2.10) may be established.

$$2\,P_2O_7^{44} \;2\; 2\,F^{4} \;\ddot{Y}\!\!\leftarrow\; 2\,PO_4^{34} \;2\; P_2O_6F_2^{44} \tag{2.10}$$

Del Campo [9] studied the system cryolite - sodium pyrophosphate by determining the phase diagram. The system was found to be a simple eutectic, and the eutectic point was determined to be 748 ºC at 71.7 wt% $Na_4P_2O_7$.
Three years later Bratland et al. [10] revised the dissociation schemes proposed by Del Campo and came up with new ones that fitted better to the experimental data. In the pyrophosphate-rich melt added cryolite was interpreted as a source of fluoride ions, according to the assumptions made by Julsrud [8]. Cryolite was assumed to dissociate as follows:

$$AlF_6^{34} \;\ddot{Y}\!\!\leftarrow\; AlF_4^{4} \;2\; 2\,F^{4} \tag{2.11}$$

The free fluoride ions would react further with the pyrophosphate ion:

$$P_2O_7^{44} + F^- \rightleftharpoons PO_4^{3-} + PO_3F^{2-} \quad (2.12)$$

The formation of the dimer of PO_3F^{2-} was considered, as proposed in reaction (2.10), but the assumption that only the monomeric form, PO_3F^{2-}, is formed, fitted better with the experimental data of Del Campo. For the cryolite-rich side of the phase diagram, Bratland et al. [10] proposed the following reaction:

$$2AlF_6^{3-} + P_2O_7^{4-} \rightleftharpoons Al_2OF_8^{4-} + 2PO_4^{3-} + 2F^- \quad (2.13)$$

Reaction (2.13) is taken from the original article of Bratland et al. and as can be seen not balanced when assuming PO_4^{3-} as product. Another fivevalent phosphorus compound might form as product and the following reaction might fit as well with the cryoscopic results concerning the number of species formed:

$$2AlF_6^{3-} + P_2O_7^{4-} \rightleftharpoons Al_2OF_8^{4-} + 2PO_3^- + 4F^- \quad (2.14)$$

The study of Del Campo originated in the interest at that time concerning the influence of phosphorus compounds on the current efficiency of the Hall-Héroult process. An adequate phosphorus compound had to be found, which was suitable for use in fundamental studies. Because of its high solubility in molten cryolite, good thermal stability and low volatility, sodium pyrophosphate was then chosen.

In recent years several authors reported about the stability of different ortho- and metaphosphates in cryolite-based melts. Danĺk et al. [11] claimed that when mixing cryolite with sodium phosphate, Na_3PO_4, the phosphorus-containing compound in the solidified melt should be $Na_2P_4O_7$. When $Al(PO_3)_3$ was added to a cryolite melt, the formation of gaseous phosphorus oxyfluoride should occur,

$$Na_3AlF_{6(l)} + Al(PO_3)_{3(l)} \rightleftharpoons 3NaF_{(l)} + 2AlPO_{4(l)} + POF_{3(g)} \quad (2.15)$$

The presence of $AlPO_4$ and $POF_{3(g)}$ was confirmed by XRD and IR spectroscopy respectively. In another publication the same authors showed by thermodynamical calculation that in the presence of aluminium, compounds of phosphate may be reduced to elemental phosphorus, which may either escape as gas or dissolve in the aluminium [12].

Furthermore, cryoscopic measurements were performed by Chrenková et al. [13] on the systems Na_3AlF_6-Na_3PO_4, Na_3AlF_6-$AlPO_4$ and Na_3AlF_6-$Al(PO_3)_3$. The results for the systems with the orthophosphates, Na_3PO_4 and $AlPO_4$, showed that only one new particle forms, i.e. PO_4^{3-}. This indicates that the orthophosphate ion is stable in molten cryolite. In the system with the metaphosphate, three new species were believed to be formed, as shown in reaction (2.15).

Tkatcheva et al. [14] measured the stability of $AlPO_4$ in a Na_3AlF_6-NaF melt with and without additional alumina. The results by ICP-AES spectroscopy and LECO oxygen analysis confirmed that $AlPO_4$ is stable in cryolite-based melts. The ratio between oxygen and phosphorus was found to be 4, also in the presence of Al_2O_3. Another report by the same authors [15] investigated the stability of the aluminium metaphosphate, $Al(PO_3)_3$, in cryolite based melts. Tkatcheva found that the oxygen to phosphorus ratio was stable at 3 during the experiment. No evolution of gaseous POF_3 could be detected. The existence of PO_3^- as a stable anion in cryolite-based melts was suggested.

When reacting with aluminium, it was believed that elemental phosphorus forms and evaporates from the cryolite based melt, as shown in reaction (1.10). In a recent investigations, Østvold et al. [16] found that, when adding an equivalent amount of aluminium to the phosphate present in a cryolite-based melt, phosphorus does not evaporate completely. The mechanism of reduction of phosphate in cryolite-based melts is, therefore, probably not as straight-forward as was believed earlier.

In chloride-based melts Combes et al. [17] studied reactions between oxide ions and soluble, five-valent phosphorus species like, PO_3^-, PO_4^{3-} or $P_2O_7^{4-}$. With the help of a calcia-stabilizied-zirconia membrane electrode, titration curves of O^{2-}, added as Na_2O, by PO_3^-, added as $NaPO_3$, could be measured by potentiometry in a NaCl-KCl melt at 727 ºC. With increasing concentration of oxide ions the formation of the orthophosphate from metaphosphate could be confirmed.

$$O^{24} \; 2\, PO_3^4 \mid PO_4^{34} \tag{2.16}$$

Further reactions were suggested, where newly formed phosphorus species reacted further and formed new equilibria,

$$PO_4^{34}\ 2\ PO_3^4\ |\ P_2O_7^{44} \quad (2.17)$$

$$2PO_4^{34}\ |\ P_2O_7^{44}\ 2\ O^{24} \quad (2.18)$$

$$P_2O_7^{44}\ |\ 2PO_3^4\ 2\ O^{24} \quad (2.19)$$

Chaudhuri [18] studied the loss of aluminium in cryolite-based melts when different bath additives and impurities were added. No electrolysis was performed during the experiments. Among several impurities he also added phosphorus in the form of P_2O_5 to cryolite melts with different alumina contents.

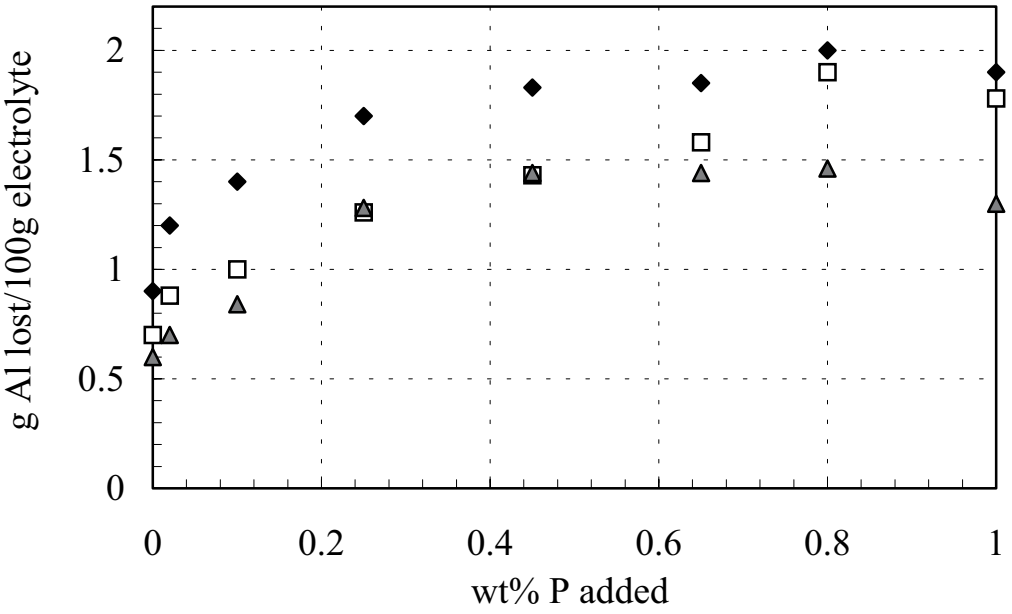

Fig. 2-6: *Loss of aluminium in a cryolite-based electrolyte versus the added amount of phosphorus in the form of P_2O_5. Different alumina concentrations are shown: ◆ 4 wt% Al_2O_3, □ 8 wt% Al_2O_3, △ 12 wt% Al_2O_3 [18].*

Figure 2-6 indicates that the loss of aluminium increased with increasing amount of phosphorus added to the melt. When more alumina was added, less aluminium seemed to be lost.

2.1.3 Phosphorus in an electrochemical context

Phosphorus can be present in many other oxidation states than +5. Like the homologous nitrogen, phosphorus can attain all oxidation states from –3 to +5, as shown by the series of compounds in Figure 2-7.

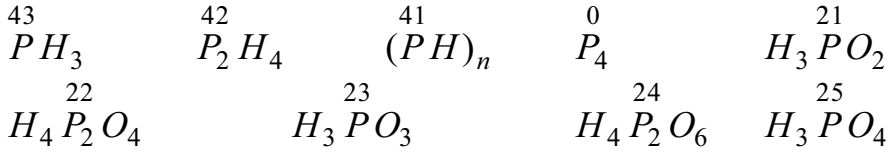

Fig. 2-7: *Compounds of phosphorus with different valencies of phosphorus.*

For some of the compounds shown in Figure 2-7, the thermodynamic stability can be questioned, but the figure illustrates the enormous variety of the phosphorus chemistry. In aqueous solutions the electrochemical behaviour of phosphorus is well investigated. Different potential diagrams (Latimer diagrams) are obtained for different pH values by thermodynamic calculations and partly supported by experiments. In Figure 2-8 the potentials are referred to the hydrogen reference electrode at 298 K.

pH = 0

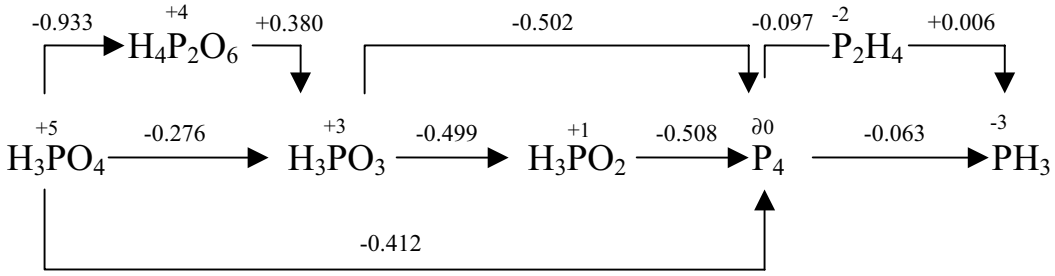

pH = 14

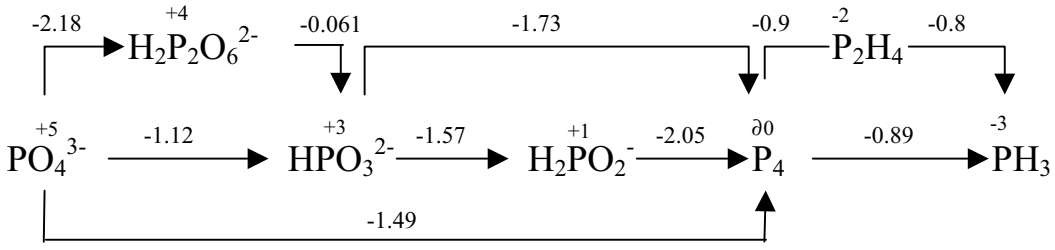

Fig. 2-8: *Potential diagrams at pH = 0 and 14, potentials in Volts are given on arrows, valency of the phosphorus species are indicated above the formula, T = 298 K [19].*

From Figure 2-8 the potentials show that phosphorus species can function either as oxidising or reducing agents if present in acidic or basic solution respectively. As can be seen, elemental phosphorus can disproportionate into phosphine and monovalent, trivalent or pentavalent phosphorus in both acidic and basic solution.
Even though properties of solvents do affect the behaviour of compounds dissolved in them, it might be interesting to pretend that the potentials in Figure 2-8 might form a similar order in molten salts, in particular in cryolite. The potentials can be referred to an aluminium reference electrode, which was normally used for electrochemical investigations in this thesis. The reference electrode reactions and their corresponding standard potentials at 298 K are,

SHE $H^{2}\ 2\ e^{4} \Downarrow \frac{1}{2}H_{2(g)},\ E^{o} = 0\ V$ (2.20)

Aluminium ref. electrode $Al^{32}\ 2\ 3e^{4} \Downarrow Al_{(l)},\ E^{o} = -1.68\ V$ (2.21).

Since in salt melts the compounds will be dissolved as free ions, the closest case to compare the two solvents would be to take the potentials from the basic solution. By doing so, the following shift in potentials given in Table 2-3 would occur :

Table 2-3: *Standard potentials of redox couples of phosphorus compounds and their change in valency. Standard potentials related to SHE and aluminium as reference in aqueous solution at 298 K.*

Couple	Change in valency	$E^{o}_{SHE}[V]$	$E^{o}_{Al^{32}/Al}[V]$
PO_4^{3-}/HPO_3^{2-}	+5 Ÿ +3	-1.12	0.56
$PO_4^{3-}/H_2P_2O_6^{2-}$	+5 Ÿ +4	-2.18	-0.50
$H_2P_2O_6^{2-}/HPO_3^{2-}$	+4 Ÿ +3	-0.06	1.62
$HPO_3^{2-}/H_2PO_2^{-}$	+3 Ÿ +1	-1.57	0.11
HPO_3^{2-}/P_4	+3 Ÿ 0	-1.73	-0.05
$H_2PO_2^{-}/P_4$	+1 Ÿ 0	-2.05	-0.37
PO_4^{3-}/P_4	+5 Ÿ 0	-1.49	0.19
P_4/PH_3	0 Ÿ -3	-0.89	0.79
P_4/P_2H_4	0 Ÿ -2	-0.9	0.78
P_2H_4/PH_3	-2 Ÿ -3	-0.8	0.88

In a cryolite-based melt saturated with alumina, the electrochemical window between a tungsten electrode as working electrode and an aluminium reference electrode is about 1 V.
If we use the values given in the last column in Table 2-3 as they stand, we can envisage the following sequence. When adding phosphorus in form of an orthophosphate, PO_4^{3-}, the first reduction to PO_3^{3-} would occur at 0.56 V. Assuming all orthophosphate present is reduced in this step, the only phosphorus species in the melt would be the phosphite, PO_3^{3-}. Its further reduction would occur at 0.11 V where it forms hypophosphite PO_2^{3-}. The further reduction to elemental phosphorus would occur at –0.37 V, well below the reduction of aluminium. If not all orthophosphate is reduced to phosphite, another direct reduction to elemental phosphorus could take place at 0.19 V.

In case of molten salts, the most obvious differences in comparison to water as a solvent are the strongly bonded and stable nature of the solvent. Higher concentration of various species, in particular co-ordinated anions, can be obtained in these solutions. It should be kept in mind that this reduction model is based on the assumption that the potentials obtained in aqueous solutions are somehow comparable with the ones in molten salts. But this is not necessarily the case. It might not be entirely correct to make generalisations or to draw conclusions from the behaviour of species in different solvents. Even in different molten salts, the reaction behaviour of the same species does not have to be similar.

Studies of oxyanions in molten salts by means of polarography have been reviewed by Laitinen [20]. Besides chromate, CrO_4^{2-}, the review included nitrate and nitrite ions, NO_3^- and NO_2^-, respectively, the sulphate ion, SO_4^{2-}, and other oxyanions like carbonate, CO_3^{2-}, metaphosphate, PO_3^-, and metavanadate, VO_3^-. The review did not include fluorides as solvents, but nitrates and chlorides. A more detailed study on the electroreduction of metaphosphate in molten LiCl-KCl eutectic by Laitinen and Lucas [21] was published later. In the temperature range from 450 ºC to 700 ºC the reduction mechanism of metaphosphate was investigated by voltammetry, chronopotentiometry and coulometry. Different phosphate compounds like sodium trimetaphosphate, glassy trisodium metaphosphate, sodium pyro- and orthophosphates as well as sodium tripolyphosphate were used in the investigations.

The reduction process was observed to be very complex in the case of the trimetaphosphate. Therefore, simpler phosphorus compounds like pyro-

and orthophosphate were investigated by coulometric measurements as well and it was established that a two-electron reduction to a lower-valent species occurred. Film formation on the platinum electrode was observed during electrolysis and it was studied by X-ray diffraction. They found that the film consisted of $Li_4P_2O_7$, PtP_2 and Pt. Since the elemental phosphorus that had combined with platinum could hardly be a product from a direct reduction process (since the number of electrons transferred was found to be only two), a chemical reaction was assumed, forming phosphorus after the reduction step. The electrochemical and chemical results indicated that for a trimetaphosphate the following reduction mechanism might be reasonable:

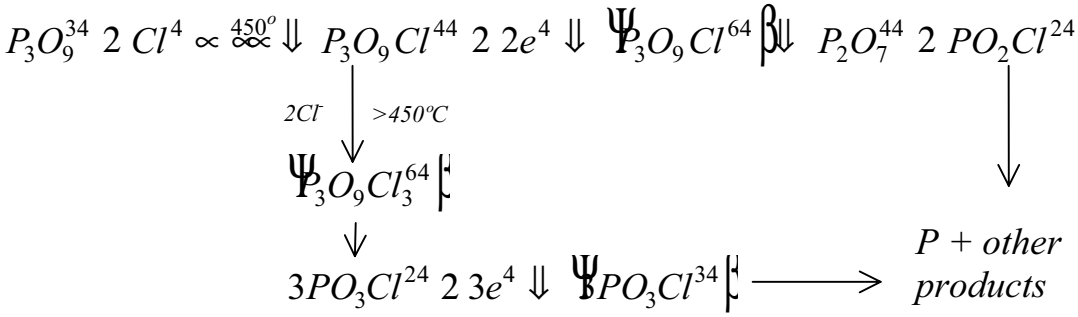

As can be seen, the proposed mechanism is not simple. “In general, the electrochemical behaviour of oxyanions is far more complex than that of simple metal ions” according to Laitinen and Lucas [21].

By chronopotentiometric studies Franks and Inman [22] tried to determine the mechanism of the cathode process concerning the electroreduction of molten phosphates in the temperature range of 400 ºC to 800 ºC. They studied different pentavalent phosphorus, like sodium metaphosphate, sodium orthophosphate, sodium pyrophosphate and sodium tripolyphosphate and compared the results. With Na_3PO_4 in a NaCl-KCl mixture, they found the reduction to be reversible with soluble reactants and products, and the number of electrons transferred was determined to be two. The following reduction mechanism was suggested for the orthophosphate:

$$PO_4^{3-} + 2e^- \Rightarrow PO_2^- + 2O^{2-} \quad (2.22)$$

$$5PO_2^- + 2O^{2-} \Rightarrow 3PO_4^{3-} + 2P \quad (2.23)$$

The diffusion coefficient of the orthophosphate ion in NaCl-KCl was found to be $8.2 \cdot 10^{-6}$ $cm^2 \cdot s^{-1}$ at 780 ºC. It should be mentioned that the authors named the reduction product of step (2.22) hypophosphite, even though in

aqueous systems the term hypophosphite represents monovalent phosphorus species, $H_2PO_2^-$. In addition, an ion like PO_2^- is not known to exist in aqueous solutions.

Furthermore, in the case of sodium pyrophosphate, two steps in a potential-time curve were obtained, which either could be interpreted as a single electroactive ion being reduced in two steps or the presence of two different ions that are reduced at different potentials. The second assumption fitted best with the experimental results. A depolymerization reaction like reaction (2.9) was not considered, since this would include a third ionic species, $P_3O_{10}^{5-}$, besides orthophosphates. Instead the following reaction was assumed:

$$P_2O_7^{44} + 2\,O^{24} \rightleftharpoons 2PO_4^{34} \qquad (2.24)$$

The pyrophosphate was found to be reduced in a two-electron step to a trivalent phosphorus species. The reduction of sodium tripolyphosphate, $Na_5P_3O_{10}$, revealed three transistion steps, where two of them were found to equal the ones for the orthophosphate and pyrophosphate. For the sodium trimetaphosphate three transition times were found as well. The results of this investigation manifest that the tendency to depolymerization of higher molecular phosphorus compounds increases with increasing temperature.

The electrochemical behaviour of phosphorus in fluoride melts has not been a subject of extended investigations. There exist only two literature sources, i.e. from Kerouanton et al. [23] and Charlot et al. [24]. They investigated the behaviour of alkaline phosphates in molten cryolite at 1030 ºC. The experiments showed that the added phosphorus, in form of alkaline orthophosphates, was reduced in a two-electron step to a three-valent species. The following reaction was suggested:

$$P(V) + 2e^- \Rightarrow P(III) \qquad (2.25)$$

They also claimed that additions of aluminium to the melt would reduce the five-valent phosphorus to elementary, gaseous P by a chemical reaction.

Deininger and Gerlach [25] studied the effects on the current efficiency in aluminium electrolysis in a laboratory cell by adding phosphorus as P_2O_5 as well as other impurities to a cryolite based electrolyte. The results showed a change in reaction behaviour when the phosphorus addition reached 0.12 wt% in the electrolyte. They proposed that pentavalent phosphorus is

reduced to trivalent up to 0.12 wt% P addition. Above this concentration phosphorus was reduced to its elemental state.

2.1.4 Phosphorus in industrial aluminium cells

As mentioned in Chapter 1, phosphorus enters the alumina reduction cell via raw materials. The use of natural cryolite in alumina reduction cells is no longer practicable, since the only mining facility in Greenland is exhausted. Instead, synthetic cryolite is produced to serve as a substitute. The history of how these raw materials like cryolite are produced might explain why they contain phosphorus. Table 2-4 shows examples of phosphorus pentoxide contents in the main raw materials for the aluminium production process.

Table 2-4: *Contents of phosphorus expressed as P_2O_5 in different raw materials, values in wt%.*

Cryolite	Aluminium fluoride	Alumina	Literature source
0.008-0.013	0.016-0.021	0.001-0.005	[26]
-	0.010	0.0009	[27]
-	-	0.001-0.003	[28]

Even though it seems like alumina has the lowest phosphorus content, it should be kept in mind that the amounts added per tonn aluminium produced differ a lot between the different raw materials. The addition of alumina per tonn aluminium was set to 1890 kg. For the aluminium fluoride a maximum of 20 kg per tonn aluminium was assumed. Since the introduction of additional bath is not a routine procedure, the amount added per tonn aluminium will be rather low. A value of maximum 10 kg of cryolite per tonn aluminium was assumed. Table 2-5 will show the distribution of phosphorus when the amount added to an industrial cell per tonn aluminium produced is taken account for.

Table 2-5: *Contents of phosphorus expressed by P_2O_5 in different raw materials per ton aluminium produced, values in ppm.*

Cryolite	Aluminium fluoride	Alumina	Literature source
0.8-1.3	3.2-4.2	20-100	[26]
-	2	18	[27]
-	-	20-60	[28]

As can be seen from Table 2-5, the major amount of phosphorus in industrial cells originates from the alumina added. The contribution from cryolite and aluminium fluoride could be neglected. However, it might be interesting to look at the production of the two raw materials to understand why the level of phosphorus is higher than in alumina.

The relatively high contents of phosphorus in cryolite and aluminium fluoride originates from hydrogen fluoride, which is used to produce these raw materials. For economic reasons it is favourable to use hydrogen fluoride from superphosphate production where it occurs as a by-product [26]. The reactions involved in the production of synthetic cryolite are as follows:

$$Na_2CO_3 \; 2 \; HF \Downarrow \; NaF \; 2 \; NaHCO_3 \qquad (2.26)$$

$$6NaF \; 2 \; NaAlO_2 \; 2 \; 2H_2O \Downarrow \; Na_3AlF_6 \; 2 \; 4NaOH \qquad (2.27)$$

$$NaOH \; 2 \; NaHCO_3 \Downarrow \; Na_2CO_3 \; 2 \; H_2O \qquad (2.28)$$

Since sodium fluoride and cryolite do have a low solubility in an aqueous solution, they will precipitate and can thereby be removed. As stated by Grjotheim [29] it is often difficult to keep the P_2O_5 content in the cryolite below a certain limit as required by smelters.

The reaction of a slurry of aluminium hydroxide with gaseous hydrogen fluoride is used to produce aluminium fluoride in the so-called wet fume scrubbing process.

$$Al(OH)_3 \; 2 \; 3HF \Downarrow \; AlF_3 \; 2 \; 3H_2O \qquad (2.29)$$

Normally the hydrogen fluoride for the production of aluminium fluoride originates from superphosphate manufacturing. Therefore, aluminium fluoride is more contaminated with phosphorus than alumina.

Besides the wet fume scrubbing process, a dry process for the production of aluminium fluoride is known as well, which is used at NORZINK in Odda (Norway). Calcium fluoride is treated with sulphuric acid to form gaseous hydrogen fluoride, which reacts with activated alumina, and aluminium fluoride is obtained.

The production of alumina from bauxite by the Bayer process leaves impurities in the product as well, but to a much lower extent than for cryolite or aluminium fluoride. Nevertheless, in bauxite deposits the hydrated aluminium oxide is invariably associated with small amounts of impurities, which follow through the production process for the alumina and end up in it to a minor extent [26].

For other additives to an industrial aluminium cell like NaF, CaF_2, MgF_2 or LiF as well as Na_2CO_3 no specifications on phosphorus contents were found in the literature. Since relatively small amounts of these substances are added to cells, their contribution to the phosphorus content in the cell may be negligible.

Some phosphorus is also present in the anode carbon. Industrial data showed an average concentration of 7 ppm [30], but this may vary according to the quality of raw material used for anode production. Since the carbon is electrochemically oxidized, any impurity in it will pass into the electrolyte or form volatile compounds and evaporate with the anode gases.

2.1.4.1. Laboratory studies

A laboratory study on impurity distribution in bath and metal in aluminium electrolysis by Qui et al. [31] showed that phosphorus had the highest distribution coefficient between bath and metal compared to other elements like Fe, Si, Ti, V and Ni. They studied thermochemical reduction of the impurities when aluminium was present and when running electrolysis for a certain time period. The impurities were blended into the bath mixture before the experiment. About 65 g of aluminium was added after melting the bath. Distribution coefficients for some impurities investigated are presented in Table 2-6.

Table 2-6: *Laboratory data on the distribution coefficients between bath and metal for various impurities at 970 ∀C (see text). Impurity level A equals 0.0025 wt% P, 0.01 wt% Fe and 0.02 wt% Si in the bath, 2A corresponds to twice the impurity concentrations of A, and so forth, Qui et al. [31].*

Impurity level	type of experiment, duration: 4 hours	Distribution coefficients for various impurities, c_{bath}/c_{metal}		
		P	Fe	Si
A	no electrolysis	0.81	0.147	0.662
	electrolysis	-	0.147	0.602
2A	no electrolysis	0.833	0.084	0.681
	electrolysis	0.764	0.134	0.277
4A	no electrolysis	0.871	0.105	0.383
	electrolysis	0.815	0.102	0.223
8A	no electrolysis	1	0.221	0.367
	electrolysis	-	0.069	0.091

Apart from the impurities given in the table above, the distribution coefficients for titanium, vanadium, nickel and gallium were determined as well. As Table 2-6 shows, the distribution coefficient for phosphorus in a laboratory cell was determined to be close to or equal to 1, which is very different from the coefficient found for industrial cells, expected to be 6.2 [32]. However, it should be mentioned, that Sturm and Wedde [32] had a dry-scrubbing unit involved, which captured the volatile phosphorus compounds and thereby increased the amount of phosphorus in the secondary alumina.

Investigations of changes in current efficiency by addition of several impurities to a laboratory cell by Solli [33], showed that an addition of 0.01 wt% P reduced the CE by 0.68% ± 0.18%. Phosphorus was added in form of P_2O_5 and $Ca_3(PO_4)_2$. The obtained value for CE reduction was a little lower than usually assumed in industrial cells. As stated in Chapter 1, it is assumed that the current efficiency decreases by 1% according to when 100 ppm of phosphorus, P, is present in the bath of industrial cells.

2.1.4.2. Industrial studies

In 1983 an article was published by Langerweger [34] on accompanying metallic elements in electrolytic aluminium metal and their effect on the aluminium products. Factors, considered to have an influence, were the quality of raw materials, especially anode carbon, installation of potgas collection system, as well as computer controlled cell operations and the recycling of used aluminium. Phosphorus was not considered as one of the elements severely affecting the quality of the metal. Neither was phosphorus considered to be an element that will increase in concentration due to changes in the factors mentioned above. However, a decade earlier two publications from Sparwald [35] and Frankenfeldt and Mannweiler [36] showed that the installation of dry scrubber systems into the cell cycle will affect the content of phosphorus in the process. A distribution coefficient between gas and metal/bath phase was determined to be between 6 and 8.25 for phosphorus. Frankenfeldt and Mannweiler investigated the behaviour of silicon, zinc, iron, titanium, gallium and nickel as well. They noted that volatile compounds of nickel and iron are most likely in form of carbonyls or fluorides. However, metal carbonyls are not stable at the operating temperature in an alumina reduction cell.

In the early 1980s the demand for environmental protection increased, forcing the aluminium producers world-wide to improve collection and cleaning efficiency of the waste gases from the Hall-Héroult process. Therefore, processes for cleaning pot gases with alumina gained increasing significance.

Böhm et al. [37] studied possibilities of removing impurities from the secondary alumina. A mass balance on phosphorus in a test potline showed that 72% of the phosphorus will form volatile compounds and evaporate from the cell, which was supported by previous results [35, 36]. Böhm et al. also confirmed that an enrichment of phosphorus in the system will lower the current efficiency. Since impurities seemed to be concentrated in

the fine grain fraction (< 1 μm), removal of impurities by means of grain size classification was found to be very effective. They also claimed that the degree of removal of impurities depends to a certain extent on the type of alumina. Separation of up to 90% of the impurities was reported, when dedusting the pot gas by means of an electrostatic precipitator before it entered the dry scrubber (DS) unit. The use of alumina fines separation after the DS unit resulted in an impurity removal of 50 to 70%.

Further work on how to remove phosphorus from secondary alumina was presented by Cutshall [38]. He investigated several methods of purifying secondary alumina from phosphorus and found that flotation seemed to be the most practical and useful. The P_2O_5 level in the secondary alumina was reduced by 80%. He claimed that a high phosphorus level in the cell leads to higher operating temperatures and reduced current efficiency. Particle size analysis showed that the phosphorus concentration increased with decreasing particle size of alumina, due to the larger surface area of the smaller-sized particles.
In general, the transfer of impurities from the bath to the gas cannot be ascribed to evaporation only. A transfer in connection with carbon dust seems to be important according to Thonstad et al. [39].

Augood [40] reviewed the effects resulting from the installation of a DS unit in an alumina reduction cell-room. He came up with different plant models of how to distribute the impure fine fraction of the secondary alumina in an industrial plant. However, the effect on the current efficiency (CE) due to impurities in the process cannot be improved by this procedure. The distribution ratio between gas and metal, ə, for phosphorus was assumed to be 10. A similar distribution ratio can be defined between gas and feed of the cell as Ŭ. Augood found the following relation for the two distribution ratios:

$$\zeta \mid \frac{\rho}{/1\,2\,\rho\,0} \tag{2.30}$$

Since ə was found to be 10 for phosphorus, Ŭ was calculated to be 0.91, which was confirmed by earlier data [35, 36, 37].

Anufrieva et al. [41] proved that the relationship between phosphorus in the alumina and phosphorus in the bath is linear and that most of the phosphorus enters the cell with the alumina.

Another work on the removal of impurities from dry scrubbed fluoride enriched alumina by Schuh and Wedde [42], showed that the impurity-rich fine fraction (< 10 μm) can be removed more effectively from the coarser fraction by selective impact milling. By leading secondary alumina towards an impact mill, rotating at a speed of at least 900 rpm, successful detachment of the impurity-rich particles from larger secondary alumina particles is achieved. A subsequent separator divides the product into impurity-enriched fines and purified, coarse secondary alumina, which is returned to the cell. For iron and phosphorus about 30 to 70% were removed respectively by separation of 0.5 to 1% of the total quantity of alumina.

A dry scrubber study at a Søderberg reduction plant by Augood [43] showed that the off gas particulates contained about 0.07 wt% P, 0.27 wt% Fe and 15.3 wt% C among other impurities. Related to the cell-room operations, the impurity concentrations in the afternoon were generally lower than those in the morning.

Besides fines separation and electrostatic precipitators Martins [44] reported about a primary cyclone as a third possibility to remove impurities from the off gas of the cells. Its efficiency regarding phosphorus was found to be 48%.

Lossius and Øye [45] were looking for possibilities of removing impurities from the secondary alumina fines and to recover fluoride and alumina. They found that only a wet fractionation process combined good alumina and fluoride recovery with significant impurity removal. In the secondary alumina fines the existence of iron phosphide, Fe_2P, was proved by XRD studies. Other phosphorus compounds like $AlPO_4$ or AlP were assumed to be present as well, but they were not detected by XRD.

When changing from CWPB to PFPB cells at Hamburger Aluminium Werke (HAW), Albers and Wrigge [46] reported an increase of phosphorus in the bath. They came up with a relationship for the PFPB cells between the concentration of phosphorus in bath, $c_{P,\,bath}$, and in metal, $c_{P,\,metal}$,

$$c_{P,\,bath} = 130/21 \cdot c_{P,\,metal} + 10 \text{ ppm P} \qquad (2.31)$$

They confirmed the relationship of 1% loss in current efficiency when 100 ppm of phosphorus (P) was present in the bath. They also set up a flow sheet for phosphorus for the HAW plant.

Sturm and Wedde [32] extended the studies of Albers and Wrigge [46] and reported an improvement of the impurity removal in industrial cells by using selective impact milling as explained above [42]. Nevertheless, they claimed that a loss of current efficiency by 1% is to be expected when 100 ppm of P_2O_5 is present in the bath, which corresponds to about 44 ppm P. In some literature [11] it is asserted that a P_2O_5 content of 100 ppm in the bath will lead to a loss of 1% in current efficiency.

The stable operation of a cell is also related to the quality of the primary alumina added. With regard to phosphorus Dahlmann and Wittner [47] reported about different grades of primary alumina, containing between 10 and 50 ppm P_2O_5 (4.4 to 21.8 ppm P). They referred to a current efficiency loss of 0.95% for each 100 ppm P present in the bath and concluded that impurities in the alumina lead to an important reduction of the CE, especially in case of the use of a DS unit.

Since the phosphorus mainly originates from the alumina added to the cell, several authors have tried to estimate an acceptable concentration limit of phosphorus in the alumina. Richards [28] recommended that the P_2O_5 content in alumina should be lower than 0.0010 wt% for use in aluminium production plants. This recommendation was supported by Grjotheim and Welch [26]. Homsi [48] suggested a somewhat higher P_2O_5 limit, up to 0.0012 wt%, for a smelter.

In a recent report of Thonstad [49] about impurity problems related to point-feeding, a complete review about published work on impurity distribution and problems in both lab and industry scale was presented. The author implied that the behaviour of impurities in general cannot be explained by a simple dissolution mechanism where some of the impurities are reduced and some escape due to evaporation. A more complex mechanism was proposed, where impurities in the bath are apparently divided into at least two fractions, of which one is in solution and the other is attached to carbon particles. Freely dispersed metal particles where also considered to be present in the bath, as suggested by Keller [50] as well.

Concerning the complex environment of phosphorus in the bath, Peterson and Tabereaux [51] suggested that phosphorus will exist as fluoride or oxyfluoride in the cryolite solvent.

As stated earlier, carbon in the electrolyte seems to have a relationship to the transfer of phosphorus in the bath. Carbon particles in the bath act as electrical insulators, causing a higher bath resistance and thereby a higher operational temperature. Foosnæs et al. [52] investigated the dusting of anodes in Hall-Héroult cells and found that the dust seems to accumulate close to the bath surface as well as at the metal-bath interface. The results revealed also that the dust level in Søderberg cell-lines is twice that in prebake cells.

By investigating different industrial bath samples, Oblakowski and Pietrzyk [53] found a linear relationship between the carbon and phosphorus contents in the bath. They concluded that increased contents of C, P_2O_5 and Al_4C_3 in the electrolyte are responsible for an increased operating temperature of industrial cells. The relationship between carbon and phosphorus was explained by the increased wettability of carbon particles by the electrolyte in the presence of phosphorus. This makes it more difficult for the carbon to reach the bath surface and be oxidized to CO_2.

Most of the relevant articles concentrate on the distribution of phosphorus between bath and metal as well as its removal from the DS unit. During a study of sludge in alumina reduction cells, Geay et al. [54] found 120 ppm of silicon and 40 ppm of phosphorus in it. This indicates that sludge might act as an impurity "reservoir". The impurities might return to the electrolyte when the sludge dissolves, or even end up in the metal. Other authors [55] claimed that there are no enrichments of impurities in sludge or ledge.

As pointed out earlier, Øye [27] stated that the use of dry-scrubbing systems leads to recycling and enhancement of the content of impurities in the bath. The distribution factor of impurities between aluminium and alumina was calculated to be < 0.1 for phosphorus, which was supported by experimental results. A mass balance for phosphorus for a prebake reduction cell with DS unit, showed that the total input of phosphorus was 0.08 kg/day. When looking at the output figures for phosphorus, about 10% leaves the cell via the metal phase, while the cell off gas and anode cover material accounts for 65%. About 15% can be found in the anode butts; the remaining phosphorus is present in the bath.

A mass balance study of phosphorus in alumina reduction cells was presented by Danĺk et al. [11, 12]. The cycle of phosphorus in the Slovalco production plant in Slovakia was followed over a three years period. The

increase of phosphorus in the aluminium produced over the investigated period was claimed to originate from an accumulation of phosphorus in the cells, even though the phosphorus content in the secondary alumina seemed to decrease and the phosphorus content in the primary alumina was constant over this time period. All incoming phosphorus was believed to end up eventually in the produced aluminium. A significant increase in the phosphorus content in the aluminium was observed after that highly phosphorus-contaminated dust from the sweeping machines was added to the cells. DanΠk's suggestion that all phosphorus introduced should theoretically end up in the metal, was not in agreement with results from other authors [27, 35, 36, 37, 56]. They suggested that most of the phosphorus present in the cell will be collected in the DS unit and returned to the bath with the secondary alumina. Therefore phosphorus is only forced into the metal because the off gas system with a DS unit recycles most of the phosphorus back to the cell. This is primarily the reason why 80% of P may leave the cell with the metal [56].

The effect of phosphorus on the industrial process of producing aluminium was studied by Frolova et al. [57], who stated that phosphorus is an unwanted impurity due to the fact that it lowers current efficiency. It was assumed that cyclic reduction and re-oxidation between the elemental state and phosphorus pentoxide was responsible for the high loss in CE. Apparently phosphorus was believed to be adsorbed by the carbon dust. From the publication date of the article, it can be assumed that no DS unit was installed at that time. Frolova stated that 50% of the phosphorus escapes with the off gases, while the rest is skimmed off the cells with the carbon dust. An increasing amount of carbon in the bath would affect the phosphorus content in the bath. The article did not state what type of cells the study was performed on, but since the Soviet aluminium production at this time was mainly based on the Søderberg technology, it can be assumed that the study was based on this technology.

Based on an investigation of the distribution of gallium, vanadium and titanium in industrial cells, Liu et al. [55] stated that there exists a strong and positive correlation between the concentration of carbon and the concentration of impurities. The removal of impurities from the process might be possible, if particles in the off gas could be removed effectively.

An industrial report by Handå [58] showed that the quality of the alumina with regard to phosphorus is vital for having an optimal production of aluminium. He stated that the normal phosphorus content in primary

alumina used at the KUBAL plant (Sweden) had been lower than or maximum 10 ppm (as P_2O_5) over the last two decades, before it increased. Different primary alumina shipments showed different P_2O_5 levels, as can be seen in Table 2-7.

Table 2-7: *Primary alumina from different producers and with different dates of arrival. Their content of P_2O_5 are given in ppm.*

Type of alumina (date of arrival)	Content of P_2O_5 [ppm]
Alumina A1 (7/6-1999)	14
Alumina B (17/1-2000)	17
Alumina A2 (31/3-2000)	28
Alumina A3 (18/5-2000)	19

Due to operational problems at the KUBAL plant and a decrease in current efficiency in the prebake line, all standard practices were checked. The phosphorus content in the bath had increased from 43±3 ppm P up to 126 ±11 ppm. The thumb rule that 100 ppm P in the bath decreases the CE by 1% was proved, since the increase by about 83 ppm P in the bath reduced the CE by 0.8% at the KUBAL plant.

The current efficiency at the Søderberg plant in KUBAL, which was fed with the same grade of alumina, did not show any decrease in current efficiency, while the prebake line did when alumina A2 was introduced. In contrast to the prebake line, the off gases from the Søderberg cells were first led through an electrostatic precipitator before going to the DS unit. It was found that the electrostatic precipitator picked up the phosphorus impurities, so that there was no enrichment of phosphorus in the Søderberg cells.

Since the problems in the prebake line were found to be due to an increased amount of phosphorus in the bath, originating from the alumina, the anode cover material from the prebake line having an increased amount of phosphorus was fed to the Søderberg cells. The phosphorus was thereby removed from the process when reaching the electrostatic precipitator. The time period for “cleaning” the prebake line was set to be about four weeks after the use of alumina A2 was terminated.

2.2. Theoretical considerations

2.2.1. Thermodynamics

With the help of thermodynamical data it is possible to calculate the Gibbs energy of reactions and predict their feasibility. However, a complete picture of the probability of these reactions to occur can only be obtained if kinetics is considered as well. Nevertheless, such calculations will indicate how compounds could react with each other. Thermodynamic calculations for different aluminium phosphate compounds were performed by Danïk [11] considering reactions in the electrolyte and in the dry scrubber unit. The Gibbs energy of reactions for 1200 K and 400 K were calculated in the electrolyte and in the dry scrubber unit respectively.

Table 2-8: *Gibbs energies for reactions of phosphorus compounds with electrolyte components and with alumina in the DS unit at 1200 and 400 K respectively [11].*

Reactions in the electrolyte at 1200 K		$\div G^{rx}$ [kJ/mole]
1	$Na_3AlF_{6(l)} + Al(PO_3)_{3(l)} = 3\ NaF_{(l)} + 2\ AlPO_{4(l)} + POF_{3(g)}$	-525
2	$2\ Na_3AlF_{6(l)} + 2\ Al(PO_3)_{3(l)} = 6\ NaF_{(l)} + 2\ AlPO_{4(l)} + Al_2O_{3(l)} + P_2O_{5(g)} + POF_{3(g)}$	-412
3	$P_2O_{5(g)} + Al_2O_{3(l)} = 2\ AlPO_{4(l)}$	-230
4	$P_2O_{5(g)} + 2\ AlF_{3(g)} = Al_2O_{3(s)} + 2POF_{3(g)}$	-120
5	$AlPO_{4(l)} + 2\ C_{(s)} = Al_{(l)} + P_{(g,\ sol)} + 2\ CO_{2(g)}$	+643
6	$2\ Al(PO_3)_{3(l)} + 9\ C_{(s)} = 2\ Al_{(l)} + 6\ P_{(g,\ sol)} + 9\ CO_{2(g)}$	+631
7	$3\ AlPO_{4(l)} + 5\ Al_{(l)} = 4\ Al_2O_{3(l)} + 3\ P_{(g,\ sol)}$	-873
8	$Al(PO_3)_{3(l)} + 5\ Al_{(l)} = 3\ Al_2O_{3(l)} + 3\ P_{(g,\ sol)}$	-1782
9	$P_2O_{5(l)} + 10\ Al_{(l)} = 5\ Al_2O_{3(l)} + 3\ P_{(g,\ sol)}$	-908
Reactions in the dry scrubber unit at 400 K		
11	$3\ POF_{3(g)} + 2\ Al_2O_{3(s)} = Al(PO_3)_{3(s)} + 3\ AlF_{3(s)}$	-290
12	$POF_{3(g)} + Al_2O_{3(s)} = AlPO_{4(s)} + AlF_{3(s)}$	-253

The aluminium phosphate compounds considered to be present were aluminium orthophosphate, $AlPO_4$, and aluminium metaphosphate, $Al(PO_3)_3$. The data for these compounds should be available in the JANAF Thermochemical Tables as stated by Danïk [11]. However, the existence of the metaphosphate compound was not found in these tables. Using the Gibbs energy for the reactions in Danïk's article, a standard Gibbs energy of formation for $Al(PO_3)_3$ was calculated from reactions 1, 2, 6 and 8 and

found to be –3421.8 ±179.7 kJ/mole at 1200 K. Due to the large standard deviation of the average value calculated, this substance was not considered in the thermodynamic calculations for this work.

The data available in the thermodynamic calculation programme [6] used for further calculations, are given in Table 2-9.

Table 2-9: *Standard Gibbs energy of formation for several compounds at 400 and 1200 K from HSC3 software [5], (* - for data for gaseous species, a – no data available).*

Species	÷Gº(400 K) [kJ/mole]	÷Gº(1200 K) [kJ/mole]	Species	÷Gº(400 K) [kJ/mole]	÷Gº(1200 K) [kJ/mole]
Na_3AlF_6	-3417.9	-3812.1	Al_4C_3	-249.4	-437.7
Al_2O_3	-1699.4	-1821.9	P_2O_5	-1544.1	a*
CaF_2	-1257.2	-1372.6	P_4O_{10}	-3144.3	-3605.1*
AlF_3	-1541.0	-1666.3	$AlPO_4$	-1775.0	-1946.7
NaF	-598.6	-680.2	Na_3PO_4	-1996.3	-2295.9
Al	0	0	AlP	-185.8	-260.4
C	0	0	P	0	0
$CO_{(g)}$	-196.3	-378.2	$PF_{3(g)}$	-1077.4	-1351.1
$CO_{2(g)}$	-486.4	-693.1	$PF_{5(g)}$	-1726.1	-2051.9
$NaAlF_{4(g)}$	-1992.1	-2360.9	$POF_{3(g)}$	-1361.2	-1656.5

As can be seen in Table 2-9, most of the bath components have been taken into account as well as aluminium and anode gases like CO and CO_2. Carbon can be seen as anode carbon or carbon particles in the electrolyte. Aluminium carbide can reach a solubility of ~2.15 wt% in a cryolite based melt with a CR ratio of 1.8 and should therefore also be considered.

The following Table 2-10 gives an overview of possible reactions in both electrolyte and dry scrubber. The electrolyte temperature was chosen to be 1230 K or 957 ºC. The temperature of the off gas reaching the dry scrubber unit was assumed to be 430 K or 157 ºC.

Table 2-10: *Reactions and calculated Gibbs energies for possible reactions involving phosphorus compounds in the electrolyte and in the DS unit [6].*

Reactions in the electrolyte at 1230 K		**$\div G^{rx}$ [kJ/mole]**
1	$Na_3AlF_{6(l)} + AlPO_{4(l)} = 3\ NaF_{(l)} + Al_2O_{3(l)} + POF_{3(g)}$	239.7
2	$2\ Na_3AlF_{6(l)} + Na_3PO_{4(l)} = 9\ NaF_{(l)} + Al_2O_{3(l)} + POF_{3(g)}$	319.6
3	$Na_3AlF_{6(l)} + P_4O_{10(g)} = 12\ NaF_{(l)} + 2\ Al_2O_{3(l)} + 4\ POF_{3(g)}$	420.9
4	$Na_3AlF_{6(l)} + AlPO_{4(l)} = Na_3PO_{4(l)} + 2\ AlF_{3(l)}$	130.1
5	$Na_3AlF_{6(l)} + Na_3PO_{4(l)} = AlPO_{4(l)} + 6\ NaF_{(l)}$	79.9
6	$Al_2O_{3(l)} + P_4O_{10(g)} = 4\ AlPO_{4(l)}$	-602.4
7	$1/3\ Al_2O_{3(l)} + PF_{5(g)} = AlPO_{4(l)} + 2/3\ AlF_{3(l)}$	-243.9
8	$Al_2O_{3(l)} + POF_{3(g)} = AlPO_{4(l)} + AlF_{3(l)}$	-134.6
9	$10/3\ Al_2O_{3(l)} + 4\ AlP_{(s)} = P_4O_{10} + 32/10\ Al_{(l)}$	2929.4
10	$5\ NaF_{(l)} + Na_3PO_{4(l)} = 4\ Na_2O_{(l)} + PF_{5(g)}$	1339.5
11	$NaF_{(l)} + AlPO_{4(l)} = Na_3PO_{4(l)} + AlF_{3(l)}$	6.0
12	$5/3\ AlF_{3(l)} + AlP_{(s)} = PF_{5(g)} + 8/3\ Al_{(l)}$	825.3
13	$5/3\ AlF_{3(l)} + AlPO_{4(l)} = PF_{5(g)} + 4/3\ Al_2O_{3(l)}$	243.9
14	$10\ CaF_{2(l)} + P_4O_{10(g)} = 4\ PF_{5(g)} + 10\ CaO_{(l)}$	1909.2
15	$3\ CaF_{2(l)} + 2\ AlPO_{4(l)} = 2\ AlF_{3(l)} + Ca_3(PO_4)_{2(l)}$	53.9
16	$3\ CaF_{2(l)} + Na_3PO_{4(l)} = 6\ NaF_{(l)} + Ca_3(PO_4)_{2(l)}$	3.8
17	$10/3\ Al_{(l)} + 2\ AlPO_{4(l)} = P_{2(g,\ sol)} + 8/3\ Al_2O_{3(l)}$	-454.9
18	$8/3\ Al_{(l)} + AlPO_{4(l)} = AlP_{(s)} + 4/3\ Al_2O_{3(l)}$	-917.1
19	$32/3\ Al_{(l)} + P_4O_{10(g)} = 4\ AlP_{(s)} + 10/3\ Al_2O_{3(l)}$	-2929.4
20	$2\ Al_{(l)} + P_{2(g,\ sol)} = 2\ AlP_{(s)}$	-247.4
21	$2\ C_{(s)} + AlPO_{4(l)} = AlP_{(s)} + 2\ CO_{2(g)}$	337.8
22	$4\ C_{(s)} + 2\ AlPO_{4(l)} = 2\ Al_{(l)} + P_{2(g)} + 4\ CO_{2(g)}$	923.0
23	$5\ C_{(s)} + 2\ AlPO_{4(l)} = Al_2O_{3(l)} + P_{2(g)} + 5\ CO_{(g)}$	122.3
24	$3\ C_{(s)} + 4\ AlP_{(s)} = Al_4C_{3(l)} + 2\ P_{2(g)}$	355.2
25	$C_{(s)} + P_4O_{10(g)} = 2\ P_2O_{3(g)} + CO_{2(g)}$	-22.4
26	$5\ C_{(s)} + P_4O_{10(g)} = 2\ P_{2(g)} + 5\ CO_{2(g)}$	-71.4
27	$5\ CO_{(g)} + 2\ AlPO_{4(l)} = Al_2O_{3(l)} + 5\ CO_{2(g)} + P_{2(g)}$	344.1
28	$4\ CO_{(g)} + AlPO_{4(l)} = AlP_{(s)} + 4\ CO_{2(g)}$	426.5
29	$10\ CO_{(g)} + 2\ P_{2(g)} = P_4O_{10(g)} + 10\ C_{(s)}$	293.2
30	$4\ CO_{(g)} + AlP_{(s)} = AlPO_{4(l)} + 4\ C_{(s)}$	-249.1
31	$Al_4C_{3(l)} + 12/5\ AlPO_{4(l)} = 16/5\ Al_2O_{3(l)} + 6/5\ P_{2(g)} + 3\ C_{(s)}$	-960.2
Reactions in the dry scrubber unit at 430 K		**$\div G^{rx}$ [kJ/mole]**
32	$POF_{3(g)} + Al_2O_{3(s)} = AlPO_{4(s)} + AlF_{3(s)}$	-255.4
33	$P_4O_{10(g)} + 2\ Al_2O_{3(s)} = 4\ AlPO_{4(s)}$	-586.9
34	$PF_{5(g)} + 4/3\ Al_2O_{3(s)} = AlPO_{4(s)} + 5/3\ AlF_{3(s)}$	-352.5

Even though reactions 17, 22-24, 26, 27, 29 and 31 in Table 2-10 propose the evolution of gaseous elemental phosphorus, it is rather unlikely to find elemental phosphorus in the off gas of the cell, since it would react immediately with the oxygen molecules in the air to form phosphorus pentoxide. Therefore, elemental phosphorus was not considered when looking at reactions in the dry scrubber unit. For the calculations $P_{2(g)}$ was selected as the form of elemental phosphorus, since besides $P_{4(g)}$ it can be considered as the dominant species at these temperature as explained earlier in Section 2.1.1.1.

The reactions of phosphorus compounds with cryolite (reaction 1 and 2 in Table 2-10) do not seem to be likely to happen, which is also confirmed by measurement by Tkatcheva et al. [14]. As stated by Danik [11], reaction 6 in Table 2-10 might explain how the escape of phosphorus as P_4O_{10} can be hindered by getting adsorbed on the alumina covering of the cell. Particles or pieces of the crust may fall into the electrolyte and thereby return the phosphorus to the bath. Reaction 7 and 8 in Table 2-10 can be interpreted the same way.

Considering the influence of phosphorus compounds on the cryolite ratio (CR), reaction 11 in Table 2-10 might indicate that by the exchange of cations of the fluoride and phosphate species the local cryolite ratio is affected.

Reaction 17 in Table 2-10 shows that the reduction of aluminium orthophosphate with aluminium is thermodynamically favoured, evolving elemental phosphorus. This reaction is even more shifted when producing aluminium phosphide, as shown in reaction 18 in the same table.

Since phosphorus is produced in a carbothermal process as described in reaction (2.1), one might expect that carbon in contact with phosphates could lead to a reduction reaction. As can be seen from reaction 21-23 in Table 2-10, this does not seem to be the case at this temperature. However, if gaseous P_4O_{10} is getting in contact with carbon, a reduction might be possible (reactions 25 and 26, Table 2-10).

In contact with anode gases, aluminium phosphate or gaseous phosphorus do not seem to be reduced or oxidized respectively (reactions 27-29). However, if dissolved aluminium phosphide would be present in the

electrolyte, reactions with CO and CO_2 might be possible, as shown in reactions 21 and 30.

Looking at reaction 31, dissolved aluminium carbide in the electrolyte may react with aluminium phosphate, forming finely dispersed carbon particles in the vicinity of elemental phosphorus. This might be an explanation of how phosphorus as well as other impurities like iron are adsorbed on carbon particles in the bath.

Only gaseous species of phosphorus were considered when looking at reactions with alumina in the DS unit. All assumed reactions show a negative Gibbs energy, which indicates that aluminium orthophosphate is the most stable phosphorus compound in secondary alumina.

The transport towards the DS unit of phosphorus species adsorbed on carbon and dust particles was not taken into account in the thermodynamic calculations. As mentioned in Section 2.1.4.2., this might be an important way of transport for phosphorus as stated by Thonstad et al. [39].

2.2.2. Decomposition potential / deposition potential

In the case of alumina the electrolytic decomposition can simply be expressed by reaction (2.32), where aluminium oxide splits into its elements, aluminium and oxygen.

$$Al_2O_{3(dissolved)} \mid 2Al_{(l)}21.5O_{2(g)} \tag{2.32}$$

As already pointed out in Chapter 1, the overall reaction by which aluminium is produced using carbon anodes, can be written as:

$$Al_2O_{3(dissolved)}\ 2\,1.5C_{(s)} \mid 2Al_{(l)}21.5CO_{2(g)} \tag{2.33}$$

From these equations it is possible to calculate the standard decomposition potential by means of thermodynamic data when reactants and products are in their standard states.

$$E^o \mid 4\frac{\div G^o}{n\ \lceil F} \tag{2.34}$$

If some or all components are not in their standard state, the Nernst equation can be used to calculate the reversible or decomposition potential,

$$E_d = E^o - \frac{RT}{nF} \ln Q \quad (2.35),$$

where the reaction constant Q for reaction (2.33) can be written as

$$Q = \frac{a_{Al}^2 \, p_{CO_2}^{1.5}}{a_{Al_2O_3} \, a_C^{1.5}} \quad (2.36).$$

Since Al, CO_2 and C are assumed to have unit activity, the reaction constant is inversely proportional to the alumina activity. Equation (2.35) can therefore be written as:

$$E_d = E^o - \frac{RT}{nF} \ln \frac{1}{a_{Al_2O_3}} \quad (2.37)$$

It can be concluded, that the decomposition potential of alumina is dependent on temperature and alumina activity, when the components are not in their standard states [59].

If sufficient thermodynamic data is available, decomposition potentials can be determined for different compounds of interest. “In this context it should be noted that in molten salts no general electrochemical series can be formulated, since the deposition potentials of different metals vary with the anionic environment” [60], which could also be valid for non-metals like phosphorus. Changes in temperature might also affect the sequence of the decomposition potentials. Reported potentials of decomposition have been obtained over a wide range of experimental conditions and different cell designs. Therefore, it is not necessarily correct to compare the obtained values, but a trend can be predicted.

The decomposition potentials of the impurities concerning the aluminium production process are of great importance, since conclusions can be drawn about the stability of those in cryolite-based melts. The relevant reactions, which will be discussed in the following, can be generally formulated as,

$$M_x O_{y(dissolved)} = x\, M_{(l)} + \frac{y}{2} O_{2(g)} \quad (2.38)$$

$$M_xO_{y(dissolved)} \; 2\; y\, C_{(s)} \;|\; \; x\, M_{(l)} \; 2\; \frac{y}{2}\, CO_{2(g)} \qquad (2.39).$$

A large number of metallic impurities have been investigated. Theoretical and experimental values of their decomposition potentials are given in Table 2-11.

Table 2-11: *Decomposition potentials of metal oxide impurities, theoretical and experimental values in Volts. Theoretical values are calculated according to reactions (2.38) and (2.39).*

Oxide	theoretical values		Experimental E_d values (reaction 2.39)		
	$E^\circ_{d,\,1300\,K}$ (reaction 2.38)[a]	$E^\circ_{d,\,1300\,K}$ (reaction 2.39)[a]	†	‡	*
Al_2O_3	-2.18	-1.15	-1.07±0.01	-1.45	-1.45
BeO	-2.49	-1.47	-1.07		
MgO	-2.37	-1.35	-1.07		
CaO	-2.59	-1.56	-1.07		
SrO	-2.38	-1.36	-1.07		
BaO	-2.21	-1.18	-1.07		
Cr_2O_3	-1.38	-0.36	-0.75±0.05		
MnO	-1.50	-0.47	-0.81±0.01		
MnO_2	-0.74	0.29	-0.81±0.01		
Mn_3O_4	-1.22	-0.19	-0.81±0.01		
FeO	-0.93	0.10	-0.23±0.03		
Fe_3O_4	-0.91	0.12	-0.23±0.03		
Co_3O_4	-0.54	0.49	-0.13±0.03		
NiO	-0.64	0.39	0		
Ta_2O_5	-1.54	-0.51	-0.83±0.02	-0.91	
Nb_2O_5	-1.39	-0.36	-0.71±0.01	-0.64	
TiO_2	-1.84	-0.81	-0.50±0.02		
WO_3	-0.89	0.14	-0.40±0.01		
MoO_3	-0.75	0.28	-0.10±0.03		
ZrO_2	-2.21	-1.18	-1.07		
V_2O_5	-1.07	-0.04	-0.08±0.01	-0.60	
SiO_2	-1.76	-0.73	-1.07±0.01		-(1.0-1.25)
La_2O_3	-2.46	-1.43	-1.07		

[a] from HSC3 software

† 1020 ºC, anode and cathode material: graphite, 0.25g equivalent of the oxide in 160g cryolite [61]

‡ 1040 ºC, anode material: graphite, cathode material: graphite or nickel [62]

* 1000 ºC for alumina saturated melts, for melts with silica: temperature unknown (for more detailed information see Appendix A) [63]

The difference between the theoretical potentials for reaction (2.39) and the experimental ones could be due to polarisation of the carbon electrodes, or that the impurity oxide concerned was not in its standard state during the

measurement. Experiments with metal oxides with more negative decomposition potentials than alumina had a decomposition potential, which resembled E_d for alumina. As it can be seen also from thermodynamic calculations, aluminium will deposit before any metal of this group. This indicates no metallic ions of this group should ideally be found in the metal, but should stay in the bath in an alumina reduction cell. Mergault [61] exposed pure cryolite for 1 hour to air while keeping it near the melting point and obtained from this melt a decomposition potential similar to that of alumina. This indicates that dissolved oxygen from air is present in the melt, forming oxyfluoride complexes as when alumina is added. The decomposition potentials are therefore equal. A similar behaviour can be assumed for metal oxides with a lower decomposition potential than alumina, where the oxide ions form oxyfluoride compounds. The metal ions stay in the electrolyte.
Metal oxides with a lower decomposition potential than alumina, will mainly be deposited with the aluminium in a reduction cell.

Mergault [61] found, that independent of the valency of the metal in the added oxide, the measured decomposition potential was the same, e.g. for metal oxides like FeO and Fe_3O_4.

Monnier et al. [62] and Bøe et al. [63] found a decomposition potential for alumina at 1.45V, but did not comment on the results from Mergault, who obtained a decomposition potential about 0.4 V lower.

For metallic impurities in cryolite melts, a wide range of measurements on decomposition potentials has been performed. On non-metallic impurities like phosphorus or boron, no literature was found about experimentally determined decomposition potentials. However, by means of thermodynamic data, theoretical decomposition voltages of substances containing phosphorus can be determined. The reactions, for which the decomposition potentials will be shown in Table 2-12, are the following,

$$FePO_4 + 2\,C \rightarrow Fe + P + 2\,CO_{2(g)} \quad (2.40)$$
$$P_2O_5 + 2\,C \rightarrow 2\,P + 2.5\,CO_{2(g)} \quad (2.41)$$
$$NaPO_3 + 1.5\,C \rightarrow Na + P + 1.5\,CO_{2(g)} \quad (2.42)$$
$$(NaPO_3)_3 + 4.5\,C \rightarrow 3\,Na + 3\,P + 4.5\,CO_{2(g)} \quad (2.43)$$
$$AlPO_4 + 2\,C \rightarrow Al + P + 2\,CO_{2(g)} \quad (2.44)$$
$$Na_4P_2O_7 + 3.5\,C \rightarrow 4\,Na + 2\,P + 3.5\,CO_{2(g)} \quad (2.45)$$
$$Na_3PO_4 + 2\,C \rightarrow 3\,Na + P + 2\,CO_{2(g)} \quad (2.46)$$
$$Ca_3(PO_4)_2 + 4\,C \rightarrow 3\,Ca + 2\,P + 4\,CO_{2(g)} \quad (2.47).$$

All values in Table 2-12 are calculated according to reaction (2.39).

Table 2-12: *Decomposition potentials of phosphorus compounds and alumina in volts at 1020˚C. Data calculated with HSC3 software [6] for reaction (2.39).*

Substance	$E^{\circ}_{d,\ 1020^{\circ}C}$	$E^{\circ}_{d,\ 1020^{\circ}C}$ vs. Al^{3+}/Al
$FePO_4$	0.14	1.29
P_2O_5	0.10	1.26
$NaPO_3$	-0.35	0.81
$(NaPO_3)_3$	-0.35	0.80
$AlPO_4$	-0.57	0.59
$Na_4P_2O_7$	-0.60	0.56
Na_3PO_4	-0.74	0.42
$Ca_3(PO_4)_2$	-0.97	0.18
Al_2O_3	-1.16	0.00

From a thermodynamical point of view, it can be assumed that phosphorus in its fivevalent state will be reduced to the elemental state before aluminium is deposited. In theory phosphorus should therefore mainly be found in the metal phase of an aluminium production cell. However, this is not the case when comparing to analysis data of bath and metal in industrial cells (see Chapter 6).

References to Chapter 2

[1] A.F. Hollemann, E. Wiberg, *Lehrbuch der anorganischen Chemie,* Walter de Gruyter, Chapter XIV, 725 ff., 1995.

[2] http://pearl1.lanl.gov/periodic/elements/15.html

[3] M. Halmann, *"The role of phosphorus in the world"*, Analytical chemistry of phosphorus compounds, **37**, 1-7, 1972.

[4] F.D. Richardson, *Physical chemistry of melts in metallurgy,* Part 1 and 2, Academic Press Inc. (London) Ltd., 1974.

[5] U. Müller, *Anorganische Strukturchemie*, B.G. Teubner, Stuttgart, Chapter 12, 1991.

[6] Outokumpu HSC chemistry® for Windows, Version 3.0, software for thermodynamical calculations, www.outokumpu.fi\hsc.

[7] CRC Handbook of chemistry and physics, 1985-1986, edited by R.C. Weast.

[8] S. Julsrud, *Some oxy-anion complexes in alkali-fluoride melts: a thermodynamic investigation,* Dr. Tech. Dissertation, University of Trondheim, Norway, 1983.

[9] J.J. del Campo, *La Electrolisis de la alumina en la criolita fundida,* doctoral dissertation, Universidad de Oviedo, Escuela Tecnica Superior de Ingenieros de Minas, Oviedo, Spain, 1984.

[10] D. Bratland, H. Kvande, W.Q. Bin, *Ionic species in cryolite-sodium pyrophosphate melts*, Acta Chem. Scand. A41, 377-380, 1987.

[11] V. Danĺk, M. Chrenková, A. Silný, G. M. Haarberg, M. Staš, *Distribution of phosphorus in industrial aluminium cells*, Proc. Int. Terje Østvold Symp., Røros, Norway, pp. 161-168, 1998.

[12] V. Danĺk, M. Chrenková, A. Silný, G.M. Haarberg, M. Staš, *Distribution of phosphorus in industrial cells*, Can. Met. Quart., **38**(3), 149-156, 1999.

[13] M. Chrenková, V. Danĺk, A. Silný, *Reactions of phosphorus in molten cryolite,* X. Slovak-Norwegian Symposium on Aluminium Smelting Technology, Stará Lesná-Ziar nad Hvonom, Slovakia, Sep. 21-23, 1999.

[14] O. Tkatcheva, H. Mediaas, T. Østvold, *Phosphorus in cryolite I*, internal report at the Institute of Inorganic Chemistry, NTNU Trondheim, Norway, 1999.

[15] O. Tkatcheva, H. Mediaas, T. Østvold, *Phosphorus in cryolite II*, internal report at the Institute of Inorganic Chemistry, NTNU Trondheim, Norway, 1999.

[16] Private communication with T. Østvold, IMT, NTNU Trondheim, Norway, 2003.

[17] R.L. Combes, F. de Andrade, M. Lopez, *Study of the oxoacidobasic properties of phosphate ions in molten NaCl-KCl at 1000 K,* International Jondal Symposium on Mg electrolysis, June 2000.

[18] K.B. Chaudhuri, *Beeinflussung der Aluminiumverluste in Kryolith-Tonerde-Schmelzen durch Badverunreinigungen und Badzusätze*, Ph.D. thesis, Technical University in Berlin, 1968.

[19] K.S.V. Sanathanam, *Phosphorus,* Standard Potentials in aqueous solution, ed. A.J. Bard, R. Parsons, J. Jordan, Dekker, New York, Chapter 7, 139-162, 1985.

[20] H.A. Laitinen, *Polarography of oxyanions in molten salts,* Talanta, **12**, 1237-1241, 1965.

[21] H.A. Laitinen, K.R. Lucas, *Study of the electroreduction of metaphosphate in molten LiCl-KCl eutectic,* J. Electroanal. Chem., **12**, 553-563, 1966.

[22] E. Franks, D. Inman, *The electroreduction of molten phosphates,* J. Electroanal. Chem., **26**, 13-26, 1970.

[23] A. Kerouanton, J. Badoz-Lambling, *Comportment chimique et electrochimique de composes du phosphore dans la cryolithe fondue*, Revue de Chimie minerale, **11**, 223, 1974.

[24] G. Charlot, J. Badoz-Lambling, P. Homsi, V. Plichon, *Electrochimie dans les melanges NaF + AlF_3 fondus*, J. Electroanal. Chem., **75**, 665-675, 1977.

[25] L. Deininger and J. Gerlach, *Stromausbeutemessungen bei der Aluminiumoxidreduktionselektrolyse in Laboratoriumszellen,* Metall, **33**, 131, 1979.

[26] K. Grjotheim, B. Welch, *Aluminium Smelter Technology*, 2nd edition, Aluminium-Verlag, Düsseldorf, 1980.

[27] H.A. Øye, *Impurities in Aluminium Smelting,* 5th Australian-Asian Aluminium Smelter Technology Workshop, Sydney, Australia, October 22.-27., 660-680, 1995.

[28] N. Richards, *Alumina in Smelting,* The 19th International Course on Process Metallurgy of Aluminium, Chapter 11, Trondheim, Norway, 2000.

[29] K. Grjotheim, *Nature and origin of impurities in the Hall-Héroult electrolyte and their effect on metal purity,* International Seminar on Refining and Alloying of Liquid Aluminium and Ferro-Alloys, August 26-28, Trondheim, Norway, 1985.

[30] Industrial data from Norsk Hydro Aluminium, 2002.

[31] Z. Qui, Y. Yaxin, H. Minhong, Y. Xianjin, S. Bing Li, *Impurity distribution in bath and metal in aluminium electrolysis,* Aluminium, **75**, 1110-1113, 1999.

[32] E. Sturm, G. Wedde, *Removing impurities from the aluminium electrolysis process*, Light Metals 1998, 235-240.
[33] P.A. Solli, *Current efficiency in aluminium electrolysis cells,* Dr. ing. thesis, NTNU Trondheim, Norway, 1993.
[34] J. Langerweger, *Metallische Begleitelemente im Elektrolyse-aluminium und ihre Auswirkungen auf die Produkte*, Erzmetall, **36**(4), 181-185, 1983.
[35] V. Sparwald, *Beitrag zur Verflüchtigung der Begleitelemente bei der Aluminiumschmelzflusselektrolyse*, Erzmetall, **26**, 529 ff., 1973.
[36] R.E. Frankenfeldt, U. Mannweiler, *Correlation between potgas collection efficiency and metal purity*, Annual Meeting AIME Metallurgical Society Extractive Metallurgy Division, New York, Light Metals 1975.
[37] E. Böhm, L. Reh, V. Sparwald, G. Winkhaus, *Removal of impurities in aluminium smelter dry gas cleaning using the VAW/Lurgi process*, Light Metals 1976, 509-521.
[38] E.R. Cutshall, *Removal of phosphorus from dry scrubber alumina*, Light Metals 1979, 927-933.
[39] J. Thonstad, F. Nordmo, S. Rolseth, J.B. Paulsen, *On the transfer of some trace elements in dry scrubbing systems,* Light Metals 1979, 463-479.
[40] D.R. Augood, *Impurities distributions in alumina reduction plants*, Light Metals 1980, 413-427.
[41] N.I. Anufrieva, L.S. Baranova, I.G. Lvovskaya, *Trace impurities in the electrolyte and metal in aluminium cells,* Tsvetn. Metall, **16**, 17-19, 1982.
[42] L. Schuh, G. Wedde, *Removal of impurities from dry scrubbed fluoride enriched alumina*, Light Metals 1986, 399-403.
[43] D.R. Augood, *A dry scrubber study*, Light Metals 1987, 625-631.
[44] L.C.B. Martins, *Use of Dry scrubber primary cyclone to improve the purity of aluminium,* Light Metals 1987, 315-317.
[45] L.P. Lossius, H.A. Øye, *Removing impurities from secondary alumina fines*, Light Metals 1992, 249-258.
[46] H. Albers, H.-C. Wrigge, *The effect of reduced emissions on aluminum electrolysis process,* Travaux ICSOBA, **24**, 485-492, 1997.
[47] H.J. Dahlmann, H. Wittner, *Ofen- und Prozessfuehrung beim Einsatz von physikalisch und chemisch variablen Oxidprovenienzen in der Aluminiumelektrolyse*, Erzmetall, **31**, 515-518, 1978.

[48] P. Homsi, The 18th International Course on Process Metallurgy of Aluminium, Trondheim, Norway, 1999.

[49] J. Thonstad, *The behaviour of impurities in aluminium cells,* X. Slovak-Norwegian Symposium on Aluminium Smelting Technology, Sep. 21-23, Stará Lesná-Ziar nad Hronom, Slovakia, 5-12, 1999.

[50] R. Keller, *Laboratory study on the reaction of impurities in aluminum electrolysis,* Light Metals 1982, 295-298.

[51] R.D. Peterson, A.T. Tabereaux, *Effect of bath additives on aluminum metal purity*, Light Metals 1986, 491-499.

[52] T. Foosnæs, T. Naterstad, M. Bruheim, K. Grjotheim, *Anode dusting in Hall-Héroult cells,* Light Metals 1986, 729-738.

[53] R. Oblakowski, S. Pietrzyk, *Superheating of Na_3AlF_6-AlF_3-Al_2O_3 electrolyte in the process of aluminium electrolysis*, Metallurgy and Foundry Engineering, **21**(3), 175-183, 1995.

[54] P.-Y. Geay, B.J. Welch, P. Homsi, *Sludge in operating aluminium smelting cells,* Light Metals 2001, 541-547.

[55] X. Liu, I. Clements, S. George, *Distribution of impurities in reduction cells*, Proc. 4th Australasian Smelting Technology Workshop, Sydney, Australia, 457-473, 1992.

[56] E. Haugland, G.M. Haarberg, E. Thisted, J. Thonstad, *The behaviour of phosphorus impurities in aluminium electrolysis cells*, Light Metals 2001, 549-553.

[57] E.B. Frolova, V.B. Dobrokhotov, A.M. Tsyplakov, *Effect of phosphorus pentoxide on aluminium electrolysis,* Trudy Vami, English translation, **89**, 1-6, 1974.

[58] S. Handå, *The effect of phosphorus on aluminium cells connected to dry scrubbers. Problems caused by phosphorus in the prebake line at KUBAL Smelter in Sundsvall Sweden,* Unpublished report, July 2000.

[59] W. Haupin, *The principles of aluminium electrolysis*, The 19th International Course on Process Metallurgy of Aluminium, Chapter 2, Trondheim, Norway, 2000.

[60] K. Grjotheim, C. Krohn, M. Malinovsky, K. Matiasovsky, J. Thonstad, *Aluminium Electrolysis – Fundamentals of the Hall-Héroult Process*, 2nd edition, Aluminium-Verlag GmbH, Düsseldorf, Germany, 1982.[61] P. Mergault, *Decomposition voltages of some oxides dissolved in molten cryolite at 1020 °C,* Ann. phys., **13**(3), 179-229, 1958.

[62] R. Monnier, P. Grandjean, *Recherches sur l'obentention, la séparation et la purification du tantale et du niobium, notamment par voie électrolytique,* Helv. Chim. Acta, **43**, 2163, 1960.

[63] G. Bøe, K. Grjotheim, K. Matiašovsky, P. Fellner, *Electrolytic deposition of silicon and of silicon alloys Part II: Decomposition voltages of components and current efficiency in the electrolysis of the Na_3AlF_6-Al_2O_3-SiO_2 mixtures*, Can. Met. Quart., **10**(3), 179-183, 1972.

3. Theory of measurements

3.1. Electrochemical methods

The theory for different systems will be explained based on the following, general reaction:

$$O\,2\,n\,e^{4}\quad \ddot{Y}\quad R \tag{3.1}$$

During an experimental study of an electrode reaction the following transport processes may be significant:

$\notin$ diffusion
$\notin$ convection
$\notin$ migration

The contribution to the flux concerning migration of a species *O* can be neglected, if a large excess of supporting electrolyte is present [1].
In an unstirred solution the convective contribution can be neglected for short time scales (< 10 s). Thereafter natural convection may influence the flux of species *O*. Therefore, diffusion can be considered the only transport process for a species *O* to be considered when looking at the current flow:

$$i_O \mid n\,\lceil F\,\lceil D_O\,\lceil \subseteq c_O \tag{3.2}$$

Equation (3.2) expresses Fick's 1. law where the current density is proportional to the concentration gradient of species *O* at the electrode. The transport of species *O* can be regarded as a one-dimensional diffusion towards the electrode surface. Hence, equation (3.2) can be written as:

$$i_O \mid n\,\lceil F\,\lceil D_O\,\lceil \frac{\in c_O}{\in x} \tag{3.3}$$

For transient methods in electrochemistry Fick's 2. law has to be solved as well, to include the change of concentration of *O* with time:

$$\frac{\in c_O}{\in t} \mid D_O \frac{\in^2 c_O}{\in x^2} \tag{3.4}$$

Different methods and systems require different boundary conditions for which equation (3.4) has to be solved. In the following the techniques used in these thesis and the most significant cases will be explained in more detail.

3.1.1. Voltammetry

Voltammetry is usually the first technique used in any electrochemical investigation, since it is easy to perform and it provides quick information about the system under investigation. It is a so-called transient method, where the potential is changed at a constant speed.

$$E(t) = E_{start} \pm \tau t \tag{3.5}$$

where E_{start} is the starting potential from where the potential is swept with a constant sweep rate, τ, with time. Voltage sweeps can either be linear (single sweep) or cyclic (multi sweeps). When changing the sweep direction like in the case for cyclic voltammetry (CV), the potential at time t after changing the direction can be expressed as

$$E(t) = E_{start} \pm 2 \mp \tau \varsigma \pm \tau t \tag{3.6}$$

with ς being the time at which the direction of the potential was changed [1]. Considering a reversible electrochemical reaction where both the reactant O and the product R are soluble in the electrolyte, the following shape of the current voltage curve in a voltammogram can be expected as shown in Figure 3-1.

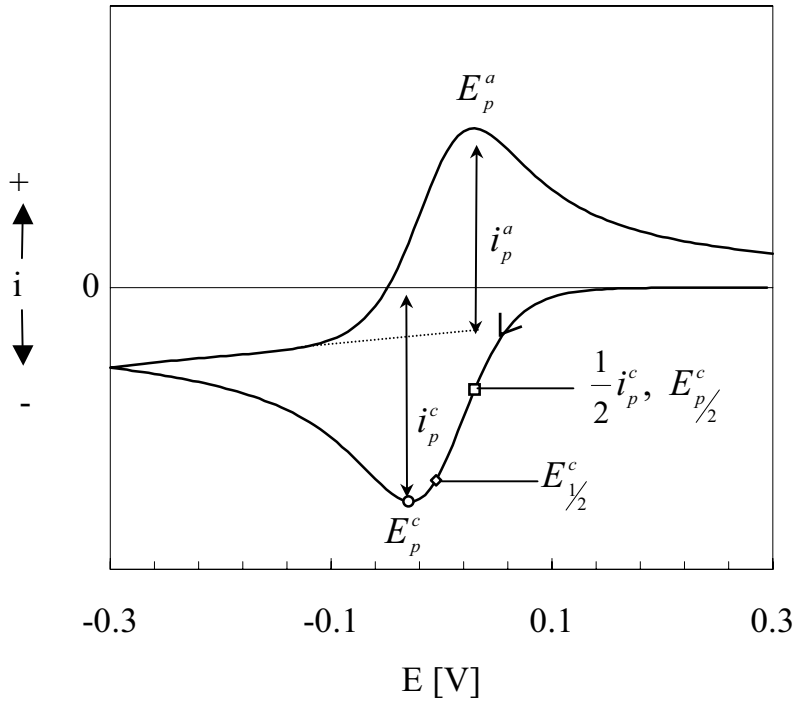

Fig. 3-1: *Theoretical cyclic voltammogram at 25 ºC for a reversible process with a soluble reactant O and a soluble product R, n = 1 [2].*

The boundary conditions for a soluble-soluble system are:

$$c_O\,(x,0) = c^o\,; \qquad c_O\,(\leftarrow,t) = c^o \tag{3.7}$$

$$c_R\,(x,0) = 0\ ; \qquad c_R\,(\leftarrow,t) = 0 \tag{3.8}$$

$$D_O \left(\frac{\partial c_o(x,t)}{\partial x}\right)_{/0,t0} = 2\, D_R \left(\frac{\partial c_R(x,t)}{\partial x}\right)_{/0,t0} \neq 0 \tag{3.9}$$

For a reversible system the surface concentration of species O and R at a given potential are given by the Nernst equation. Since the activities of the electroactive species in the electrolyte can be assumed to be low, the activity coefficients can be set to 1 and the Nernst equation can be written with concentrations of O and R instead of activities.

$$\frac{c_O/0,t0}{c_R/0,t0} = \exp\left[\frac{n\,(F}{R\,(T}/E^{rev} - E^o(\right] \tag{3.10}$$

By solving this problem with the given boundary values by using Laplace transformation, Randles [3] and Sevļik [4] found an equation for the current density.

$$i = 4n F A D_O \omega t^{1/2} c^o \phi^{1/2} \theta(\omega t) \tag{3.11}$$

where the function $\theta(\omega t)$ has the following form:

$$\theta(\omega t) = \sum_{j=1}^{\infty} (-1)^{j-1} 4 j^{1/2} \left[\operatorname{ierfc}\left(\frac{j}{E - E_{1/2}} \sqrt{\frac{nF}{RT}} \right) \right] \tag{3.12}$$

with $$\omega = \left(\frac{nF}{RT} \right) t \tag{3.13}$$

A maximum value of equation (3.12) was calculated by several authors [5, 6, 7]. It was found that $\{\phi^{1/2} \theta(\omega t)\}_{max}$ was 0.446 at the peak potential E_p (equation (3.15)). Therefore the peak current density is given by:

$$i_p = 0.446 \left(\frac{n^3 F^3}{RT} \right)^{1/2} A D_O^{1/2} c^o t^{1/2} \tag{3.14}$$

This equation is called the Randles-Sevļik equation. A plot of i_p versus $\tau^{1/2}$ will give a straight line from which slope the diffusion coefficient for species O can be calculated. The peak potential, E_p, and the half-peak potential $E_{p/2}$ are:

$$E_p = E_{1/2} - 1.109 \frac{RT}{nF} + 0.002 \left(\frac{RT}{nF} \right) \tag{3.15}$$

$$E_{p/2} = E_{1/2} + 1.109 \frac{RT}{nF} + 0.002 \left(\frac{RT}{nF} \right) \tag{3.16}$$

$E_{1/2}$ is located midway between E_p and $E_{p/2}$ and is also called the "reversible" halfway potential [8], which can be expressed by the following equation,

$$E_{1/2} = E^o - \frac{RT}{nF} \ln \left(\frac{D_R}{D_O} \right)^{1/2} \tag{3.17}$$

Since the current peak in such a voltammogram can be fairly broad and amount to several mV, it is sometimes more convenient to use the half-peak potential ($E_{p/2}$) as a reference point, although it does not have a direct thermodynamic significance [9]. It is simply defined as the potential where the current has reached half the value of the actual peak current on the rising part of the curve. Combining equation (3.15) and (3.16) gives the following relationship

$$E_p = E_{p/2} - 2.218 \frac{RT}{nF} \tag{3.18}$$

Other diagnostic tests for cyclic voltammograms of reversible processes with a soluble reactant and a soluble product are [1]:

1. $\Delta E_p = E_p^a - E_p^c = 2.2 \cdot (RT/(nF))$
2. $|I_p^a / I_p^c| = 1$
3. E_p is independent of τ
4. at potentials beyond E_p, $I \propto t^{-1/2}$

In case of the formation of an insoluble product R on the electrode, it is necessary to derive a solution of the problem where the activity of the deposit is set equal to unity. The boundary conditions only have to be considered for species O as well as the Nernst equation:

$$E^{rev} = E^o - \frac{RT}{nF} \ln c^o \tag{3.19}$$

This problem was first solved by Berzins and Delahay [9] and the current density is given in the following equation also known as the Berzins-Delahay equation:

$$i = -nFc^o \left(\frac{D_o \omega}{\pi}\right)^{1/2} A''/\omega t^{1/2} \tag{3.20}$$

with $$A/x = e^{4x^2} \int_0^x e^{t^2} dt \tag{3.21}$$

The function λ exhibits a maximum equal to 0.541, therefore, the corresponding peak current and peak potential can be expressed as:

$$i_p = 40.610 \left(\frac{nF}{RT}\right)^{1/2} D_O^{1/2} c^o \nu^{1/2} \quad (3.22)$$

$$E_p = E_{p/2} - 0.7725 \left(\frac{RT}{nF}\right) \quad (3.23)$$

From equation (3.22) it can be seen that the peak current is proportional to the square root of the sweep rate as it was the case for the soluble-soluble system. Nevertheless, from the shape of the voltammogram it is possible to distinguish a system with an insoluble product from one with a soluble one. For a deposition process, the reduction peak is steeper and narrower compared to a soluble-soluble system. The anodic dissolution of the deposit is normally not diffusion-controlled, and consequently the anodic current does increase until all the deposit has been stripped off the electrode. This can be seen on the shape of the anodic stripping peak, which is very sharp and its height is much larger than the cathodic peak height.

In Figure 3-2 a practical example for a soluble-soluble and a soluble-insoluble system of indium ions in a chloride melt can be seen. The processes are reversible. The peak couple for the In^{3+}/In^{+} system has the typical shape of a soluble-soluble system. The second peak couple of In^{+}/In^{0} is a typical example of a system with an insoluble product.

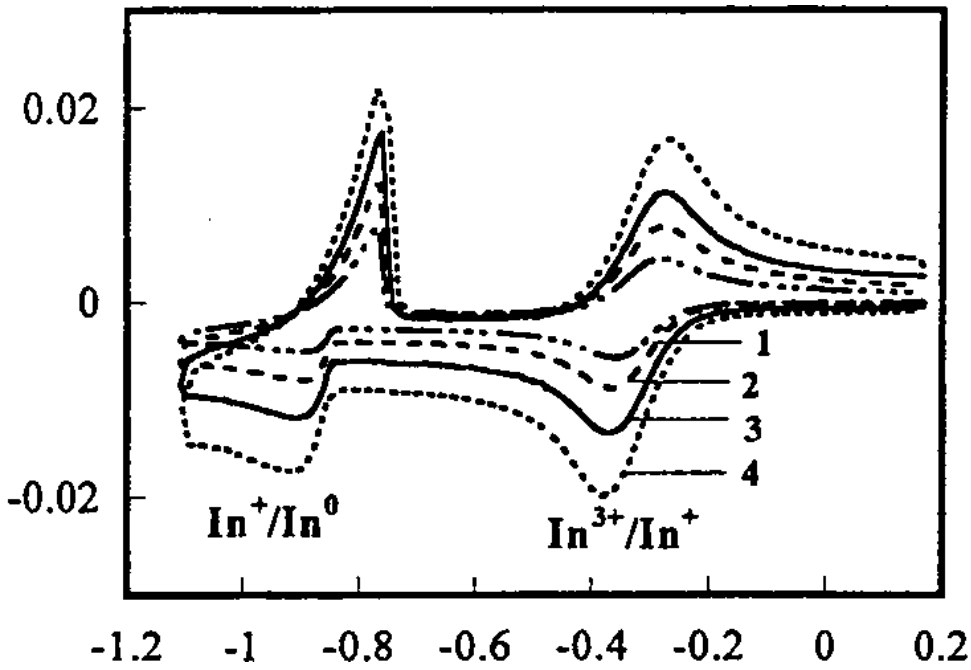

Fig. 3-2: *Cyclic voltammograms obtained at a glassy carbon electrode related to the reduction of $InCl_3$ in the fused LiCl-KCl at 450 °C, c[$InCl_3$] = $5.75 \cdot 10^{-6}$ mol/l, sweep rates: (1) 0.1, (2) 0.25, (3) 0.5, (4) 1 $V \cdot s^{-1}$, Mohamedi et al. [10].*

There are two important complications that exist in voltammetric studies:

i) the effect of the ohmic drop that can seriously distort voltammograms,
ii) the charging or discharging of the electrode double layer

A more detailed discussion of the changes on the voltammogram due to these two effects can be found in Appendix B.

3.1.2. Chronoamperometry (CA)

During chronoamperometry the potential of the working electrode is changed with respect to the open circuit potential either in the anodic or cathodic direction, while the current versus time relation is recorded. Also in this case, Fick's 2nd law (equation (3.4)) has to be solved. The boundary conditions for this method are [11]:

$$c_o\,(x,0) = c^o \qquad c_o\,(\leftarrow,t) \Downarrow\ c^o \qquad (3.24)$$

when reaching the limiting current $c_o\,(0,t) = 0$ (3.25)

When applying potentials where the surface concentration of O reaches zero, the limiting current is reached. Considering a reversible process where the equation of Nernst (3.10) is valid, the concentrations of O and R should respond immediately to changes in the potential of the electrode. When solving the boundary value problem by Laplace transformation, the limiting current density can be expressed by the so-called Cottrell equation:

$$i_l = \frac{n F D_o^{1/2} c^o}{\phi^{1/2} t^{1/2}} \qquad (3.26)$$

For a diffusion controlled process, a plot of i versus $t^{-1/2}$ should be linear. The diffusion coefficient of O can be calculated from the slope.

The determination of the rate constant for the electrode reaction can theoretically be made from data at short times of the measurement. The plot of i versus $t^{1/2}$ at short times should be a straight line with an intercept given by:

$$i_{t=0} = n F k^{\Downarrow} c^o \qquad (3.27)$$

Due to interference by double layer charging the obtained current at short times consists partly of the capacity current as well. The determination of the rate constant by chronoamperometry is therefore not an easy task, if the capacity current superimposes on the kinetically controlled, faradaic current

As mentioned above the contribution of the double layer charging has only to be considered at short times. At longer times the electrode process

becomes diffusion-controlled when applying potentials where the limiting current is reached.
The IR drop will change the actual potential applied at the electrode to a lower value. Therefore, potentials when reaching limiting conditions may seem to be somewhat larger than normal. But since the limiting current is independent of the potential, the calculation of the diffusion coefficient should not be affected by the IR drop.

3.1.3. Chronopotentiometry (CP)

While measuring the potential of the working electrode as a function of time, a constant current electrolysis of an electroactive species proceeds in an unstirred solution containing a supporting electrolyte. As the electrolysis proceeds, there is a progressive depletion of the electroactive species at the electrode surface. Assuming that diffusion is the only process responsible for the availability of the electroactive species at the electrode surface, the potential at the electrode changes very rapidly when the surface concentration of the electroactive species approaches zero. The time period during which this process happens is called the transition time.

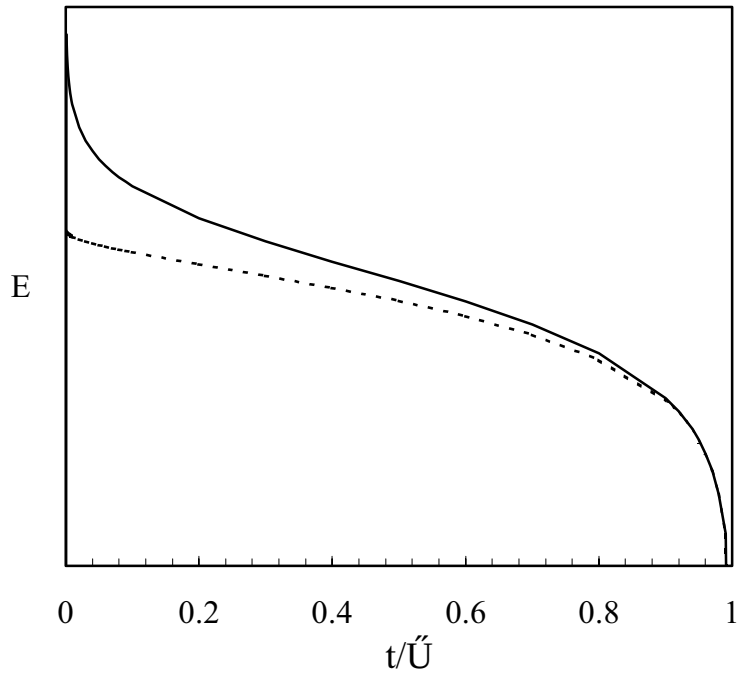

Fig. 3-3: *Chronopotentiograms at 25 ºC according to equation (3.31) and (3.33) for a soluble-soluble (full line) and a soluble-insoluble (dotted line) system respectively, where n = 1.*

The boundary conditions are similar to those for chronoamperometry in equation (3.24) (see section 3.1.2). The third boundary condition, equation (3.25) is replaced by,

$$\text{for } t > 0,\ x = 0 \qquad D_O \left(\frac{\partial c_O}{\partial x} \right) = 4\frac{i}{nF} \tag{3.28}$$

Since a constant current is applied during the measurement, the flux of the electroactive substance at the electrode surface is constant as well. In the case of electrolysis under chronopotentiometric conditions the time dependence of the concentration at the electrode surface is given by

$$c_O(0,t) = c^o - 4\frac{2 i_o t^{1/2}}{n F \pi^{1/2} D_O^{1/2}} \tag{3.29}$$

At the transition time τ the surface concentration of O is zero, and therefore equation (3.29) can be set to zero. The resulting equation is

$$\tau^{1/2} = \frac{\pi^{1/2} n F c^o D_o^{1/2}}{2 i_o} \tag{3.30}$$

which is also called Sand's equation [1]. Sand's original derivation was based upon considerations applicable to diffusion processes and can be used to determine the diffusion coefficient of O.

For a reversible process the surface concentrations of species O and R are defined by the Nernst equation (3.10). Based on this equation and the change of concentration as time passes as shown in equation (3.29), a time dependence of the potential for a soluble-soluble system can be expressed by

$$E = E_{\tau/4} - \frac{2RT}{nF} \ln\left(\frac{\tau^{1/2} - 4t^{1/2}}{t^{1/2}} \right) \tag{3.31}$$

with

$$E_{\tau/4} = E^o - \frac{2RT}{nF} \ln\left(\frac{D_R}{D_O} \right)^{1/2} \tag{3.32}$$

For an electrode reaction yielding an insoluble product R, the time dependence of the potential is different from equation (3.31).

$$E = E^{o} - \frac{RT}{nF}\ln\left(\frac{2i_{o}}{nFA\left(D_{O}^{1/2}\right)}\right) - \frac{RT}{nF}\ln\left(\vartheta^{1/2} - t^{1/2}\right)$$
$$= E^{rev} - \frac{RT}{nF}\ln\left(\frac{\vartheta^{1/2} - t^{1/2}}{\vartheta^{1/2}}\right) \qquad (3.33)$$

The correct determination of the transition time Ű seems to be a major problem when using chronopotentiometry as an analytical method.
In presence of an IR drop, the actual potentials will be smaller than the measured ones, but this should not affect the determination of Ű The double layer charging current is a more serious matter when running chronopotentiometry. Looking at the capacity current density, which can be expressed as

$$i_{c} = C_{d}\left(\frac{\partial E}{\partial t}\right) \qquad (3.34),$$

it is obvious that a change in potential during the measurement will result in a capacity current contribution to the total current. Since the change of potential with time is also largest around the potential transition, the determination of Ű can be incorrect, and thereby affecting the resulting value for the diffusion coefficient.
If $i_o \cdot Ű^{1/2}$ is independent of i_o, the requirements to use the Sand equation for determination of the diffusion coefficient are fulfilled.

3.1.4.Square wave voltammetry (SQWV)

According to Ramaley and Krause [12] applying a superposition of a synchronized square wave, ÷E, and staircase potential, E_{step}, to a stationary electrode, the double layer charging current may be neglected when measuring at a suitable time after the pulse occurred. By changing the potential in constant steps, the potential range of interest for a system can be scanned.

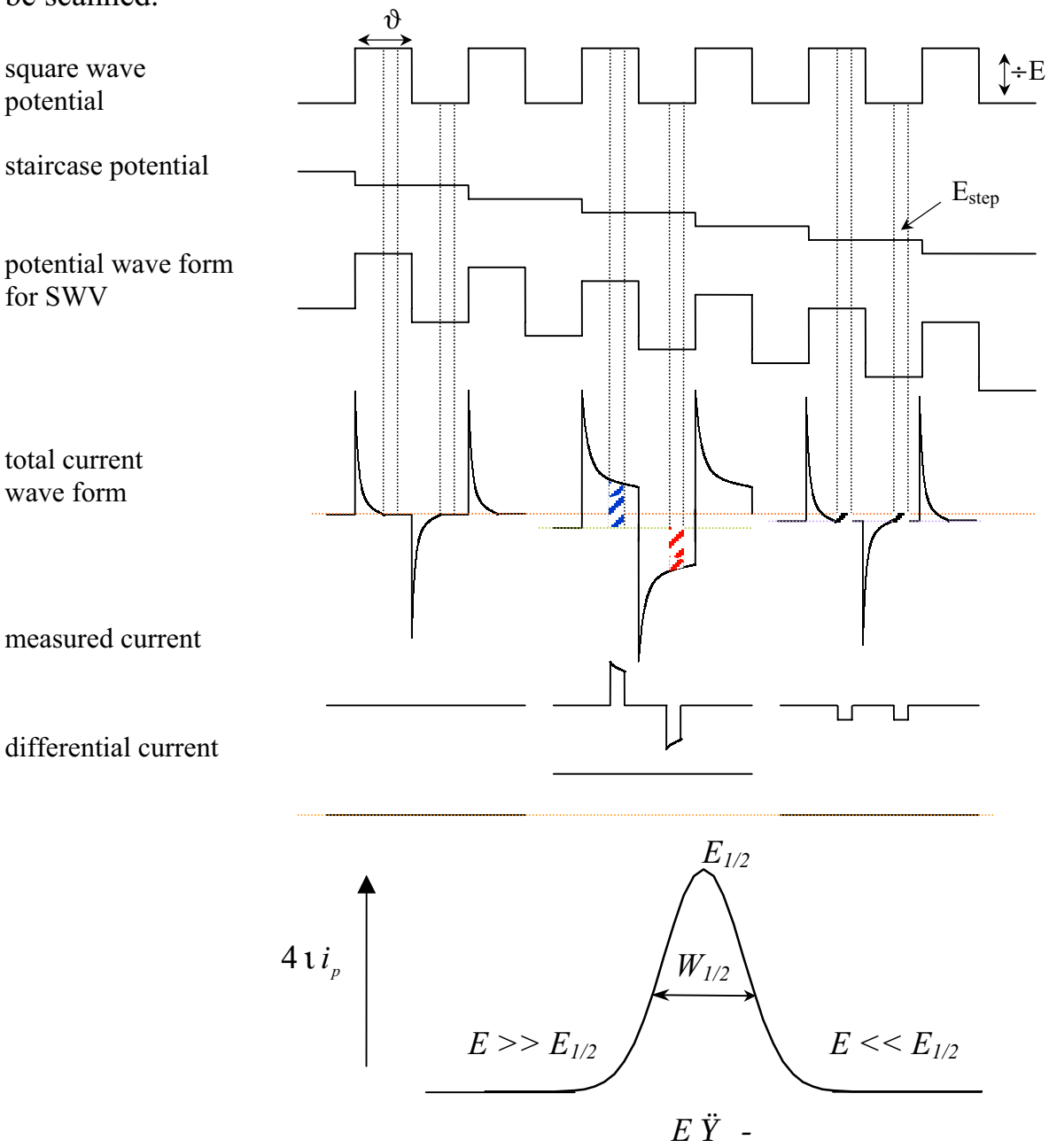

Fig. 3-4: *Waveforms employed and obtained in square wave voltammetry [12].*

The initial and boundary conditions may be stated as follows:

$$c_O(x,0) = c^o; \qquad c_O(\leftarrow,t) = c^o \tag{3.35}$$

$$c_R(x,0) = 0; \qquad c_R(\leftarrow,t) = 0 \tag{3.36}$$

and for $0 < t < \vartheta$ $c_O(0,t) = c_1$ (3.37)

$\vartheta < t < 2\vartheta$ $c_O(0,t) = c_2$ (3.38)

$(j-1)\vartheta < t < j\vartheta$ $c_O(0,t) = c_j$ (3.39)

where c_j is the concentration of the oxidized species established by electrode potential E_j during the j^{th} half period, ϑ, of the square wave. Solving Fick's 2. law (equation (3.4)) with the boundary conditions above, a complex expression for the change in concentration of species O over time is obtained [12]. The equation for $c_O(0,t)$ and the final current function as well as the expressions for the forward and backward currents are presented in Appendix C.

The theory for a reversible system with a soluble reactant and a soluble product predicts that the resulting current-time behaviour should be symmetrical and Gaussian-shaped with a peak at $E_{1/2}$, as can be seen in Figure 3-4. The width of the peak at half-height, $W_{1/2}$, is given by the following equation:

$$W_{1/2} = 3.52 \frac{RT}{nF} \tag{3.40}$$

as long as $\Delta E < 0.5\,RT/(nF)$. The maximum current, Δi_p, can be derived by differentiating the differential current function and finding the zero point [13].

$$\Delta i_p = nFc^o \frac{1.4B}{1+2B}\sqrt{\frac{D_O f}{\pi}} \tag{3.41}$$

where B is: $$B = \exp\left(\frac{nF}{RT}\frac{\Delta E}{2}\right) \tag{3.42}$$

As can be seen from equation (3.41) the differential peak current depends linearly on the concentration of the electroactive species O and on the square root of the frequency, $f^{1/2}$. A characteristic feature for a reversible system should, therefore, be a straight line when plotting Δi versus $f^{1/2}$.

3.2. Analytical methods

3.2.1. Powder X-ray Diffractometry (XRD)

In an X-ray diffraction measurement, an incident monochromatic X-ray with wavelength ς is scattered from the sample according to Braggs law,

$$d \mid \frac{\varsigma}{2\sin(\chi)} \tag{3.43}$$

By measuring the scattering angle χ one can calculate the distance d between the atomic layers in the sample. By comparing these to tabulated values, it is possible to determine which crystalline phases the sample consists of. The measurements for this thesis were performed on a Siemens X-ray diffractometer type 5005. The bath samples were ground to a fine powder with typical grain size of the order of 10 microns prior to measurements [14].

3.2.2. Inductively coupled plasma – atomic emission spectrometry (ICP-AES)

In atomic emission spectrometry (AES) the characteristic radiation energy emitted by excited atoms is used for the detection and quantitative analysis of elements. The difference between optical atomic spectra in the UV/visible range and X-ray spectra in spectrochemical analysis is depending on the wavelength of the emitted radiation.

The dissolved sample is pumped into a nebulizer chamber where it is sprayed in the form of the smallest possible droplets by argon gas. These droplets flow with the argon gas through an inductively coupled high-frequency plasma (ICP) where charged particles are generated by ionisation in the induction coil of a high-frequency generator (HF-coil). As plasma gas argon is used, which is easily ionised. In the center of the plasma, a tunnel develops where temperatures of 6000 to 8000 K are attained [14].
The ICP-AES analysis for this thesis was performed on an Atomscan 16/25 spectrometer from Thermo Jarell Ash Corporation. The wavelength of phosphorus used for analysis was 178.287 nm. By calibrating the instrument with standard solutions the intensity of the emitted radiation could be related to the concentration of the element under investigation.

References for Chapter 3:

[1] D. Pletcher, R. Greef, R. Peat, L.M. Peter, J. Robinson, *Instrumental methods in Electrochemistry*, Chapter 1, Horwood publishing, Chichester, England, 2001.

[2] M. Rudolph, S.W. Feldberg, *A cyclic voltammetric simulator for windows*, Digisim® 2.1 software, 1994-1996.

[3] J.E.B. Randles, *A cathode ray polarograph, Part II – The Current-Voltages curves,* Trans. Faraday Soc., **44**, 327 ff., 1948.

[4] A. Sevļik, *Oscillographic Polarography with Periodical Triangular Voltage,* Coll. Czech. Chem. Comm., **13**, 349 ff., 1948.

[5] M.M. Nicholson, *Diffusion currents at cylindrical electrodes. A study of organic sulfides*, J. Amer. Chem. Soc., **76**, 2539-2545., 1954.

[6] W.T. De Vries, E. van Dalen, *The current-potential equation for linear-sweep voltammetry,* J. Electroanal. Chem., **6**, 490-493, 1963.

[7] A.J. Bard, L.R. Faulkner, *Electrochemical methods,* John Wiley & Sons, New York, 2nd ed., 2001.

[8] R.S. Nicholson, I. Shain, *Theory of stationary electrode polarography,* Anal. Chem., **36**, 706 ff., 1964.

[9] T. Berzins, P. Delahay, *Oscillographic polarographic waves for the reversible deposition of metals on solid electrodes,* J. Am. Chem. Soc., **75**, 555 ff., 1953.

[10] M. Mohamedi, S. Martinet, J. Bouteillon, J.C. Poignet, *Comprehensive examination of the electrochemistry of indium in the molten LiCl-KCl eutectic,* Electrochimica Acta, **44**, 797-803, 1998.

[11] Z. Galus, *Fundamentals of electrochemical analysis,* 2nd edition, Ellis Horwood Chichester, England, 1994.

[12] L. Ramaley, M.S. Krause, Jr., *Theory of Square Wave Voltammetry*, Anal. Chem., **41**(11), 1362-1365, 1969.

[13] P. Chamelot, *The electrolytic deposit of niobium in molten salts: Electrocrystallization, study of the process with electrochemical pulse techniques,* Dissertation, Univ. Paul Sabatier, Toulouse, France, 1994.

[14] G. Schwedt, *The essential guide to analytical chemistry,* John Wiley & Sons, New York, 1997.

4. Solubility of $AlPO_4$ in cryolite melt

4.1. Introduction

Due to high current efficiency losses, phosphorus compounds are intolerable in electrolytic aluminium extraction. It is of interest to be aware of their solubility behaviour. Del Campo studied the system Na_3AlF_6-$Na_4P_2O_7$ and found that its solubility limit was at 71.7 wt% at 748 ºC. As pointed out in Section 2.1.2., the high solubility, good thermal stability and the low volatility made sodium pyrophosphate an adequate phosphate to perform fundamental studies. However, the pyrophosphate ion was found to dissociate into new phosphate compounds (PO_4^{3-} or PO_3^-). The solubility study of another phosphorus compound like $AlPO_4$ will show if it is a phosphorus compound which fulfills all requirements set by Del Campo to be an appropriate species for fundamental studies.

4.2. Experimental set-up

The measurements were performed in a Kanthal-wire-heated, closed furnace with water-cooling, as shown in Figure 4-1.

The furnace consisted of a steel cylinder filled with insulating material. Kanthal wires were used as heating elements. The cell was placed inside a mullite tube, which was tightly closed to the ambient atmosphere. The atmosphere inside the furnace during measurements consisted of argon, which was flushed through the cell at a constant rate. The temperature of the furnace was controlled by a Pt-PtRh10% thermocouple, inserted horizontally through the steel cylinder of the furnace up to the pythagoras tube. The cell set-up is presented in Figure 4-1.

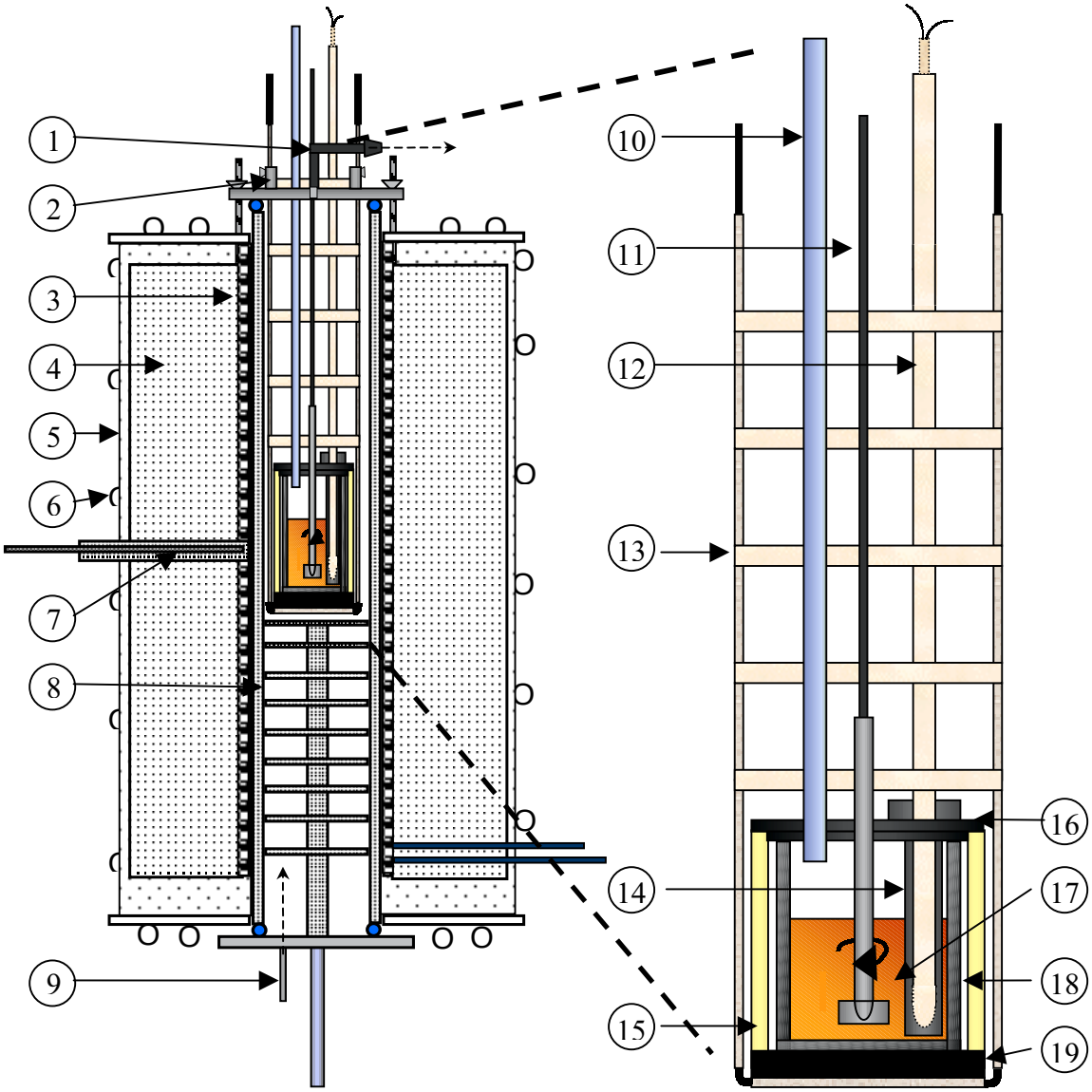

Fig. 4-1: *General experimental set-up used for measurements to the left. Cell set-up for liquidus and solubility measurements to the right. 1) gas outlet, 2) fixation screws for cell set-up, 3) kanthal wires, 4) insulation material, 5) steel cylinder, 6) water cooling pipes, 7) thermocouple for furnace temperature control, 8) pytagoras tube, 9) gas inlet, 10) feeding tube of quartz, 11) nickel stirrer mounted on stainless steel, 12) thermocouple (TC), 13) alumina radiation shields, 14) graphite TC protection, 15) alumina casing, 16) graphite lid, 17) melt, 18) nickel crucible, 19) graphite supporter.*

4.3. Chemicals

The chemicals used in the experiments are listed in Table 4-1.

Table 4-1: *Specifications of the chemicals used in the liquidus and solubility measurements.*

Chemical	Producer/quality	Pre-treatment
Na_3AlF_6	Hand-picked, natural Greenland cryolite	Crystal grains with coloured appearance were discarded. Kept at 200 ∀C in a heating chamber before use
$AlPO_4$	Riedel-de-Haën anhydrous, technical	Kept at 200 ∀C in a heating chamber before use
Ar	Argon 4.0 (99.99%), AGA	used as received

4.4. Experimental procedure

About 150 g of natural cryolite was placed in a nickel crucible (55 mm diameter, 60 mm height). The added concentrations of aluminium orthophosphate are given in mole%. In Table 4-2 to 4-4 the concentration can also be found in wt%. For liquidus measurements up to 4.04 mole% $AlPO_4$ was added in the form of pressed tablets during the experiment. The feeding tube was inserted above the melt right before addition and immediately taken out of the cell as soon as the tablets were added.

For measurements in melts containing 4.98 mole% $AlPO_4$ or more, the components were mixed before introducing them into the crucible. The crucible was placed in the cell set-up, as shown in Figure 4-1, and the furnace was tightly closed to the ambient atmosphere. Before heating the cell was flushed for at least 10 hours with argon. Thereafter the furnace was heated to a temperature which was approximately 20 ∀C above the liquidus temperature of the melt. The temperature of the melt was controlled by a Pt-PtRh10% thermocouple placed inside an alumina tube and protected from the melt by a graphite tube. The thermocouple used was calibrated with respect to the melting point of silver. When melted, the mixture was stirred for at least one hour at 300 rpm, using a nickel stirrer in order to assure stable conditions. For concentrations up to 4.04 mole% $AlPO_4$, tablets of the compound were added to the melt and the mixture

was stirred for at least two hours at the same conditions. The temperature was recorded on a computer during the experiment. The cooling rate was set to 0.7 K min^{-1}. In order to determine liquidus temperatures, the slow cooling rate and the vigorous stirring should prevent possible super-cooling of the melt.

The liquidus temperature of different melt compositions was determined from cooling curves, as shown in Figure 4-2:

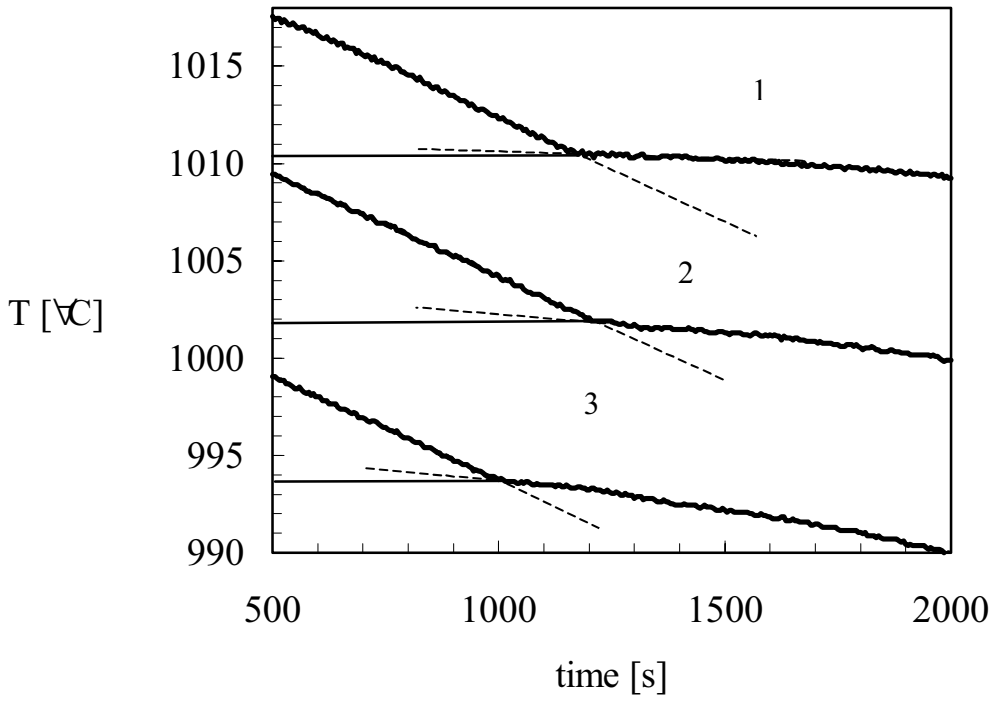

Fig. 4-2: *The cooling curves shown represent the following melt compositions: 1) Na_3AlF_6, 2) Na_3AlF_6 with 5 mole% $AlPO_4$ (2.96 wt%), 3) Na_3AlF_6 with 10 mole% $AlPO_4$ (6.08 wt%).*

By further cooling of the melt, a transition towards the solid phase can be observed. The solidus temperatures were determined for four compositions, as can be seen in Table 4-3.

The experimental set-up for the solubility measurements was the same as presented in Figure 4-1. Instead of the graphite protection tube for the thermocouple a closed nickel tube was used. The melt consisted of cryolite and an excess amount of aluminium orthophosphate (66.4 mole%). When the mixture had melted, the stirring was started and maintained for at least

two hours. Thereafter the stirring was stopped to allow solid phosphate particles that were dispersed in the melt to settle. The time allowed for settling was at least two hours. A quartz tube was immersed 1 cm into the melt, and with the help of a syringe on the top end of the sampling tube, the melt sample was sucked inside the tube. The sampling process lasted less than ten seconds. The quartz tubes were broken and the bath samples were carefully removed. Thereafter the bath samples were crushed in an agate mortar, dissolved according to a standard process (see appendix D) and analysed by ICP-AES as described in Section 3.2.2.
The solidified melts from the liquidus measurements were crushed as well, and with the help of XRD the consisting phases were determined (see Appendix E).

4.5. Theory of the cryoscopic measurements

For a binary salt system AB-AC the liquidus line of the AB side of the system can be expressed by the Gibbs-Helmholtz equation regarding the partial molar Gibbs energy, $\div\overline{G}_{AB}$, as presented by Førland [1].

$$\div\overline{G}_{AB} \mid \div\overline{H}_{AB} \; 4 \; T \; \lceil\div\overline{S}_{AB} \tag{4.1}$$

and

$$\div\overline{G}_{AB} \mid 4R \; \lceil T \; \lfloor\ln K \tag{4.2}$$

where K is the equilibrium constant between the pure liquid and the pure solid species AB. According to Raoult's law, the activity coefficient γ_{AB} for the pure, concentrated solution can be set equal to 1. The process of fusion for species AB can be written as:

$$AB_{(s)} \Diamond \quad AB_{(l)} \tag{4.3}$$

Since the activity of a solid species can be assumed to be unity, equation (4.2) can be written as:

$$\div\overline{G}_{AB} \mid 4R \; \lceil T \; \lfloor\ln a_{AB_{(l)}} \tag{4.4}$$

As can be seen the partial molar Gibbs energy, $\div\overline{G}_{AB}$, is related to the Gibbs energy of fusion, $\div G_{f(T)}$ [1].

$$\div\overline{G}_{AB} \mid G_{AB_{(l)}} \; 4 \; G_{AB_{(s)}} \mid \div G_{f(T)} \mid \div H_{f(T)} \; 4 \; T \; \lceil\div S_{f(T)} \tag{4.5}$$

When considering the difference in the specific heat, $\div c_p$, between the liquid and solid phases of AB, the partial molar Gibbs energy can be expressed as shown in equation (4.6) [1]. T_f is the melting temperature of AB.

$$\div \overline{G}_{AB} \mid \div H_f \left(1 - \frac{T}{T_f}\right) - \div c_p \left(T_f - T + T \ln \frac{T_f}{T}\right) \qquad (4.6).$$

Since $$\lim_{T \Downarrow T_f} \ln \frac{T_f}{T} - \frac{T_f - T}{T} \qquad (4.7)$$

and the difference between the heat capacity of solid and liquid AB is considered to be small, the second term in equation (4.6) can be omitted. Therefrom a relation between the change of the freezing point of solvent AB by addition of the solute AC can be expressed. The activity of the component AB can be substituted by the product of the activity coefficient and the mole fraction of AB,

$$a_{AB} \mid \nu_{AB} \cdot x_{AB} \qquad (4.8)$$

$$\ln a_{AB} \mid \ln \nu_{AB} + \ln x_{AB} \qquad (4.9)$$

The cryoscopic formula in equation (4.10) originated from combining equations (4.4) and (4.6) [1]:

$$R \cdot T \cdot \ln a_{AB_{(l)}} \mid -\div H_f \left(1 - \frac{T}{T_f}\right) \qquad (4.10)$$

$$\ln x_{AB} \mid -\frac{\div H_f}{R} \left(\frac{1}{T} - \frac{1}{T_f}\right) \qquad (4.11)$$

$$\div T \mid \lim_{T \Downarrow T_f} \left(-\frac{R}{\div H_f} \cdot T \cdot T_f \cdot \ln x_{AB}\right) - \frac{R \cdot T_f^2}{\div H_f} \cdot x_{AC} \qquad (4.12)$$

with $\ln x_{AB} \mid \ln(1 - x_{AC}) - x_{AC}$, for small x_{AC}

where $\varphi T = T_f - T$. The temperature unit is Kelvin. The term with the activity coefficient vanishes, since the solvent AB with small additions of AC assumingly follows Raoult's law, and therefore $\gamma_{AB} = 1$.

By considering the possibility that the species AC can give more than one new species when added to AB, τ can be put into equation (4.12) which expresses the number of new entities formed in the solvent AB. Finally, equation (4.12) will be,

$$\div T \mid \frac{R \left(T_f^2\right.}{\div H_f} \left(\tau\right. \left(x_{AC} \right. \tag{4.13}$$

4.6. Results and Discussion

The following tables present the results obtained for the liquidus and solubility measurements in the system Na_3AlF_6 - $AlPO_4$. The liquidus temperatures measured were corrected to the melting point of pure cryolite, since for series 1, covering the range 0.51 to 4.04 mole% $AlPO_4$, a different batch of natural cryolite was used than for series 2 for the range 4.98 to 60.87 mole%. For both series the liquidus temperature of the pure cryolite was determined, as shown in Table 4.2.

In literature concerning liquidus measurements in cryolite-based melts [2], different melting points for cryolite are reported, ranging from 1009 ºC to 1012 ºC. For the correction of the measured temperatures of the liquidus experiments, the most commonly found value of 1011.0 ºC was taken. The measured liquidus temperatures ($T_{measured}$) for pure cryolite were compared with the common value of 1011.0 ºC. For series 1 the measured values were corrected by -0.7 ºC, while for the temperatures of series 2, 0.7 ºC had to be added to be able to match the two different series. The resulting temperatures are listed in Table 4-2 as $T_{corrected}$. For each composition measured, the liquidus temperature was determined in two runs.

Table 4-2: *Results of liquidus temperature measurements in the system Na_3AlF_6 - $AlPO_4$. $T_{corrected}$ (series 1)= $T_{measured}$ – 0.7 ºC, $T_{corrected}$ (series 2)= $T_{measured}$ + 0.7ºC.*

Series	x' ($AlPO_4$) [mole%]	x ($AlPO_4$) [wt%]	$T_{measured}$ [˚C]	$T_{corrected}$ [˚C]
1	0.00	0.00	1011.7	1011.0
2	0.00	0.00	1010.3	1011.0
1	0.51	0.30	1010.9	1010.2
1	0.99	0.58	1009.9	1009.2
1	1.96	1.15	1007.7	1007.0
1	2.87	1.69	1005.9	1005.2
1	4.04	2.39	1004.4	1003.7
2	4.98	2.96	1001.7	1002.3
2	10.03	6.08	993.7	994.4
2	14.97	9.28	980.7	981.4
2	19.99	12.67	963.8	964.5
2	30.00	19.94	917.7	918.4
2	39.91	27.84	851.0	851.7
2	50.01	36.76	755.2	755.9

Table 4-3: *Results of solidus temperature measurements in the system Na_3AlF_6 - $AlPO_4$.*

Series	x' ($AlPO_4$) [mole%]	x ($AlPO_4$) [wt%]	$T_{Solidus\ 1}$ [˚C]	$T_{Solidus\ 2}$ [˚C]
2	19.99	12.67	691.0	564.5
2	39.91	27.84	702.4	-
2	50.01	36.67	695.0	565.0
2	60.87	47.47	695.0	557.0

Results of the solubility measurements in cryolite melt with an excess amount of $AlPO_4$ are given in Table 4-4:

Table 4-4: *Results of the solubility measurements in the system Na_3AlF_6 - $AlPO_4$.*

x' ($AlPO_4$) [mole%]	x ($AlPO_4$) [wt%]	$T_{measured}$ [˚C]
59.97	46.53	905.9
59.80	46.36	922.6
61.39	48.02	997.3
61.60	48.24	1041.8

The estimated uncertainty for the temperature measurements include the uncertainty of the thermocouple calibration, determined at the melting point of silver, deviation due to error in the temperature reading of the multimeter and any graphical error when determining the liquidus temperature. The total error was estimated to be ± 1 ˚C.

The error in the concentration in weight percent data was caused by the uncertainty in the balance when determining the weight of the melt components. A loss of approximately 1.5 % of the total amount of melt due to evaporation during the experiment was also accounted in the error estimated. The loss by evaporation was determined by weighing the cell before and after each experiment. A total error of ± 0.02 mole% was determined.

Based on the measured data the phase diagram for the Na_3AlF_6-$AlPO_4$ system was determined to be a simple eutectic. The phosphate-rich side was only investigated up to 61.60 mole% $AlPO_4$. The eutectic point was found to be located at 57.21 mole% $AlPO_4$ at a temperature of 695.9 ºC.

While the first solidus line represents the temperature where all melt is solidified, the second solidus line determined originates from the phase transistion of the cryolite phase. "The cubic high-temperature ß-phase transforms at 563 ± 2 ºC to the low-temperature Ü-phase, a monoclinic modification of Na_3AlF_6" [2]. The resulting phase diagram is shown in Figure 4-3.

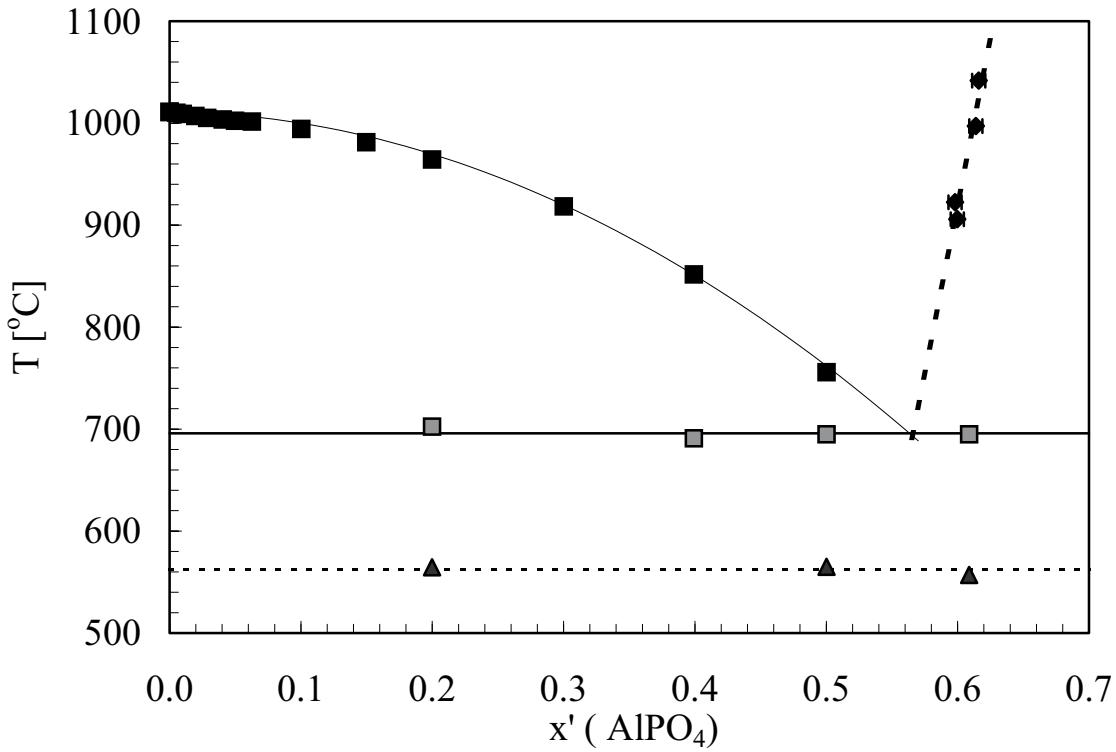

Fig. 4-3: *Phase diagram for the system Na_3AlF_6 - $AlPO_4$ determined by measurements of the liquidus and solidus temperatures and by solubility measurements (ý liquidus measurements; Ĭ, ƶ solidus measurements; ◆ solubility measurements).*

For several compositions XRD measurements on powder samples of the solidified melt were performed. The XRD diagrams revealed that Na_3AlF_6 and $AlPO_4$ were the only phases detected in the solid. In Appendix E an example of an XRD spectrum is shown.

A plot according to equation (4.13) will show how many new species appear when adding $AlPO_4$ to cryolite. Since the enthalpy of fusion for pure cryolite is known, $\div H_f(Na_3AlF_6)$ = 106.7 kJ/mole [3], theoretical curves from equation (4.13) can be calculated, assuming different numbers of new species. In Figure 4-4 the theoretical lines represent the appearance of 1, 2 and 3 new species.

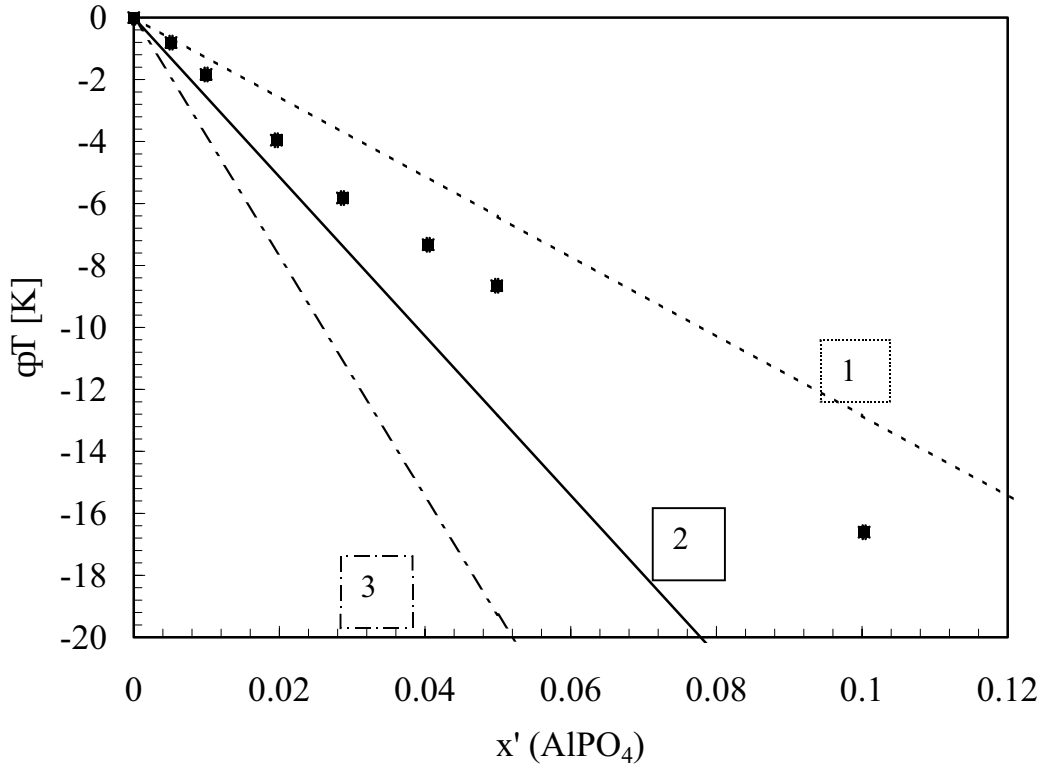

Fig. 4-4: *Calculated curves according to equation (4.13) for 1, 2 and 3 new species, as marked in the plot. Experimental data are shown as squares.*

The results are not in agreement with the findings by Chrenkova et al. [4], who determined one new species being formed when aluminium orthophosphate was added to pure cryolite. The experimental points in Figure 4-4 cannot clearly be assigned to one or two new species forming in the melt when $AlPO_4$ is added.

4.6.1. Model 1

If we assume that the following equilibrium influences the cryoscopic measurements,

$$\begin{array}{ccccc} PO_4^{34} & \Downarrow & PO_3^4 & 2 & O^{24} \\ (1\,4\,\eta) & & \eta & & \eta \end{array} \qquad (4.14),$$

the calculation of the freezing point depression has to be done with respect to equation (4.14). By adding aluminium orthophosphate to pure cryolite, the orthophosphate anion could dissociate into a metaphosphate anion and an oxide ion. If a complete dissociation of the orthophosphate occurs, ϭ would be equal to 1 and the measured liquidus data should follow the calculated curve in Figure 4-4 representing two new species. If the orthophosphate is stable, ϭ = 0 and the experimental data should follow the curve calculated for one new species in Figure 4-4.

The ionic nature of molten salts has to be considered when working with these media, and the calculated mole fractions have to be referred to each ion. For an ideal ionic mixture of molten salts the activity for a component can be calculated according to the Temkin model [5]. Briefly summarised the model includes the following:

1) The entropy of mixing is completely configurational.
2) The molten salt is seen as two separate networks, one consisting of anions and one of cations.
3) Regardless of the magnitude of charges, the cations and anions are randomly distributed all over the cation and anion positions respectively.

The activity of the component AB can be expressed as

$$a_{AB}^{id} = x_{A^2} \cdot x_{B^4} = \frac{n_{A^2}}{\sum_i n_{M_i^2}} \cdot \frac{n_{B^4}}{\sum_i n_{Z_i^4}} \qquad (4.15)$$

where n is the number of moles and x_{A^2} is the cation fraction, which is obtained by dividing the number of moles of A^+ by the total number of moles of cations. The anionic fraction, x_{B^4}, is calculated correspondingly.

The dissociation reaction for cryolite can be written as presented in reaction (4.16). The degree of dissociation of the cryolite is given by Ŭ.

$$\begin{array}{ccccc} AlF_6^{34} & \Downarrow & AlF_4^4 & 2 & 2\ F^4 \\ (1 4 \zeta) & & \zeta & & 2\ \zeta \end{array} \qquad (4.16)$$

When adding x mole% $AlPO_4$ to cryolite, the mole fractions in the melt change and reaction (4.16) has to be multiplied with (1-x). With regard to the aluminium orthophosphate the following dissociation reaction can be written.

$$x\ AlPO_4 \Downarrow \quad x\ Al^{32}\ 2\ (1 4 \eta)\ x\ PO_4^{34}\ 2\ \eta\ x\ PO_3^4\ 2\ \eta\ x\ O^{24} \qquad (4.17)$$

Table 4-5 presents all ionic species, in equations (4.16) and (4.17). The aluminium ions in reaction (4.17) cannot exist freely in the melt and will apparently form fluoride complexes. In the model it is assumed that this will not affect the degree of dissociation for cryolite for small additions of aluminium phosphate.

Table 4-5: *All cationic and anionic species in a cryolite melt with additions of aluminium orthophosphate.*

Anionic species	Cationic species
$AlF_6^{34}, AlF_4^4, F^4, PO_4^{34}, PO_3^4, O^{24}$	Na^2

The number of moles for each species can be seen from reactions (4.16) and (4.17).

$$\begin{array}{ll} n_{AlF_6^{34}} \mid (1 4 \zeta)(1 4 x) & n_{Na^2} \mid 3(1 4 x) \\ n_{AlF_4^4} \mid \zeta (1 4 x) & \\ n_{F^4} \mid 2\zeta (1 4 x) & \\ n_{PO_4^{34}} \mid (1 4 \eta) x & \\ n_{PO_3^4} \mid \eta x & \\ n_{O^{24}} \mid \eta x & \end{array} \qquad (4.18)$$

The total number of moles for all anions and cations is,

$$\sum_i n_{Z_i^4} = 1 2 2\zeta (1 4 x) 2 \eta x \qquad \sum_i n_{M_i^2} = 3(1 4 x) \quad (4.19)$$

For pure cryolite (x = 0) the equilibrium constant for the dissociation reaction (4.16) is

$$K = \frac{n_{AlF_4^4} \cdot n_{F^4}^2}{n_{AlF_6^{34}} \cdot (\sum_i n_{Z_i^4})^2} = \frac{4\zeta^3}{(1 4 \zeta) \cdot (1 2 2\zeta)^2} \quad (4.20)$$

When aluminium orthophosphate is added to cryolite, the expression for the new equilibrium constant K' for the dissociation reaction (4.16) can be written

$$K' = \frac{n_{AlF_4^4} \cdot n_{F^4}^2}{n_{AlF_6^{34}} \cdot (\sum_i n_{Z_i^4})^2} = \frac{\zeta \cdot (1 4 x) \cdot (2\zeta \cdot (1 4 x))^2}{(1 4 \zeta) \cdot (1 4 x) \cdot (1 2 2\zeta \cdot (1 4 x) 2 \eta x)^2} \quad (4.21)$$

Assuming that K = K', a value of α for each composition x can be calculated. The degree of dissociation for cryolite is usually about 0.3, as reported in the literature [2, 6]. The equilibrium constant K is, therefore, calculated with α = 0.3, and the resulting K equals 0.06. To calculate new degrees of dissociation for each composition, equation (4.21) has to be rearranged and a cubic equation results:

$$0 = a \xi^3 2 b \xi^2 2 c \xi 2 d \quad (4.22)$$

with $a = 4\cdot(K' + 1)\cdot(- x^2 + 2x - 1)$

$b = 4\cdot K'(x^2 - \beta\cdot x + \beta\cdot x^2)$

$c = K'(3 – 4x + 2\beta x - 4\beta x^2 – \beta^2 x^2)$

$d = K'(1 + 2\beta x + \beta^2 x^2)$

The solutions for each composition and β-value can be found in Table 4-6.

***Table 4-6**: Mole fraction of added $AlPO_4$ and the corresponding degree of dissociation.*

x'($AlPO_4$)/100 [mole%/100]	Ŭs for different for different values of ɓ		
	ɓ = 0	ɓ = 0.5	ɓ = 1
0	0.3000	0.3000	0.3000
0.01	0.3016	0.3023	0.3030
0.02	0.3033	0.3047	0.3061
0.03	0.3050	0.3071	0.3092
0.04	0.3067	0.3096	0.3124
0.05	0.3085	0.3121	0.3156
0.06	0.3103	0.3146	0.3188
0.07	0.3121	0.3171	0.3221
0.08	0.3140	0.3197	0.3254
0.09	0.3159	0.3224	0.3287
0.1	0.3179	0.3251	0.3321

From the alpha's obtained the ionic fraction of AlF_6^{34} according to the Temkin model (equation 4.15) can be calculated. Since the activity of the cryolite equals its mole fraction for ɔ = 1 (equation 4.8), the following equation is obtained,

$$a^{id}_{Na_3AlF_6} \mid x^3_{Na^2} \; \text{ſ}x_{AlF_6^{34}} \tag{4.23}$$

In the composition range covered in Table 4-6, x_{Na^2} can be set equal to 1 and the mole fraction of Na_3AlF_6 can therefore be expressed by the ionic fraction of AlF_6^{34}.

$$\ln a^{id}_{Na_3AlF} \mid \ln x^3_{Na^2} \; 2\ln x_{AlF_6^{34}} - \ln x_{AlF_6^{34}} \tag{4.24}$$

The resulting ionic fractions of the hexafluoroaluminate ion for each composition can be used in equation (4.12) to find the liquidus temperatures.

$$\div T \mid \text{®©4}\text{©}_{\text{TM}} \frac{R}{\div H_f} \text{ſ}T \; \text{ſ}T_f \; \text{ſln}\, x_{AlF_6^{34}} \tag{4.25}$$

or $$T \mid \frac{1}{\frac{1}{T_f} - \frac{R}{H_f} \ln x_{AlF_6^{3-}}}$$

Table 4-7: *Theoretical liquidus temperatures at different degrees of dissociation of phosphate.*

x'($AlPO_4$)	Temperature [K] ƃ = 0	ƃ = 0.5	ƃ = 1
0	1284.00	1284.00	1284.00
0.01	1282.63	1281.99	1281.35
0.02	1281.24	1279.97	1278.70
0.03	1279.84	1277.93	1276.05
0.04	1278.43	1275.89	1273.40
0.05	1276.99	1273.83	1270.74
0.06	1275.54	1271.76	1268.08
0.07	1274.08	1269.67	1265.41
0.08	1272.59	1267.57	1262.74
0.09	1271.09	1265.46	1260.06
0.1	1269.57	1263.33	1257.37

Table 4-7 shows liquidus temperatures for different values of ƃ at each composition. The data from Table 4-7 are plotted in Figure 4-5 together with the experimental data.

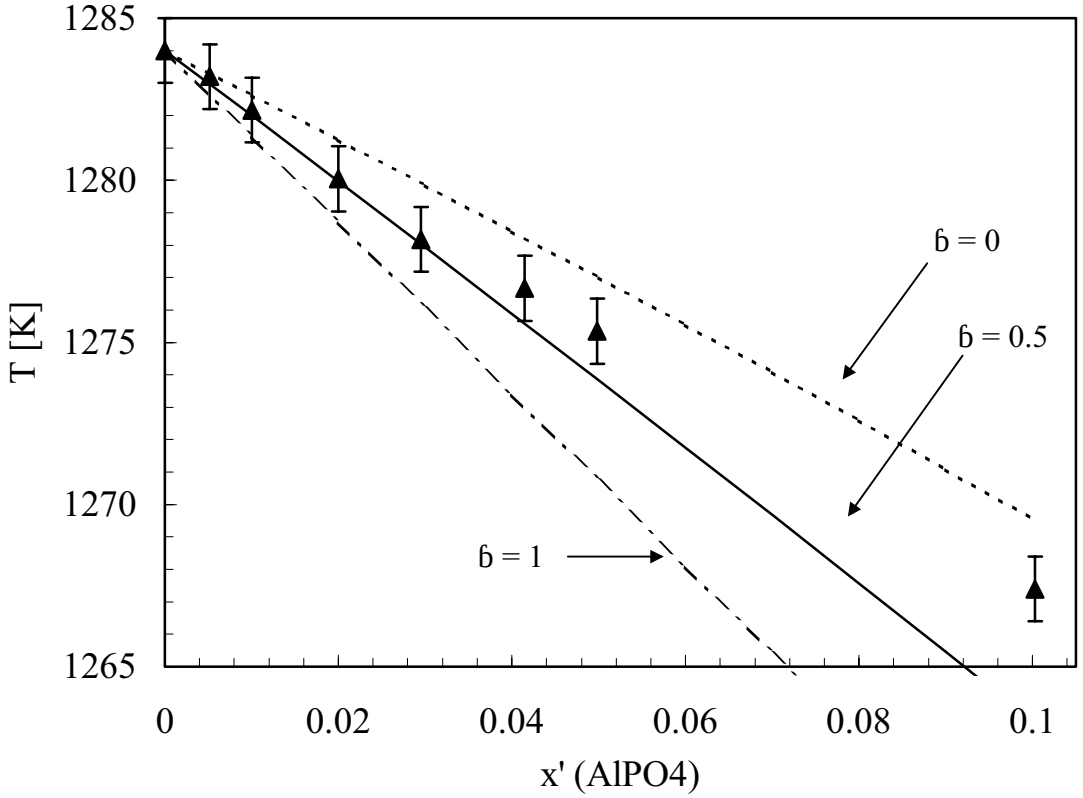

Fig. 4-5: *Experimental data (triangles) and theoretical temperature lines with regard to different values of the dissociation degrees of the orthophosphate, ϧ (see reaction (4.17)), as indicated.*

As can be seen, Figure 4-5 shows a better agreement of the theoretical freezing point lines with the experimental data when equation (4.14) is included than in Figure 4-4, where only the limiting cases of ϧ = 0 or 1 were considered (i.e. one or two new particles).

The experimental data approach the curve of ϧ = 0.5 up to approximately 3 mole% $AlPO_4$, which indicates a partial dissociation of $AlPO_4$ according to reaction (4.17). For higher concentrations of $AlPO_4$, the data show that the degree of dissociation for the phosphate is less than 0.5.

4.6.2. Model 2

Instead of using the Temkin model to describe the dissociation of the orthophosphate as an ion, it might fit as well to describe the process by reactions with neutral substances. When adding aluminium orthophosphate to a cryolite melt, the following reactions can be assumed:

$$AlPO_4 + 3NaF \Rightarrow Na_3PO_4 + AlF_3 \tag{4.26}$$

$$\begin{array}{l} Na_3PO_4 \Rightarrow NaPO_3 + Na_2O \\ (1-\eta) \qquad\quad \eta \qquad\quad \eta \end{array} \tag{4.27}$$

$$2AlF_3 + 3Na_2O \Rightarrow 6NaF + Al_2O_3 \tag{4.28}$$

For an ideal mixture the activity of cryolite can be calculated as

$$a_{Na_3AlF_6} = \frac{n_{Na_3AlF_6}}{n_{Na_3AlF_6} + \sum_i n_i} \tag{4.29}$$

where n is the number of moles of species i and з is the amount of foreign species.

The dissociation of the orthophosphate for this model is expressed by equation (4.27). Since the species in this equation are the only new ones introduced into the cryolite system, equation (4.29) can be rewritten as

$$a_{Na_3AlF_6} = \frac{n_{Na_3AlF_6}}{n_{Na_3AlF_6} + (1-\eta)n_{Na_3PO_4} + \eta n_{NaPO_3} + \eta n_{Na_2O}} \tag{4.30}$$

As can be seen from equation (4.28) n_{Na_2O} can be replaced by $1/3\, n_{Al_2O_3}$, but since alumina is known to dissociate into three particles in dilute solutions [2], this makes no difference. By calculating the activity of cryolite according to equation (4.30), the liquidus temperatures for different betas can be obtained from equation (4.12). The resulting data are presented in Table 4-8.

***Table 4-8**: Calculated activity of cryolite and corresponding liquidus temperature of the mixture Na_3AlF_6 – $AlPO_4$. Different dissociation degrees of the reaction $Na_3PO_4 \div NaPO_3 + Na_2O$ are expressed as ϧ.*

x'($AlPO_4$)	$a_{Na_3AlF_6}$			T [K]		
	ϧ = 0	ϧ = 0.5	ϧ = 1	ϧ = 0	ϧ = 0.5	ϧ = 1
0	1.000	1.000	1.000	1284.0	1284.0	1284.0
0.01	0.990	0.985	0.980	1282.7	1282.1	1281.4
0.02	0.980	0.970	0.961	1281.4	1280.1	1278.9
0.03	0.970	0.956	0.942	1280.1	1278.2	1276.3
0.04	0.960	0.941	0.923	1278.8	1276.3	1273.8
0.05	0.950	0.927	0.905	1277.4	1274.3	1271.3
0.06	0.940	0.913	0.887	1276.1	1272.4	1268.7
0.07	0.930	0.899	0.869	1274.7	1270.4	1266.2
0.08	0.920	0.885	0.852	1273.4	1268.4	1263.7
0.09	0.910	0.871	0.835	1272.0	1266.5	1261.2
0.1	0.900	0.857	0.818	1270.6	1264.5	1258.7

In Figure 4-6 the obtained data from Table 4-8 are presented with the experimental data from Table 4-2.

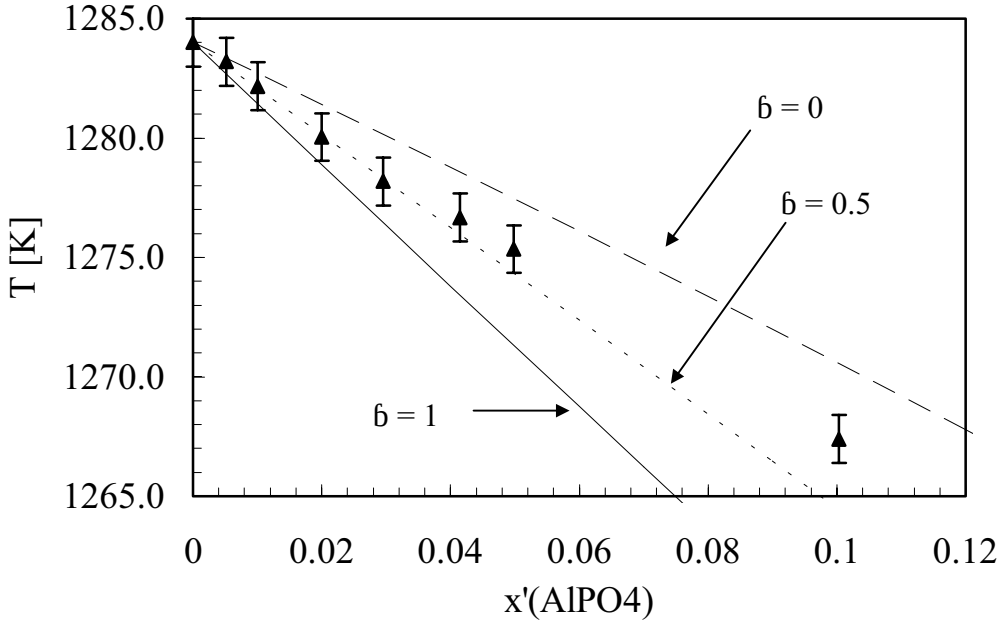

***Fig. 4-6**: Theoretical liquidus temperatures for different dissociation degrees of the orthophosphate (see reaction (4-27)) and experimental data (triangles).*

The experimental data also fit with Model 2, which actually is a simpler approach than Model 1. From both models compared with the experimental data we can draw the conclusion that the orthophosphate dissociates partly to metaphosphate and an oxide ion as proposed in reaction (4.14). The degree of dissociation is decreasing as the concentration of $AlPO_4$ increases. This can be seen when written the reaction (4.14) as

$$K_{eq} = \frac{[PO_4^{3-}]}{[PO_3^{-}]} \cdot [O^{2-}] \qquad (4.31)$$

It is believed that in a melt system with additional oxide e.g. from alumina will influence the dissociation reaction by shifting to the left. Since the entropy of the system increases when dissociation of orthophosphate occurs, it might be possible that the degree of dissociation is dependent on the temperature. It can therefore be concluded that the three main influencing factors on the reaction (4.14) are concentration of $AlPO_4$, concentration of additional oxide and temperature.

Considering at the data obtained by Chrenkova et al. [4], it can be seen that the melting point of the natural, hand-picked cryolite from Greenland used in their experiments was 1004 ºC. As mentioned in Section 4.6., p. 85, the melting point of pure cryolite lies between 1009 and 1012 ºC, which was found as well for the measurements in this work. This indicates that the cryolite used was rather impure. Since oxides are likely to be present among impurities in cryolite, it is possible that in the measurements by Chrenkova equilibrium (4.14) was shifted to the left due to the presence of additional oxide ions. Hence, the results of those measurements indicated only one new species, PO_4^{3-}.

The results obtained by Tkatcheva et al. [7] do not contradict the findings presented in this chapter. As already pointed out in Chapter 2.1.2., the ratio between oxygen and phosphorus was found to be 4 by Tkatcheva in Na_3AlF_6-NaF-$AlPO_4$ melts, also in the presence of Al_2O_3. This does not necessarily imply that the PO_4^{3-} anion is stable, but that the P and O components of the ion do not escape from the melt by forming volatile species. Assuming that the metaphosphate ions and oxide ions are stable species in the cryolite melt, the results obtained are supported by the findings of Tkatcheva.

References for Chapter 4:

[1] T. Førland, *Thermodynamic properties of fused-salt systems,* Chap.2, ed. B. Sundheim, *Fused Salts*, McGraw-Hill, New York, 1964.

[2] J. Thonstad, P. Fellner, G.M. Haarberg, J. Hives, H. Kvande, Å. Sterten, *Aluminium Electrolysis – Fundamentals of the Hall-Héroult Process*, 3rd edition, Aluminium-Verlag GmbH, Düsseldorf, Germany, 2001.

[3] Å. Sterten, I. Mæland, *Thermodynamics of molten mixtures of Na_3AlF_6-Al_2O_3 and NaF-AlF_3*, Acta Chem. Scand., **A39**, 241, 1985.

[4] M. Chrenková, V. Danĺk, A. Silný, *Reactions of phosphorus in molten cryolite,* X. Proceedings, Slovak-Norwegian Symposium on Aluminium Smelting Technology, Stará Lesná-Ziar nad Hvonom, Slovakia, Sept. 21-23, 1999.

[5] T. Østvold, J. Løvland, *Applied chemical thermodynamics*, lecture notes, NTNU Trondheim, Norway, 1994.

[6] T. Østvold, *Molten Salt Chemistry – Thermodynamics of liquid salt mixtures and their vapours*, lecture notes, NTNU Trondheim, Norway, 1998.

[7] O. Tkatcheva, H. Mediaas, T. Østvold, *Phosphorus in cryolite I*, internal report at the Institute of Inorganic Chemistry, NTNU Trondheim, Norway, 1999.

5. Electrochemical measurements

5.1. Introduction

Phosphorus is known to be an impurity that reduces the current efficiency significantly. The assumed mechanism is a reduction oxidation cycle of the phosphorus between the bath and metal in an industrial cell. The aim of this work was to elaborate in what different kind of oxidation states phosphorus is existing in fluoride based melts. While Kerouanton et al. [1] found a two electron step from P(V) to P(III), Deininger and Gerlach [2] concluded that at a certain concentration of phosphorus in the melt (> 0.12 wt%), the reduction from P(V) to elemental phosphorus is possible.
Since phosphorus can be found in the aluminium as well, lower valent oxidation states than P(III) have to exist.

5.2. Experimental set-up

The type of furnace used is the same as presented in Section 4.1. The cell arrangement for the electrochemical measurements is shown in Figure 5-1. The atmosphere in the furnace was argon, as mentioned in Section 4.1.

As reference electrodes platinum was mostly used in oxide-free melts and aluminium was used in alumina-saturated melts. The reference electrode presented in Figure 5-1 is an aluminium reference electrode with an alumina casing and a hole making contact to the melt. An aluminium pool was contained inside the alumina casing. A tungsten wire, protected from the incoming melt by an alumina tube, was used as connection to the measurement device.

In the beginning of the work the measurements were performed with a Radiometer DEA-I digital electrochemical analyser, which consisted of a DEA332 potentiostat (maximum current output 2 A) and an IMT 102 electrochemical interface, which had a response time of less than 3 μs. The obtained data were handled by the Windows-based VoltMaster 2 software.
The measurements with this unit concern only cyclic voltammetry measurements of alumina-saturated cryolite melts with addition of aluminium orthophosphate. The other measurement unit used was an Autolab PGSTAT30 with a maximum current range of 1 A. Application of the electrochemical techniques and preliminary treatment of the obtained

data were performed with the General Purpose Electrochemical System (GPES). When necessary ohmic drop compensation was applied. The ohmic drop values measured will be given for the respective experiment in the text. The ohmic resistance was typically between 0.1 and 0.5 q .

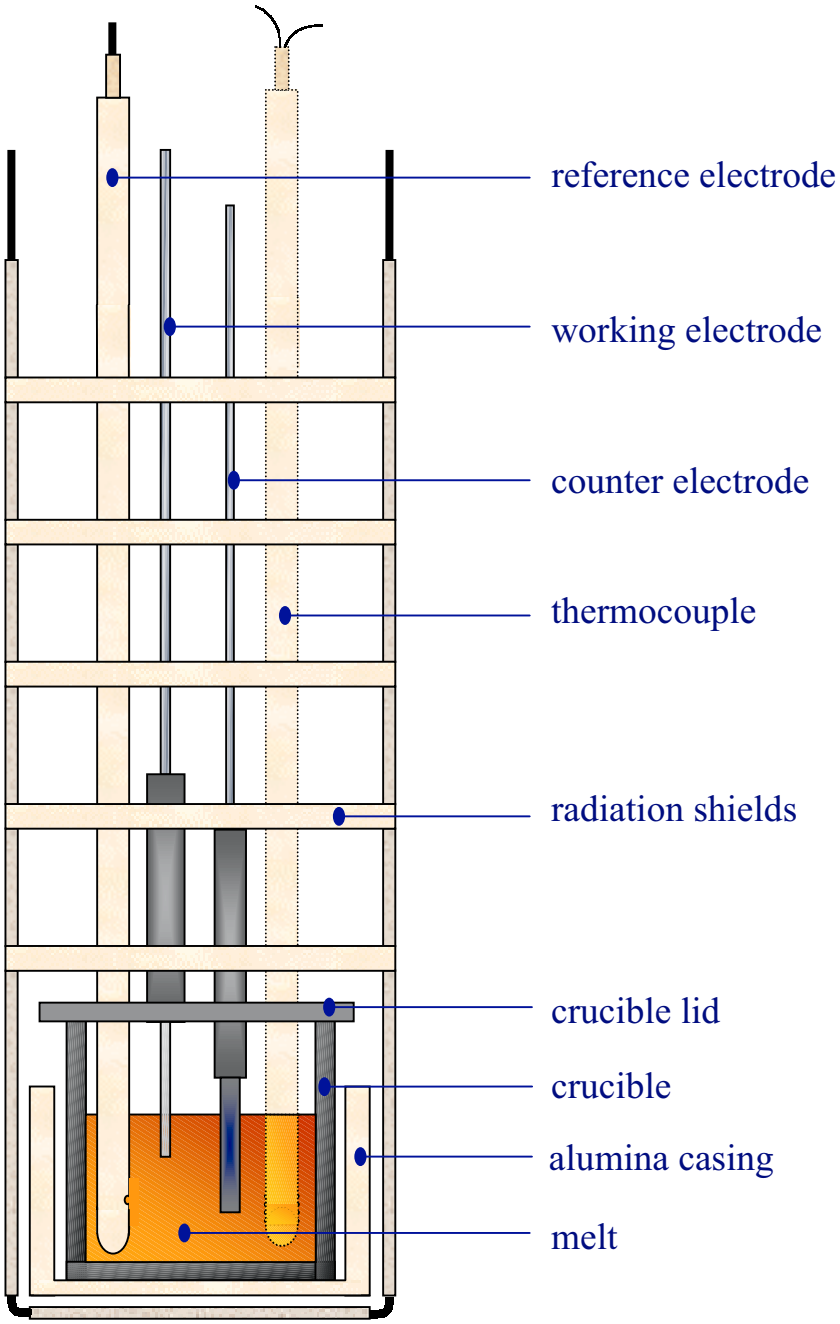

Fig. 5-1: *Cell arrangement used for electrochemical measurements presented in Chapter 5.*

The working electrodes were tungsten and copper wires, as they seemed to be the best materials for investigating the behaviour of phosphorus compounds in fluoride melts.
Glassy carbon was not found to be suitable as working electrode. Deposition of aluminium and oxidation of the carbon by formation of CO_2 were observed in the case of alumina-saturated melts. However, no current signal could be detected after addition of phosphate. Platinum was considered as well, but alloy formation with aluminium restricted its use at cathodic potentials. The current response of a platinum electrode in a cryolite melt when running cyclic voltammetry was investigated by Duruz et al. [3]. They observed alloy formation with aluminium as shown in Figure 5-2. It should be noticed that the axis are reversed compared to the voltammograms presented elsewhere in this thesis.

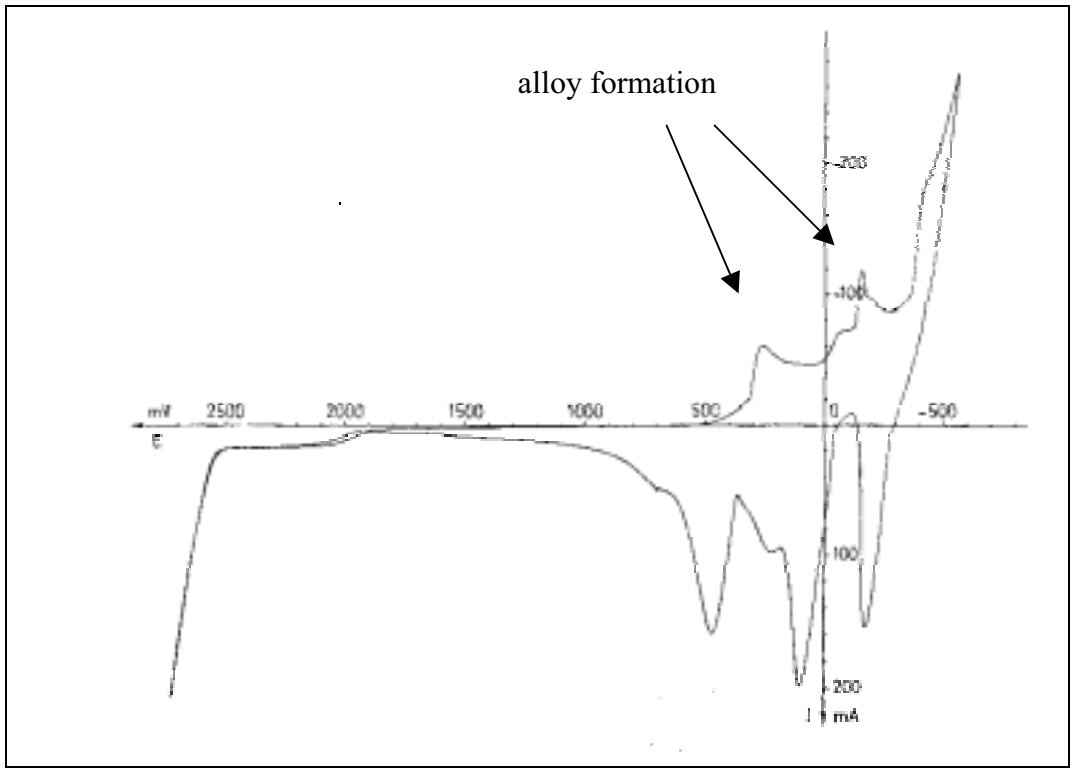

Fig. 5-2: *Platinum as working electrode in a cryolite melt at 1010 ˚C, electrode area 0.32 cm^2, sweep rate 0.05 V/s, ref. el. Mn/Mn^{2+}, from Duruz et al. [3].*

The determination of the electrode area was performed by either determination of the peak current at different immersion depths (see Appendix F) and/or by visual inspection. The error made by visual inspection was usually not more than 5% of the value determined by the method described in Appendix F.

As counter electrodes different materials were used: glassy carbon, graphite, nickel. In some cases the crucible (nickel or graphite) was connected to serve as a counter electrode. If electrodes as shown in Figure 5-1 were used as counter electrode, the area of the counter electrode was considerably larger than for the working electrode.

In case of alumina-saturated melts, the melt container usually consisted of sintered alumina. Sometimes nickel or graphite crucibles were used as well. For alumina-free melts the container either consisted of nickel or graphite. Various container materials were used and the actual materials will be specified.

5.3. Chemicals

The chemicals used for the experiments are listed in Table 5-1.

Table 5-1: *Specifications of the chemicals used for electrochemical measurements.*

Chemical	Producer/quality	Pre-treatment
Na_3AlF_6	Hand-picked, natural Greenland cryolite	Grains with coloured appearance were discarded. Kept at 200 ∀C in a heating chamber before use
Al_2O_3	Fluka, p. a.	Heated to 1200 ˚C for 4 hours, thereafter stored at 200 ∀C in a heating chamber before use
NaF	Merck, p.a.	Kept at 200 ˚C in a heating chamber before use, for some experiments recrystallized
AlF_3	Norzink	Sublimed at 1090 ˚C under vacuum for at least 12 hours. Kept at 200 ˚C in a heating chamber before use
Na_3PO_4	Riedel-de-Haën, pure	Kept at 200 ˚C in a heating chamber before use
$AlPO_4$	Riedel-de-Haën anhydrous, technical	Kept at 200 ˚C in a heating chamber before use
Ar	Argon 4.0 (99.99%), AGA	used as received

5.4. Electrochemistry of phosphates in fluoride based melts

5.4.1. The Na_3AlF_6 and the Na_3AlF_6-$Al_2O_{3(sat.)}$-systems

This section gives an introduction to the basic molten salt systems by presenting cyclic voltammograms without addition of phosphates. The electrode materials are given in the figure legends.

A mixture of NaF (re-crystallized) and AlF_3 in a molar ratio equivalent to cryolite and hand-picked natural Greenland cryolite were used when investigating the Na_3AlF_6 system. The voltammogram in Figure 5-3 shows the current signals of the cryolite mixed from its components. Voltammograms recorded with natural cryolite were similar to Figure 5-3.

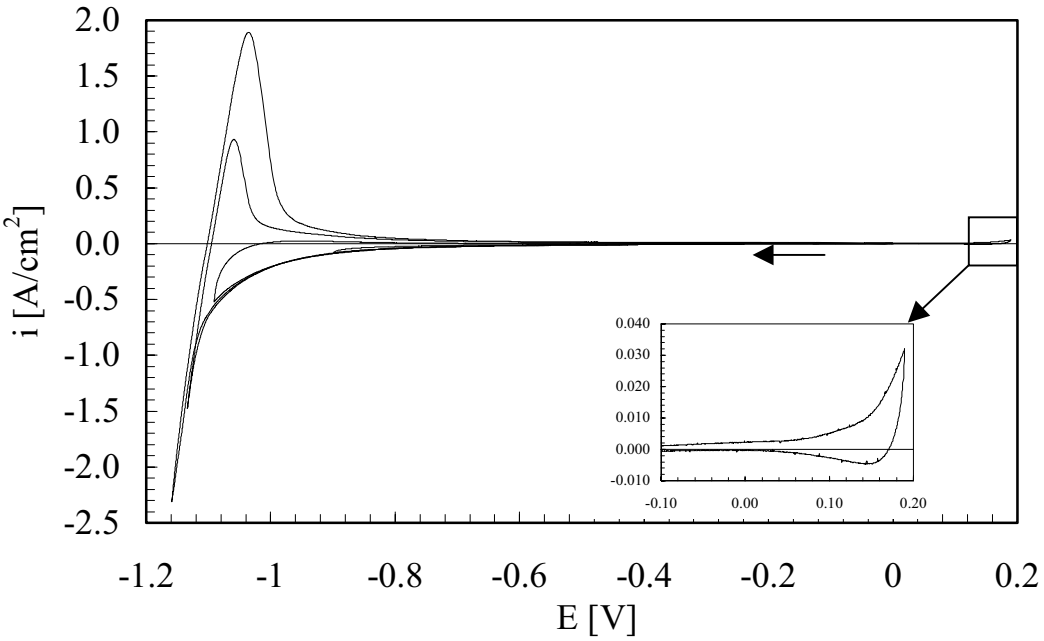

Fig. 5-3: *Cyclic voltammogram of a mixture of NaF and AlF_3 equal to the cryolite composition with a tungsten electrode, T = 1020 ºC, ɜ = 0.2 V/s. Electrodes: working: tungsten; ref.: platinum; counter: graphite crucible. Arrow shows the sweep direction.*

Platinum was used as reference electrode although it does not give a well-defined thermodynamic potential. At the cathodic side of the voltammogram reduction to aluminium is shown. The potentials of the different sweeps were reversed at -0.9, -1.1, -1.15 and -1.2 V to determine the deposition potential of aluminium. The cathodic current increases

slowly with decreasing potential up to the point were aluminium starts to deposit (~-1.1V). This might be due to alloying between tungsten and aluminium. The steep increase of the cathodic current signal at even more cathodic potentials implies the deposition of liquid aluminium on the tungsten electrode. For vertex potentials below –1.1 V a typical stripping peak is observed when the potential is reversed.

Towards the anodic limit of the system, Figure 5-3 indicates that at ~ +0.2 V the current starts to increase slightly. In a publication by Duruz et al. [3] on electrode materials in fluoride melts, a voltammogram of the Na_3AlF_6 system with a tungsten working electrode is presented, shown in Figure 5-4. It should be noticed that the axes are reversed compared to the voltammograms presented elsewhere in this thesis.

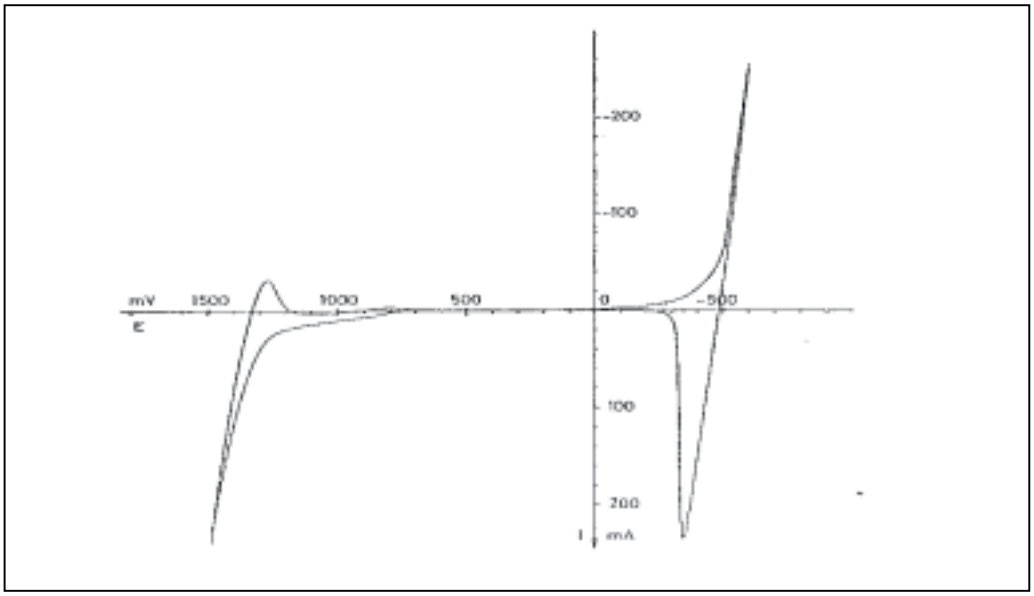

Fig. 5-4: *Cyclic voltammogram of the Na_3AlF_6 system with a tungsten electrode of an area of 0.32 cm^2, T = 1020 °C, ϑ = 0.05 V/s, with a Mn^{2+}/Mn reference electrode; from Duruz et al. [3].*

Even though the anodic limit was not reached as clearly as in Figure 5-4, the voltamograms obtained in Figure 5-3 are in agreement with the results of Duruz et al. [3]. Most likely the small current increase at about +0.2 V in Figure 5-3 can be compared to the minor current rise at +0.8 V in Figure 5-4. This also corresponds to the electrochemical window (~1.3 V) observed in Figure 5-3.

For molten cryolite saturated with alumina the voltammograms obtained are somewhat different, as can be seen in Figure 5-5.

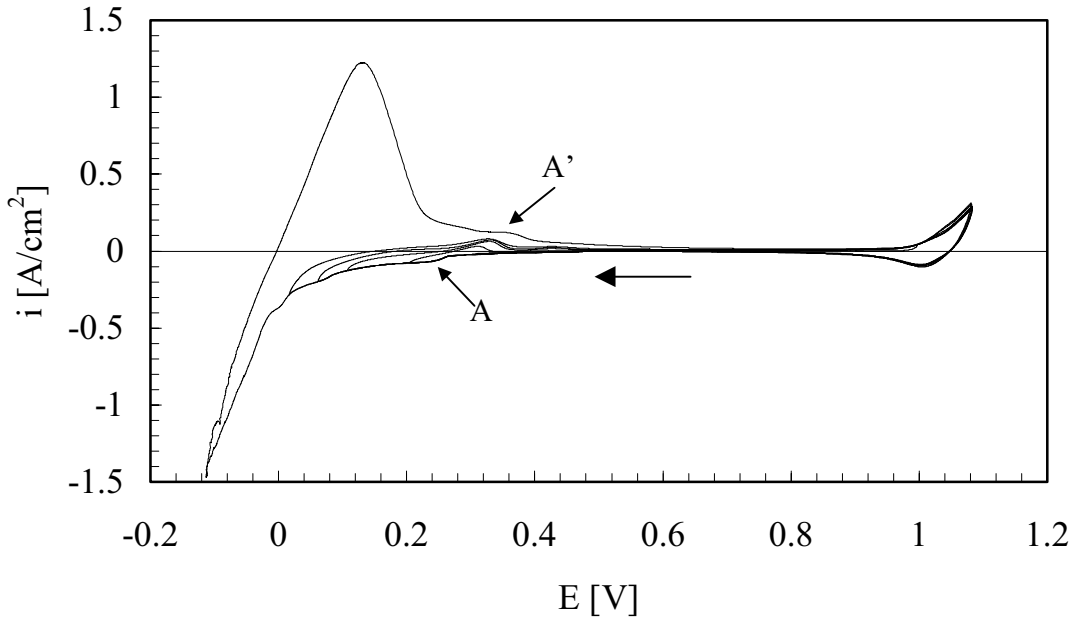

Fig. 5-5: *Cyclic voltammogram of a Na_3AlF_6-$Al_2O_{3(sat)}$ melt with a tungsten electrode, T = 1000 ºC, ϑ = 0.1 V/s, ref. el.: aluminium, counter el.: glassy carbon. Arrow shows start direction.*

In melts containing alumina, an aluminium reference electrode could be used. An alumina crucible served as container. The electrochemical window is smaller in the case of the alumina-saturated melt (~1 V). This implies that the presence of oxide influences the anodic limit. Formation of tungsten oxide or tungstenate ions (WO_x^{n+}) apparently take place, which occurs before the tungsten electrode is oxidised. An investigation of the behaviour of tungsten anodes in cryolite-alumina melts at 1000 ºC by Shternberg et al. [4] showed that the potential between an aluminium reference electrode and a tungsten electrode was about 1.07 V. They assumed that chemisorption of oxygen or formation of intermediate oxide species take place at tungsten. Furthermore they suggested that the potential might be determined by the formation of tungsten oxide (WO_2 or WO_3).

The potential range for the electrochemical window found by Shternberg et al. [4] is in good agreement with the value determined from the measurements in this thesis.

As for the pure cryolite system, the potential was reversed at different values in order to explore the system and to determine the deposition potential of aluminium. The deposition of aluminium starts at 0 V, as expected considering that an aluminium reference was used for the measurements presented in Figure 5-5. An additional reduction (A) and oxidation current signal (A') can be observed in Figure 5-5, which always appeared when measuring in alumina-saturated cryolite melts using a tungsten working electrode. A close-up of this region taken from a similar experiment, can be seen in Figure 5-6.

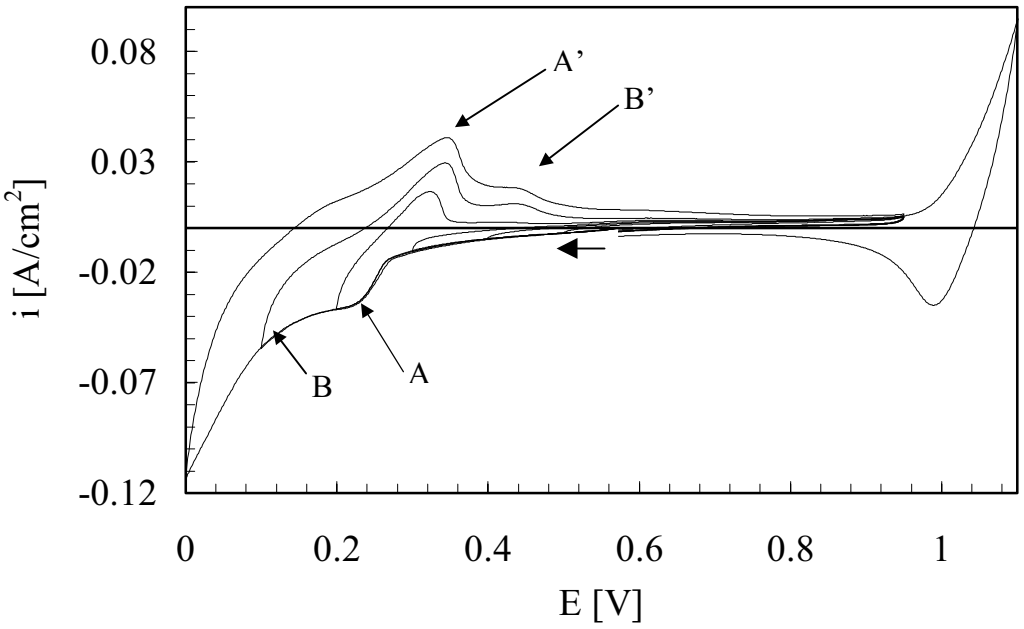

Fig. 5-6: *Close-up of the additional peak couple in Figure 5-5, T = 1000 °C, ϑ = 0.1 V/s. Arrow shows direction of the sweep.*

The appearance of the two peak couples, A/A' and B/B', can be attributed to the addition of alumina to the cryolite melt. The reduction peak A appears at potentials below 0.25 V. Its corresponding oxidation peak A' can be seen from the voltammogram reversed at 0.2 V. If the cathodic limit is chosen more cathodic (0.1 V) a second peak couple B/B' appears.

If the peak couples A/A' and B/B' would be due to alloying of aluminium with tungsten, the peaks should appear in the pure cryolite system as well. A possible explanation for the appearance of those peaks might be additional impurities introduced to the melt by alumina. Looking at the oxidation peak A' the slope after the peak current is rather steep for a soluble-soluble system. Therefore, judging from the shape of the peak couple A/A', a deposition/dissolution process might be assumed. The number of electrons transferred can be calculated when determining the

peak and half peak potentials. The calculation gives n = 2. Therefore, if the peaks are due to a metallic impurity, the metal ion in the melt has to be divalent.
A third possibility might be a change in the nature of the substrate. As indicated by Sthernberg et al. [4], the formation of an oxide layer on the tungsten electrode takes place. The assumed change in the nature of the substrate could influence the current signal in the pure alumina-saturated cryolite melt compared to pure molten cryolite.

We shall later see that the peak couples A/A' and B/B' are influenced by phosphate additions to the melt.

Copper was also used as working electrode material. In the pure cryolite system the following voltammogram was obtained, as shown in Fig. 5-7.

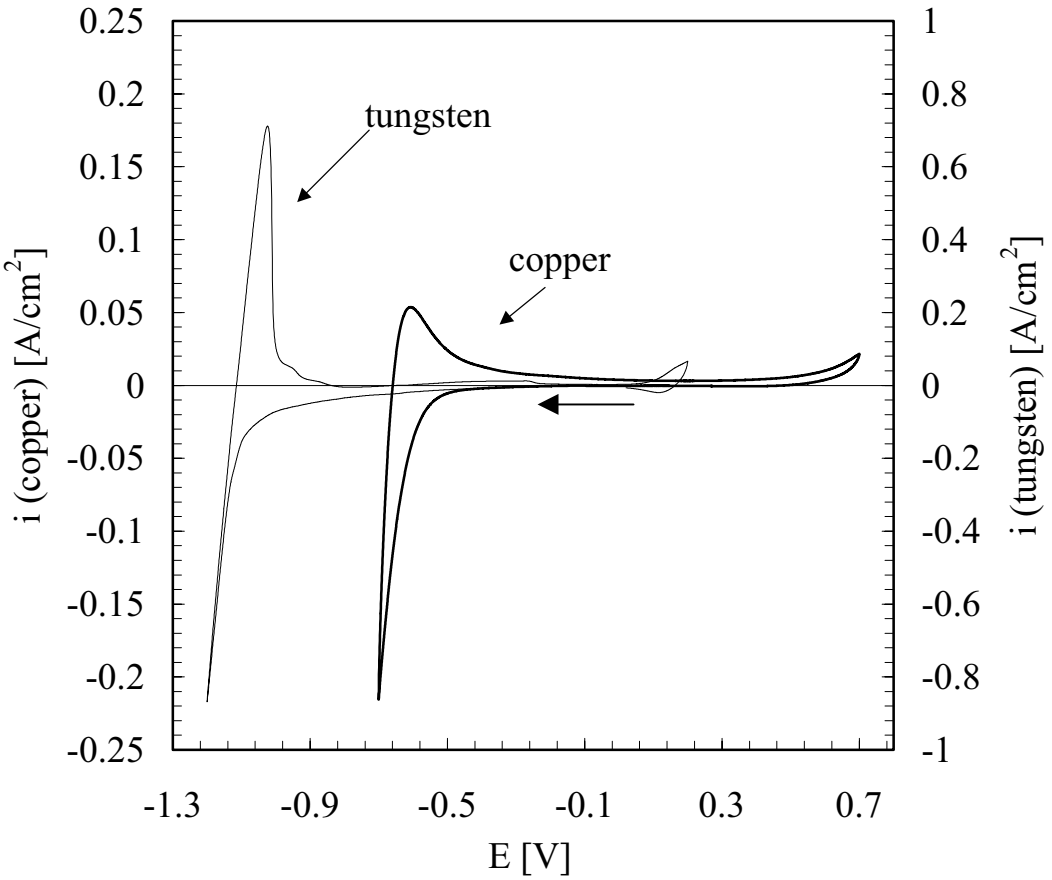

Fig. 5-7: *Cyclic voltammogram of a pure cryolite melt at 1020 °C, ϑ = 0.2 V/s; Electrodes: working: tungsten and copper, ref.: platinum. The arrow indicates the direction of the sweep for both curves.*

Sweeping the potential from the OCP towards the cathodic limit of -0.7 V in case of the copper working electrode, Figure 5-7 shows that aluminium

deposits at about -0.54 V on the copper substrate, while on the tungsten electrode the deposition potential was determined to be –1.1 V. In both cases platinum was used as reference electrode. It is believed that in the case of the copper electrode aluminium is forming an alloy with copper, which has a more positive deposition potential than for aluminium on tungsten.

When reversing the potential the aluminium deposit is stripped off. The electrochemical window is limited on the anodic side due to the anodic dissolution of the copper electrode. The crucibles used for these experiments were graphite or nickel when using copper as a working electrode.

5.4.2 The Na_3AlF_6-$Al_2O_{3(sat.)}$-Na_3PO_4 system

The measurements in this system were made with a tungsten wire as working electrode. An aluminium reference electrode was used and an alumina crucible served as container. Typical voltammograms obtained in this system are shown in Figure 5-8.

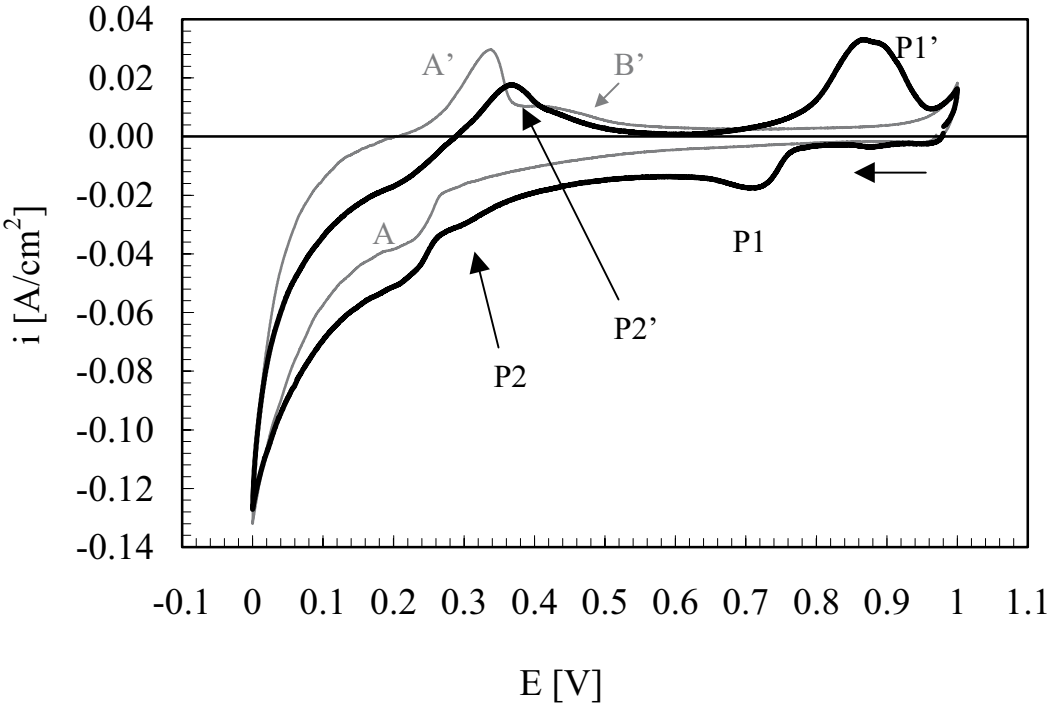

Fig. 5-8: *Cyclic voltammograms of the pure alumina-saturated cryolite system (thin, grey curve) and after addition of 0.16 wt% Na_3PO_4 (bold, black curve); ϑ = 0.2 V/s, T = 1000 °C; Electrodes: working: tungsten, ref.: aluminium.*

From Figure 5-8 we can see that after addition of sodium orthophosphate two new peak couples appear, P1/P1' and P2/P2'. While the peak P1 is clearly defined at 0.71 V and P1' at 0.88 V, the peak couple P2/P2' is not easy to distinguish from the previously discussed peak couples A/A' and B/B' (see Section 5.4.1).
Starting from the OCP at 0.97 V after addition of sodium orthophosphate an immediate slight increase in current (~- 0.0022 A/cm^2) can be observed in Figure 5-8 compared to the system without addition. Since the formation of oxide species at the tungsten electrode surface was mentioned earlier (Section 5.4.1), the constant cathodic current from 0.97 to 0.8 V could be interpreted as a capacitive current due to the oxide layer. Thereafter a first reduction peak appears at 0.7 V, which must be due to reduction of the added phosphate. While sweeping the potential further in the cathodic

direction, the current increased slightly. A small current wave can be observed at 0.28 V directly followed by the wave A at 0.2 V. After reversing the potential, changes in peaks A' and B' appear after the addition of phosphate. The oxidation peak P2' seems to mask both peaks A' and B'. When reaching 0.72 V a new anodic peak P1' appears with a peak potential of 0.88V.

The voltammograms in Figure 5-9 resulted from stepping the potential more cathodic for each run to investigate the P1/P1' reactions.

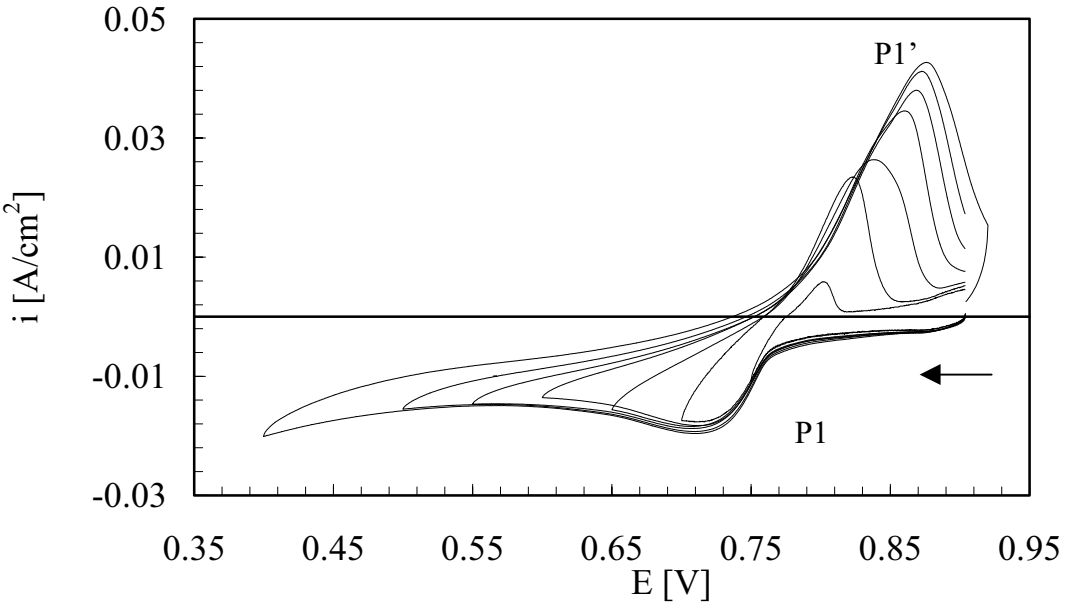

Fig. 5-9: *Voltammograms of the Na_3AlF_6-Al_2O_3 system after addition of 0.16 wt% Na_3PO_4, ʒ = 0.2 V/s, T = 1000 ˚C, Electrodes: working: tungsten; ref.: aluminium.*

It can be seen that the cathodic peak potential remains stable at 0.71 V, independent of the reversing potential of the scan. The anodic peak potential, however, shifts about 0.06 V when changing the reversing potential from 0.7 to 0.4 V. This behaviour indicates that either the anode process is irreversible (slow kinetics) or that a deposit is formed during the cathodic scan. The more cathodic the vertex potential is chosen, the higher is the anodic peak current of P1' and the larger is the area under peak P1'.

By applying a potential more cathodic than 0.4 V, the voltammograms shown in Figure 5-10 were obtained. The anodic peak potential of P1' has a stable value at 0.88 V.

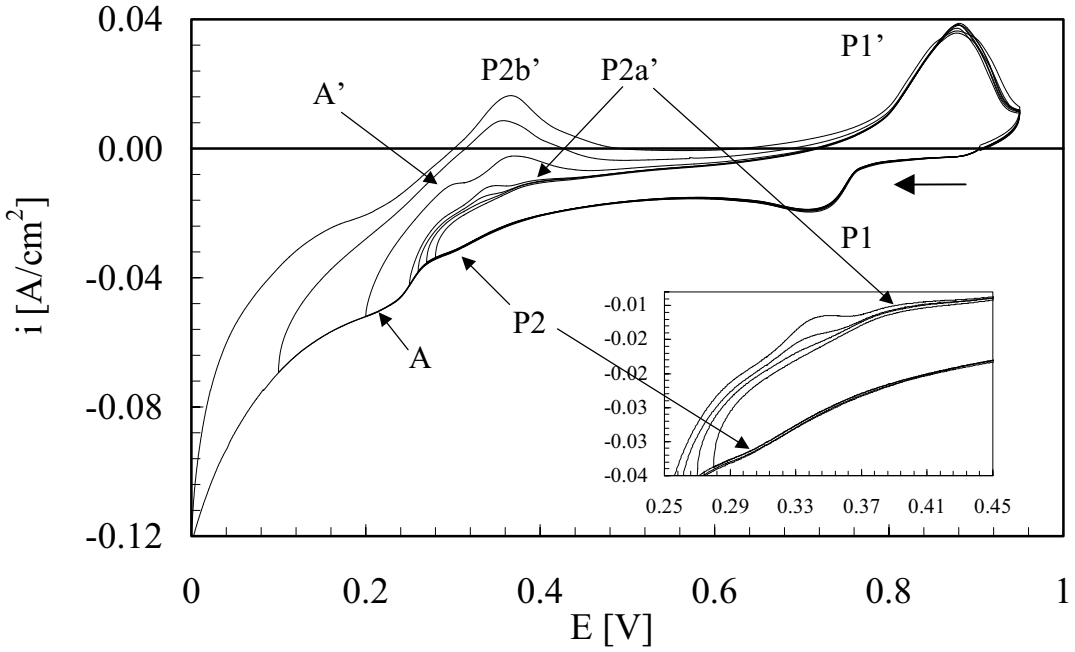

Fig. 5-10: *Voltammograms of the Na_3AlF_6-Al_2O_3 system with addition of 0.16 wt% Na_3PO_4, ϑ = 0.2 V/s, T = 1000 °C;, Electrodes: working: tungsten, ref.: aluminium; different vertex potentials.*

By stepping the cathodic limit in small steps from 0.28 to 0.25 V, the small current wave P2 can be observed. A small anodic peak, P2a', at about 0.4 V appears when the potential is reversed. The potential difference between P2 and P2a' is 0.12 V. From the shape of the peak the assumption can be made that the system is soluble-soluble. The number of electrons transferred is calculated to be 2.

When reaching the potential limit at 0.27 and 0.28 V, a new anodic peak evolves, P2b'. The appearance of P2b' indicates that the product of the reaction at peak A reacts with the product of peak P2 forming a new species. The oxidation peak A' is visible as well, when reversing the potential at 0.2 V. Otherwise, the peaks A' and P2b' are covering each other by forming one peak, earlier named P2' in Figure 5-8.

Peak P2 is more well-defined when recording a square wave voltammogram going from the OCP at 0.95 V to 0 V. Square wave voltammograms with and without addition of sodium orthophosphate are shown in Figure 5-11. The corresponding cyclic voltammogram from Figure 5-10 with the cathodic limit at 0 V is presented as well.

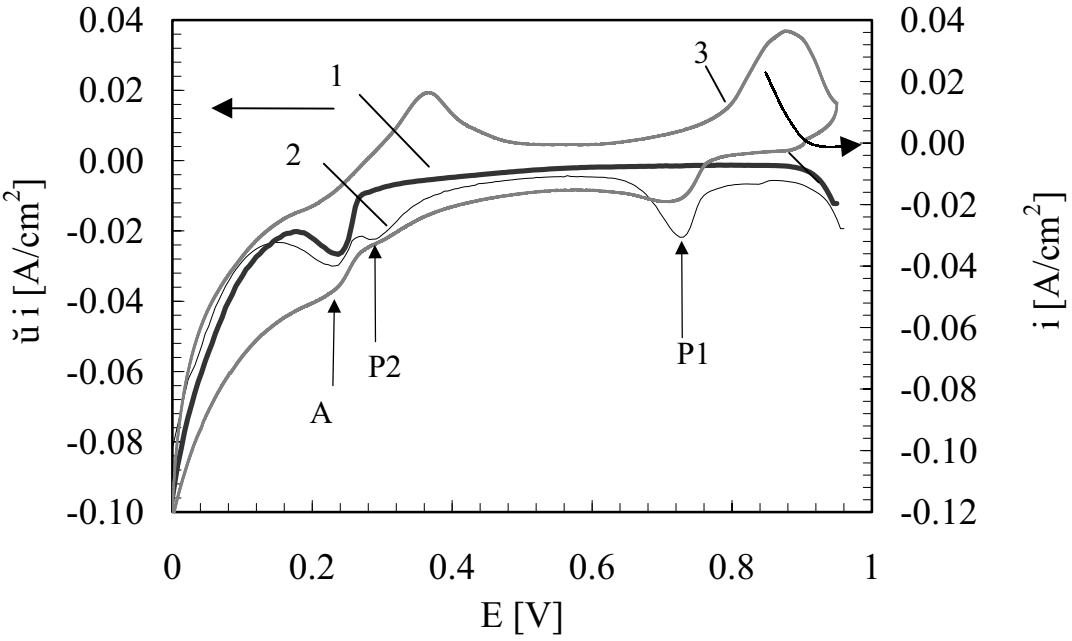

Fig. 5-11: *Two square wave voltammograms with (0.16 wt% Na_3PO_4) (2), and without addition (1), f = 20 Hz, in the system Na_3AlF_6-Al_2O_3. Cyclic voltammogram from the same system (3), T = 1000 ˚C.*

As can be seen from Figure 5-11, in the square wave voltammogram the addition of sodium orthophosphate gives two new current signals, P1 and P2, , which are clearly defined. The half wave potentials for the two peaks as well as for peak A, can be read from the curves:

$$E_{1/2}\ (P1) = 0.734\ V$$
$$E_{1/2}\ (P2) = 0.286\ V$$
$$E_{1/2}\ (A) = 0.232\ V$$

For a reversible, soluble-soluble system the half wave potential is equal to the standard potential (see equation (3.17)). However, as pointed out in Section 5.4.1., peak A has more the shape of a deposition. Also peak P1 in the square wave voltammogram does not look like a typical Gaussian curve for a soluble-soluble system. This means that only for peak P2, the half wave potential can be assumed to correspond to the standard potential of the process.

The recording of square wave voltammograms of peak P1 at different frequencies gives information about the relationship between $ŭi_p$ and the square root of the frequency. If the relationship is linear, the system is reversible as explained in Section 3.1.4.

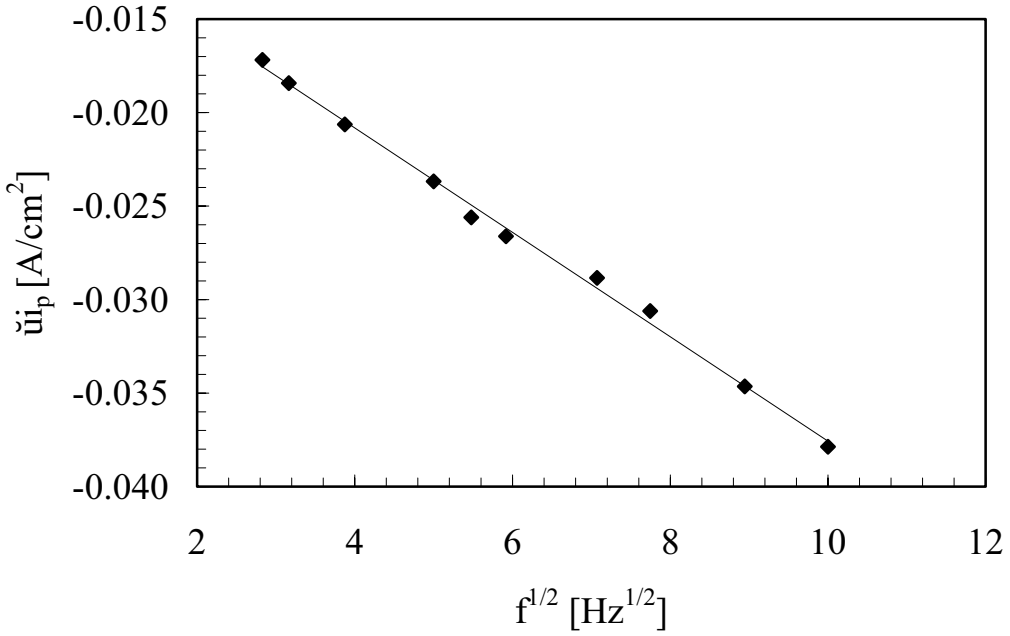

Fig. 5-12: *Differential peak current for peak P1 (see Figure 5-11) versus the square root of the frequency obtained in an alumina-saturated cryolite melt with additions of 0.16 wt% Na_3PO_4, T = 1000 ˚C. Frequencies from 8 to 100 Hz.*

Since Figure 5-12 shows a linear relationship between the differential peak current and the square root of the frequency, the reaction at peak P1 is assumed to be reversible.

The peak couple P1/P1' was investigated by cyclic voltammetry at different sweep rates. Voltammograms obtained at sweep rates of 0.1, 0.2 and 0.3 V/s are presented in Figure 5-13. For voltammograms as in Figure 5-13, the cathodic peak current density was determined and plotted versus the square root of the sweep rate, which is shown in Figure 5-14.

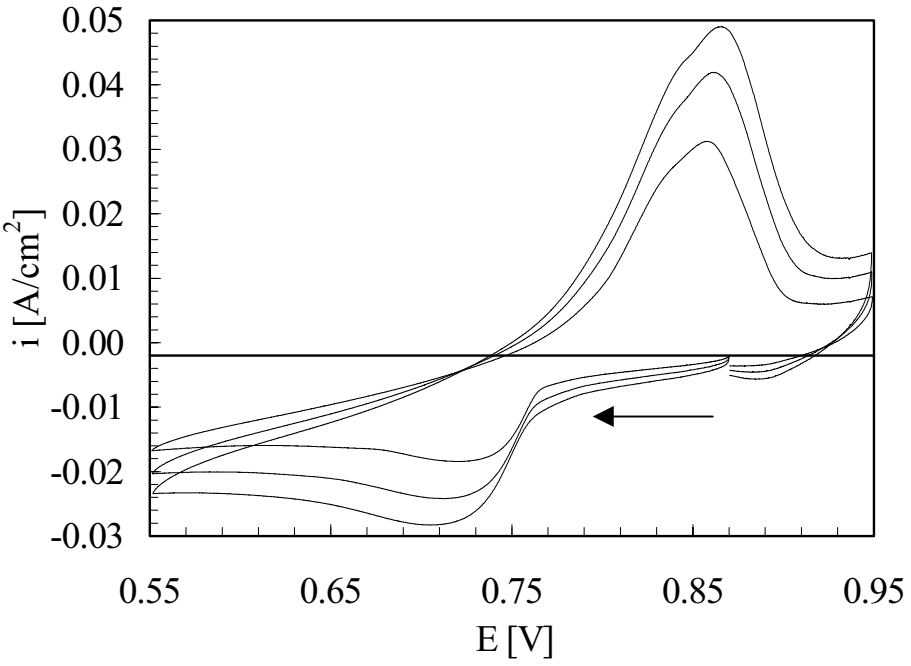

Fig. 5-13: *Voltammograms of Na_3PO_4 (0.16 wt%) in an alumina-saturated Na_3AlF_6 melt at 1000 ˚C for peak P1 (see Figure 5-10). Sweep rates are 0.1, 0.2 and 0.3 V/s.*

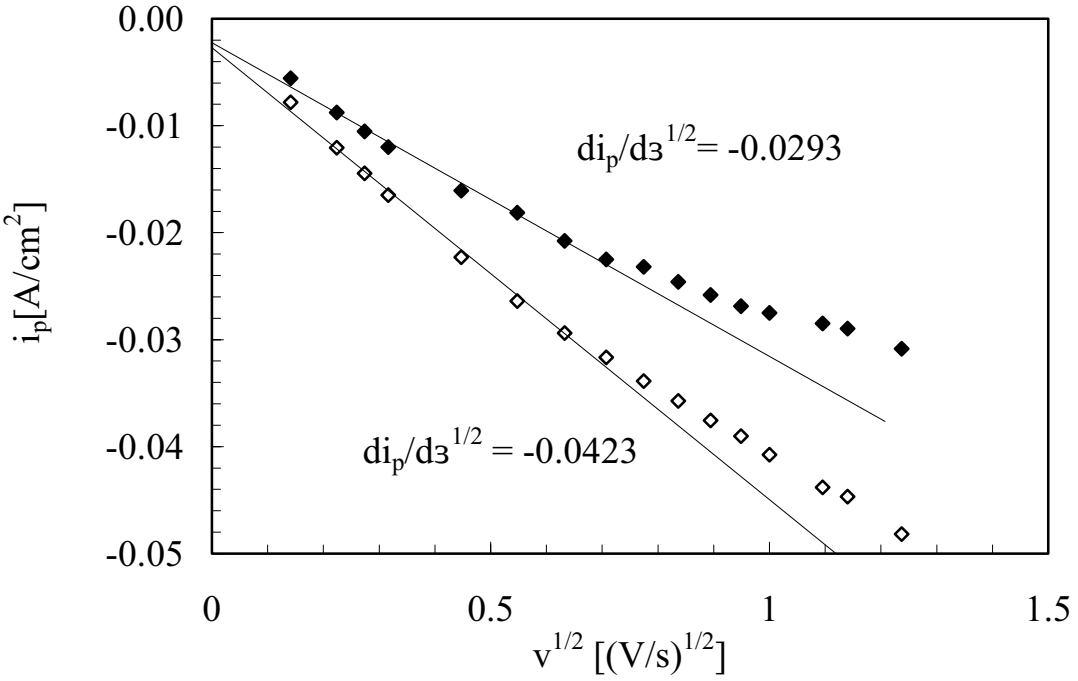

Fig. 5-14: *Plot of the cathodic peak current density versus the square root of the sweep rate, obtained in an alumina saturated Na_3AlF_6 melt at 1000 ˚C with 0.16 wt% Na_3PO_4 added. Sweep rates were varied from 0.02 to 1.53 V/s. Open diamonds: uncorrected peak current values; filled diamonds: background current substracted from the initial data.*

The data plotted in Figure 5-14 can be found in Table 5-2. Since the plot of the peak current density versus the square root of the sweep rate is linear for sweep rates up to 0.5 V/s, it can be assumed that the reaction is diffusion controlled in this range. As shown by square wave voltammetric investigations of peak P1, the system seems to be reversible for frequencies between 8 and 100 Hz (equal to a change in sweep rate between 0.04 and 0.5 V/s). For a reversible system the peak potential of the cathodic wave should be independent of the logarithm of the sweep rate. This was, however, not the case, even though corrections for the ohmic drop (R = 0.3 q) were performed. A negative shift of the cathodic peak potential E_p with increasing з is observed, becoming significant at sweep rates larger than 0.5 V/s.

Due to the fact that the ratio between the anodic and cathodic peak current densities of peak couple P1/P1' is about 2 (see Figure 5-13) and on the basis of the shape of the curve, a soluble-insoluble system is assumed. However, it should be emphasised that the system is not a soluble-insoluble one in terms of a metal deposition. The assumption is made that a reduction product forms, adhering to the electrode.

The deviation from the relationship between the peak current densities and the square root of the sweep rate with increasing sweep rates (see Figure 5-14) could be interpreted as a sign of one of the criteria indicating a change in the behaviour of the system, shifting from reversible into quasi-reversible. An increasing separation of the cathodic and anodic peak potentials with increasing sweep rate, implies this as well. However, the theoretical treatment of the soluble-insoluble system presupposes that the activity of a deposit is unity. In cases where the surface of the electrode gets covered within a few mV after the start of the deposition, the assumption that the activity of the deposit is unity is sustained. This may be valid at slow sweep rates like 0.1 V/s. For higher sweep rates as for example 1 V/s, complete coverage of the electrode may be reached later. The shape and position of the cathodic peaks are, therefore, influenced by the rate of the formation of the deposit and thereby by the sweep rate applied to the system. A shift towards lower potential values at higher sweep rates can be expected.

This means that in the case of the formation of an insoluble product the cathodic peak potential can be shifted with the sweep rate even for a reversible reaction.

Table 5-2: *Cyclic voltammetric data for the reduction of Na_3PO_4 (0.16 wt% added) at a tungsten electrode in an alumina-saturated cryolite melt at 1000 ˚C for peak P1; i_b is the background current.*

ɜ [V/s]	i_p^c [A/cm^2]	i_b [A/cm^2]	E_p^c [V]	$E_{p/2}^c$ [V]	n
0.020	-0.0078	-0.0022	0.730	0.761	2.7
0.050	-0.0121	-0.0033	0.727	0.758	2.7
0.075	-0.0145	-0.0039	0.722	0.756	2.5
0.100	-0.0165	-0.0045	0.720	0.754	2.5
0.200	-0.0223	-0.0062	0.711	0.749	2.2
0.300	-0.0264	-0.0082	0.702	0.745	1.9
0.400	-0.0294	-0.0086	0.697	0.743	1.8
0.500	-0.0317	-0.0091	0.696	0.742	1.8
0.600	-0.0339	-0.0107	0.694	0.740	1.8
0.700	-0.0357	-0.0111	0.688	0.739	1.7
0.800	-0.0376	-0.0117	0.688	0.738	1.7
0.900	-0.0390	-0.0121	0.683	0.737	1.6
1.000	-0.0408	-0.0132	0.683	0.736	1.6
1.200	-0.0438	-0.0153	0.682	0.734	1.6
1.300	-0.0447	-0.0156	0.681	0.734	1.6
1.530	-0.0482	-0.0173	0.670	0.732	1.4

The average number of electrons calculated in Table 5-2 by means of equation (3.23) is 1.94. Using Berzins-Delahay's equation for the peak current density of a reversible, soluble-insoluble system (equation (3.22), the diffusion coefficient can be calculated by using the slope from the corrected current values in Figure 5-14 for sweep rates between 0.02 and 0.5 V/s. At 1000 ˚C the diffusion coefficient was found to be

$$D = (9.2 \pm 1.0)\cdot 10^{-6}\ cm^2/s$$

for a concentration of $1.93\cdot 10^{-5}$ mol/cm^3 Na_3PO_4. The error estimate for the diffusion coefficient included a maximum temperature error of 2 ºC, an error of 1% when weighing the pressed tablets of sodium orthophosphate before addition and an error in the electrode area by 5%.

Chronopotentiometry

Investigation of the phosphate reduction by chronopotentiometry gave the curves shown in Figure 5-15.

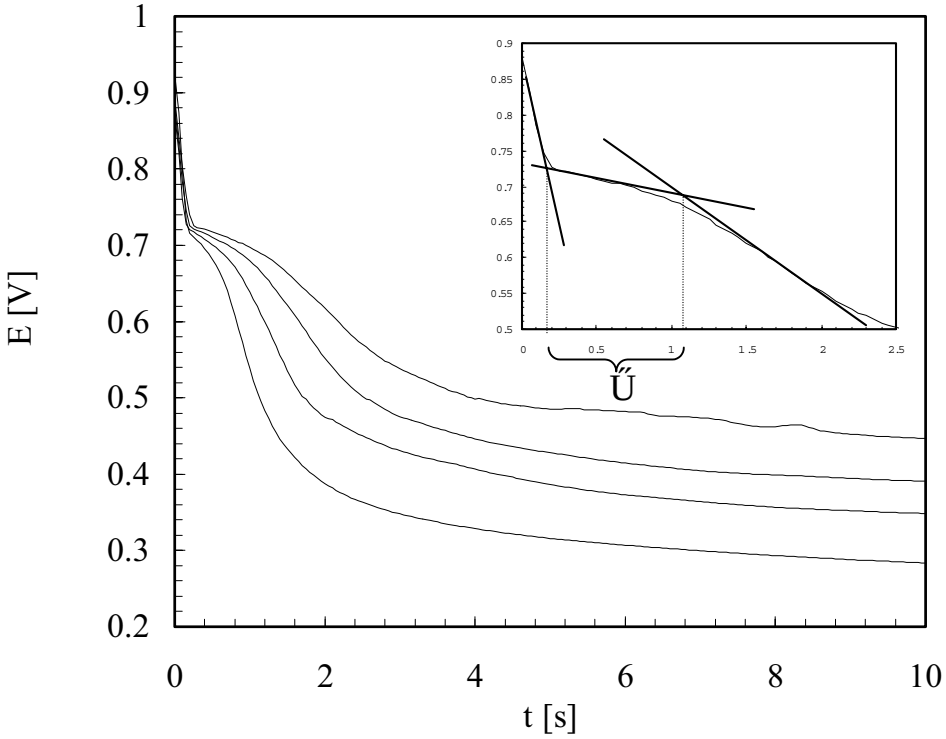

Fig. 5-15: *Chronopotentiometric curves for different current densities: -10.7, -11.9, -14.2 and -16.6 mA/cm^2. The inset shows the procedure used to determine Ű*

The first potential plateau in the E-t-curves is determined by the reduction of the phosphate ion. As soon as the surface concentration of the phosphate reaches zero, the potential drops to a lower level where the next electroactive species is reduced.
The transition time (Ű) for the phosphate reduction was determined by fitting tangents on the curve at the inflection points, as shown in Figure 5-15. The distance between the intersections of the tangents was taken as Ű The results are presented in Table 5-3. According to Sand's equation (equation (3.30)), a plot of i_o versus $1/Ű^{1/2}$ should give a straight line passing through the origin. Due to residual currents, this was not the case, as can be seen from Figure 5-16.

***Table 5-3**: Experimental data (i_o and Ű obtained by chronopotentiometry in the system Na_3AlF_6-$Al_2O_{3(sat.)}$ with Na_3PO_4 ($c = 1.93 \cdot 10^{-5}$ mol/cm^3), T = 1000 °C; i_r is the residual current.*

i_o [A/cm^2]	i_o-i_r [A/cm^2]	Ű[s]	D [cm^2/s]·10^6
0.0107	0.0079	1.087	6.2
0.0119	0.0091	0.922	7.0
0.0130	0.0102	0.685	6.6
0.0142	0.0114	0.577	6.9
0.0154	0.0126	0.458	6.7
0.0166	0.0138	0.420	7.4
0.0178	0.0150	0.357	7.4
0.0190	0.0162	0.263	6.3
0.0201	0.0173	0.245	6.8

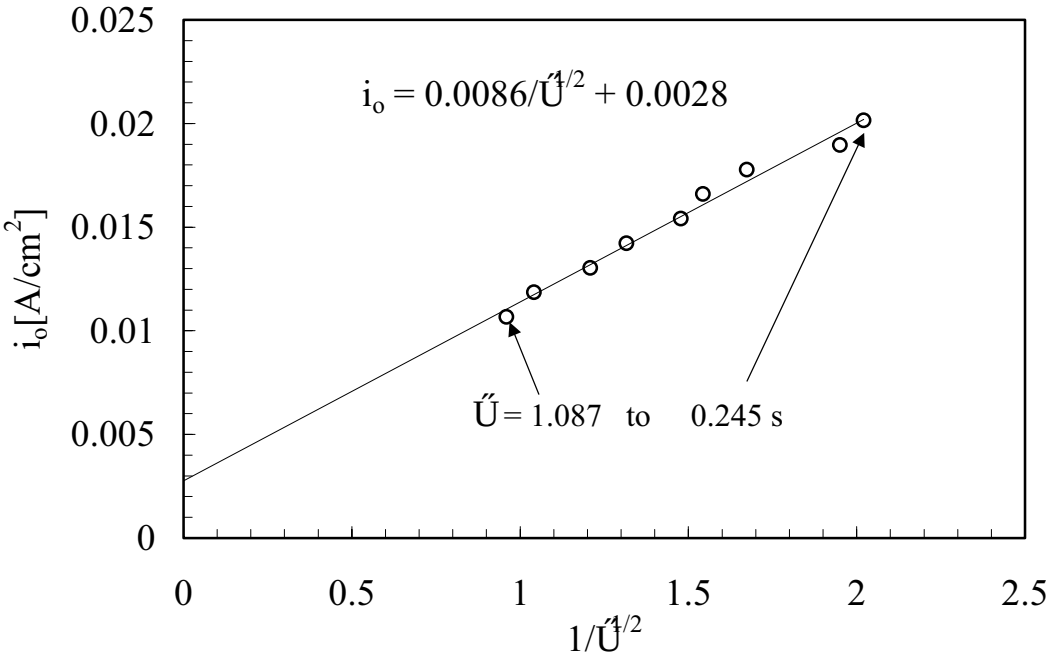

***Fig. 5-16:** Plot of i_o versus $1/Ű^{1/2}$. The equation of the linear fit is given in the figure.*

The curve in Figure 5-16 shows a linear relationship between the constant current density and the inverse of the square root of Ű However, the line does not pass through the origin, as expected from the Sand equation, but crosses the current density axis at 2.8 mA/cm^2. This value is referred to as the residual current density i_r. A calculation of $(i_o-i_r)/Ű^{1/2}$ versus i_o should

yield a constant value (see Figure 5-17). If this criterion is obeyed, the Sand equation can be applied to calculate the diffusion coefficient.

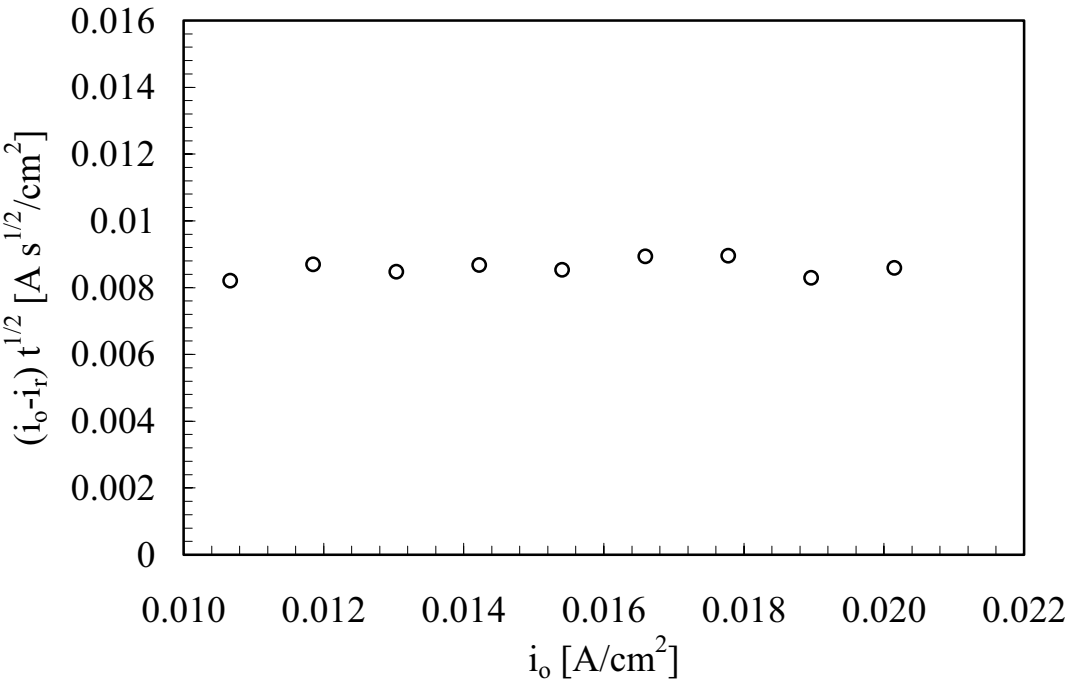

Fig. 5-17: *Plot of $(i_o-i_r)\cdot t^{1/2}$ versus the applied current density at a tungsten electrode in the system Na_3AlF_6-$Al_2O_{3(sat.)}$ with 0.16 wt% Na_3PO_4.*

As can be seen from Figure 5-17, the criterion is fulfilled to calculate the diffusion coefficient of the phosphate species by means of the Sand equation.

The diffusion coefficients obtained from the experimental data presented in Table 5-3, give an average value of $(6.8 \pm 0.7)\cdot 10^{-6}$ cm^2/s.

The results obtained for the diffusion coefficient of the phosphate species ($1.93\cdot 10^{-5}$ mole/cm^3) by cyclic voltammetry (CV) and chronopotentiometry (CP) are in reasonable agreement:

$$D^{CV}_{PO_4^{3-}} \mid \quad (9.2 \pm 1.0)\cdot 10^{-6}\ cm^2/s$$
$$D^{CP}_{PO_4^{3-}} \mid \quad (6.8 \pm 0.7)\cdot 10^{-6}\ cm^2/s$$

The diffusion coefficients obtained seem to be slightly lower than expected for diffusion coefficients in salt melts (~ 10^{-5} cm^2/s). However, the deviation from the usual order of magnitude is minor.

Shortly after the addition of the sodium orthophosphate, the current signals for the cyclic voltammetry and square wave voltammetry were disturbed on the cathodic side, which is shown in Figure G-1 in Appendix G. Usually, the appearance of such current fluctuations are interpreted as gas evolution. When adding phosphate, moisture might have been introduced to the system and the reduction of hydrogen ions could occur, evolving hydrogen.

5.4.3. The Na_3AlF_6-$Al_2O_{3(sat.)}$-$AlPO_4$ system

For systems with an alumina-saturated melt, an aluminium reference electrode placed inside an alumina tube was chosen. The melt container was an alumina crucible, and graphite was used as the counter electrode material. In Figure 5-18 cyclic voltammograms of an alumina-saturated cryolite melt with (thick, black curve) and without (thin, grey curve) addition of aluminium orthophosphate are shown.

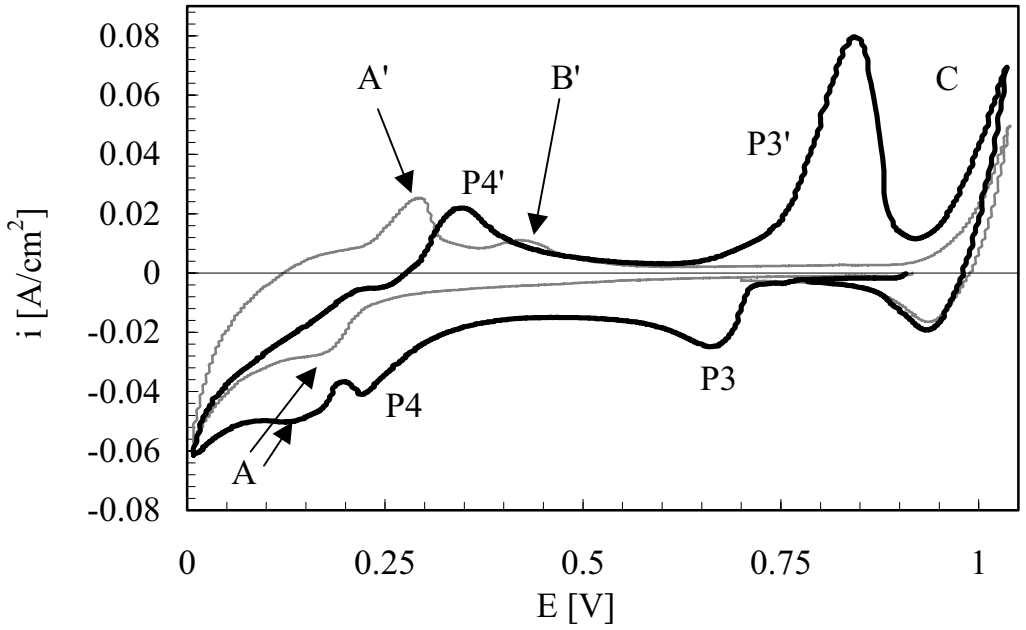

Fig. 5-18: *Cyclic voltammograms of an alumina-saturated cryolite melt with (bold, black curve) and without (thin, grey curve) addition of $AlPO_4$, Electrodes: working: tungsten, ref.: aluminium, T = 1000 ˚C, ʒ = 0.2 V/s.*

The cyclic voltammogram without addition of aluminium orthophosphate is similar to the one shown in Section 5.4.2. for the system without additions of sodium orthophosphate. Therefore the peaks are named with the same symbols. After addition of $AlPO_4$ new peak couples, P3/P3' and P4/P4' are observed. The addition of the phosphate changes the appearance of the peak couple A/A' and peak B as well, as was also the case for sodium orthophosphate (Section 5.4.2). The behaviour of sodium and aluminium orthophosphates is apparently similar. However, the oxidation peak P3' seems to have a different shape than P1' in the Na_3AlF_6-Al_2O_3-Na_3PO_4 system. The current increase at C represents the oxidation of the tungsten working electrode.

The peak couple P3/P3' was investigated as shown in Figure 5-19 at different sweep rates for з = 0.075, 0.2 and 0.5 V/s. The voltammograms are corrected for the ohmic drop in the melt (R = 0.25 q). The increase in current before reaching peak P3 is probably due to a capacitive current, which was subtracted from the measured data in Table 5-4, named i_b.

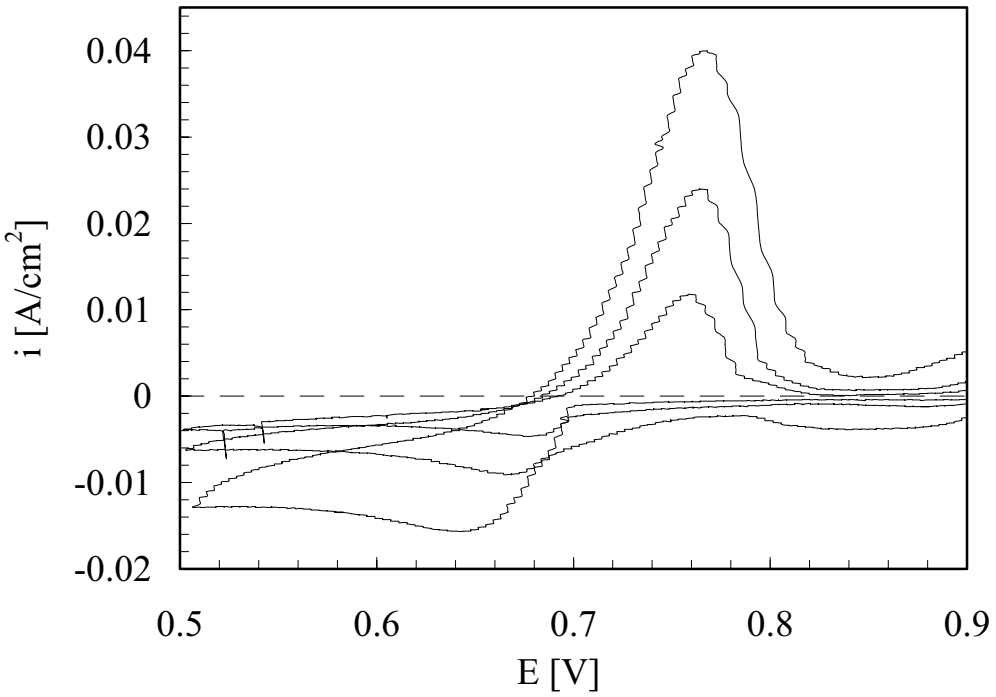

Fig. 5-19: *Cyclic voltammograms of the peak couple P3/P3' (shown in Figure 5-18) at different sweep rates (0.075, 0.2 and 0.5 V/s). The voltammograms are corrected for the ohmic drop (R = 0.25 q). The concentration of $AlPO_4$ was 0.049 wt%.*

Voltammograms were recorded for sweep rates between 0.075 and 1.2 V/s. The data presented in Table 5-4 were obtained.

Table 5-4: *Data for the reduction peak P3 obtained from voltammograms of peak couple P3/P3' at different sweep rates, 0.049 wt% $AlPO_4$, T = 1000 ˚C.*

ɜ [V/s]	i_p^c [A/cm^2]	i_b [A/cm^2]	E_p^c[V]	$E_{p/2}^c$ [V]	n
1.000	-0.01922	-0.0033	0.624	0.680	1.5
0.769	-0.01723	-0.00275	0.628	0.678	1.7
0.625	-0.01563	-0.0024	0.632	0.680	1.8
0.400	-0.01518	-0.0021	0.636	0.676	2.1
0.500	-0.01433	-0.00215	0.636	0.680	1.9
0.300	-0.01368	-0.00205	0.648	0.684	2.4
0.200	-0.01188	-0.0018	0.656	0.684	3.0
0.150	-0.01089	-0.00155	0.656	0.684	3.0
0.175	-0.01049	-0.0016	0.652	0.690	2.2
0.125	-0.01034	-0.0014	0.660	0.692	2.6
0.100	-0.00894	-0.00135	0.66	0.692	2.6
0.075	-0.00829	-0.00135	0.664	0.692	3.0

By assuming that the reduction product of peak P3 is somehow adhering to the electrode, the number of electrons involved can be calculated by using the equation for the soluble-insoluble system, as done in Section 5.4.2. for sodium orthophosphate. The average number of electrons from Table 5-4 is 2. As for the system with sodium orthophosphate, the cathodic peak potential shifts to more negative potential with increasing sweep rate. The reason for this is believed to be the same as for the system with sodium orthophosphate.

A plot of the cathodic peak current versus the square root of the sweep rate is shown in Figure 5-20. The criteria for having a diffusion controlled mass transport are met up to 0.2 V/s. For sweep rates higher than 0.2 V/s, the data-points deviate from the curve, indicating a change in the behaviour of the system. For the data up to 0.2 V/s a slope could be determined from the plot of i_p versus $ɜ^{1/2}$, from which the diffusion coefficient for the phosphate species is calculated.

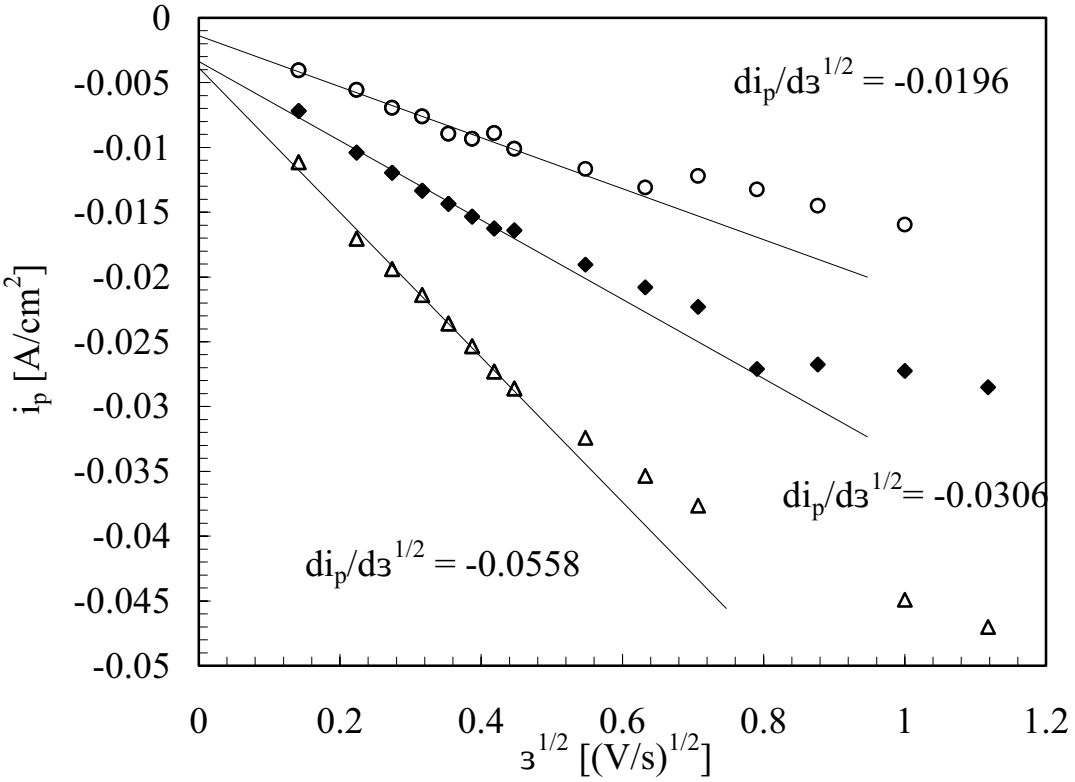

Fig. 5-20: *Plot of cathodic peak current densities versus the square root of the sweep rate for additions of 0.049 (open circles), 0.103 (filled diamonds) and 0.180 wt% (open triangles) $AlPO_4$ to a Na_3AlF_6-Al_2O_3 melt. Regression lines are fitted to data for з Ò 0.2 V/s.*

For calculation of the diffusion coefficients in Table 5-5, the Berzins-Delahay equation was used. The error estimate for the diffusion coefficient was made as explained in Section 5.4.2.

Table 5-5: *Diffusion coefficients for phosphate determined from slopes from Figure 5-20 for different concentrations of $AlPO_4$, T = 1000 ºC, n = 2.*

c($AlPO_4$) [mol/cm^3]	slope $di_p/dз^{1/2}$ [(A/cm^2)/(V/s)$^{1/2}$]	D(PO_4^{3-}) [cm^2/s]·10^5	error estimate [cm^2/s]·10^5
$8.19\cdot10^{-6}$	-0.0196	2.2	0.4
$1.72\cdot10^{-5}$	-0.0306	1.2	0.2
$3.00\cdot10^{-5}$	-0.0558	1.3	0.2

Chronopotentiometry

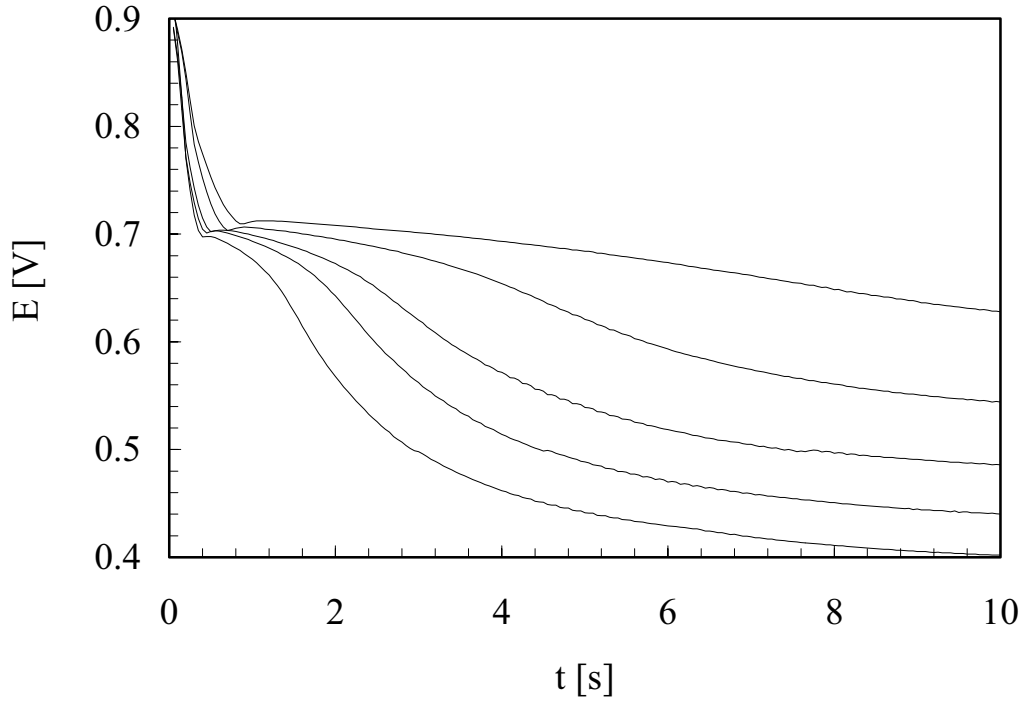

Fig. 5-21: *Chronopotentiograms at a tungsten electrode in a Na_3AlF_6-Al_2O_3-$AlPO_4$, T = 1000 ºC, current densities applied: -4.0, -4.8, -5.6, -6.4 and –7.2 mA/cm^2; c($AlPO_4$) = 7·10^{-6} mole/cm^3.*

Figure 5-21 shows some typical chronopotentiograms for the reduction of phosphate at 1000 ºC. The transition times for the various current densities applied were determined as described in Section 5.4.2. Although it is not apparent from Figure 5-21, a potential minimum can be observed in the initial part of the curves. A close-up of the potential minima for an experiment with $1.7 \cdot 10^{-5}$ mole/cm^3 $AlPO_4$ in the Na_3AlF_6-Al_2O_3 melt is shown in Figure 5-22.

The chronopotentiometric measurements were performed for two different concentrations of aluminium orthophosphate in the melt. The results are presented in Table 5-6.

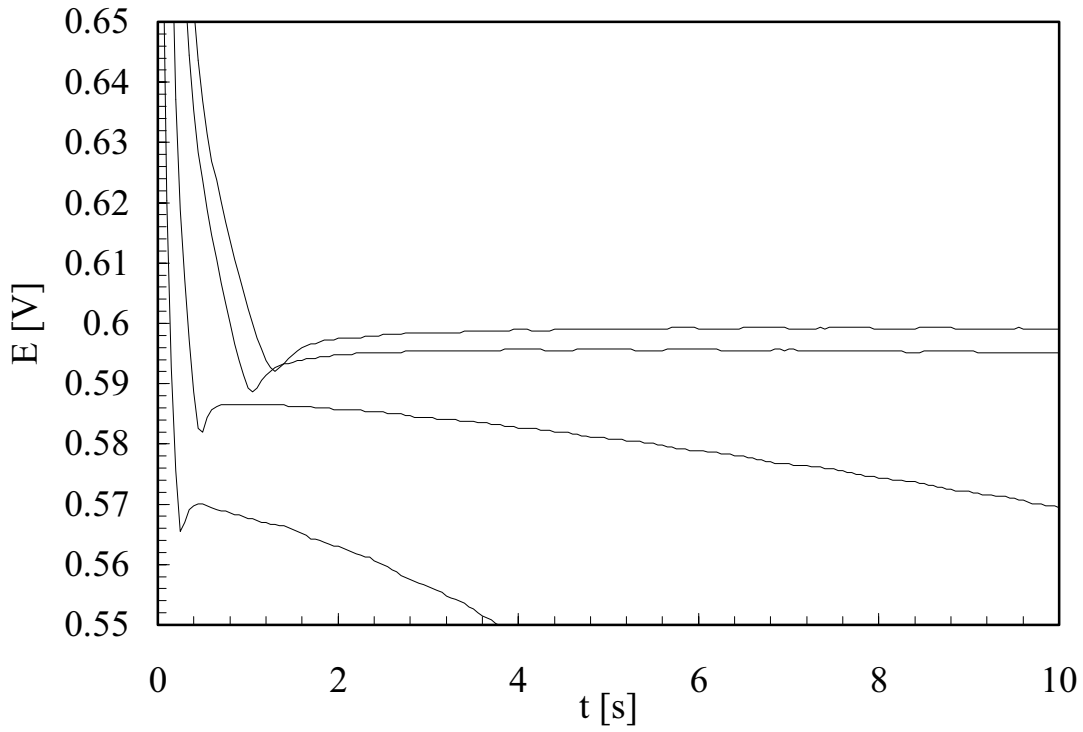

Fig. 5-22: *Initial part of chronopotentiograms at a tungsten electrode in a Na_3AlF_6-Al_2O_3-$AlPO_4$ melt, T = 1000 ºC, current densities applied: -1.8, -2.2, -4.3 and –6.5 mA/cm^2; c($AlPO_4$) = 1.7·10^{-5} mole/cm^3.*

From Figure 5-22 it seems obvious that a nucleation process occurs in the reduction process of the phosphate ion. From the potential minima the nucleation overpotentials for various applied current densities can be found. The minima appear earlier the higher the applied current density becomes. For the curves shown in Figure 5-22 the nucleation overpotential varies in the range of 6.7 to 4.6 mV with increasing current density. It is obvious that a nucleation process occurs at the tungsten electrode when aluminium orthophosphate is present in the melt. These results support the notion that the system is a soluble-insoluble one.

For the chronopotentiometric measurements the following results were obtained for 7·10^{-6} and 1.7·10^{-5} mole/cm^3 $AlPO_4$, as presented in Table 5-6. The transition times and the residual currents were determined as described in Section 5.4.2.

Table 5-6: *Chronopotentiometric data for $7 \cdot 10^{-6}$ and $1.7 \cdot 10^{-5}$ mole/cm^3 $AlPO_4$ added to an alumina-saturated cryolite melt.*

c ($AlPO_4$) [mol/cm^3]	i_o [mA/cm^2]	i_o-i_r [mA/cm^2]	Ű[s]	D [cm^2/s] $\cdot 10^5$
$7 \cdot 10^{-6}$	-4.84	-3.64	2.694	2.5
	-5.65	-4.45	1.643	2.3
	-6.45	-5.25	1.361	2.6
	-7.26	-6.06	0.945	2.4
$1.7 \cdot 10^{-5}$	-8.68	-6.76	1.986	1.5
	-13.02	-11.10	1.776	2.9
	-10.85	-8.93	1.258	1.3
	-15.19	-13.27	0.879	2.0

Average diffusion coefficients of $(1.9 \pm 0.6) \cdot 10^{-5}$ cm^2/s and $(2.5 \pm 0.1) \cdot 10^{-5}$ cm^2/s for $7 \cdot 10^{-6}$ and $1.7 \cdot 10^{-5}$ mole/cm^3 $AlPO_4$ are calculated from the results in Table 5-6.

Chronoamperometry

Chronoamperometry was applied to determine the diffusion coefficient for the orthophosphate ion. The measured curves revealed, as the results from the chronopotentiometry, that a nucleation process takes place when the orthophosphate is reduced. Chronoamperometric curves with different applied potentials were obtained with a tungsten working electrode, as shown in Figure 5-23. The concentration of aluminium orthophosphate present in the melt was $1.7 \cdot 10^{-5}$ mole/cm^3.

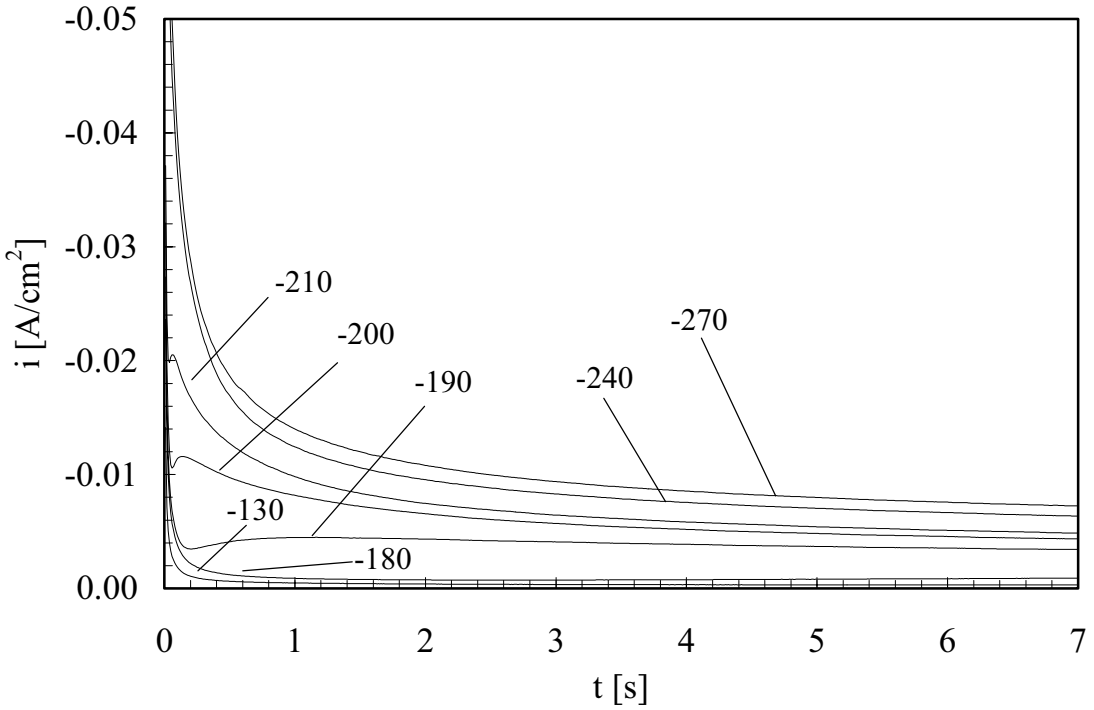

Fig. 5-23: *Potentiostatic current transients on a tungsten electrode at 1000 ºC. The potentials applied with respect to the open circuit potential (~ 895 mV) in mV are indicated in the figure, $c(AlPO_4) = 1.7 \cdot 10^{-5}$ mole/cm^3 in Na_3AlF_6-$Al_2O_{3(sat.)}$ melt.*

With increasing overpotential the height of the current maximum increases, and it shifts towards shorter times. At long times, the chronoamperometric curves approach the limiting current due to diffusion. By plotting the current density i versus the inverse square root of the time t, a curve should be obtained, containing a linear part. For this linear part the slope can be determined by linear regression, as shown in Figure 5-24. Assuming that the limiting current density is reached, the diffusion coefficient can be calculated from the slope according to the Cottrell equation (equation (3.26)).

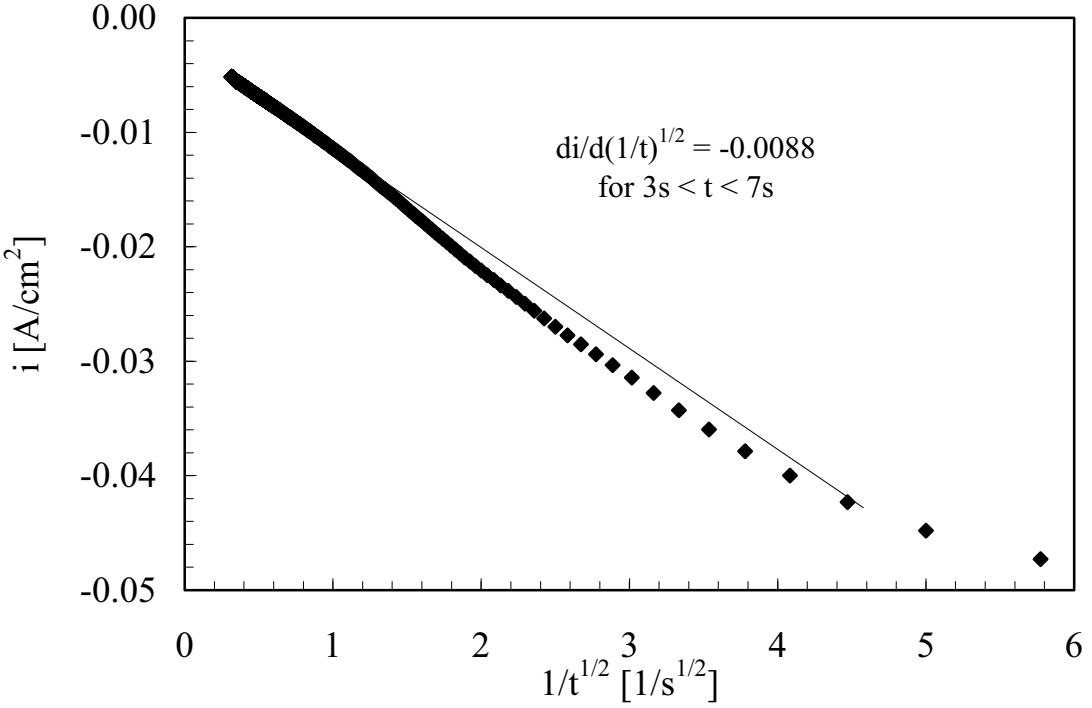

Fig. 5-24: *Plot of i versus $1/t^{1/2}$; the linear part of the curve represents the Cottrell equation, applied potential -250 mV with respect to the OCP.*

From the slopes of curves like in Figure 5-24 for each measurement at a certain applied potential, the diffusion coefficient can be determined, as presented in Table 5-7 under the assumption that limiting conditions are reached.

Table 5-7*: Data and diffusion coefficients derived by determining the slopes from i versus $(1/t)^{1/2}$ plots, $1.75 \cdot 10^{-5}$ mole /cm^3 $AlPO_4$, n = 2.*

Applied potential versus OCP [mV]	$i \cdot t^{1/2}$ [mA·s$^{1/2}$·cm^{-2}]	D [cm^2/s] · 10^5
-240	-8.8	1.7
-250	-8.8	2.1
-260	-10.0	2.1
-270	-9.7	2.6
-280	-10.2	2.9
-300	-10.7	3.1
-320	-8.5	1.9

From Table 5-7 the average diffusion coefficient determined by chronoamperometry is $(2.4 \cdot \pm\ 0.4) \cdot 10^{-5}$ cm^2/s.

Comparing the diffusion coefficients for the phosphate species determined by different electrochemical methods, we see that the diffusion coefficient calculated from chronoamperometric measurements (CA) is higher than for the other techniques.

Table 5-8: *Diffusion coefficients for $AlPO_4$ in cryolite-alumina melts at 1000 ºC determined by different methods.*

Method	c($AlPO_4$) [mole/cm^3] $\cdot 10^5$	D [cm^2/s] $\cdot 10^5$
CV	0.8	2.1 ± 0.4
	1.7	1.2 ± 0.2
	3.0	1.3 ± 0.2
CP	0.7	1.9 ± 0.6
	1.7	2.5 ± 0.1
CA	1.7	2.4 ± 0.4

It was confirmed by ICP-AES analysis that the actual concentration in the melt during the experiments corresponded to the added amount of $AlPO_4$.

Looking at Table 5-8, the diffusion coefficients obtained by CV are slightly lower than the ones measured for CP and CA. The formation of an insoluble product changes the effective area of the electrode. This effect is more likely to influence the results measured by the CP and CA methods. To determine the diffusion coefficient the CV method uses the peak current density, which is measured before any significant layer formation has occurred.

Recently, measurements with the AUTOLAB unit performed together with doctor student Martin Keppert supported the results concerning the formation of an insoluble phosphorus-containing product on a tungsten electrode. By applying a constant potential beyond the peak potential of peak P3 in Figure 5-19 at a tungsten electrode, an insoluble product should form at the electrode. Doubling the time period of applying the potential of + 0.4 V, should give twice the amount of the product, according to Faraday's law. This can be checked by running cyclic voltammetry toward

an anodic limit of + 1 V right after having applied the potential of + 0.4 V. The voltammograms obtained in this way are shown in Figure 5-25.

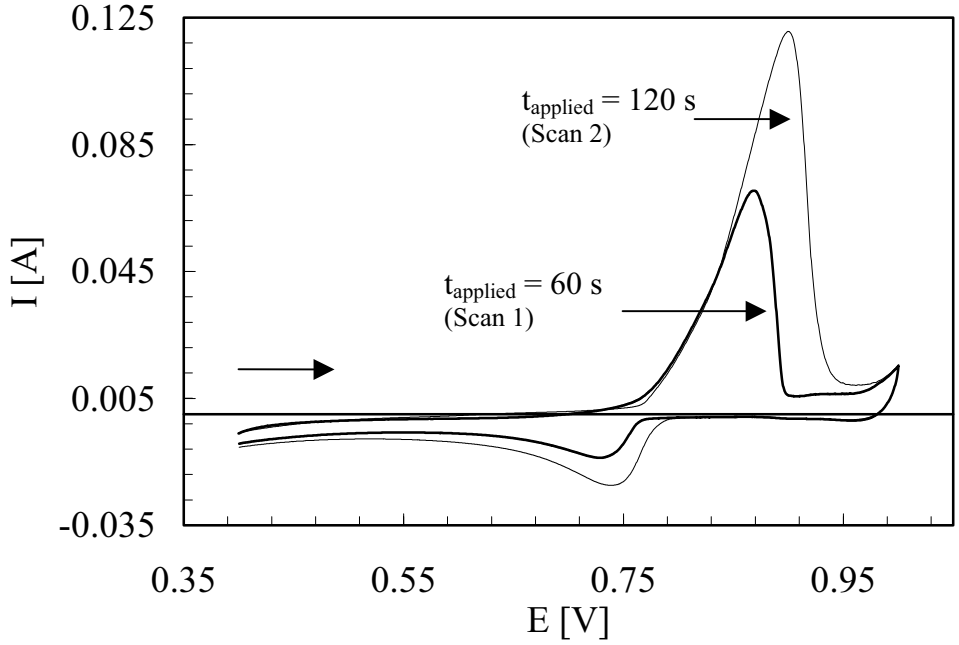

Fig. 5-25: *Voltammograms obtained after applying a potential of +0.4 V to the tungsten working electrode for different time intervals, ɜ = 0.05 V/s, T = 1020 ˚C, Electrodes: ref.: aluminium, counter: graphite.*

The amount of charge transferred during the anodic scan can be found be calculating the area under the oxidation peak P3'.

Table 5-9: *Experimental data obtained by analysing the voltammograms in Figure 5-25.*

	Scan 1	Scan 2	ratio
time [s] for applying potential before scan	60	120	2
anodic charge Q_a [C]	0.095	0.192	2

As can be seen from Table 5-9, the results shows that the amount of product oxidized is proportional to the time period for which the potential was applied. This confirms the assumption that an insoluble product is formed when reducing orthophosphate in an alumina-saturated cryolite melt.

5.4.4. The Na_3AlF_6-$AlPO_4$ system

The investigations of this system were performed with working electrodes of tungsten and copper. The voltammograms obtained with the tungsten electrode for different concentrations of $AlPO_4$ are shown in Figure 5-26. Both graphite and nickel were used as melt containers.

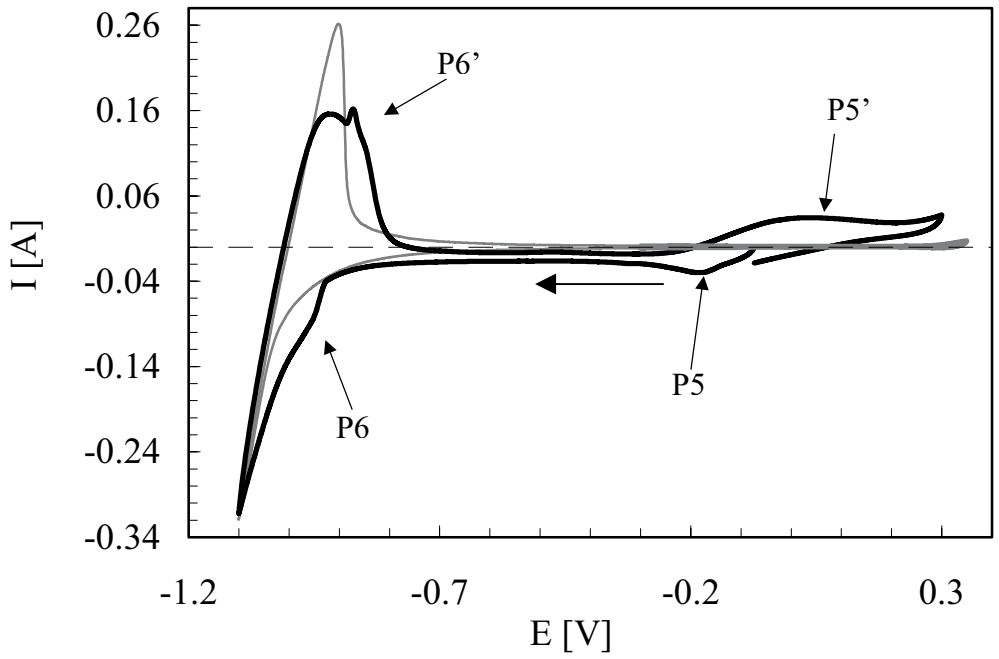

Fig. 5-26: *Voltammograms before (thin, grey curve) and after addition of 0.148 wt% $AlPO_4$ (bold, black curve) at 1020 °C, ʒ = 0.2 V/s; Electrodes: working: tungsten; ref.: platinum; counter: graphite.*

When adding aluminium orthophosphate to a pure cryolite melt two peak couples appear, P5/P5' and P6/P6'. The open circuit potential is found to be between peaks P5 and P5'. The shape of the peak couple P5/P5' was changed compared to the peak couple P3/P3' in the alumina-saturated cryolite melt with $AlPO_4$ addition. The oxidation peak P5' is similar in height to the reduction peak P5, which indicates that the system is soluble-soluble for this melt. The peak couple P6/P6' indicates a further reduction-oxidation process of the phosphorus species present in the melt.

The peak couple P6/P6' was observed in more detail by changing the cathodic limit in steps of 10 mV for each scan, as shown in Figure 5-27. A

square wave voltammogram at 20 Hz is shown as well to emphasize the reduction peak P6.

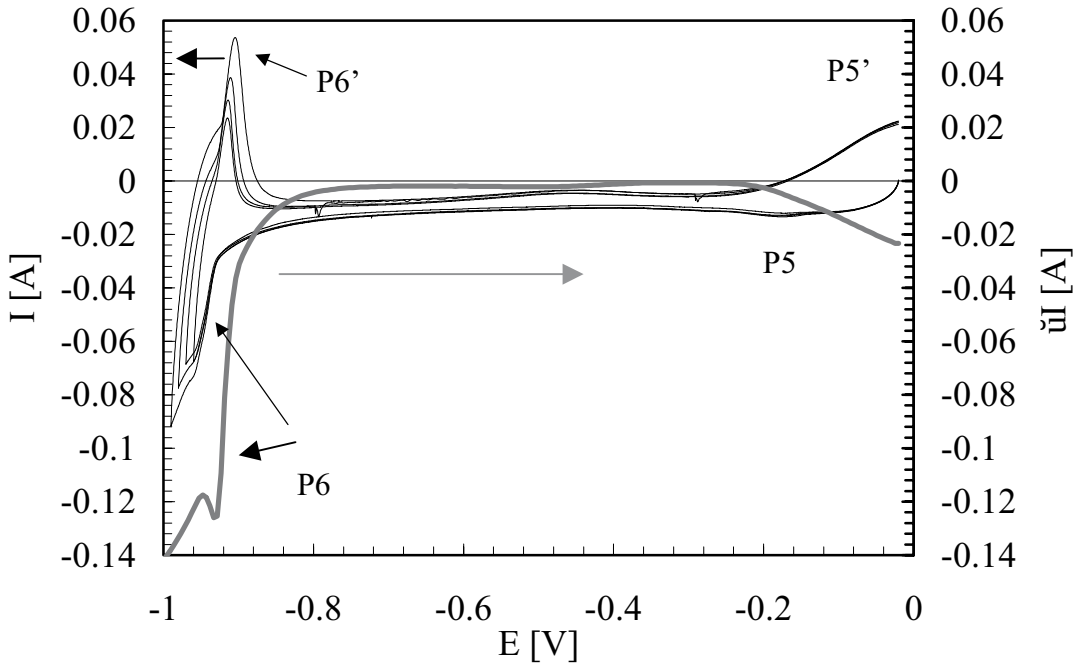

Fig. 5-27: *Cyclic voltammograms with different cathodic limits (black) and a square wave voltammogram at 20 Hz (grey) identifying the peak couple P6/P6' and peak P6 respectively, 0.072 wt% $AlPO_4$ added to a cryolite melt.*

The reaction mechanism behind the peak couple P6/P6' is not well understood. The cathodic wave can be assumed to be due to a further reduction of a phosphorus species evolving from the former reduction at peak P5.

The peak couple P5/P5' was investigated more closely for different additions of aluminium orthophosphate. In Figure 5-26 this peak couple appears to be a soluble-soluble system, but as we can see from Figure 5-28, it actually consists of two separate peak couples. As the concentration of the orthophosphate increases in the melt, the capacitive current increases correspondingly at the beginning of the scan. Of the two reduction peaks, P5a and P5b, the former grows the higher the phosphate concentration becomes.

In Figure 5-26, where the added amount of $AlPO_4$, was higher than in Figure 5-28, the peak P5a covers the peak P5b completely. The same occurs for the oxidations peaks in that P5a' covers P5b' entirely. The peak couple appears to have a shape of a soluble-soluble system.

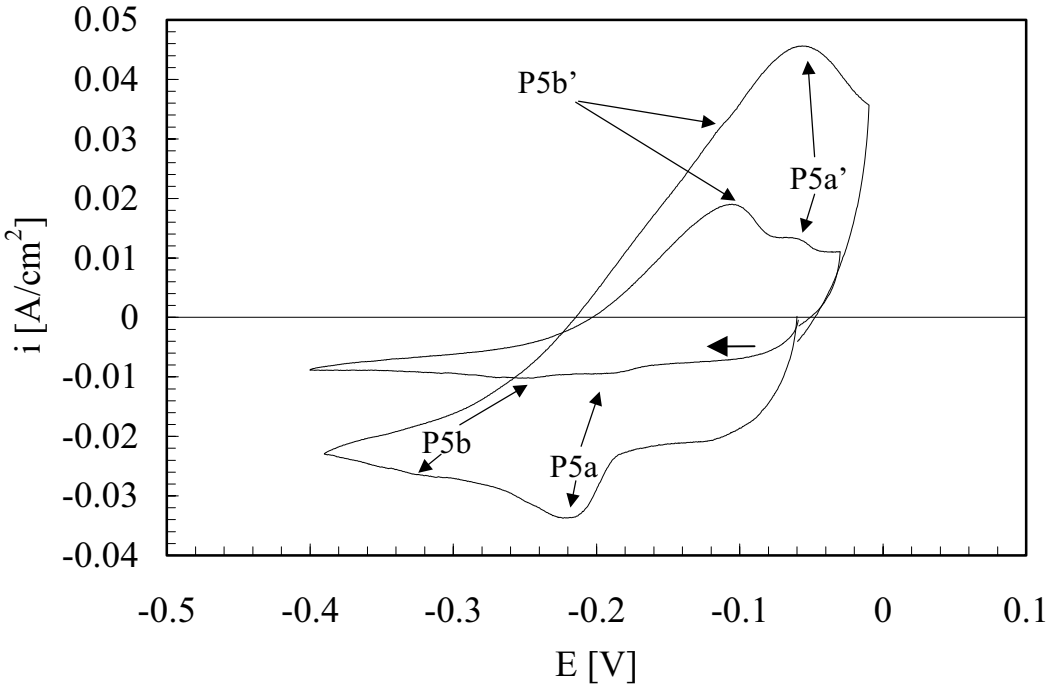

***Fig. 5-28**: Voltammograms of peak couple P5/P5' from Figure 5-26 at two different concentrations, 0.022 and 0.072 wt% $AlPO_4$ present in the melt, ɜ = 0.2 V/s, T = 1020 ˚C, Electrode: working: tungsten; ref.: platinum.*

For a similar experiment the peak couples P5a/P5a' and P5b/P5b' are shown in Figure 5-29 at different sweep rates. From Figure 5-29 it can clearly be seen that for a pure cryolite melt the reduction of phosphate seems to be different from the alumina-saturated melt. Comparing alumina-free and alumina-saturated melts with additions of aluminium phosphate is difficult, since the tungsten working electrode seems to be influenced by the presence of oxides. Figure 5-30 shows the phosphate reduction peaks without and in the presence of alumina in the cryolite melt. The potentials are shifted for the alumina-free melt according to the deposition potential for aluminium, which occurs with a platinum reference electrode at -1.1 V.

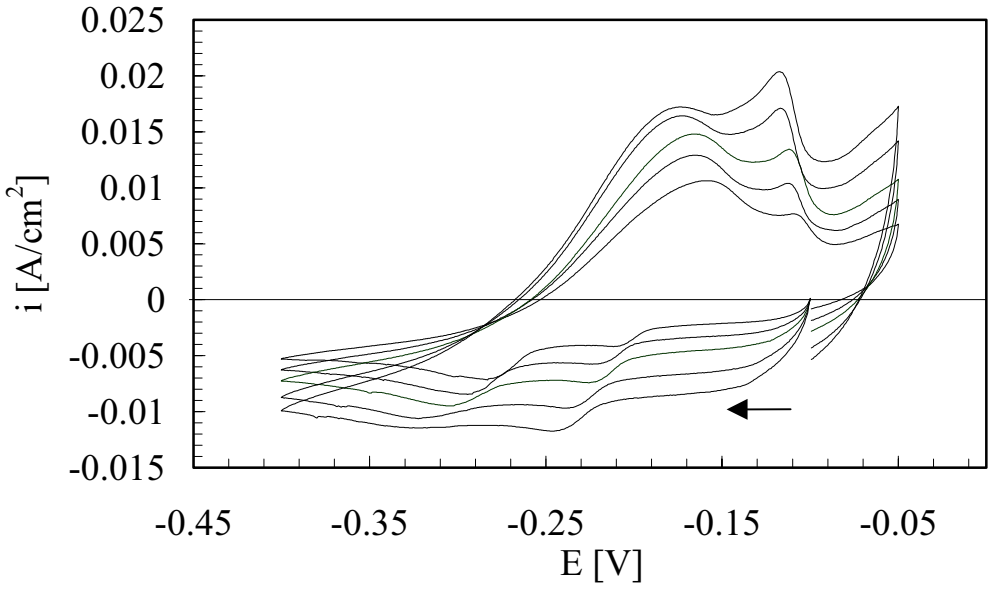

Fig. 5-29: *Voltammograms of peak couples P5a and P5b at different sweep rates (0.175, 0.3, 0.45, 0.7, 0.95 V/s), T = 1020 ˚C, 0.044 wt% $AlPO_4$ added; Electrodes: working: tungsten; ref.: platinum.*

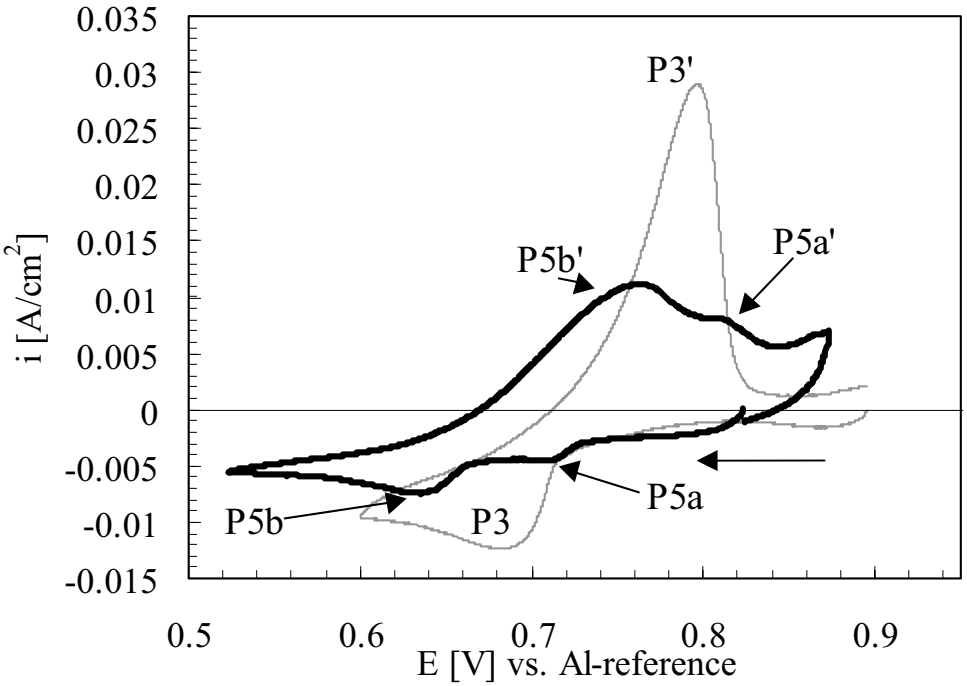

Fig. 5-30: *Comparison of phosphate reduction in pure cryolite (black curve, 0.044 wt% $AlPO_4$ added) and alumina-saturated cryolite melts (grey curve, 0.043 wt% $AlPO_4$ added), potentials from pure cryolite melt adjusted accordingly, ɜ = 0.2 V/s, T = 1020 ºC.*

There are two possible explanations for the appearance of the two peaks, P5a and P5b.

Under the assumption that the peak couples are soluble-soluble, the number of electrons can be estimated from the difference between the cathodic and anodic peak potentials, which is 2 in both cases (P5a/P5a' and P5b/P5b'). The reduction product of the penta-valent phosphorus species might not get stabilized as it might be the case for an alumina-saturated melt. Therefore, a further reduction was assumed to monovalent phosphorus species. The phosphorus species in the start was assumed to be metaphosphate coming from the equilibrium between ortho- and metaphosphate (reaction (4.14)),

Peak 5a $$PO_3^4 \; 2 \; 2e^4 \Downarrow PO_2^4 \; 2 \; O^{24} \qquad (5.1)$$

Peak 5b $$PO_2^4 \; 2 \; 2e^4 \Downarrow PO^4 \; 2 \; O^{24} \qquad (5.2)$$

As mentioned in Section 2.1.3., the existence of the species PO_2^- is not known in aqueous solutions, which does not exclude the existence of it in a salt melt. However, another mechanism might be possible as well, involving the following species,

$$PO_3^4 \; 2 \; 2e^4 \Downarrow PO_3^{34} \qquad (5.3)$$

$$PO_3^{34} \; 2 \; 2e^4 \Downarrow PO^4 \; 2 \; 2O^{24} \qquad (5.4)$$

The second hypothesis to explain the appearance of peaks P5a and P5b is based on the findings from the cryoscopic measurements, where both the orthophosphate and the metaphosphate were assumed to be existing in an equilibrium (see Chapter 4) and both are reducible species. It might, therefore, be possible that both the meta- and orthophosphate are reduced.

Peak 5a $$PO_4^{34} \; 2 \; 2e^4 \Downarrow PO_3^{34} \; 2 \; O^{24} \qquad (5.5)$$

Peak 5b $$PO_3^4 \; 2 \; 2e^4 \Downarrow PO_3^{34} \qquad (5.6)$$

Regardless which explanation might give the best fit for the results obtained, the oxide ion from the equilibrium $PO_4^{34} \; \Diamond \; PO_3^4 \; 2 \; O^{24}$ is

assumed to be responsible for the background current in the start of the scan. An oxide layer may form on the tungsten electrode surface. With increasing concentration this background current increases, as shown in Figure 5-28. The reaction happening at peak P5a is more pronounced at higher concentration, and it appears as if mainly this process contributes to the current signal, shown in Figure 5-31.

The shape of the voltammograms shown in Figure 5-31 resembles the typical shape of a soluble-soluble system. The criterion of reversibility demanding that the peak potential is independent of the sweep rate, is followed from 0.15 V/s up to 5 V/s.

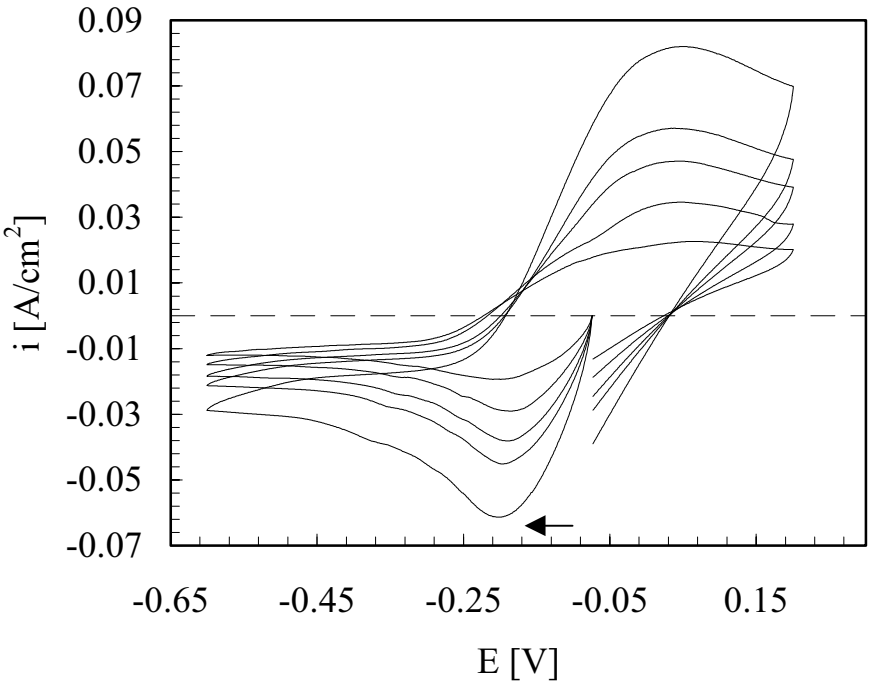

Fig. 5-31: *Voltammograms of peak system P5/P5' after addition of 0.148 wt% $AlPO_4$ to a pure cryolite melt. Sweep rates presented: 0.2, 0.4, 0.7, 1.0 and 2.0 V/s, T = 1020 ˚C, Electrodes: working: tungsten; ref.: platinum.*

When plotting the cathodic peak current density versus the square root of the sweep rate for the curves presented in Figure 5-31, the following figure is obtained.

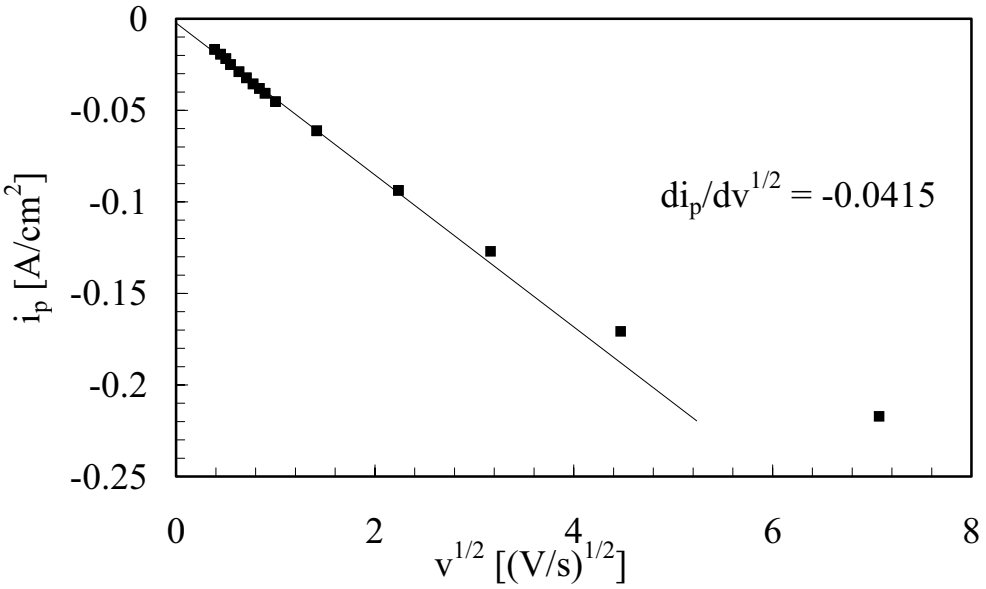

Fig. 5-32: *Plot of cathodic i_p versus $з^{1/2}$ for 0.148wt% $AlPO_4$ added to cryolite.*

The diffusion coefficient can be found from the slope when applying the Randles-Sevļik equation for a soluble-soluble system. The diffusion coefficient of the species investigated is found to be $(2.2 \pm 0.4)\cdot10^{-5}$ cm^2/s. For lower concentrations of $AlPO_4$ the diffusion coefficient was calculated for the first reduction peak P5a by subtracting the background current preceding peak P5a (as shown in Figure 5-29). At 0.044 wt% the diffusion coefficient was found to be $(1.9 \pm 0.3)\cdot10^{-5}$ cm^2/s. Under the assumption that the diffusion coefficients obtained for different concentrations are related to the same process, these values are in reasonable agreement with each other. The error estimate for the diffusion coefficient was made as shown in Section 5.4.2..

Similar investigations were performed with a copper wire as working electrode. Figure 5-33 shows the system before and after addition of 0.072 wt% $AlPO_4$ to a pure cryolite melt.

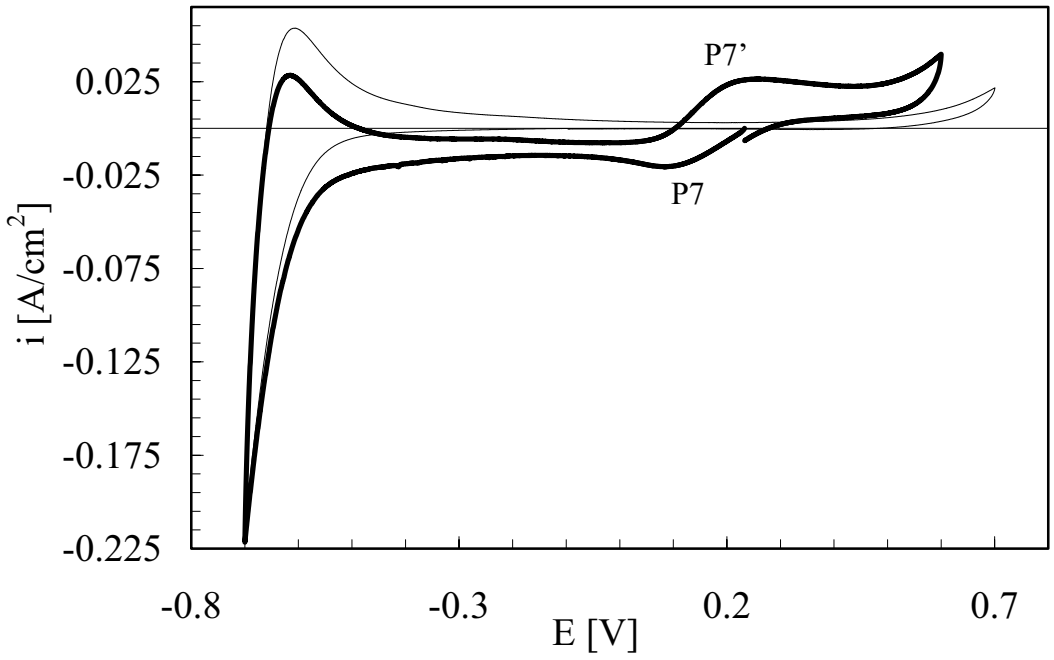

***Fig. 5-33**: Voltammograms in pure cryolite before (thin curve) and after addition of 0.072 wt% $AlPO_4$ (thick curve) with a copper working electrode, T = 1020 ºC, з = 0.2 V/s, ref. electrodes: platinum.*

For a copper working electrode only one peak couple is observed after addition of $AlPO_4$ to the cryolite melt, having the shape of a soluble-soluble system. The peak couple P7 was investigated at different sweep rates, for which some of the obtained curves are shown in Figure 5-34.

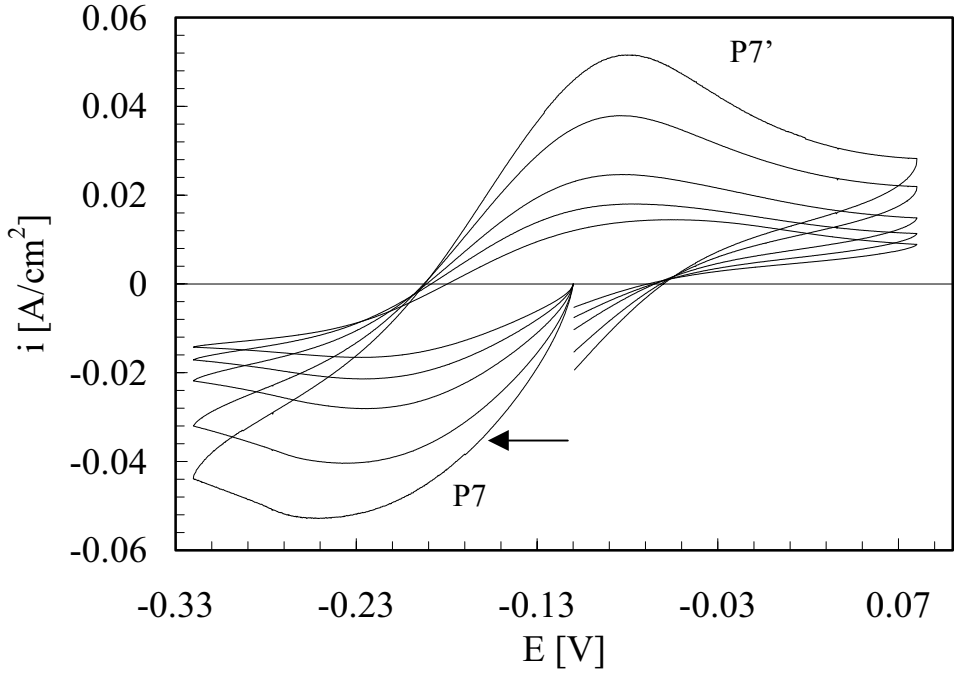

Fig. 5-34: *Voltammograms of the system $Na_3AlF_6 - AlPO_4$ at a copper electrode with different sweep rates (0.1, 0.2, 0.4, 1.0 and 2.0 V/s), 0.072 wt% $AlPO_4$, T = 1020 °C.*

Table 5-10: *Data obtained by analysing voltammograms of peak couple P7 from Figure 5-34 for different sweep rates.*

ν [V/s]	i_p^c [A/cm^2]	E_p^c [V]	$E_{p/2}^c$ [V]	n
0.05	-0.013	-0.239	-0.145	2.7
0.1	-0.016	-0.229	-0.142	2.9
0.2	-0.022	-0.225	-0.140	3.0
0.4	-0.029	-0.229	-0.139	2.9
0.6	-0.033	-0.231	-0.139	2.8
0.8	-0.037	-0.233	-0.139	2.7
1	-0.041	-0.239	-0.140	2.6
2	-0.053	-0.253	-0.143	2.3
5	-0.081	-0.272	-0.150	2.1

The number of electrons transferred was calculated by using the difference between the peak and half peak potentials. The average number of electrons was determined to be 3 from the data in Table 5-10. A plot of the cathodic peak current versus the square root of the sweep rate is shown in Figure 5-35.

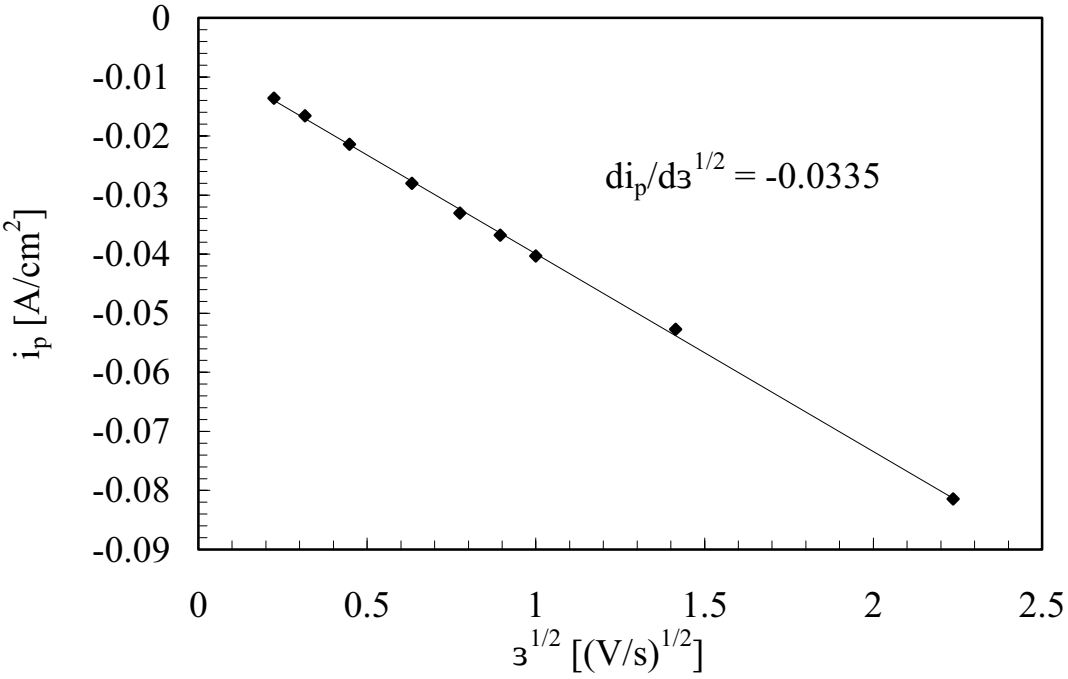

Fig. 5-35: *Plot of peak current versus square root of the sweep rate for reduction peak P7 from Figure 5-34.*

The added amount of 0.072 wt% $AlPO_4$ is equal to $1.24 \cdot 10^{-5}$ mole/cm^3 $AlPO_4$. From the slope of Figure 5-34, the diffusion coefficient of the phosphate species can be calculated using the Randles-Sevļik equation for soluble-soluble systems. The diffusion coefficient was found to be $(1.6 \pm 0.3) \cdot 10^{-5}$ cm^2/s at 1020 ºC. For a higher concentration ($2.53 \cdot 10^{-5}$ mole/cm^3 $AlPO_4$) the diffusion coefficient was found to be $(1.8 \pm 0.3) \cdot 10^{-5}$ cm^2/s at 1020 ºC. The error estimate for the diffusion coefficients was done as described in Section 5.4.2.

From the investigations presented it can be concluded that the mechanism of phosphate reduction is dependent on the concentration (for the tungsten working electrode) and the type of working electrode. The reactions occuring can be summarized as follows:

Tungsten electrode $P(V) + 2e^- \rightarrow P(III)$ (5.7)

for low phosphate concentrations a second reduction peak is visible
(I) $P(V) + 2e^- \rightarrow P(III)$ (5.8)
(II) $P(III) + 2e^- \rightarrow P(I)$

For the copper electrode $P(V) + 3e^- \rightarrow P(II)$ (5.9)

While for the tungsten substrate a further reduction peak couple due to phosphate was observed; with the copper working electrode no further reduction peak was observed. This might be due to the limitation set by the electrochemical window, since alloy formation between aluminium and copper occurs. With a copper working electrode, the potential to reduce phosphorus further cannot be reached. The diffusion coefficients of P(V) species obtained using the two different electrode materials are,

Electrode	concentration $AlPO_4$ [mole/cm^3]	D [cm^2/s] $\cdot 10^5$
Tungsten	$1.18 \cdot 10^{-5}$	1.9 ± 0.3
	$2.41 \cdot 10^{-5}$	2.2 ± 0.4
Copper	$1.24 \cdot 10^{-5}$	1.6 ± 0.3
	$2.53 \cdot 10^{-5}$	1.8 ± 0.3

The diffusion coefficients obtained are in good agreement with each other regardless of the electrode material.

5.4.5. The $NaF\text{-}Na_3PO_4$ system

In Section 5.4.2. to 5.4.4. no further reduction of phosphorus to lower valent species than P(I) was observed. The deposition of aluminium in those systems might cover the current signal of a further reduction process involving phosphorus. Since sodium deposits at a more cathodic potential than aluminium, it seemed reasonable to try the pure sodium fluoride melt as solvent with additions of sodium orthophosphate. Thereby it might be possible to detect processes due to phosphorus reduction, which were not able to see in a melt containing aluminium ions.

The electrochemical behaviour of Na_3PO_4, and i.e. P(V), in a sodium fluoride melt was investigated by cyclic voltammetry (CV) and square wave voltammetry (SQWV). As working electrode a tungsten wire was used in all experiments, while the counter electrode either consisted of a platinum wire or the nickel crucible.

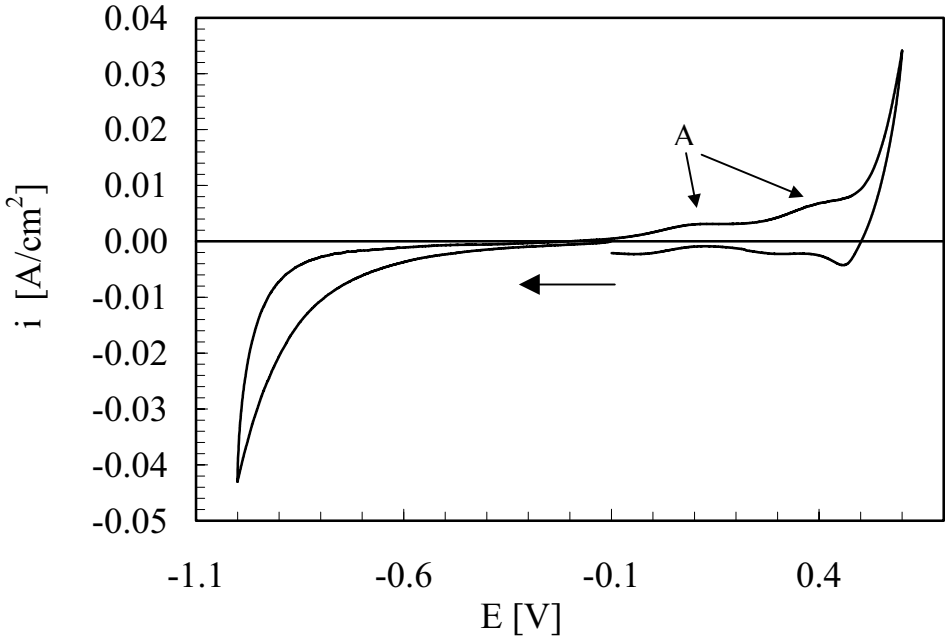

Fig. 5-36: *Cyclic voltammogram at a tungsten electrode in molten sodium fluoride at 1005 °C, v = 0.2 V/s, reference electrode: platinum. Arrow shows scan direction.*

A voltammogram obtained in NaF before addition of Na_3PO_4 is presented in Figure 5-36. A platinum wire was used as reference electrode. The potential sweep was started from the open circuit potential. The cathodic current increased slowly with decreasing potential until a distinct increase

in current was observed due to the formation of sodium at the tungsten electrode. Since the temperature of the melt is well above the boiling temperature of sodium (883 ºC), the reduction of the sodium ions will produce gaseous sodium or sodium dissolved in sodium fluoride. No typical stripping peak for an oxidation of a metal deposit can therefore be detected after reversing the potential. The deposited sodium apparently dissolves in the electrolyte.

The waves named A on the reverse sweep are most likely oxidation peaks due to the formation of tungsten oxides from the tungsten electrode, which may dissolve in the sodium fluoride. Since the sodium fluoride used was not purified by re-crystallisation, a certain amount of oxide impurities might be present. The dissolution of the tungsten electrode is responsible for the current increase at the anodic limit of the voltammogram. The melt used in the next figure was not the same as the one shown in Figure 5-36. The initial oxide concentration of the sodium fluoride apparently was not the same, the oxidation peaks are, therefore, different.

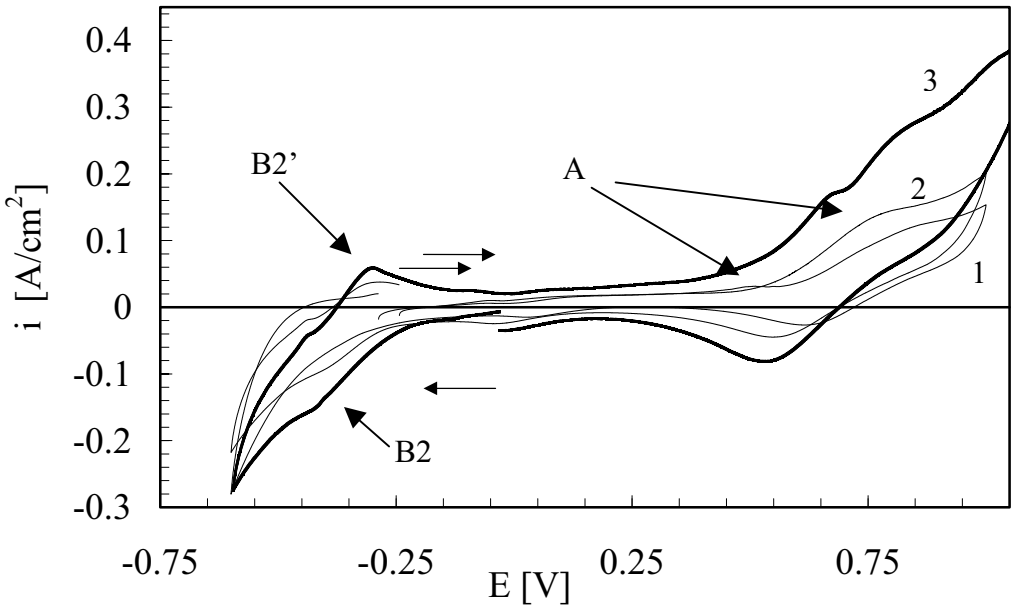

Fig. 5-37: *Cyclic voltammogram on a tungsten electrode in sodium fluoride at 1000 ºC before addition of Na_3PO_4 (curve 1) and after addition of 0.072 wt% (curve 2) and 0.167 wt% Na_3PO_4 (curve 3) , sweep rate v = 0.2 V/s, ref. electrode: tungsten. Arrows show sweep direction.*

Figure 5-37 shows the change in the current signal when sodium orthophosphate was added to NaF. It can clearly be seen that the assumed oxide peak A increases and a new peak couple appears at about –0.4 V on the cathodic side (B2) and at –0.28 V on the anodic side (B2').

Since sodium orthophosphate was added, the following dissociation reaction can be assumed,

$$Na_3PO_4 \Downarrow\!\!\!\!\leftarrow NaPO_3\ 2\ Na_2O \qquad (5.10),$$

which might explain an increase in the oxide peak current A. The peak couple B2/B2' may represent the reduction and oxidation of the metaphosphate ion, PO_3^-. An investigation of the peak couple B2/B2' at different sweep rates is presented in Figure 5-38.

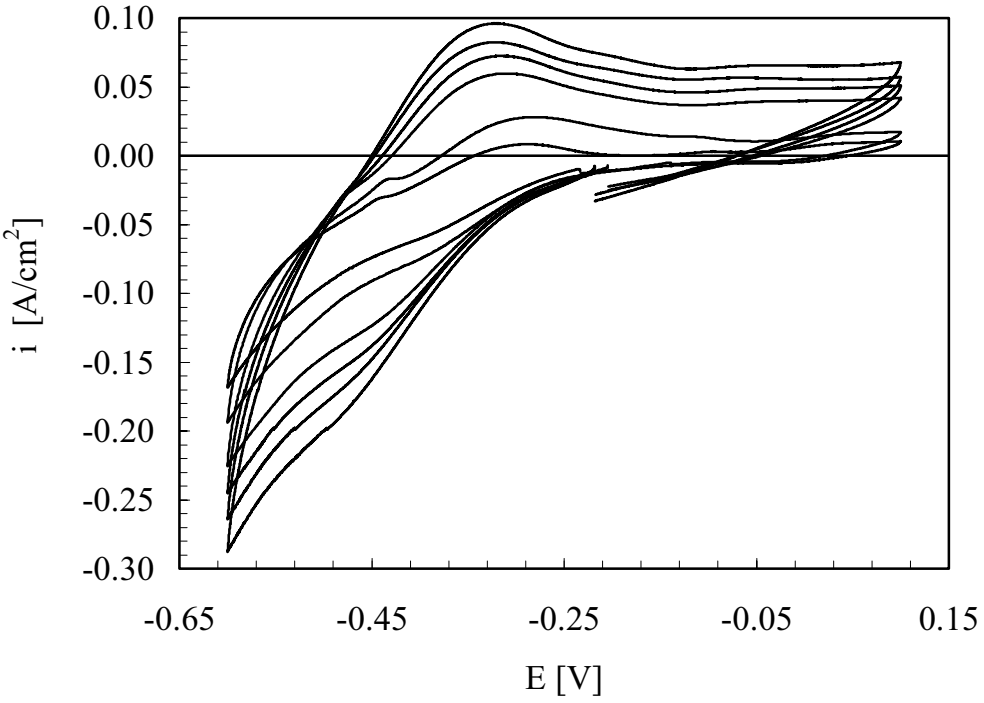

Fig. 5-38: *Cyclic voltammograms on a tungsten electrode in sodium fluoride at 1000 °C when 0.072 wt% of Na_3PO_4 was added (v = 0.075, 0.15, 0.45, 0.65, 0.9 and 1.2 V/s), ref. electrode: tungsten.*

The cathodic peak current was not well developed, but the second derivative of the current function with respect to the potentials was determined. The maximum of the second derivative in the range of –0.3 to

–0.55 V revealed the peak potential for the peak under investigation. Therefrom the peak current could be determined.

The plot of i_p versus $\tau^{1/2}$ for the cathodic peak gave a straight line, as shown in Figure 5-39.

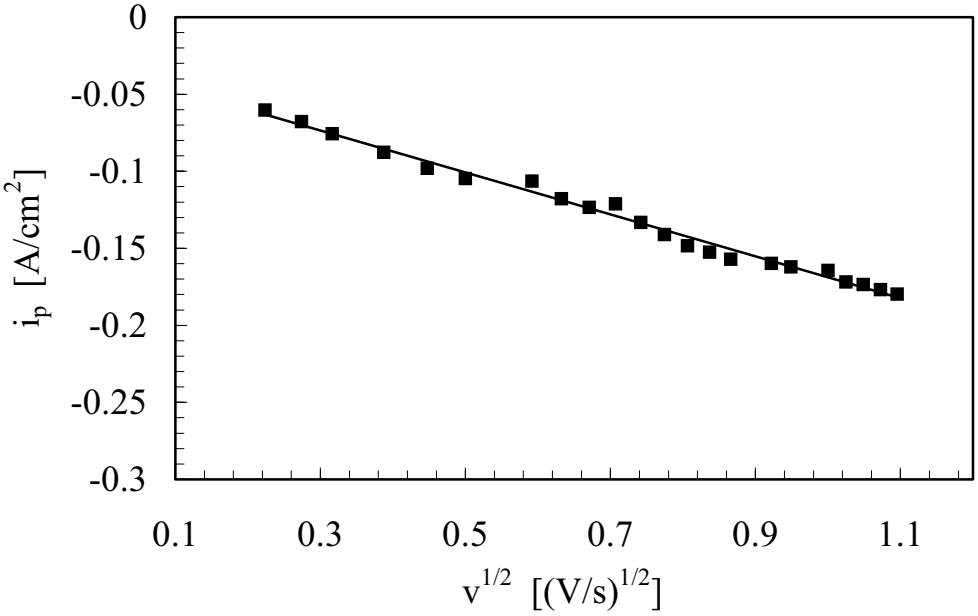

Fig. 5-39: *Plot of cathodic peak current for peak B2 versus the square root of the sweep rate, according to Figure 5-38.*

A straight line was also obtained for the better defined anodic peak current of the peak B2'. This indicates that the mass transport in this system is diffusion controlled. More information about the reversibility of systems was obtained by SQWV. Figure 5-40 shows potential sweeps at different frequencies for the peak B2.

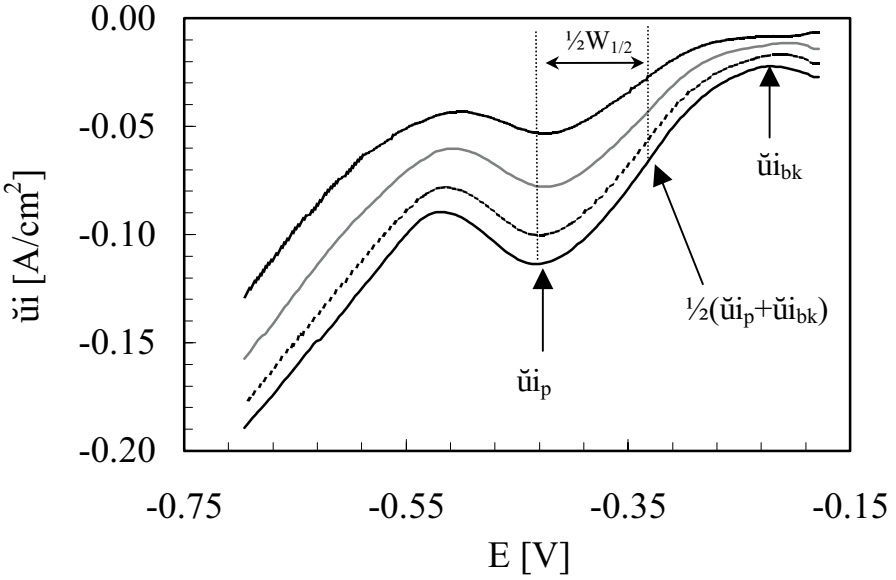

Fig. 5-40: *Square wave voltammograms at different frequencies for the cathodic peak B2, f = 8, 20, 40 and 60 Hz.*

A plot of the peak current $ŭi_p$ versus $f^{1/2}$ gives a straight line, as shown in Figure 5-41. This indicates that the system is reversible. By assuming that we are dealing with a soluble-soluble system, the half height potential width, $W_{1/2}$, might yield the number of electrons involved in the reduction process.

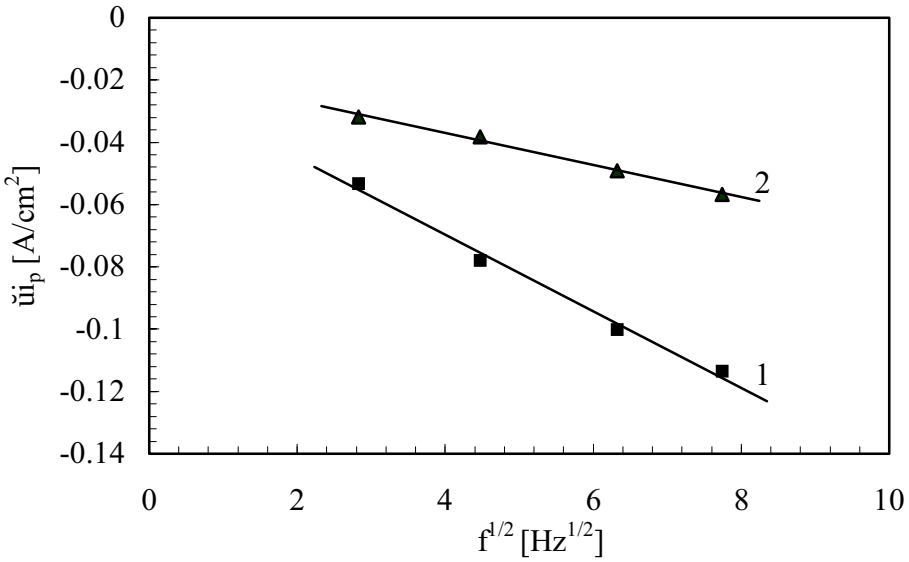

Fig. 5-41: *Plot of the differential peak current versus the square root of the frequency from Fig. 5-39. Line 2 is corrected for the background current for each frequency.*

The peaks obtained in Figure 5-40 do not have similar bell shapes, as shown in the theoretical treatment of the SQWV (Figure 3-4), since they are superimposed on the signal for sodium deposition. The values of $W_{1/2}$ at each frequency, shown in Table 5-1, was, therefore, determined as indicated in Figure 5-40.

Table 5-11: *Square wave voltammetric data for the reduction peak B2 at 1000 ºC, as shown in Figure 5-40.*

f [Hz]	$W_{1/2}$ [V]	n
8	0.176	2.2
20	0.186	2.1
40	0.206	1.9
60	0.196	2.0

The number of electrons was determined to be 2. This was also confirmed by measurements at higher concentrations of Na_3PO_4 added.

When comparing the results from SQWV with CV measurements, the criterion of the difference in peak potential of the cathodic and anodic peaks for a soluble-soluble system, it confirms that two electrons are transferred.

In Figure 5-42 the oxidation peak A is shown at different sweep rates after addition of 0.072 wt% Na_3PO_4 to a NaF melt. The anodic peaks are somewhat ill-defined with shapes like stationary curves. Determining the approximate anodic peak current for each sweep rate, a plot of i_p^a versus $\nu^{1/2}$ yielded a straight line.

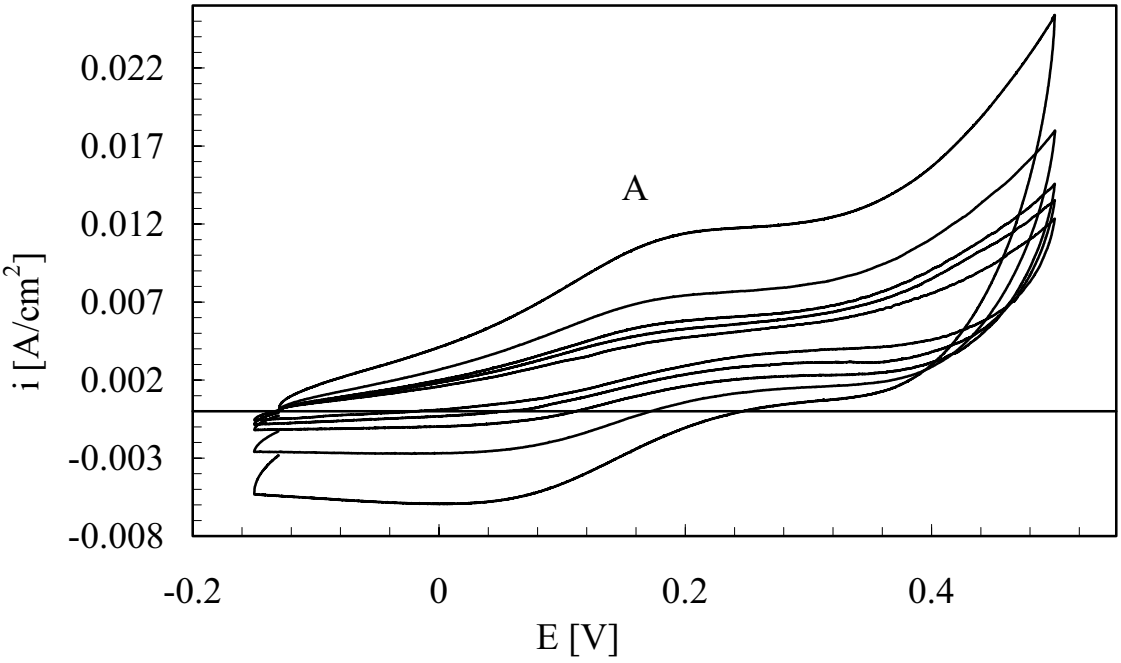

Fig. 5-42: *Cyclic voltammograms at different sweep rates (0.05, 0.075, 0.1, 0.2 and 0.5 V/s) for the peak couple of the oxidation and reduction at T = 1002 ºC in a NaF melt with 0.072 wt% Na_3PO_4 added.*

The peak potential and the respective peak current were determined as described before by calculating the second derivative of the current function with respect to the potential. The maximum of the function in the potential range from 0.1 to 0.3 V gave the peak potential of the peak A.

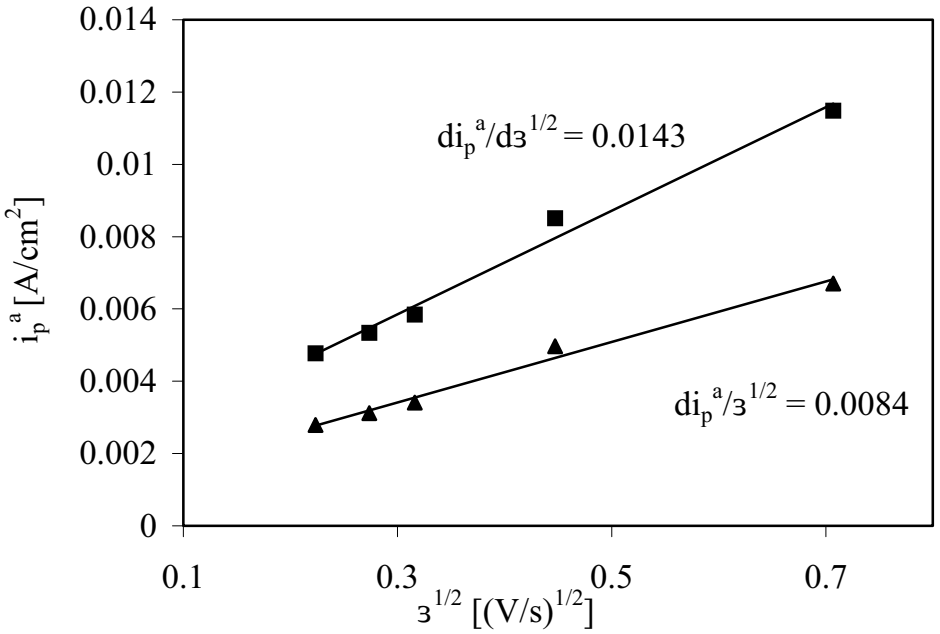

Fig. 5-43: *Plot of anodic peak current versus square root of sweep rates without background current correction (squares) and with background current correction (triangles).*

By adding more Na_3PO_4 the anodic peak current increased linearly, as can be seen in Figure 5-44. This is again an substantiation that the increase of the oxide peak A is related to the orthophosphate added.

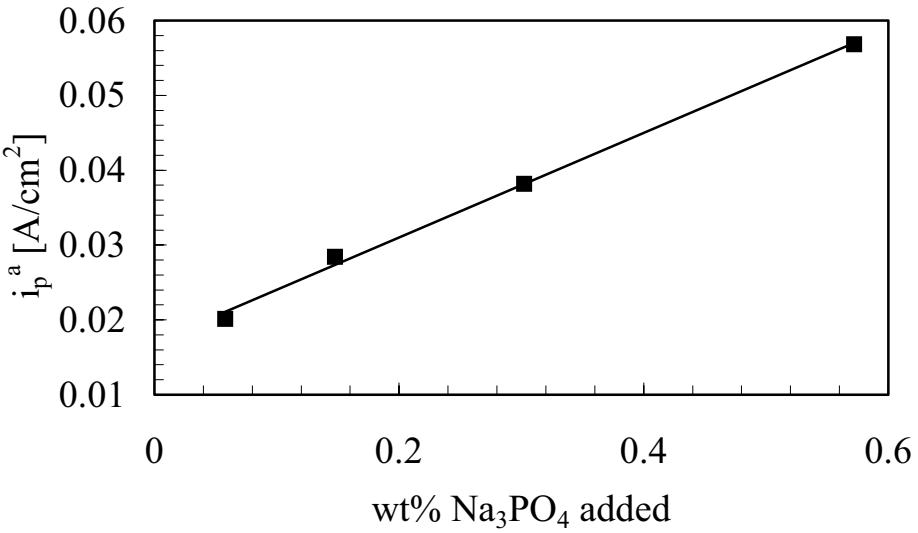

Fig. 5-44: *Anodic peak current versus added amount of sodium orthophosphate, all peak currents determined for з = 0.2 V/s; T = 1000 ºC.*

The number of electrons for this peak couple is determined by the difference in the cathodic and anodic peak potentials obtained by cyclic voltammetry. Since the peaks are not well defined, the obtained electron number may just be seen as an approximation, but it turns out to be equal to 1. The reaction can be assumed to proceed as follows:

$$O^{24} \quad 2 \quad W \quad \Downarrow \quad WO^{4} \quad 2 \quad e^{4} \tag{5.11}$$

According to this reaction a soluble tungsten oxide ion is formed. The process is controlled by the diffusion of the oxide ions towards the tungsten electrode. For a soluble-soluble system, the equation of Randles-Sevļik for the peak current (equation 3.14) will yield a diffusion coefficient for the species O^{2-} in a sodium fluoride melt at 1000 ºC. Results from two separate experiments are presented in Table 5-12.

***Table 5-12**: Experimental data and resulting diffusion coefficients by investigation of the peak couple presented in Figure 5-42.*

T [ºC]	slope i_p^a vs. з$^{1/2}$ [AŢs$^{1/2}$/(V$^{1/2}$Ţcm^2)]	c (O^{2-}) [mole/cm^3]	D [cm^2/s] Ţ10^5
1002	0.00835	1.147Ţ10^{-5}	3.2 ± 0.5
1005	0.07595	6.827Ţ10^{-5}	7.4 ± 0.5

The resulting diffusion coefficient of Figure 5-43 for the data corrected for the background current are presented in the first row of Table 5-12. The concentration of the O^{2-} species was calculated according to reaction (5.10) assuming that sodium orthophosphate dissociates completely after addition.

The results were compared with a diffusion coefficient for O^{2-} calculated by the Stokes-Einstein equation [5]

$$D \mid \frac{k_B \, \text{ſ} T}{6 \, \text{ſ} \phi \, \text{ſ} r_i \, \text{ſ} \xi} \tag{5.12},$$

where k_B is the Boltzmann constant, r_i is the radius of the ion and ą is the viscosity of the electrolyte. The viscosity of sodium fluoride at 1000 ºC can be calculated from an equation due to Brockner et al. [6], and was found to be 1.46 mPa·s. With a radius of 140 pm for the O^{2-} species [7], the diffusion coefficient was determined to be 4.6Ţ10^{-5} cm^2/s. Comparing the calculated diffusion coefficient and the experimentally determined values,

it can be seen that the experimental values lies close to the calculated diffusion coefficient. We may, therefore, draw the conclusion that the current response of the system (peak A) is controlled by the diffusion of the O^{2-} species originating from the added sodium orthophosphate.

It should be mentioned that for both diffusion coefficients presented in Table 5-12, the change in sweep rate when determining the slope covered only one order of magnitude. In the literature it is claimed that results should be obtained over a wider range of sweep rates, preferably two orders of magnitude [8].

The results obtained can be interpreted as if a dissociation reaction takes places when sodium orthophosphate is added to sodium fluoride. The assumed new species are $NaPO_3$ and Na_2O. The increase of the oxide concentration can be related to the increase of the anodic current of peak A (see Figure 5-37).

Concerning the peak couple B2/B2', the two-electron transfer steps might be related to a reduction of a phosphorus compound, which according to reaction (5.10), can be PO_3^-. However, it seems quite improbable that the reduction of a P(V) species would take place so far cathodic. The only visible reduction assumed to involve phosphorus included a two-electron step. Provided that a P(V) species is the reactant, a further reduction step for phosphorus could not be detected. This might lead to the conclusion that in a sodium fluoride melt the reduction of phosphorus towards its elemental state cannot be achieved before sodium is deposited.

However, as mentioned above, it seems odd that a penta-valent phosphorus species is reduced so close towards the deposition of sodium. Looking at the cryolite system, the reduction of the P(V)-containing ion took place some hundreds of mV before the reduction of aluminium (and sodium) occurred. This might indicate that the P(V)-containing ion is not stable in molten sodium fluoride. A chemical reaction between the components of the melt or a dissociation reaction of the metaphosphate might result in a lower valent phosphorus species, as for example:

$$^{2V}PO_3^4 \rightleftarrows {}^{2III}PO_2^4 \quad 2 \quad 1/2\,O_{2(g)} \tag{5.13}$$

or

$$^{2V}PO_3^4 \rightleftarrows {}^{2I}PO^4 \quad 2 \quad O_{2(g)} \tag{5.14}$$

as well as $\overset{2V}{P}O_3^{4} \Downarrow \overset{4I}{P}\ 2\ \ 3/2\ \ O_{2(g)}$ (5.15)

As pointed out in Section 2.1.3., the existence of the PO_2^- species is not known in aqueous solutions, which, nevertheless, does not exclude its existence in molten salts. All proposed dissociation reactions give a phosphorus species, which can be reduced in a process involving two electrons.

In terms of differences in the cryolite ratio in the bath of an industrial cell, local changes towards more basic melts with a high content of NaF might influence the behaviour of phosphorus.

References of Chapter 5:

[1] A. Kerouanton, J. Badoz-Lambling, *Comportment chimique et electrochimique de composes du phosphore dans la cryolithe fondue*., Revue de Chimie minerale, **11**, 223, 1974.

[2] L. Deininger and J. Gerlach, *Stromausbeutemessungen bei der Aluminiumoxidreduktionselektrolyse in Laboratoriumszellen,* Metall, **33**, 131, 1979.

[3] J.J. Duruz, G. Stehle, D. Landolt, *On the role of electrode material during cathodic deposition of sodium and aluminum from molten fluorides,* Electrochimica Acta, **26**(6), 771-779, 1981.

[4] Gmelin Handbook W, Suppl. Vol A 5a and references therein.

[5] K. Grjotheim, C. Krohn, M. Malinovsky, K. Matiasovsky, J. Thonstad, *Aluminium Electrolysis – Fundamentals of the Hall-Héroult Process*, 2nd edition, Aluminium-Verlag GmbH, Düsseldorf, Germany, 1982.

[6] J. Thonstad, P. Fellner, G.M. Haarberg J. Híveš, H. Kvande, Å. Sterten, *Aluminium Electrolysis – Fundamentals of the Hall-Héroult Process*, 3rd edition, Aluminium-Verlag GmbH, Düsseldorf, Germany, 2001.

[7] G.H. Aylward, T.J.V. Findlay, *SI chemical data*, 4th edition, John Wiley & Sons, 1998.

[8] D. Pletcher, R. Greef, R. Peat, L.M. Peter, J. Robinson, *Instrumental Methods in Electrochemistry*, Horwood publishing, Chichester, England, Chapter 1, 2001.

6. Behaviour of phosphorus compounds in industrial cells

6.1. Introduction

The interest in phosphorus and its behaviour in industrial cells became significant when hooded cells and dry scrubbing were introduced. The alumina from the dry scrubber was returned to the cell as feed, thereby recycling impurities carried by the off gases, including phosphorus. Numerous industrial studies were performed, as presented in Section 2.1.4.2., which gave an impression of the distribution of phosphorus between bath and metal and the distribution between bath and gas phase. The main reason for the interest in phosphorus is its deleterious effect on the current efficiency and the effect on metal quality, as pointed out in Chapter 1.

Metallic impurities, e.g. iron, titanium or manganese, behave differently from non-metallic element such as phosphorus. Studies of mass transfer of iron, titanium and silicon by Jentoftsen [1] showed that these metallic impurities mainly accumulate in the metal phase as expected, since they are more noble than aluminium. Theoretically this should also be the case for phosphorus (see equation (1.10)).

The mass transport between bath and metal in an alumina reduction cell occurs continuously, where in general a species M^{n+} that is more noble than aluminium, can either be transferred chemically or electrochemically into the metal phase. The electrochemical reaction at the cathode can be divided into several steps [1, 2] as shown in Figure 6-1.

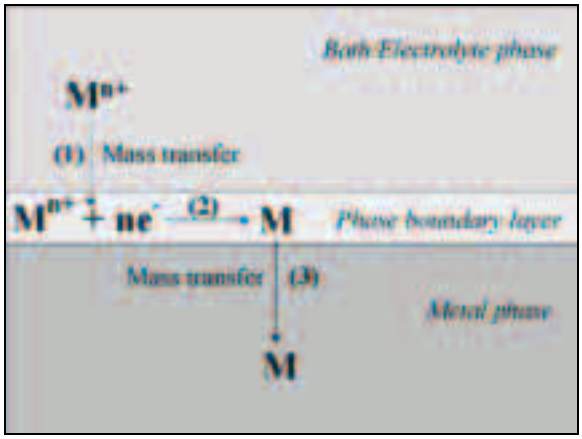

(1) Transport of species M^{n+} through the boundary layer between bath and metal
(2) Reduction of M^{n+} to M at the interface
(3) Further transport of M from the interface into the metal phase

Fig. 6-1: *Model of mass transport of species M^{n+} from the bath into the metal phase [1, 2].*

Johansen [2] showed that in the case of iron the reaction rate for the reduction is determined by the mass transfer of M^{n+} from the bath to the interface (step (1)). According to this mechanism an impurity element will be reduced at the cathode at its limiting current density (i_{lim}), which depends on the concentration of the element in the bath, c^o, and on the mass transfer coefficient, k_m:

$$i_l = n \cdot F \cdot k_m \cdot c^o \tag{6.1}$$

Johansen [2] and Jentoftsen [1] showed that the decay over time of a metallic impurity added could be fitted to the following equation, which is based on the theory of mass transport (see Appendix I).

$$c_{bath}/t0| \ c_{bc} \ 2 \ c_{added} \ (e^{4\,A\,V\cdot 41\ k_{bath}\ f} \tag{6.2}$$

where c_{added} can either be expressed as the concentration of impurity added or the difference between the concentration in the electrolyte immediately after addition and the background concentration, c_{bc}, which basically should be the same, if the addition is complete. Mass transfer coefficients were calculated by Jentoftsen [1] for iron, titanium and silicon, and turned out to be $(10\pm3)\cdot10^{-6}$ m/s, $(7\pm3)\cdot10^{-6}$ m/s and $(5\pm2)\cdot10^{-6}$ m/s respectively.

6.2. Experimental

Experiments similar to those of Jentoftsen [1] were performed with respect to phosphorus in industrial cells. Bath and metal samples were analysed as a function of time after adding a certain amount of orthophosphate to the bath. Several process variables were studied in connection with the concentration of phosphorus in the cell. The effect of additions of carbon particles and a change in the anode-cathode distance (ACD) on the phosphorus distribution were investigated. On one occasion an accidental current interruption occurred after addition of phosphate, and the effect on the phosphorus concentration could be followed. Trends in phosphorus content in aluminium produced in industrial cells were also studied from analytical data.

Since the major part of the phosphorus impurity enters the process with the alumina additions, presumably in its highest oxidation state, phosphorus was added in the five-valent form either as Na_3PO_4 or $AlPO_4$. Besides phosphates, some other impurities in the form of oxides, LiCl and in one

occasion $NiCO_3$ were added. A complete list of all chemicals added in each experiment can be found in Appendix H.

All measurements were carried out in industrial cells at Hydro Aluminium Årdal. Samples were taken from bath and metal at regular intervals for analyses. The addition and sampling positions are shown in Figure 6-2. Bath samples were analysed by XRF. Metal samples were analysed with an automated optical emission spectrograph. The standard deviation for the metal samples was ± 2.5 ppm. The standard deviation for the bath samples was in the range of ± 2 ppm.

The cell type used for the experiments was a side-by-side prebake cell, which had 30 anodes and operated at 230 - 250 kA. This cell was fed by secondary alumina. The addition routines were mostly the same, divergences from the usual adding and sampling procedures will be specified for each experiment. At position A (see Figure 6-2) the aluminium produced in the cell is tapped once a day. A detailed description on the addition and sampling positions is given in Table 6-1.

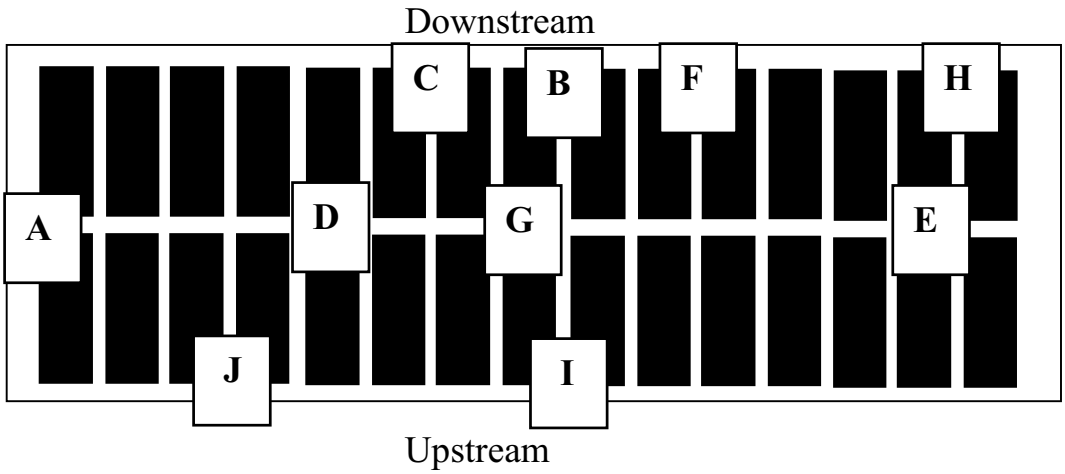

***Fig. 6-2**: Sketch of the SBS prebake cell. Addition and sampling positions for various experiments are marked with letters; a more detailed description can be found in Table 6-1.*

Table 6-1: *Positions (see Figure 6-2) of addition of chemicals and positions where bath and metal samples were taken, for all experiments. Whenever carbon dust was added, the position of the addition is given.*

Series	Positions of phosphorus addition	kg P added	Position of bath sampling	Position of metal sampling	Position of carbon dust addition
1	A, B	0.531	A	A	-
2	A, F, G	0.905	A	A	-
3	A, G, H	1.022	A	A	-
4	A, B, I	1.059	A	A	?
5	A, G, E	1.018	A	A	A, G, E
6	G, E	0.945	A	A	G, E
7	D	0.939	A	A	-
8	D	0.946	A	A	D
9	A	0.949	A, J	A	-
10	A	0.947	A	A	-

6.3. Results and Discussion

6.3.1. Distribution of phosphorus after addition

Figure 6-3 presents the variation of the phosphorus concentration in bath and metal over time for series 7 (see Table 6-1). To compare the behaviour of phosphorus to that of metallic impurities, results for manganese are shown as well.

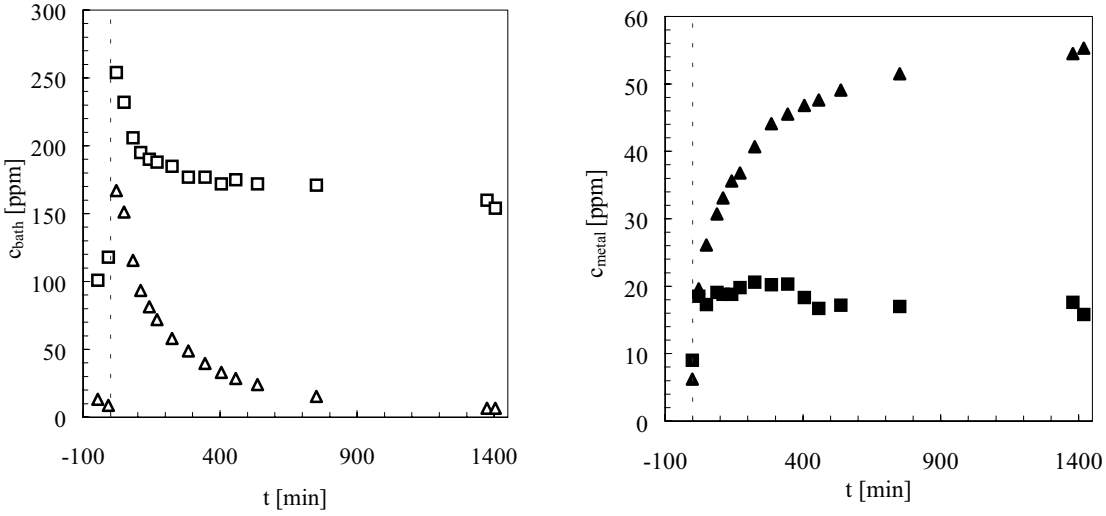

Fig. 6-3: *Distribution of phosphorus (as squares) and manganese (as triangles) in the bath (to the left) and in the metal (to the right) in a SBS-cell after addition of 4.969 kg Na_3PO_4 and 2.003 kg Mn_2O_3 (Series 7). The dotted lines mark the time of addition.*

As can be seen, phosphorus has a much longer retention time in the bath than manganese. While it is obvious in the case of manganese that the decrease in the bath leads to a corresponding increase in the metal, the concentration of phosphorus in the bath seems to decrease far more slowly. The increase in the metal is almost immediate after addition, and the concentration remains more or less constant throughout the time span of the measurement. This shows that even though phosphorus is a more electropositive element than aluminium, the main part of it was found to remain in the bath phase.

The slow mass transfer from bath into metal by phosphorus compared to manganese cannot be explained by reaching the solubility limit. As shown by Beer [3], the solubility of phosphorus in aluminium at a temperature of 960 ºC is about 0.19 wt%. Phosphorus in aluminium should be present in

the form of phosphides in the solid state. Since the added phosphorus was five-valent, a reduction process probably passes through the elemental state, P^0. But one has to consider that the boiling point of elemental phosphorus is at 280 ºC. If phosphorus is reduced at the bath/metal interface, it may have a tendency to escape in its elemental state rather than to get reduced all the way to form phosphides. This reaction may be sensitive to temperature changes in the cell.

A reduction-oxidation cycle for phosphorus has been suggested [4, 5], where phosphorus is cycling between the oxidation states of +5 and +3 in the bath. Deininger and Gerlach [6] found that the reoxidation concept was depending on the concentration of phosphorus in the bath. They claimed that a reduction to elemental phosphorus occurs only at concentrations higher than 0.12 wt% P, which is an unlikely high concentration range for an industrial cell.

However, as Figure 6-3 shows, part of the phosphorus ends up in the metal when going through the redox cycle. A great part of the current loss due to phosphorus can be ascribed to this redox cycle.

$$P(V) + 2e^- \rightleftarrows P(III) \qquad (6.3)$$

In primary alumina the dominant valency of phosphorus is believed to be five. However, in secondary alumina, Lossius [7] found some phosphorus in the form of iron phosphide, Fe_2P. In a later publication by Lossius and Øye [8], the suggestion was made that AlP or $AlPO_4$ could be present as well in the secondary alumina. Those compounds were not detected by XRD, whereas Fe_2P was.

6.3.2. Effect of carbon particles

As mentioned earlier, carbon dust in the electrolyte may play an important role on the behaviour of phosphorus in the cell. It is known that carbon dust in the electrolyte seems to be a medium to which impurities get attached and get transported out of the bath [9]. From investigations of secondary alumina by Lossius [7], it seems that an increasing carbon content in secondary alumina leads to an increased concentration of phosphorus. Carbon particles from industrial electrolytes were analyzed by SEM/EDS and showed an enrichment of phosphorus on carbon [10]. Apart from phosphorus, other impurities, e.g. iron, were found on these carbon particles as well.

Due to these findings, test were run where carbon dust skimmed from Søderberg cells was added to a prebake cell a certain time period after the phosphate addition, as shown in Figure 6-4 for series 8.

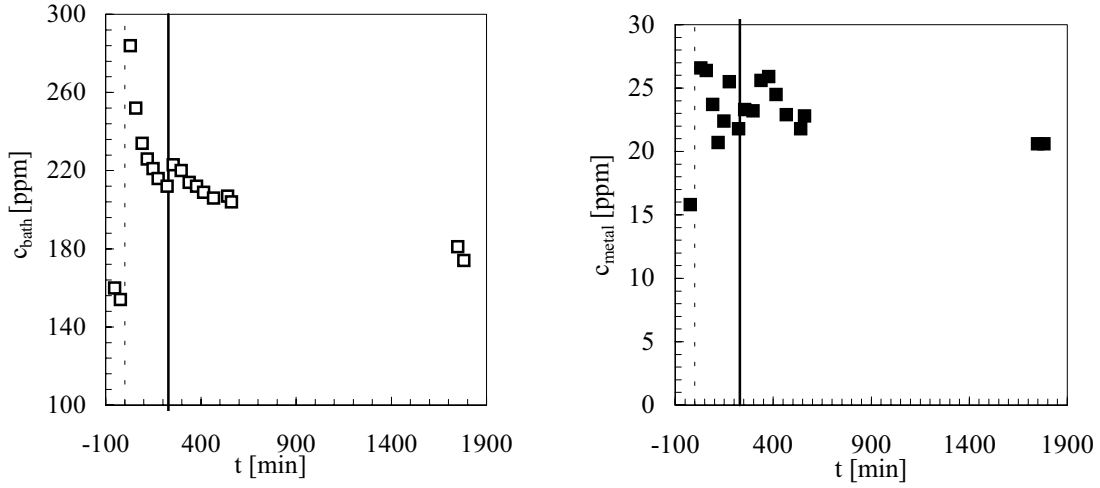

Fig. 6-4: *Distribution of phosphorus in bath (to the left) and metal (to the right) after addition of 5.003 kg Na_3PO_4 (dotted line). Time of addition of 16.6 kg carbon dust marked as thick full line (series 8).*

By the addition of carbon to the cell, it was expected that the phosphorus level in the bath should decrease, since the carbon added should facilitate the transport for phosphorus out of the cell. However, a minor increase of phosphorus in the bath was observed for all experiments where carbon was added. In Figure 6-4 the increase is about 11 ppm P. In several experiments (series 4, 5, 6 and 8), carbon dust was added, and it showed always the same behaviour.

Characteristic for the curves, which represent the phosphorus concentration in the bath when carbon dust was added, is a slight increase in phosphorus in the bath. The increase of the phosphorus level in the bath might be due to the carbon dust coming from Søderberg cells, which could be enriched in impurities. Analysis of the carbon dust added in series 8 showed that it contained 0.16 wt% P. Assuming an average bath weight of 7000 kg in the cell used, an addition of 16.6 kg carbon dust should lead to an increase of about 4 ppm P in the bath. In series 5 and 6 about 40 kg carbon dust was added, which had a phosphorus content of 0.01 wt% P. The amount of phosphorus, introduced by adding carbon dust, should result in an increase of 0.6 ppm P. However, there was a sudden increase of phosphorus in the bath by 8 ppm. Therefore, even though the carbon added contained a

certain amount of phosphorus, the increase after addition of carbon dust cannot be ascribed to this effect alone.

The sampling of bath and metal was done at random depths in the bath. Since carbon dust accumulates in the vicinity of the bath surface, it might be possible that an increased amount of carbon in the bath samples led to a higher concentration of phosphorus analysed. However, the bath samples taken were checked visually to assure that no major amounts of carbon were present.

During the measurement period, when carbon dust was added to the cell, gas was withdrawn through a hole in the gas duct and passed through a gas filter and a pump, in order to sample particulates in the gas stream. Analysis of the particulates on the filter showed that the amount of phosphorus and iron had increased during the measurement period. In the aluminium phase the phosphorus concentrations increased or varied randomly after addition of sodium phosphate. No clear trend could be seen from phosphorus in aluminium after addition of carbon.

6.3.3. Effect of current interruption

In one experiment the current was interrupted accidentially for one hour shortly after adding phosphate (series 2). The concentration of phosphorus in both bath and metal as a function of time can be seen in Figure 6-5.

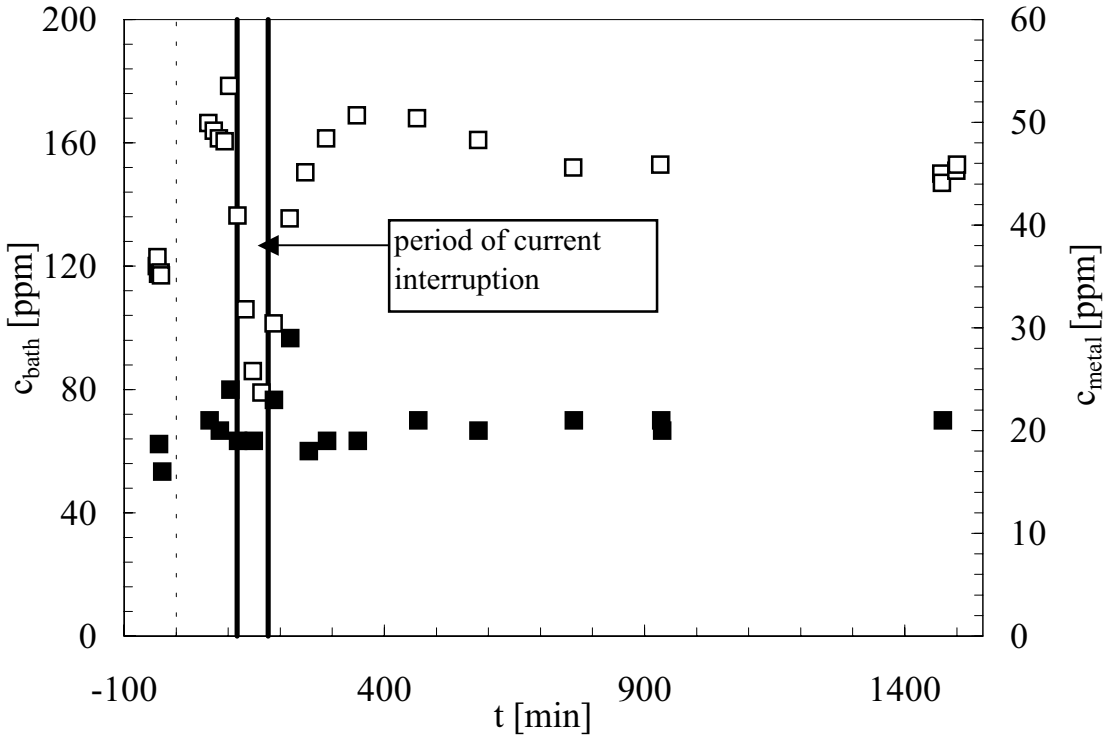

***Fig. 6-5**: Concentration of phosphorus in bath (□) and metal (■) when the current had been interrupted for one hour (Series 2). The dotted line shows the time of addition of phosphate. The thick lines mark the period of the current interruption.*

Together with the phosphate there were also added other impurities: i.e. Fe_2O_3, SiO_2, TiO_2 and Mn_2O_3. More detailed information on the behaviour of iron, silicon and titanium during the current interruption can be found in the thesis of Jentoftsen [1]. It should be mentioned, that only iron showed a similar behaviour as phosphorus when no current was passing through the cell. All the other impurities were more or less unaffected.

Current interruption leads to several changes in the cell. The gas-driven and magnetically driven circulation ceases and the concentration of dissolved aluminium in the electrolyte increases. In this reducing environment the metallic impurities can be reduced to their elemental state and sink to the metal-bath interface. Phosphorus has to form phosphides to undergo the

same process. When the current is turned on again, the elements could be reoxidized and dissolve in the bath, and therefore be present when taking bath samples. Furthermore, there is a significant drop in temperature, which leads to increasing side ledge thickness. Impurities might be included with the frozen bath. After the current interruption the bath temperature would again rise, and the impurities could be released from the diminishing side ledge. But if dissolved aluminium in the bath or freezing of the side ledge influenced the concentration of the impurities, one could ask the question why do not they all behave in the same way, but only iron and phosphorus react as shown in Figure 6-5?

The presence of carbon particles in the bath might explain the interaction between iron and phosphorus. Reviewing previous work, Thonstad [9] concluded that the carbon particles will tend to accumulate at the bath surface. A decrease in convection due to the stop of CO_2 evolution, will enhance the transport of the carbon particles to the bath surface, since the surface tension between the solid carbon particles and the bath is high. A characterisation study of carbon dust in industrial bath samples by Rørvik [11] showed that carbon particles (Ó 1 μm) were apparently situated on the boundary between bath and gas bubbles. Since the CO_2 evolution had ceased, the gas bubbles, which seemingly tend to eject carbon particles out of the bath, were not present.

Therefore, it seems that iron and phosphorus attached to carbon particles follow the transport towards the bath surface and stay there until the convection due to CO_2 evolution is re-established. This will bring the carbon particles, floating on the surface, back into the bulk of the bath and establish a more homogeneous distribution of the impurities. It has to be considered that during a current interruption a decrease in the bath temperature will lead to local density variations and, therefore, a uniform distribution of the impurities in the bath cannot be taken for granted. However, the variation in density will initiate natural convection. Nevertheless, the bath samples taken during the off period may not have been representative of the entire electrolyte. The concentration of phosphorus in the metal seems to be unaffected.

6.3.4. Effect of change in ACD

When changing the distance between the anode and the cathode (ACD), the impurities in the bath and metal are affected. The phosphorus concentrations in bath and metal are shown as a function of time in an experiment where the ACD was changed as indicated in Figure 6-6.

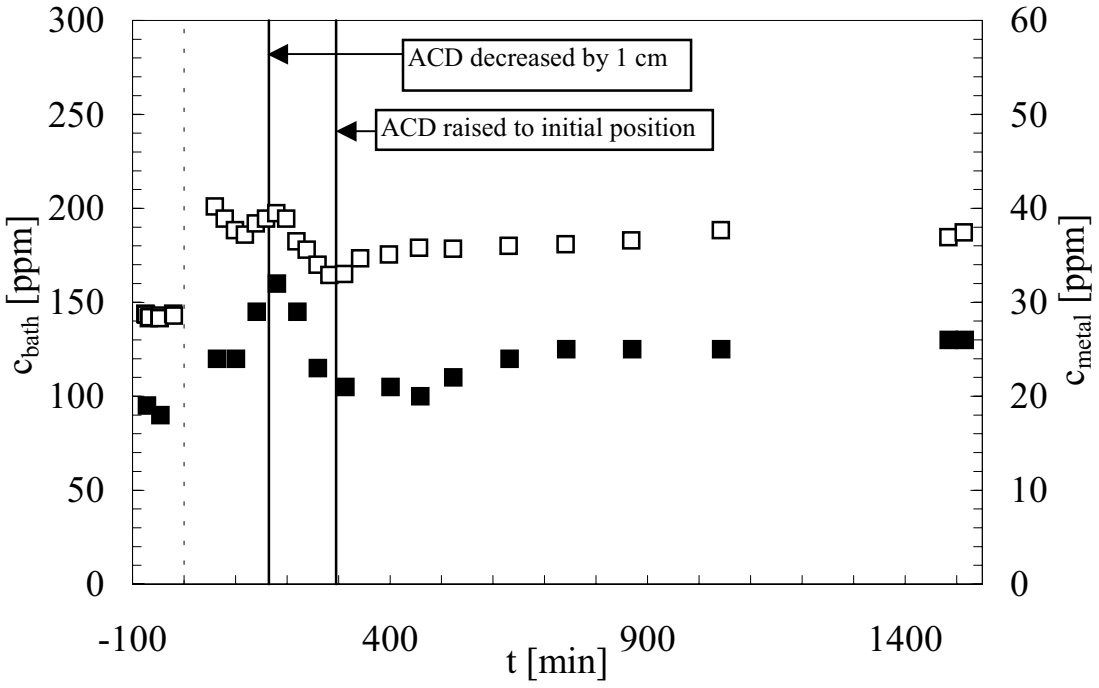

Fig. 6-6: *Effect on the phosphorus concentration of bath (□) and metal (■) when the interpolar distance was changed (thick black lines). The dotted line shows the time of addition of phosphate.*

A reduced interpolar distance may enhance the gas induced convection in the bath in the space between anode and cathode. The diffusion layer thickness will decrease, and an increase in the mass transfer coefficient is to be expected. The mass transfer coefficients for iron, silicon and titanium, when the ACD was reduced, were calculated by Jentoftsen [1] and confirmed this assumption. The bath temperature decreased by about 10 ºC during the period with lowered ACD.

The concentration of phosphorus in the bath and in the metal decreased immediately when the ACD was reduced. Due to the increased flow rate of the electrolyte between anode and cathode, it might be assumed that the carbon dust present in the cell is transported more rapidly out of the space between anode and cathode towards the bath surface. This might be particularly important for carbon dust accumulated at the metal-bath

interface. As mentioned in Section 2.1.4.2., Foosnæs et al. [12] found that the carbon dust seems to accumulate close to the bath surface as well as at the metal-bath interface.

The increased convection in the vicinity of the bath-metal interface will affect the thickness of the diffusion layer. A decrease in its thickness might facilitate the "back reaction" in the case of phosphorus.

The lowering of the anodes causes an increase in bath height. Thereby the electrolyte gets in contact with areas of the anodes and the side ledge, that are usually only exposed to the gas phase between bath and crust. The electrolyte might "wash" those areas and return any impurities to the bulk of the bath.

As shown in Figure 6-6- the phosphorus concentration in the bath increased after the anodes were raised to the initial position. In the metal this reaction was delayed by about 2½ hours. One has to consider that after elevating the anodes to the initial position, the diffusion layer thickness increases. The mass transfer coefficient, therefore, decreases, which should result in slower transport of phosphorus from the bath into the metal. However, the response of the phosphorus concentration in the metal when adding phosphate to the bath is usually almost immediate.

6.3.5. Effect of temperature

As mentioned in Section 6.3.1, the reaction of phosphorus at the bath/metal interface might be dependent on temperature. Since Søderberg cells generally operate at higher temperature than prebake cells, the concentration of phosphorus in the metal for prebake and Søderberg lines (VSS, 115 kA) for a time period of approximately nine months are shown in Figure 6-7. It should be mentioned that the Søderberg cells are fed with primary alumina. This is certainly the main reason why the phosphorus concentration in this type of cell is lower than for the prebake. However, it is obvious that the temperature influences the concentration of phosphorus in the metal, as indicated in Figure 6-7.

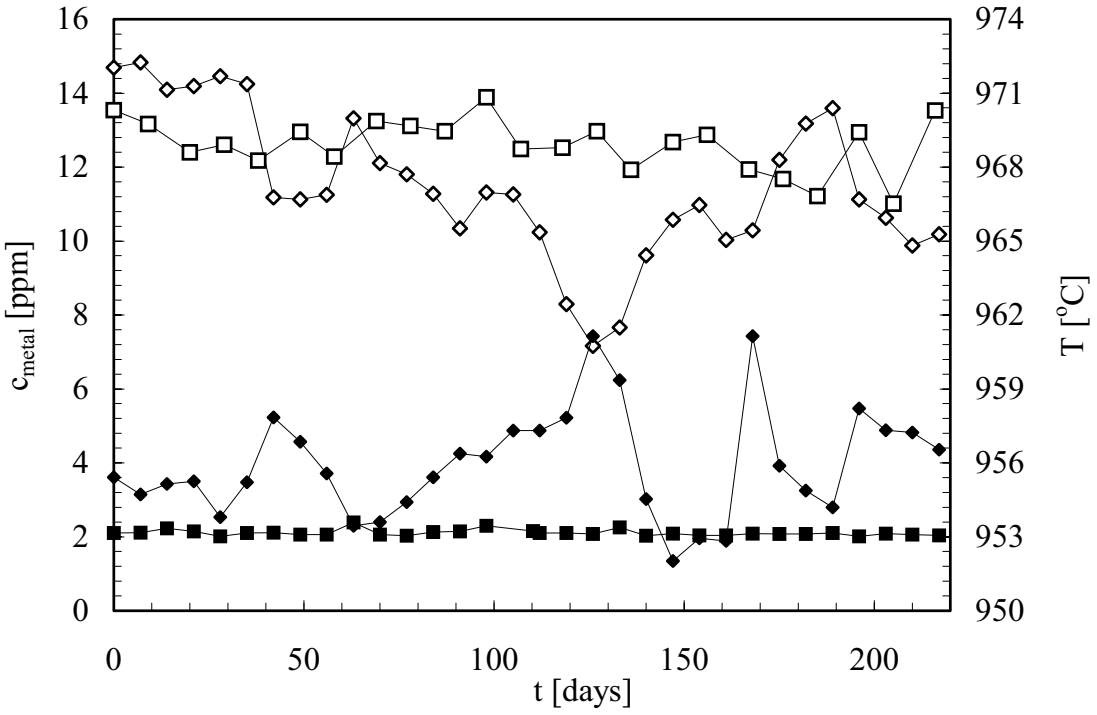

Fig. 6-7: *Average values for the phosphorus contents in aluminium for Søderberg (■) and prebake cells (◆) (scale on the left hand axis) and the bath temperature for Søderberg (□) and prebake cells (◇) (scale on the right hand axis) as a function of time.*

The phosphorus concentration in the Søderberg line was close to the detection limit for the metal analysis, which is approximately 2-5 ppm, so the analysis was probably insensitive to any variations. In the prebake line the concentration was 8-15 ppm.

As already mentioned there is a difference of the average bath temperature between prebake and Søderberg cells. From Figure 6-7 it can be seen that the average bath temperature is 965 - 970 ^{o}C and 950 - 960 ^{o}C in the Søderberg line and in the prebake line respectively. In the case of Søderberg cells the single anode has a larger area along which the evolving gas bubbles have to travel until they reach the anode edges and can rise to the bath surface. This may lead to a more intense gas-induced convection compared to prebake cells. In Hydro Aluminium Årdal the Søderberg line is fed with primary alumina, while the prebake line is fed with secondary alumina from the dry scrubber. Since the phosphorus content in secondary alumina is usually much higher compared to the primary quality (see Section 6.3.7.), one should expect a lower phosphorus content in the Søderberg cells.

Even though different raw materials are used, the phosphorus content in the metal shows a striking trend with temperature. In the case of the prebake line a temperature increase leads to a decrease in the concentration of phosphorus in the metal. The Søderberg line operating at a rather constant, high temperature, does not show such fluctuations. However, the accuracy of the XRF analysis with approximately 2 - 5 ppm, is reached when it comes to such low concentrations, and the fluctuations in concentration due to temperature changes may not be visible.

Other observations also indicate that the phosphorus content in the metal is mainly determined by the temperature. Figure 6-8 shows average values from a complete line of prebake cells for the phosphorus content in the metal and the bath temperature as a function of time. Considering the relatively small temperature variations there seems to be a clear correlation between high phosphorus concentration in the metal and low temperature.

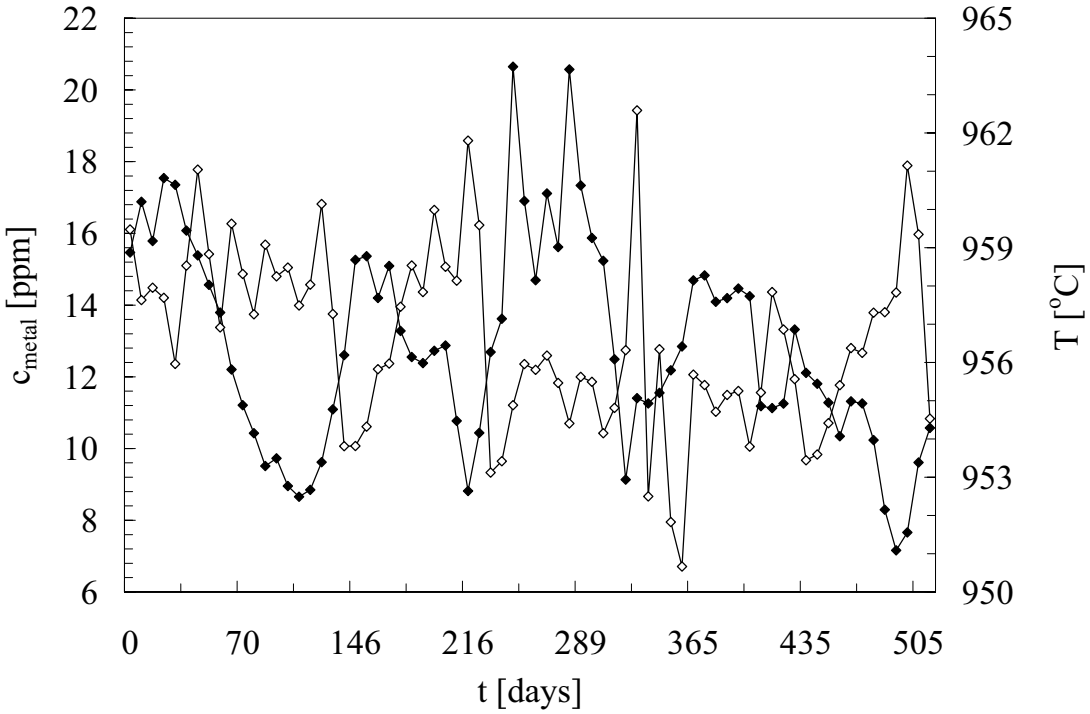

Fig. 6-8: *Average values for the phosphorus content in aluminium (◆) and bath temperature (◇) for a line of prebake cells as a function of time.*

Even though the data in Figure 6-8 are rather scattered, we can see the trend of lower phosphorus in aluminium when the bath temperature is high and vice versa.

From the results of Oblakowski and Pietrzyk [13] the conclusions might be drawn that an increased content of C, Al_4C_3 and P_2O_5 in the electrolyte leads to an increased bath temperature. However, as observed for a single prebake cell, depicted in Figure 6-9, this may not always be the case.

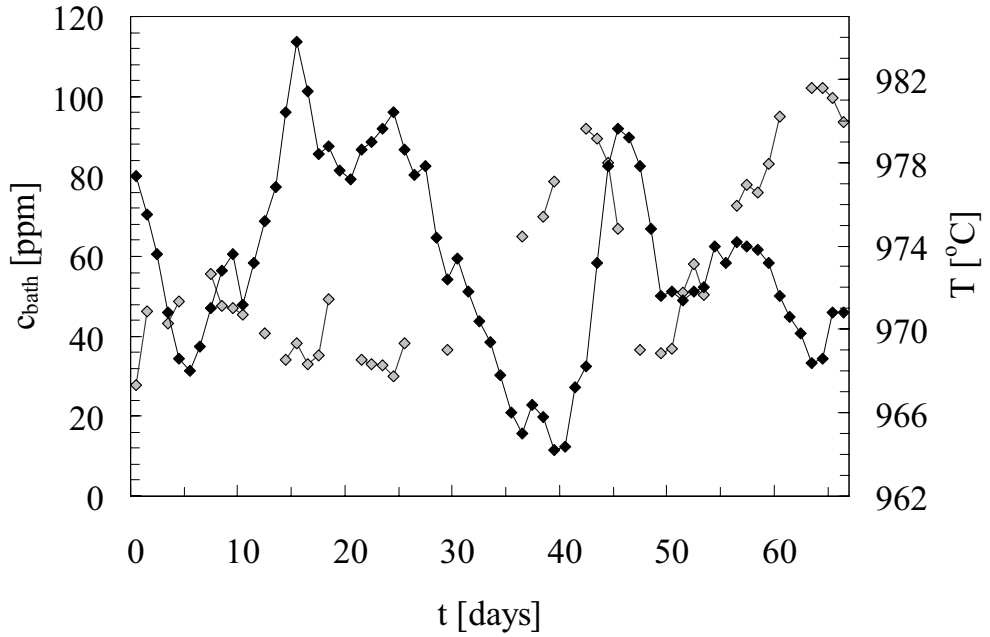

Fig. 6-9: *Phosphorus content in the bath (◇) and bath temperature (◆) for one prebake cell as a function of time.*

The results from Figure 6-8 and 6-9 show that variations in bath temperature are reflected by inverse changes in the phosphorus content in the bath and in the metal. A possible explanation for the findings of Oblakowski and Pietryzk [13] may be that the carbon particles act as electric insulators causing an increase in the bath temperature, and in addition act as nucleation sites for impurities such as phosphorus. The increase in bath temperature with increasing content of phosphorus in the electrolyte may, therefore, be only a secondary effect.

It seems that an increase in temperature leads to a decrease in the phosphorus content in both bath and metal. Phosphorus appears as an impurity, which may establish a kind of steady state distribution between bath and metal.

Variations in temperature are usually linked with variations in the electrolyte composition. In other cases changes of the interpolar distance and disturbances such as anode failures or anode effect may be responsible for temperature variations.

Analysis of aluminium produced in periods before and after anode effects showed that the phosphorus content in aluminium decreased dramatically after the occurrence of an anode effect. As expected the temperature increased markedly during the same period. Other effects than the

temperature increase, such as increased electrolyte convection and reduced cover of the cells during anode effects, could also contribute to the low phosphorus content in the metal.

6.3.6. Modelling the transfer of phosphorus from bath to metal

In Section 6.1 a short introduction was given to how the transfer of metallic impurities between bath and metal could be fitted to an exponential function (equation (6.2)). From Series 1 the variation of the concentration of titanium, silicon and phosphorus in the bath as a function of time is shown in Figure 6-10:

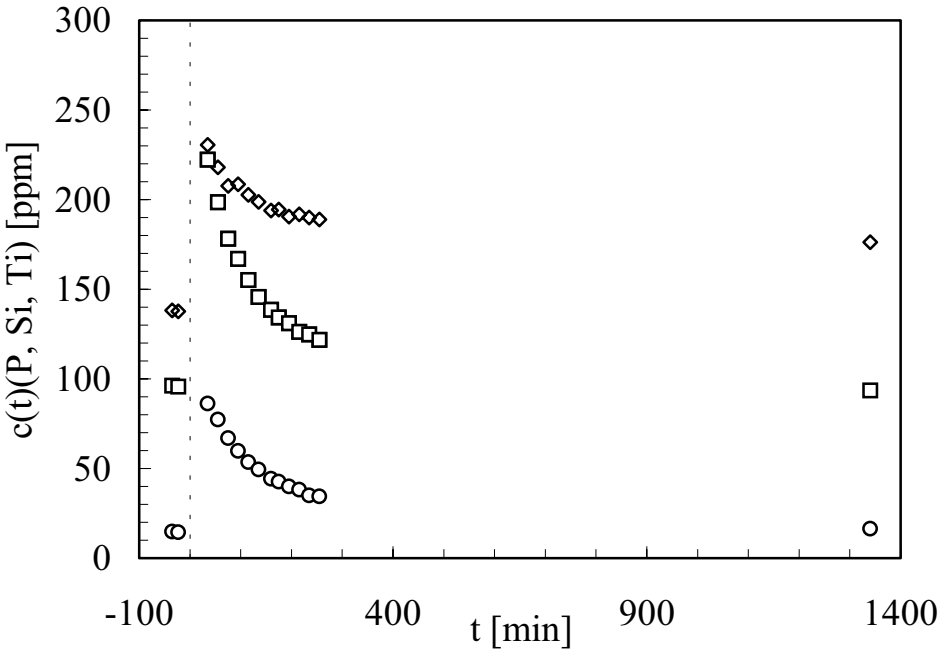

Fig. 6-10: *Concentrations of phosphorus (◇), silicon (□) and titanium (○) in bath from Series 1 versus time.*

In Figure 6-10 it is obvious that the retention time for phosphorus in the bath is much longer than for the other metallic impurities added. A similar behaviour was observed earlier in Figure 6-3 for Series 7. If the theory that the mass transport of the metallic impurities follows an exponential function is correct, a plot of concentration on a logarithmic scale versus time should yield a straight line.

However, as shown in Figure 6-11, the fitting to a straight line for each data series illustrates a systematic trend of the concentrations for every impurity added. Starting sampling at 35 minutes after addition of the impurity compounds, all of the first data points lie above the straight line

fit. With proceeding time the concentrations are below the linear fit and finally get above again after ~24 hours. The deviation from the linear fit could be assigned to analytical error, however, the deviation appears rather systematic and independent of the kind of impurity. This implies that one straight line does not give the best fit. It seems more like two different regimes, which control the decay of the concentrations. While the latter may be ascribed to mass transport, the first regime might be due to the distribution of the added compounds in the bath.

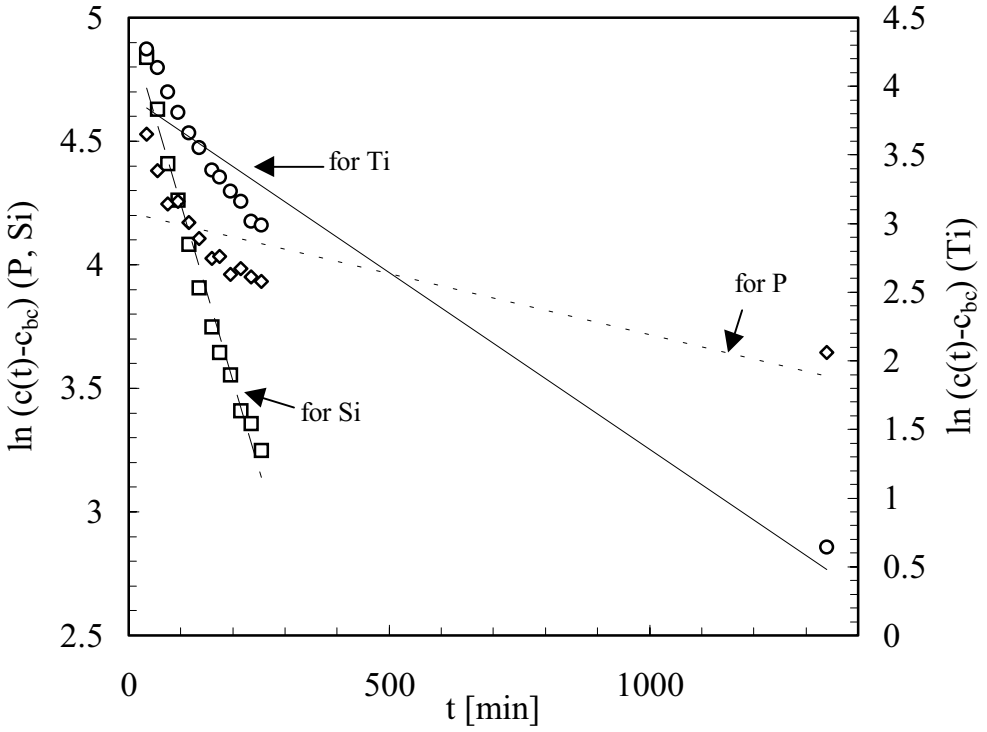

Fig. 6-11: *Plot of ln(c(t)-c_{bc}) versus time for phosphorus (◇), silicon (□) and titanium (○) (Series 1) with linear fits.*

Since the measurements in this work were made in a larger and different type of cell than the one used by Johansen [2] in 1975 (Søderberg, ~100 kA), the time of distribution might be longer than assumed. The distribution time expresses the time elapsed, from when the addition is made until it is evenly distributed in the bath. A common value for the distribution time is 30 - 40 minutes, as can be found in literature [15-19]. When adding the chemicals in several positions of the cell, the distribution proceeds faster, as made for Series 1 – 6 (see Table 6-1).

The distribution times should be rather equal for all compounds added, since turbulent diffusion should be independent of the type of species. The

distribution was found to be adequately represented by an exponential function (for theoretical derivation, see Appendix J).

The mass transfer between bath and metal is expressed by equation (6.2). As mentioned in Section 6.1, step (1) in Figure 6-1 controls the process regarding the variation in concentration for different metallic impurities. The flux for step (1) can be expressed as:

$$J = V\frac{\partial c}{\partial t} = k\,A\,(c_{bath} - c_{boundary}) \tag{6.4}$$

Presuming that the reactions in step (2) and (3) in Figure 6-1 proceed at a higher rate, the boundary concentration is equal to zero.
In the model for the phosphorus transfer we assume that phosphorus behaves in a similar way as metallic impurities. Its concentration at the phase boundary is, therefore, assumed to be zero. The mass transport for phosphorus can thereby be expressed by equation (6.4), which results in an exponential dependence for the concentration of P in the bath over time (see equation (6.2)). The mass transfer coefficient obtained for phosphorus is, however, an apparent value, which may not reflect the reality.

Therefore, when estimating the time constant for the transfer of phosphorus to the metal phase there are two approaches. Either one excludes measurements taken before a given time until it is assumed that phosphorus is evenly distributed in the bath, or one incorporates the effect of the distribution process by fitting the data to a double exponential function. Since it can be difficult to distinguish the effects of distribution and of transfer to the metal, especially if the two time constants involved are almost equal, it is preferable to use the method of fitting the data to a double exponential function,

$$c(t) = c_{bc} + \underbrace{c^{*}\,(\exp(-k_1\,t))}_{\text{distribution}} + \underbrace{c_{added}\,(\exp(-k_2\,t))}_{\text{mass transfer}} \tag{6.5}$$

where c_{bc} is the background concentration of phosphorus, since it is being introduced continuously with the raw materials. Equation (6.5) is similar to equation (6.2), however, the first exponential term expresses the distribution of the compounds added. The concentration c^{*} specifies how concentrated the solution with phosphorus was locally right after addition, while c_{added} should give the initial concentration of phosphorus in the cell

right after addition if it had been evenly distributed. The concentration c* is dependent on the amount added, the number of feeding positions and the distance between feeding and sampling holes. If the addition is complete, c_{added} should be equivalent to the amount of phosphorus added to the cell. The time constant k_1 reflects how fast the phosphorus concentration decreases at the position where the addition is made, while k_2 is connected to the mass transfer coefficient out of the bath, k_{bath}.

$$k_{bath} \mid \frac{V}{A} \int k_2 \tag{6.6}$$

Fitting of equation (6.5) for four separate measurements (Series 1, 7, 9 and 10) gave the following results, shown in Figure 6-12 and Table 6-2.

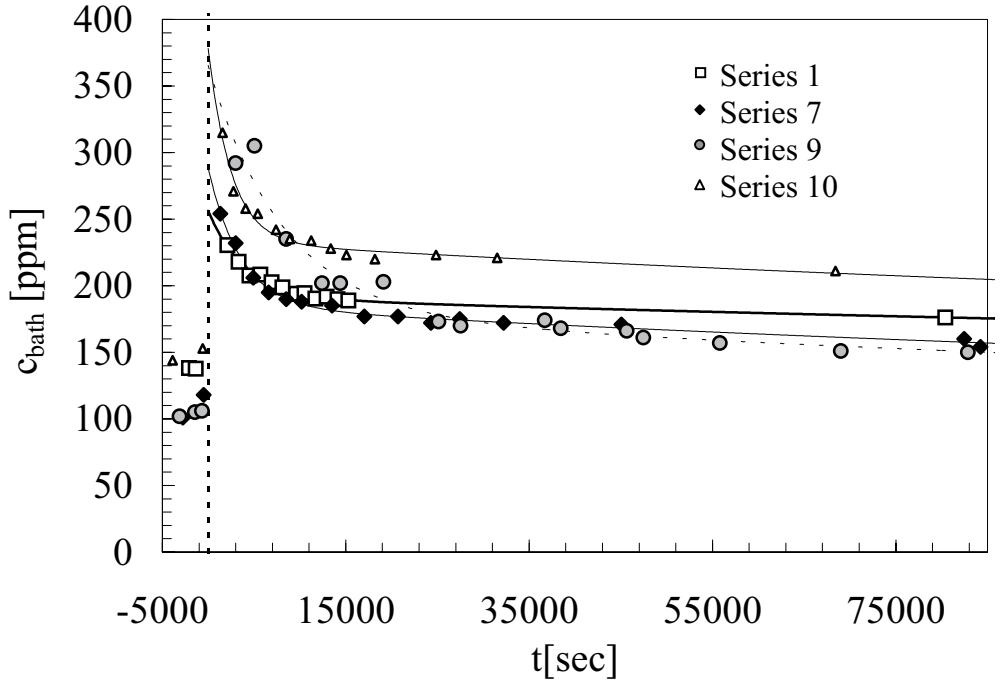

Fig. 6-12: *Concentration of phosphorus in the bath for Series 1, 7, 9 and 10 (see Table 6-1) and the fitted curves.*

For Series 9 only samples taken from sampling position A are presented. In the same series the first value for the concentration in the bath was disregarded, since the distribution function cannot be expressed satisfactorily by an exponential function when the time periods are very short (see Appendix J).

Table 6-2: *Coefficients of equation (6.5) for Series 1, 7, 9 and 10 (with A = 40.1 m^2, m_{bath} = 7000 kg and ρ = 2100 kg/m^3); * - apparent values.*

Series	c_{bc} [ppm]	c^* [ppm]	k_1 [s^{-1}]	c_{added} [ppm]	k_2 [s^{-1}]	k_{bath}^* [$m \cdot s^{-1}$]
1	138.0	65.2	$2.5 \cdot 10^{-4}$	53.1	$4.1 \cdot 10^{-6}$	$3.4 \cdot 10^{-7}$
7	109.5	109.5	$2.8 \cdot 10^{-4}$	74.9	$5.4 \cdot 10^{-6}$	$4.5 \cdot 10^{-7}$
9	104.3	185.1	$1.2 \cdot 10^{-4}$	75.8	$5.9 \cdot 10^{-6}$	$4.9 \cdot 10^{-7}$
10	150.7	145.4	$4.0 \cdot 10^{-4}$	82.1	$4.9 \cdot 10^{-6}$	$4.1 \cdot 10^{-7}$

When looking at the values of c^* and comparing them to the amount of phosphate added, the position where it was added to the cell and where sampling was performed (see Table 6-1), a trend can be foreseen. For Series 1 the amount of phosphorus added was one half of the amount brought into the cell for Series 7, 9 and 10 (see Table 6-1). In addition two feeding holes were used to introduce the impurities into the bath. The value for c^* for Series 1 is, therefore, lower in comparison to the c^* values for Series 7, 9 and 10. The difference between Series 7 and Series 9 and 10 could be assigned to the different feeding holes used.

The time constant k_1 varies between $1.2 \cdot 10^{-4}$ and $4 \cdot 10^{-4}$ s^{-1}, i.e. 139 and 42 minutes respectively. This value is dependent on the convection in the cell when samples were taken. In case of increased convection due to e.g. an anode effect, increased temperature, etc., this value will change to shorter times. The time constant k_1 is not equal to the time at which a homogeneous distribution has been reached, although the two are related.

In Table 6-3 the obtained values for c_{added} (from Table 6-2) are compared to the amount of phosphorus added to the cell (see Table 6-1).

Table 6-3: *Comparison of the amount of phosphorus added to the amount calculated in the bath by fitting equation (6.5). The bath weights (m_{bath} calculated) are calculated.*

Series	kg P added	c_{added} (Table 6-2) [ppm]	m_{bath} calculated [kg]	c_{added}^{o} calculated (assuming m_{bath} = 7000 kg) [ppm]	Ratio c_{added}/c_{added}^{o}
1	0.531	53.1	10000	75.9	0.70
7	0.939	74.9	13060	134.1	0.56
9	0.949	75.8	12520	135.6	0.56
10	0.947	82.1	11535	135.3	0.61

A typical bath weight, for the cell under study, is 7000 kg [14]. As Table 6-3 shows, the amount of bath calculated from the amount of phosphorus added (c_{added}^{o}) and the amount present in the electrolyte after addition, corrected for the initial content, (c_{added}), is too high. Under the assumption that c_{added} represents the initial excess concentration of phosphorus in the bath, the last column in Table 6-3 shows that 30 to 40% of the added phosphorus may not have ended up in the electrolyte.

The time constant k_2 is related to the apparent mass transfer coefficient for phosphorus, as shown by equation (6.5). The values obtained for $k_{bath}(P)$ are in good mutual agreement with each other and 10 – 20 times lower than the values obtained by Jentoftsen [1] for iron, titanium and silicon.

When plotting the natural logarithm of the concentration of phosphorus in the bath minus its background concentration versus time as in Figure 6-14, the appearance of two regimes, as expressed by equation (6.5) is obvious.

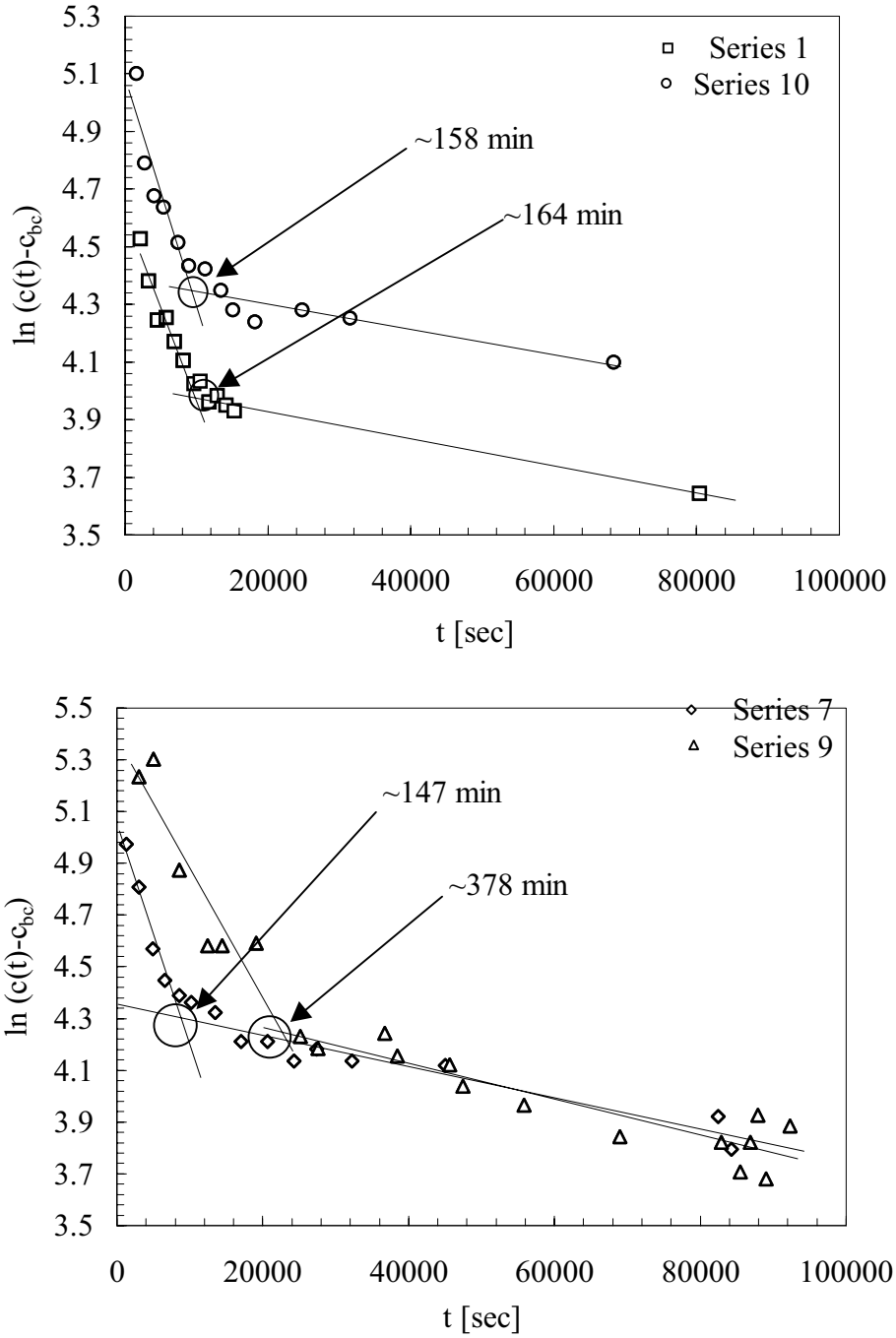

Fig. 6-13: *Plots of ln(c(t)-c_{bc}) versus time for all series presented in Figure 6-13. Intercepts of the straight lines give times of distribution, as indicated in minutes.*

As indicated by Figure 6-13, the decrease in concentration changes its regime from distribution controlled to mass transfer controlled. A change in the slope occurs for each measurement series in Figure 6-13. This is equivalent to a change in the time constant from k_1 to k_2 at longer times

(see equation 6.5). From the intercept of the two lines for each series, the distribution time can be determined, as shown in Figure 6-13. It seems as if the distribution time is normally 2½ to 3 hours. Series 9 shows an extreme value of almost 6½ hours. It cannot be concluded if this very high value is due to measurement error or due to operational problems of the cell.

When taking a closer look at the literature where distribution times in industrial cells are reported [15-19], it seems that the cell size in most cases was smaller than the prebake cell used in this work. Walker et al. [18] reported distribution times for a prebake cell with 20 anodes, which seemed to be the largest cell among all publications found. Some of the studies were performed on water models [16, 17]. Not all authors specified the type of cell under study. Tørklep [15] reported distribution times for Søderberg cells (115 kA) and end-to-end (ETE) prebake cells (155 kA), to be about 30 to 40 minutes. Jentoftsen [1] found a distribution time below one hour for an ETE prebake cell (170 kA, 22 anodes).

It can be concluded that the distribution times reported in the literature are for smaller cells and different types of cells compared to this work. The length of the cell seems to be one of the main factors when it comes to distribution processes. The positioning of the cell, if end-to-end or side-by-side, may also influence the magnetically-induced convection and thereby the distribution time.

For the similar type of cell as used in this work, Rolseth et al. [14] reported a distribution time of 1.5 hours when adding LiCl to the cell. For a another measurement series with LiCl in the same cell, Rolseth [20] found a distribution time of about 3 hours. These results are in reasonable agreement with the distribution times found for phosphorus in this work.

Purdie et al. [17] mentioned that anode replacement could in some cases delay the distribution time close to the new anode. The anode current distribution is altered and thereby the gas-induced convection pattern.

In 1975 Johansen [2] used equation (6.2) to fit his measurements by additions of Fe_2O_3 and $FeSO_4$ into a 105 kA Søderberg cell (VSS), and he calculated the mass transfer coefficient for iron (k_{Fe} = 1.25·10^{-5} m/s). Jentoftsen [1] determined mass transfer coefficients for iron, titanium and silicon (Section 6.1) in prebake cells (230 kA) and found them to be in reasonable agreement with the results for iron determined by Johansen.

The bath concentrations of the metallic impurities added together with the sodium orthophosphate (see Appendix H), were fitted to the double exponential function (Equation (6.5)), since the distribution should also affect the decrease in concentration of those impurities. This becomes important when determining the mass transfer coefficient, since data at short times, where the distribution function controls the process, will influence k_{bath} (see equation (6.5)), giving a value that is too large. Since the time constants, k_1 and k_2, in this cases are more similar to one another, e.g. for iron, a single exponential function will give a satisfactory fit. However, the change of course of the concentration values when looking at such a plot (see Figure 6-11) seems to be rather systematic. This becomes clear when plotting the concentrations of the metallic impurities minus their background concentrations in the electrolyte on a logarithmic scale versus time. A distinct change in slope can be observed. Some examples are shown in Figure 6-14.

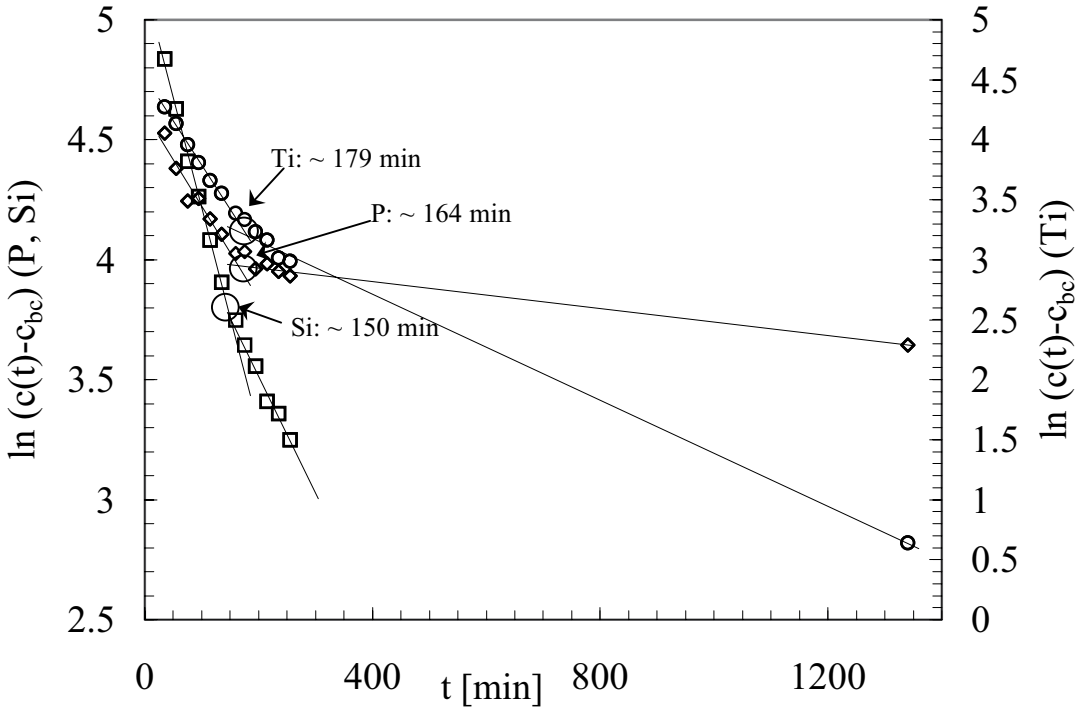

***Fig. 6-14**: Plots of ln(c(t)-c_{bk}) versus time for silicon (□), titanium (○) and phosphorus (◇) (Series 1). Intercept shows distribution time for each impurity.*

The sampling of bath was rather frequent in the first six hours after addition of phosphate. The long distance up to the last data point is due to the fact that there was no sampling performed during the night. The last data point

for silicon is not given, since the difference between c(t) and c_{bc} was negative.

In Table 6-4 time constants for the impurities presented in Figure 6-14 are given, when a double exponential function was fitted.

***Table 6-4**: Time constants for silicon, titanium and phosphorus for Series 1 when fitted to a double exponential function; * apparent value.*

Impurity	k_1 [s^{-1}]	k_2 [s^{-1}]	k_{bath} [m^3s^{-1}]
Si	$2.5 \cdot 10^{-4}$	$4.6 \cdot 10^{-5}$	$3.8 \cdot 10^{-6}$
Ti	$2.0 \cdot 10^{-4}$	$3.2 \cdot 10^{-5}$	$2.7 \cdot 10^{-6}$
P	$2.5 \cdot 10^{-4}$	$4.1 \cdot 10^{-6}$	$3.4\ 10^{-7}$ *

In Figure 6-14 the change in the slope for silicon is not as marked as for titanium and phosphorus, but a trend can still be seen. A similar behaviour is seen for other metallic impurities, e.g. iron. The distribution times in Figure 6-14 are rather similar for all impurities in this series, with an average of 164 minutes.

For metallic impurities, such as manganese, iron, silicon, etc., the time constant k_1 for the distribution is similar to the mass transfer dependent time constant k_2. Since Jentoftsen [1] considered data points with t > 1 hour, the mass transfer coefficients determined for iron, silicon and titanium might be slightly influenced by the distribution effect. However, the discrepancy is assumed to be smaller than the estimated error.

Another explanation why plots of $\ln(c(t)-c_{bc})$ versus time do not give a straight line for the metallic impurities, could also be due to reoxidation of the impurity from the metal to the bath. This would increase the concentration of the impurity in the bath, and the conditions for equation (6.2), where mass transfer from the bath into the metal is the only mechanism considered, are not fulfilled. This may be true for lithium, which establishes an equilibrium in the cell. Even though phosphorus appears also to reach a steady state, phosphorus is not assumed be in a chemical equilibrium between bath and metal as in the case of lithium or sodium. Furthermore, it is a more noble element compared to aluminium, so theoretically a mass transfer towards the metal phase should occur. The less noble impurities like Li and Na are not expected to undergo a complete

mass transfer process into the metal like nobler metallic impurities e.g. iron.

These nobler impurities, e.g. manganese or titanium, have a strong tendency to report to the metal phase according to thermodynamics. This is also obvious when looking at the bath concentrations for manganese and titanium in the beginning and at the end of the experiments presented in Figures 6-3 and 6-10.

Even though a reoxidation of the impurity cannot be completely excluded, it is rather striking that the change in slope for plots of $\ln(c(t)-c_{bc})$ versus time occurs for all elements, both the more noble and less noble impurities, compared to aluminium.

The model considered, irrespective if a single or double exponential function is applied, is based on the assumption that mass transfer takes place from bath to metal only. In addition the concentration of the species M^{n+} was set equal to zero at the phase boundary. Losses due to dusting while adding or evaporation during cell operation are not taken into account either. The additions made to the cell are assumed to be complete. However, as shown in Table 6-3, this was certainly not the case for phosphorus.

In addition, it is known that phosphorus is an impurity that interacts strongly with the gas phase (see Section 2.1.4.2.). Therefore, modelling the transfer of phosphorus from bath into metal may not be entirely correct.

6.3.7. Mass balance of phosphorus for prebake and Søderberg cells

For a typical prebake line at Hydro Aluminium Årdal, a mass balance concerning phosphorus was derived by Haugland et al. [10]. The results are briefly sketched here. The cells were fed with secondary alumina from the dry scrubber. The anodes were covered with a mixture of crushed electrolyte and alumina. Cover material and solidified electrolyte leave the cell when an anode is changed.

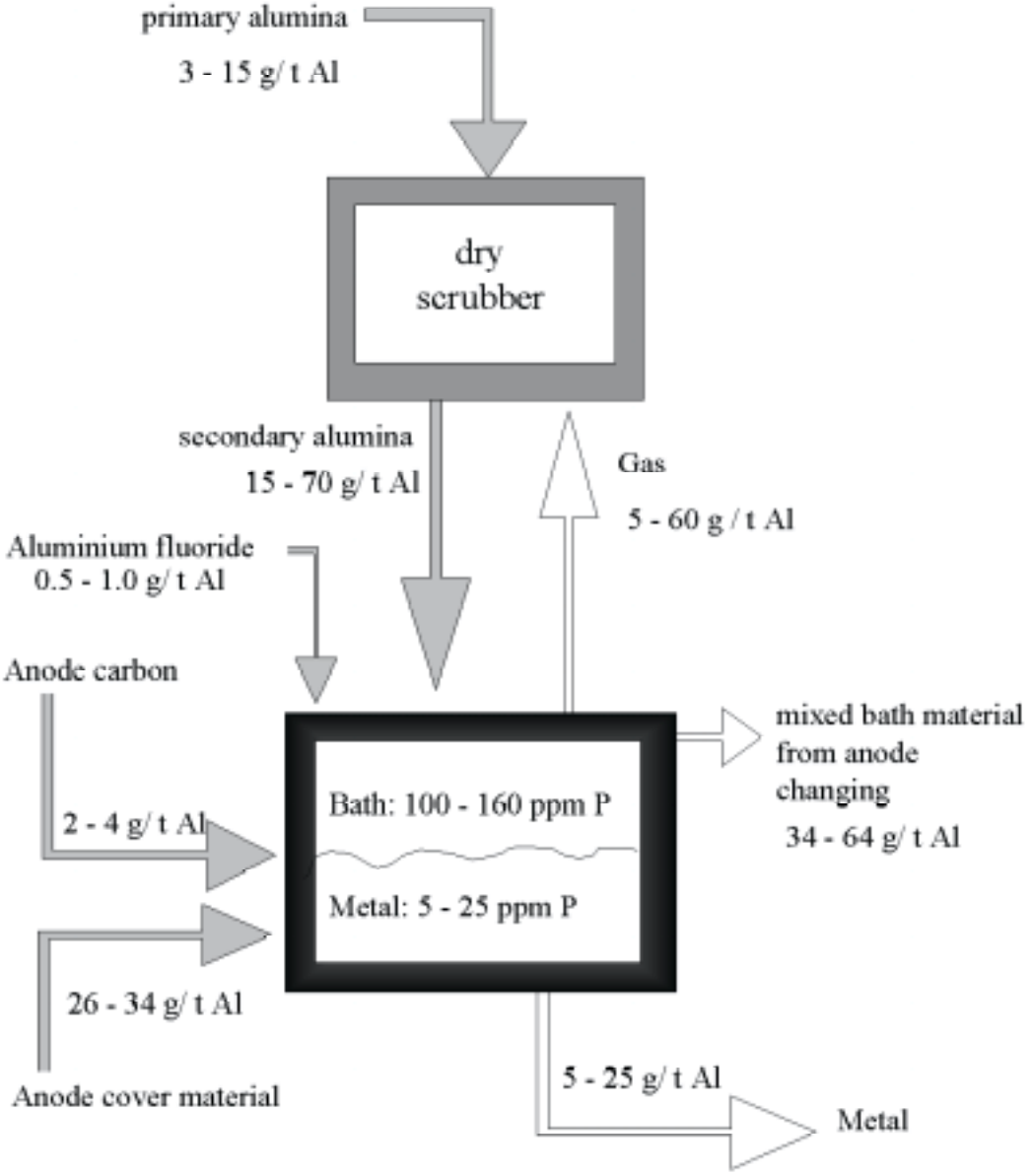

Fig. 6-15: *Mass balance for phosphorus. The phosphorus content in the various mass flows for a typical prebake Hydro Aluminium line is given [10].*

The difference in phosphorus concentration between primary and secondary alumina depends on the amount of P escaping from the cell with the process gas. High temperature and high concentration of carbon dust in the electrolyte result in an increased amount of P escaping the cell with the process gas or with the covering material.

Most of the phosphorus in the process gas will be collected in the dry scrubber and recycled to the cells with the secondary alumina. Also the phosphorus in the cover material and in the electrolyte removed during anode changing is recycled to the cells as new cover material.

Due to the large variations of phosphorus in the raw materials, it is not a straightforward matter to determine the percentage of the ingoing phosphorus leaving with the metal. However, if less phosphorus leaves the cell with the aluminium than what enters with the raw materials, there may be a gradual build-up of P in the system. Haugland et al. [10] claimed that up to 80% of the phosphorus entering the process with primary alumina ends up in the metal.
There is, however, a large uncertainty associated with this estimate, as the numbers in Figure 6-15 indicate.

A similar mass balance was performed for a Søderberg line at Hydro Aluminium, Årdal. The cells are fed with primary alumina. The top crust of the cell consists of a mixture of primary alumina and solidified electrolyte. The bath chemistry is different from a prebake cell with regards to the aluminium fluoride content. About 9 to 10 wt% excess AlF_3 is typical in relation to 12 to 13 wt% AlF_3 in a prebake cell. Consequently, the operating temperature is about 10 ºC higher than for a prebake cell.

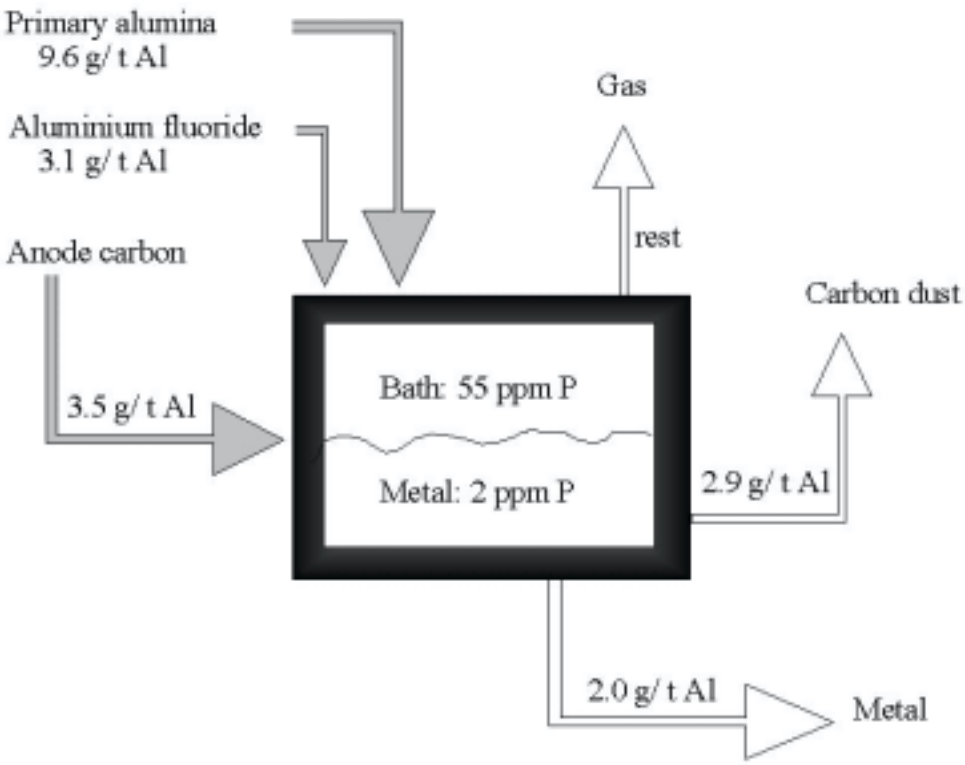

Fig. 6-16: *Mass balance for phosphorus. The phosphorus content of the different mass flows for a typical Hydro Aluminium Søderberg line (115 kA) is given.*

As Figure 6-16 shows, only about 10 % of the phosphorus leaves the cell with the metal. When carbon dust is skimmed from the cell, 20% of the phosphorus is removed from the cell. The rest is assumed to leave with the off gases. Part of it will escape through the roof, while most of it will leave the line with the gas collection system and be trapped in the dry scrubber. The secondary alumina from the dry scrubber goes to the prebake cells at the Årdal plant.

When comparing the mass balances of phosphorus for the two different cell types, it is obvious that the hooding of the cell and the type of alumina feed

influence the amount of phosphorus transferred through the cell and in what way phosphorus escapes. The bath/metal ratio with respect to phosphorus is usually about 10 for the prebake cells, while in the Søderberg cells the ratio seems to be much larger, with 27.5 as an average, as the mass balance in Figure 6-16 shows.

There are two main differences in operation between the two technologies, which result in a lower phosphorus content in the Søderberg cells. The input of phosphorus to the prebake cells is higher than for the Søderberg cells, since it is fed with secondary alumina. However, we also have to consider the higher operating temperature, the higher content of carbon particles in the bath and the difference in bath chemistry of the Søderberg cells in comparison to the prebake cells. Furthermore, a more intense gas-induced convection may be present in the Søderberg cells, as mentioned in Section 6.3.5.

6.3.8. A model for reactions involving phosphorus and its transport

During normal operation, the transfer of phosphorus in and out of a cell can be illustrated as shown in Figure 6-17. The main source of phosphorus is the alumina. In case of feeding with secondary alumina, the amount of phosphorus added by this raw material is higher compared to primary alumina (see Figure 6-15). Aluminium fluoride, anode cover material and anode carbon contain some phosphorus as well.

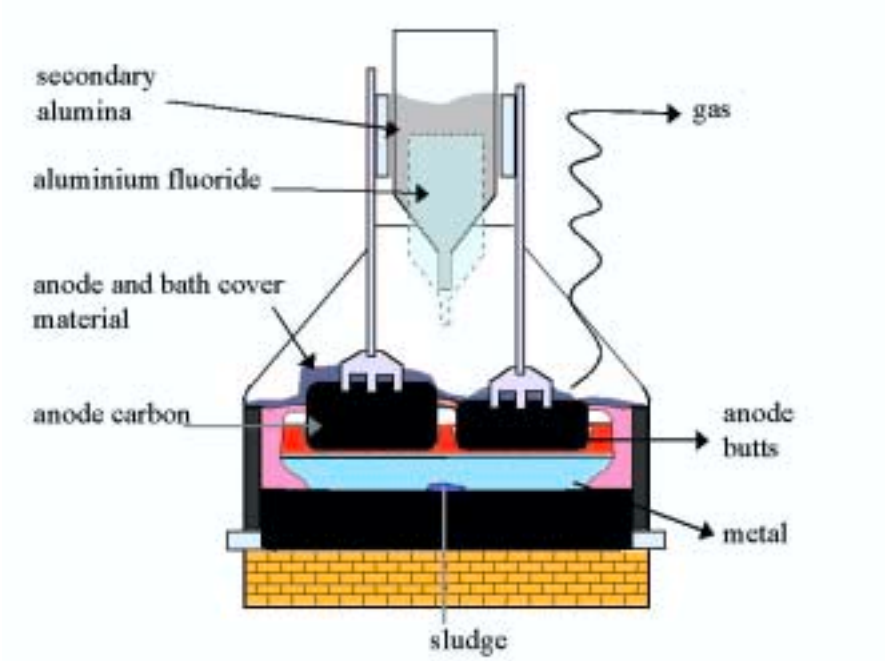

Fig. 6-17: *Transfer of phosphorus in and out of a prebake cell as indicated by the arrows pointing to the left (in) and to the right (out).*

Phosphorus leaves the cell through the off-gas, anode butts and the metal. If sludge is present, some phosphorus can also accumulate there, as found by Geay et al. [21].

A tentative mechanism for the behaviour of phosphorus impurities in the Hall-Héroult process can be proposed:

1) Phosphorus enters the process mainly with the alumina, probably in the form of $AlPO_4$, which dissolves in the bath as a P(V) species.
2) The important oxidation states of phosphorus species in cryolite-alumina melts are assumed to be +5 and +3.
3) Phosphorus species may be reduced at the cathode to elemental phosphorus. A possible formation of gaseous phosphorus may be slow, because it involves nucleation and growth of gas bubbles. It is more likely that phosphorus will dissolve in the electrolyte in a similar way as e.g. elemental sodium or a gaseous species (O_2). Alloying with aluminium may be sluggish, since elemental phosphorus may have a strong tendency to escape into the electrolyte.
4) Phosphorus, reduced to its three-valent state by dissolved aluminium, will be oxidized by dissolved CO_2 in the bath or at the anode. Repetitive reduction and oxidation of phosphorus compounds cause a loss in current efficiency with respect to aluminium.
5) Dissolved P(V) species may also be reduced by impurities in the bath. Small carbon particles (carbon dust) may act as nucleation sites for the formation of adsorbed or solid compounds.
6) Phosphorus species escape with the exit gas and are recycled back to the cells with the secondary alumina. Loss of phosphorus from the cells is mainly due to possible evaporation of phosphorus compounds or due to phosphorus attached to carbon dust that is entrained with the off gases. Evaporation of elemental phosphorus or phosphorus pentoxide seems to be unlikely, due to their reactivity in the presence of air, moisture and aluminium oxide. Some phosphorus may be lost to the environment with small carbon particles.
7) A high proportion (up to 80 %) of the phosphorus entering the process with aluminium oxide eventually ends up in the metal.
8) Increased temperature leads to increased escape of phosphorus and reduced phosphorus content in aluminium.

6.4. Conclusions

Phosphorus behaves differently from other investigated impurities that are more noble than aluminium, such as manganese. For metallic impurities more noble than aluminium a simple mass transport controlled process from bath to metal has been observed.

The retention time of phosphorus in the bath is much longer than for iron, silicon, titanium or manganese. A similar long retention time was observed when lithium was added to the bath. However the uptake of lithium is governed by a chemical equilibrium.

The addition of carbon dust did not show the expected decrease in phosphorus concentration, neither in bath nor in metal. In fact the opposite was found. An instantaneous increase of phosphorus in bath after addition of carbon dust was observed, followed by a delayed increase of phosphorus in metal. Samples of dust from the off-gas ducts showed an increased concentration of phosphorus and iron when carbon dust was added to the cell.

During a current interruption iron and phosphorus followed a similar concentration pattern. The dominating factor for this behaviour is believed to be the dispersion of carbon dust in the bath.

A decreased anode-cathode distance resulted in lower concentration of phosphorus in both bath and metal.

When adding impurities to the bath the variation in concentrations versus time in the beginning was shown to be governed by the distribution in the bath. The distribution times for different elements obtained by the model used in Section 6.3.6. were found to be in good agreement.

The mass balance for phosphorus for prebake and Søderberg cells confirmed that escape via the gas phase is the primary escape route for phosphorus out of the cell. Since dry scrubbers collect the fluorides as well as volatile impurities, phosphorus is recycled to the cell and leaves it mainly via the metal phase.

The mechanism of the reactions involved in the loss in current efficiency induced by phosphorus and its transfer into the metal is not well understood and requires further research.

References to Chapter 6:

[1] T.E. Jentoftsen, *Behaviour of iron and titanium species in cryolite-alumina melts,* Dr.ing. thesis, NTNU Trondheim, Norway, 2000.

[2] H.G. Johansen, *Jern som forurensningselement i aluminium-elektrolysen,* Doctoral Thesis, Department of Electrochemistry, NTNU Trondheim, Norway, 1975.

[3] S. Z. Beer, *The solution of aluminum phosphide in aluminium*, J. Electrochem. Soc., Vol. 116, No.2, pp. 263-265, 1969.

[4] A. Kerouanton, J. Badoz-Lambling, *Comportment chimique et electrochimique de composes du phosphore dans la cryolithe fondue*., Revue de Chimie minerale, **11**, 223, 1974.

[5] W.H. Tingle, J. Petit, W.B. Frank, *Sodium content of aluminium in equilibrium with sodium fluoride-aluminium fluoride melts*, Aluminium **57**(4), 286-288, 1981.

[6] L. Deininger and J. Gerlach, *Stromausbeutemessungen bei der Aluminiumoxidreduktionselektrolyse in Laboratoriumszellen,* Metall, **33**, 131, 1979.

[7] L.P. Lossius, *Removing impurities from secondary alumina,* Dr.ing. thesis, NTNU Trondheim, Norway, 1991.

[8] L.P. Lossius, H.A. Øye, *Removing impurities from secondary alumina fines*, Light Metals 1992, 249-258.

[9] J. Thonstad, F. Nordmo, S. Rolseth, J.B. Paulsen, *On the transfer of some trace elements in dry scrubbing systems,* Light Metals 1979, 463-479.

[10] E. Haugland, G.M. Haarberg, E. Thisted, J. Thonstad, *The behaviour of phosphorus impurities in aluminium electrolysis cells*, Light Metals 2001, 549-553.

[11] S. Rørvik, *P3.8.13 Sot i elektrolysebad*, PROSMAT-prosject, SINTEF/NTNU Trondheim, 1999.

[12] T. Foosnæs, T. Naterstad, M. Bruheim, K. Grjotheim, *Anode dusting in Hall-Héroult cells,* Light Metals 1986, 729-738.

[13] R. Oblakowski, S. Pietrzyk, *Superheating of Na_3AlF_6-AlF_3-Al_2O_3 electrolyte in the process of aluminium electrolysis*, Metallurgy and Foundry Engineering, **21**(3), 175-183, 1995.

[14] S. Rolseth, B. Moxnes, A. Gangstad, *Method for determination of volume of liquid bath in Hall-Héroult cells,* 11th International Aluminium Symposium, Sept. 19.-22., Trondheim-Bergen-Trondheim, Norway, 2001.
[15] K. Tørklep, K. Kalgraf, T. Nordbø, *Alumina distribution in point-fed Hall-Héroult cells,* Light Metals 1997, 377-386.
[16] D.C. Chesonis, A.F. LaCamera, *The influence of gas-driven circulation on alumina distribution and interface motion in a Hall-Héroult cell*, Light Metals 1990, 211-220.
[17] J.M. Purdie, M. Bilek, M.P. Taylor, W.D. Zhang, B.J. Welch, J.J.J. Chen, *Impact of anode gas evolution on electrolyte flow and mixing in aluminium electrowinning cells,* Light Metals 1993, 355-360.
[18] M.L. Walker, J.M. Purdie, N.S. Wai-Poi, B.J. Welch, J.J.J. Chen, *Design considerations for selecting the number of point feeders in modern reduction cells,* Light Metals 1995, 363-370.
[19] S. Rolseth, R. Hovland, O. Kobbeltvedt, *Alumina agglomeration and dissolution in cryolitic melts,* Light Metals 1994, 351-357.
[20] Private communication with S. Rolseth.
[21] P.-Y. Geay, B.J. Welch, P. Homsi, *Sludge in operating aluminium smelting cells,* Light Metals 2001, 541-547.

7. Behaviour of phosphorus during electrolysis – a laboratory study

7.1. Introduction

This chapter covers the results from studying the behaviour of phosphorus during electrolysis in a laboratory cell. From industrial measurements presented in Chapter 6, it was found that several parameters influence the phosphorus concentration in the cell [1, 3, 4]. An increase in bath temperature was believed to cause a decrease in the phosphorus content of the metal and an increase in the bath phase. The presence of carbon particles was assumed to influence the impurity level in the bath where carbon particles serve as nucleation sites for various impurities (Fe, Ni, P etc.).
Since an industrial cell is a complex dynamic system, several parameters were investigated independently in a laboratory cell, i.e. temperature, carbon content in the bath and current interruption, which apparently influence the phosphorus level.

7.2. Cell design

When studying the influence of different parameters in a laboratory cell, it is important that the convective conditions are reproducible. The mass transport in the bulk of the electrolyte should occur at a reasonable high rate to establish conditions that are as similar as possible to an industrial cell. Good convection leads to a decrease in the cathodic diffusion layer thickness and thereby an increase in the rate of mass transport. Therefore, a reproducible convective pattern in the laboratory cell is important. The cell design used for the experiments was developed by Solli et al. [6].

As pointed out by Solli [7], traditional laboratory cells often have a poorly wettable cathode material. This results in a hemispherical or even an almost spherical aluminium pad, as shown in Figure 7-1 a). In preliminary experiments this behaviour was observed in a cell with a graphite bottom lining. A picture of the crucible from this experiment can be seen in Appendix K, Figure K-1. Such behaviour will decrease the current efficiency (CE), since the cathodic current density approaches zero towards the side-walls, even though the average cathodic current density is high.

The CE will, therefore, be lower than in the case of a wettable cathode material, e.g. steel or copper.

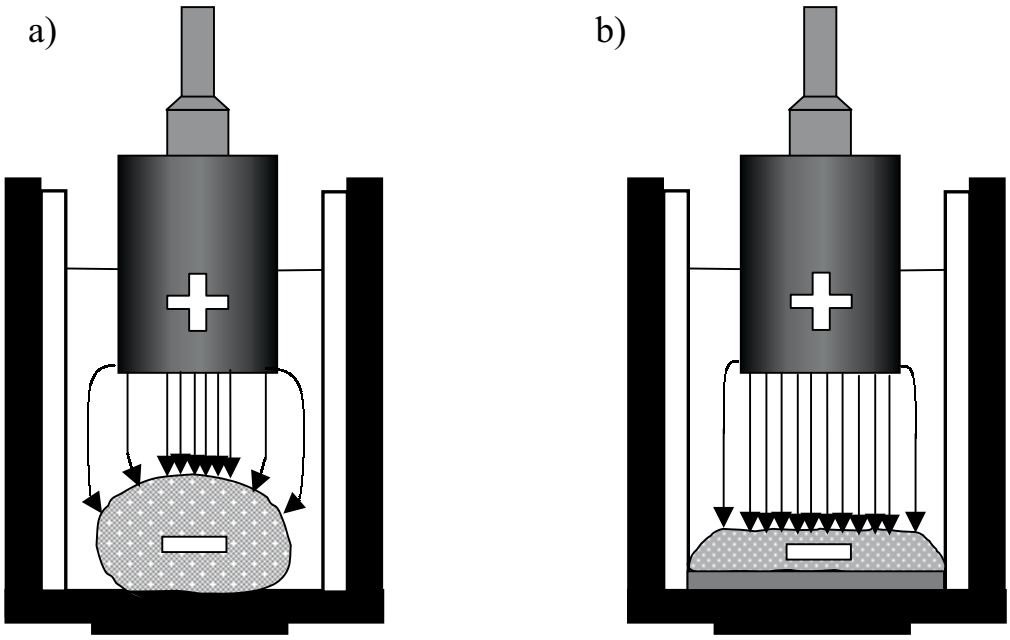

Fig. 7-1: *Sketch of laboratory cells with different substrate materials, a) cell with graphite bottom lining, b) cell with wettable bottom lining. Current lines are sketched. Side-walls of sintered alumina.*

As can be seen from Figure 7-1 b), a flat cathode surface will lead to a more uniform current distribution and probably a higher current efficiency. When it comes to current efficiency, cell design is an important factor, but bath composition, mass transfer coefficients and temperature also have some influence.

In comparison to industrial cells where current efficiencies of up to 96% are obtained, the loss in CE will be higher for this laboratory cell due to loss of aluminum into the electrolyte before starting electrolysis.

7.3. Experimental set-up and procedure

The experiments were performed in a furnace closed tightly to the ambient atmosphere, similar to the one shown in Figure 4-1 to the left. Argon was flushed through the furnace at a constant rate to avoid airburn of the crucible, the cathode supporter or the anode, which all consisted of graphite. To achieve an even current distribution, the inner wall of the graphite crucible was protected by a sintered alumina side-lining. The aluminium was deposited on a metal plate (steel or copper) instead of on the graphite bottom; this ensured a better wetting and thereby a flat cathode surface, as explained in Section 7.1. A disadvantage is the solubilities of steel and copper in aluminium. The laboratory cell used is shown in Figure 7-2.

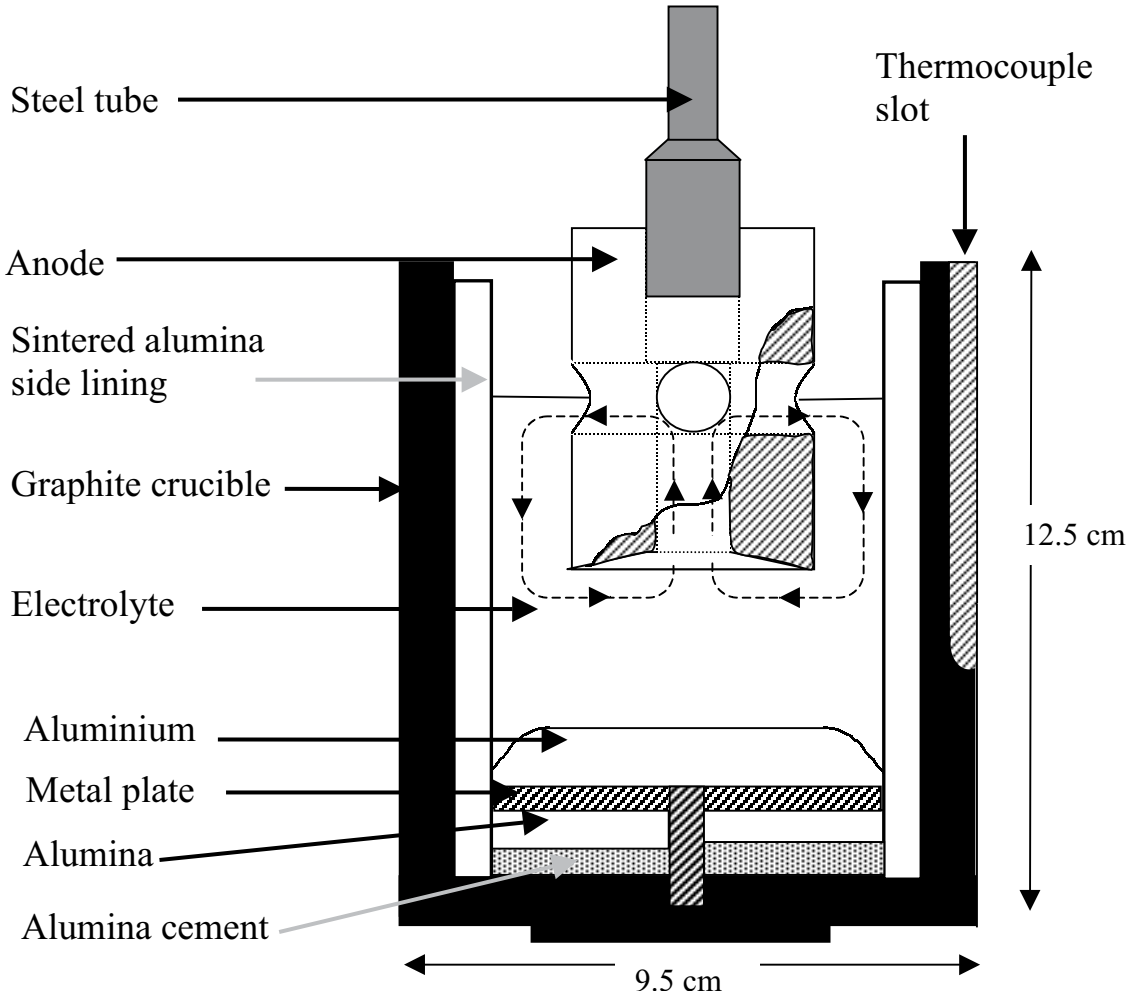

Fig. 7-2: *Electrolysis cell used in laboratory studies of the behaviour of phosphorus. The broken lines indicate the bath circulation pattern.*

A cell, similar to the one used in the current efficiency studies by Solli [7], was used for the experiments in this work. This cell should ensure reproducible convective conditions and an almost flat metal surface during electrolysis.

The anode was cylindrical with a vertical hole from the bottom to the top, where a steel tube was connected. At the bottom of the anode the surface was inclined ~10º upwards towards the center to improve the gas bubble movement to the center hole of the anode. The design of the anode with two additional holes drilled perpendicular to each other and perpendicular to the vertical hole should provide a convective pattern during electrolysis as shown in Figure 7-2. The movement of the gas bubbles through the anode should establish a uniform bath circulation.

Since steel and copper are somewhat soluble in aluminium, it might reduce the activity of aluminium at the surface. This affects the current efficiency, as is explained in detail in Appendix L. The metal plate of steel or copper was placed on a layer of alumina on top of a layer of cast alumina cement ("Termomax", see Table 7-1). With this arrangement it should be ensured that aluminium was not lost by getting into contact with the bottom of the graphite crucible, forming aluminium carbide.

Before starting the electrolysis the anode had to be positioned by lowering it until electrical contact with the bath was achieved. From there the anode was lowered an additional 2.5 cm, so that the bath surface level was at the middle of the horizontal holes in the anode, as shown in Figure 7-2. The bath temperature was measured using a Pt/Pt10Rh thermocouple, which was positioned in a slot outside the graphite crucible. In a preliminary experiment, the temperature difference between the temperature measured in the bath and the temperature measured in the slot was determined. This difference was added to the recorded temperature found in the slot. The reported temperatures are the corrected bath temperature values. The error in temperature was estimated to be ± 4 ºC.

A DC power supply (Hewlett-Packard, 0-50 A) was used to supply 26 A to the cell. The cathodic current density was determined as the total current divided by the cross-sectional area of the inside of the alumina side-lining. Typical recorded data for temperature, current and voltage can be found in Appendix M.

The electrolyte consisted of cryolite, alumina, aluminium fluoride and calcium fluoride (~350 g). The exact composition is given for each experimental series. When preparing the experiment, aluminium (130 – 150 g) was placed in the crucible to ensure that there was enough aluminium to provide a sufficient amount for analysis. After heating the furnace to the experimental temperature, samples of bath and metal were taken. As sampling device a quartz tube was used. A syring to provide suction was fixed to the tube. The height of sampling was determined by the marks of the frozen bath on a stainless steel wire, which was immersed into the cell for a very short time. Usually sodium orthophosphate was added in the form of powder (mixed with approximately 3 g of alumina) through the anode steel tube to the melt, and another set of bath and metal samples were taken.

For the experiments where stainless steel was used as wettable cathode material, the phosphate was mixed with the other bath components initially. Electrolysis was run for four hours. Sampling was performed every 30 minutes for both bath and metal, and alumina was added according to the calculated amount of aluminium produced as shown below. A current of 26 A was applied to the cell in the case of the copper cathode material, whereas in the case of the steel cathode material, 26.5 A was applied, as reported in Solli's work [7]. By means of Faraday's law the amount theoretically produced during four hours (14400 s) can be obtained,

$$m_{Al,theor} = \frac{I \cdot t \cdot M_{Al}}{n \cdot F} = \frac{26 \cdot 14400 \cdot 27}{3 \cdot 96487} = 34.9\,g \qquad (7.1),$$

For 30 minutes electrolysis time 4.4 g aluminium is produced at 100% current efficiency. To supply the electrolyte with a sufficient amount of alumina, 8.2 g of alumina was added every 30 minutes after taking a set of bath and metal samples. During the experiments between 7 and 9 g of alumina was added after each sampling procedure as long as electrolysis was performed.

After cooling of the furnace, the crucible was taken out and cut open to remove the solidified metal. The metal was carefully cleaned from residual bath. A constant estimated loss of about 0.35 g (1% of the theoretical production at a cathodic current density of 0.833-0.85 A/cm^2) due to loss of metal during cooling, penetration through the alumina cement protection and formation of carbide by contact with the graphite crucible, was added to the metal weight obtained [7]. In addition the weight of the metal

samples was taken account of as well. Thereby the total production of aluminium during the electrolysis period was obtained. The theoretical production was derived by Faraday's law as shown in equation (7.1). The current efficiency was calculated according to equation (7.2).

$$CE_{Al}[\%] = \frac{m_{Al}}{m_{Al,theor}} \cdot 100 \qquad (7.2)$$

The preparation procedure for the bath and metal samples for analysis with ICP-AES can be found in Appendix D.

7.4. Chemicals

The chemicals and metals used in the experiments are presented in Table 7-1. The concentration of phosphorus in the different raw materials was either found in the analysis rapport of the producer or determined with ICP-AES or OES (optical emission spectrometry).

Table 7-1: *Specifications of the chemicals used in the experiments and the corresponding content of phosphorus in them.*

Chemical	Producer/quality	Pretreatment	concentration of P [ppm]
Na_3AlF_6	Hand-picked, natural Greenland cryolite	stored at 200 ∀C in a heating chamber before use	4 ± 3[a)]
Al_2O_3	Fluka, p. a.	heated to 1200 ∀C for 4 hours, thereafter stored at 200 ∀C in a heating chamber before use	0[a), b)]
AlF_3	technical, Norzink, Norway	sublimated at 1000 ∀C at <1mbar for 24 hours	3 ± 3[a)]
CaF_2	gefällt rein, Merck	stored at 200 ∀C in a heating chamber before use	0[a), b)]
Al	99.99% pure, Vigeland	used as received	0[a), b)]
Steel		used as received	160-320[c)]
Cu		used as received	Ò10[b)]
Termomax alumina cement	refractable castable, Borgestad Fabrikker A.S., Norway	used as received	5 ± 4[a)]
Ar	Argon 4.0 (99.99%), AGA	used as received	0[b)]
Na_3PO_4	Riedel-de-Haën, pure	stored at 200 ∀C in a heating chamber before use	-
Carbon powder	LECO	used as received	-

a) analysed by ICP-AES, b) analysed by OES, c) analysed by producer

7.5. Results and Discussion

7.5.1. Experimental series with steel as cathode material

The electrolyte consisted of 79 wt% Na_3AlF_6, 7 wt% AlF_3 (CR = 2.5), 5 wt% CaF_2 and 9 wt% Al_2O_3. Aluminium was present from the start by placing 130 to 150 g in the crucible before the bath mixture was added. The metal samples taken during electrolysis were analysed for iron as well as phosphorus, since the steel cathode lead to dissolution of iron into aluminium. According to phase diagrams for the Al-Fe system (see Appendix N), the solubility of iron in aluminium is about 15 wt% at 980 ºC. Between 8 and 12 wt% iron was found in the aluminium samples when ICP-AES analysis was applied.

In an earlier work by Solli [7], current efficiency studies were performed in the presence of P_2O_5 or $Ca_3(PO_4)_2$. The bath composition was similar except for the alumina concentration, which in Solli's work was 4 wt%. According to the results by Solli [7], the alumina content had no influence on the current efficiency. A model developed by Sterten [8] also shows that an increase in the alumina concentration only slightly affects the current efficiency. Figure 7-3 shows the resulting current efficiency versus the added amount of phosphorus in ppm from Solli's work and from the experiments performed in this work.

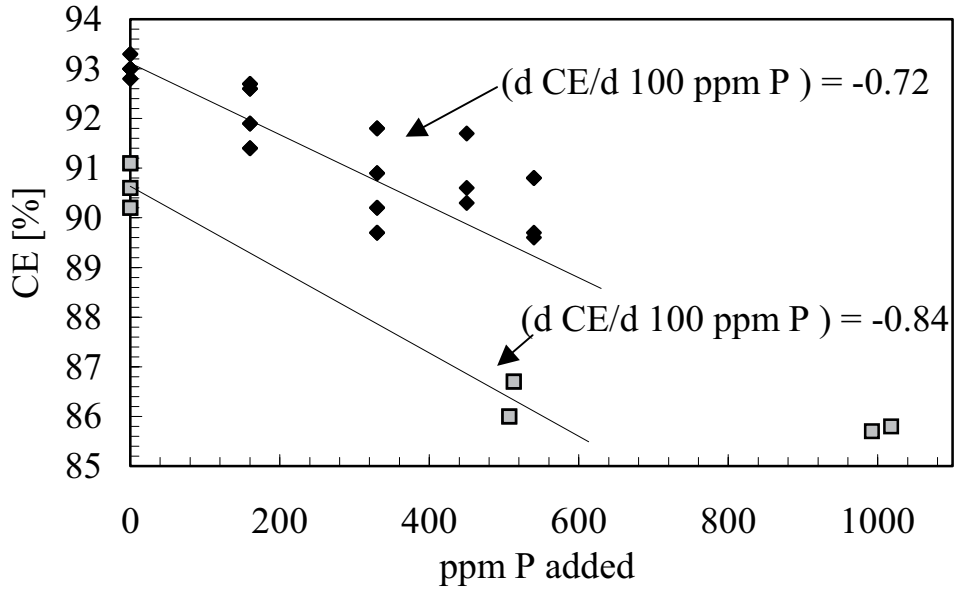

Fig. 7-3: *Current efficiency versus the amount of P added; results of Solli [7] as filled diamonds and results from this work as grey squares.*

As can be seen, the relationship between current efficiency loss and the added amount of phosphorus obtained in this work is similar to the results of Solli. Solli stated that the effect of phosphorus on CE levels off at concentrations higher than 330 ppm P. He claimed that this might be due to an increased rate of evaporation of phosphorus species, thus giving a lower phosphorus level in the bath than that actually added. Unfortunately, he did not analyse the bath to confirm his assumptions. The obtained results support the idea of Solli, but the CE levels off at higher concentrations (above 500 ppm P).

The lower current efficiency of this work compared to Solli's results cannot be due to the higher amount of alumina in the bath. The cathodic current density was similar to the one reported by Solli (0.85 A/cm^2). It should be noted, that Solli did not take samples during the electrolysis period, therefore the system was not subjected to disturbances by removing bath and metal. This may explain why the current efficiency achieved in this work was lower than in Solli's work. Replotting Solli's results gave a decrease in current efficiency by 0.72 % for each 100 ppm P added to the bath. This value obtained deviates by 0.04% from the slope given in Solli's thesis.

From the present work a decrease of 0.84 % of CE per 100 ppm P added was obtained. However, this estimate is based on values at only two concentrations. Fitting a regression line by the least squares method, the following equations are obtained,

$$\%CE = -(0.0072 \pm 0.0013) \cdot c\,(P_{added}) + (93.1 \pm 0.3) \qquad \text{(Solli)}$$

$$\%CE = -(0.0084 \pm 0.0009) \cdot c\,(P_{added}) + (90.6 \pm 0.3) \qquad \text{(this work)}$$

In Solli's work the phosphate was mixed with the other bath components before the experiment. In this work the analysis of the bath samples taken during the electrolysis period showed that the amount of phosphorus in the bath did not remain constant throughout the whole period of electrolysis. The added amounts of 500 and 1000 ppm phosphorus had decreased to about 300 and 400 ppm in average respectively. Thereby the relationship between current efficiency loss and amount of phosphorus present in the bath would show that for each 100 ppm P in the bath the current efficiency would decrease by 1.2 – 1.3 %. Considering the rule of thumb for phosphorus, by which a 1% CE loss is ascribed to about 100 ppm P in the

electrolyte, it can be seen that the results obtained for the analysed concentration of phosphorus in the electrolyte are roughly in agreement.

The phosphate added might partly have evaporated, but also transferred to the aluminium phase. The analysis of the aluminium samples by ICP-AES, however, gave a phosphorus content that was too high (~300 to 400 ppm), even when considering that part of the phosphorus added would be reduced and transferred into the metal. From the analysis of the stainless steel plate it was found that firstly the dissolution of the steel plate into the aluminium phase did introduce some phosphorus and thereby contaminated the aluminium to a certain degree (20 to 50 ppm P). Also, the analysis method by ICP-AES of the dissolved aluminium samples was found to be incorrect (see Appendix O).

The main purpose was to study the effect of phosphorus on the current efficiency and the change on the distribution of phosphorus in bath and metal with changing operating temperature. Therefore, the starting materials should not contain a significant amount of phosphorus. In order to avoid that, copper was chosen as cathode material, since it was available with less than 10 ppm P.

7.5.2. Experimental series with copper as cathode material

The influence of temperature, carbon content in the bath and current interruption during electrolysis on the concentration of phosphorus in bath and metal was investigated.

7.5.2.1. Effect of temperature

A range of temperatures between 940 ºC and 1020 ºC was chosen to study the effect on the phosphorus added to the melt. The melt composition for the experiments at 980 ºC, 1000 ºC and 1020 ºC was the same as for the experiments described in Section 7.5.1. For lower temperatures (940 ºC and 960 ºC), the bath composition had to be changed in order to keep the mixture molten. The electrolyte used for the experiments at 940 ºC and 960 ºC initially consisted of 69 wt% Na_3AlF_6, 6 wt% AlF_3 (CR = 2.5), 17 wt% CaF_2 and 6 wt% Al_2O_3. The alumina additions during electrolysis were accordingly reduced to 6 - 7 g to avoid feeding above the solubility limit of alumina in this melt composition.

In Figures 7-4 and 7-5 the results for the various electrolysis temperatures are presented with regard to phosphorus additions (added to the bath) of 0, 1000, 2000 ppm. The dotted lines mark the start of electrolysis. For measurements without phosphate addition one sample was taken of both bath and metal before electrolysis.

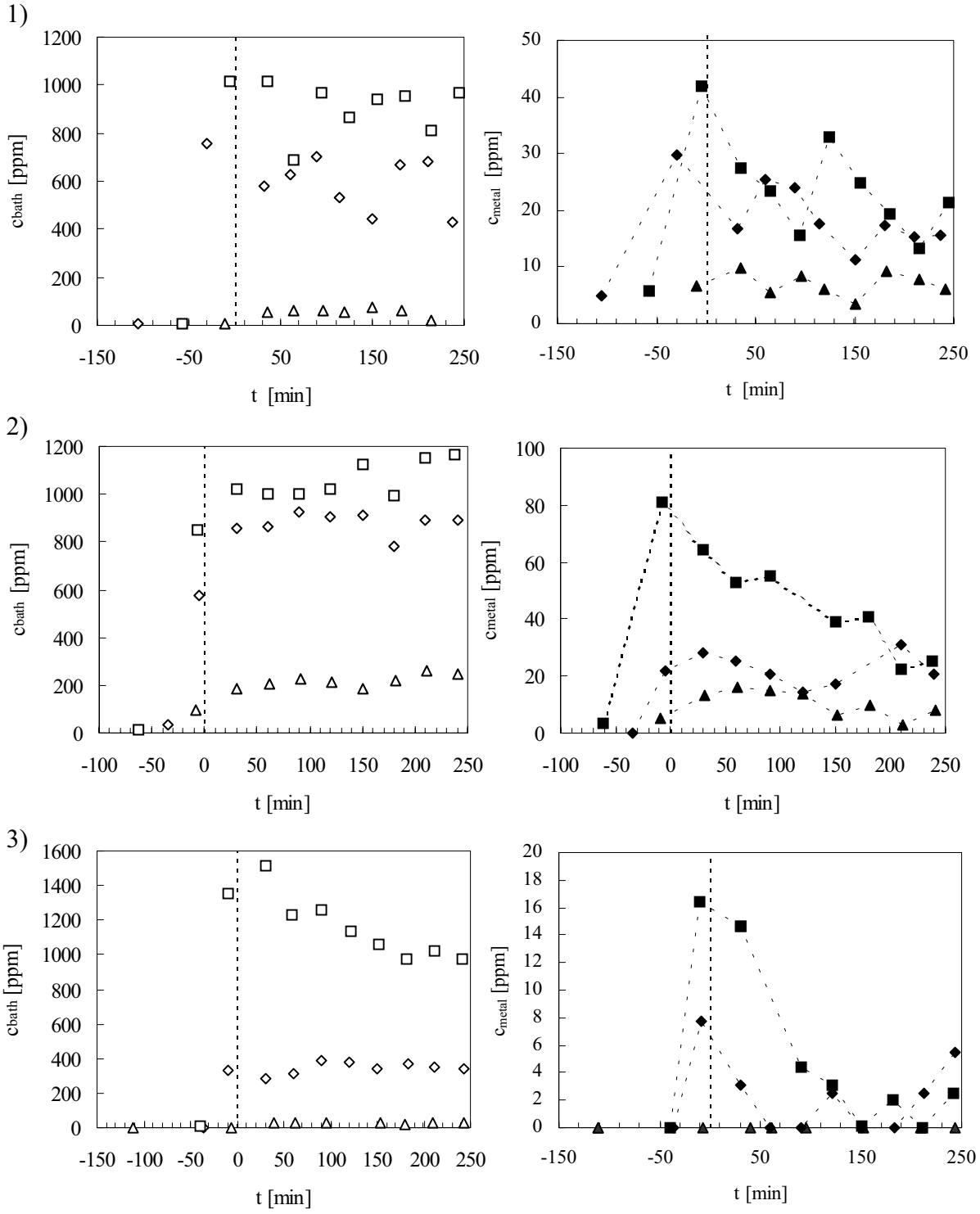

Fig. 7-4: *Temperature effect on phosphorus in bath and metal during electrolysis; 1) 940 ºC, 2) 960 ºC, 3) 980 ºC. To the left phosphorus in bath, to the right phosphorus in metal. Amount of P added [ppm]: △/▲ 0, ◇/◆ 1000, □/■ 2000. The dotted line marks the start of electrolysis.*

4)

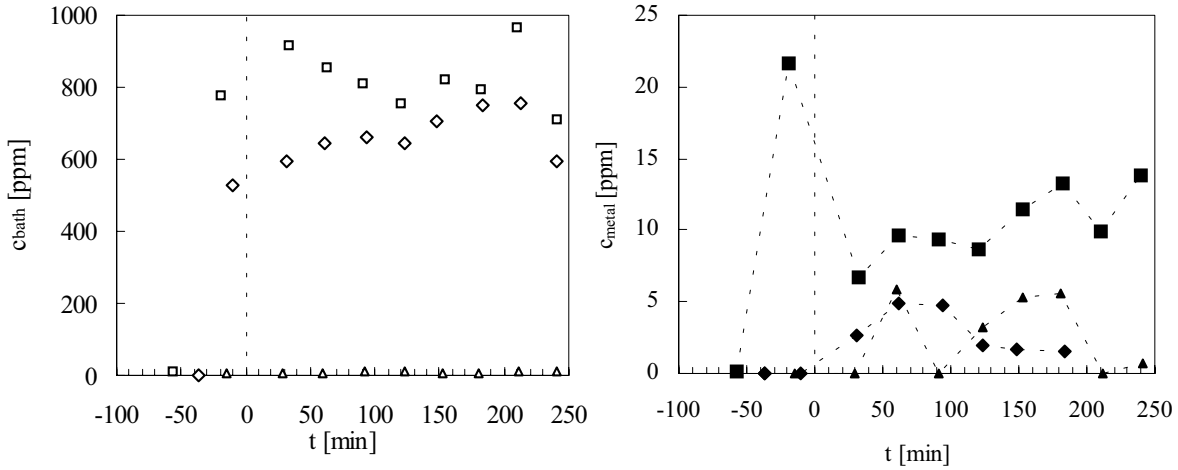

5)

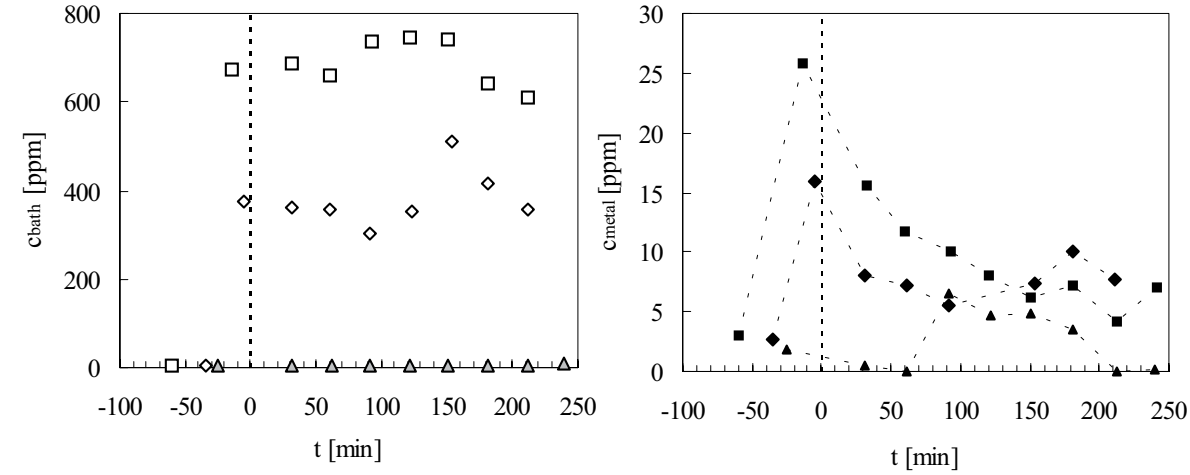

Fig. 7-5: *Temperature effect on phosphorus in bath and metal during electrolysis; 4) 1000 ºC, 5) 1020 ºC. To the left phosphorus in bath, to the right phosphorus in metal. Amount of P added [ppm]: △/▲ 0, ◇/◆ 1000, □/■ 2000. The dotted line marks the start of electrolysis.*

For measurements with phosphate additions two sets of samples were taken before the start of the electrolysis. The first one was done before sodium orthophosphate was added, while the second sampling was done after addition of phosphate.

In general it is obvious from the results that the added amounts of phosphorus are not equal to the measured amounts of phosphorus in the bath. A maximum deficit of nearly 70% can be observed when looking at the figure of the bath analysis for 980 ºC, where 1000 ppm added phosphorus resulted in an initial value of 330 ppm before electrolysis. In this particular experiment were observed blue-greenish coloured flames

were observed at the anode steel tube when the alumina-sodium orthophosphate mixture was added. For experiments without phosphate additions regardless of the operating temperature, no flames were observed at the anode steel tube when alumina was added to the melt. The evolution of the flames seemed to be related to the added phosphate. Since the phosphate was added as powder, the conclusion might be drawn that the powder got stuck in the anode steel tube. However, visual observations of the inside of the steel tube before and after addition did not show any particles adhering to the inner wall. Therefore, it might be assumed that some of the phosphate escaped right after addition.

A possible reaction, leading to evaporation of phosphorus, can be that aluminium dissolved in the electrolyte reacts with the added phosphate, forming alumina and gaseous phosphorus. Since there is no crust covering the bath in the laboratory cell, the gaseous phosphorus can easily escape through the anode steel tube. Another possibility, even though excluded by thermodynamic calculations in Section 2.1.4.2., Table 2-10, is carbothermic reduction of the added phosphate. Initially, the graphite "anode" was elevated above the bath surface when Na_3PO_4 was added. Since the sodium orthophosphate was added as powder, the large surface area might favour a direct reaction with the carbon.

The phosphorus content in the bath stayed at a rather constant level from the point of time before electrolysis is started and throughout the experiment. Minor deviations might be due to density differences in the bath, which do not ensure a uniform distribution of the phosphorus species in the melt. Monnier et al. [9] studied the evolution of elementary phosphorus and production of nickel phosphides during electrolysis of a eutectic Na_3AlF_6-NaF melt at 900 ºC, containing 3% P_2O_5. They found that this melt could be electrolysed for several hours (0.2 – 0.75 A/cm^2) without observing a significant loss of phosphorus. The cathodes used by Monnier et al. [9] were carbon and nickel, where gaseous phosphorus and nickel phosphide respectively, were formed during electrolysis. The anode always consisted of carbon. However, the concentration of phosphorus in the melt used by Monnier surmounts the highest concentration added in this work (2000 ppm P) by 150 times.

Concluding from Monnier's work, the reduction of five-valent phosphorus to elemental phosphorus is concentration dependent, since, even though gaseous phosphorus or nickel phosphide were produced, the major part remained at a stable concentration in the bath. This conclusion is supported

by Deininger and Gerlach [10], who found a change in the reduction mechanism when the concentration of phosphorus in the bath exceeded 0.12 wt%. When looking at the phosphorus concentration in the bath for the addition of 2000 ppm P at 980 ºC (Fig. 7-4 3)), we can see that the phosphorus concentration decreased from 1520 ppm towards 1000 ppm. In all other cases the phosphorus concentration in the bath was at or below 1000 ppm P, and as mentioned above, remained constant throughout the period of electrolysis. Since the solubility of phosphates is high in cryolite-based melts, as shown in Chapter 4 for $AlPO_4$, and reported by Del Campo [11] for $Na_4P_2O_7$, the low contents of phosphorus observed in the bath cannot be related to low solubility.

A general feature for the phosphorus concentration in the aluminium phase in the experiments where phosphate was added, is a rapid increase followed by a decrease when starting the electrolysis. A trend towards lower concentration of phosphorus in the aluminium metal when the bath temperature was increased is not obvious, as it was found in industrial cells [1, 3]. The concentration of phosphorus in aluminium seems to vary rather randomly at different bath temperatures. Nevertheless, regarding one experimental series at one bath temperature, an increased amount of phosphorus in the bath corresponds to an increased amount of phosphorus in the aluminium phase.

However, it should be considered that the bath used in the experiments at 940 ºC and 960 ºC had a high content of CaF_2. According to Simensen [12], phosphorus in aluminium alloys is mainly present as Na-Ca-K-P compounds and not AlP, as might be expected. The increased amount of calcium in the bath would lead to an increased amount of calcium in the aluminium and thereby favour the formation of an alkaline-earth alkali-metal-phosphorus liquid alloys. This might be a possible explanation for the higher phosphorus concentrations in aluminium in the experiments at 940 ºC and 960 ºC.

The current efficiency data obtained with copper as cathode material were about 10% lower than the ones obtained with the stainless steel plate as cathode plate. Since copper and aluminium formed a liquid alloy during the experiment at the operating temperatures (see Appendix N), the contact to the bottom of the graphite crucible may have been disturbed. In Figure 7-6 the shapes of the cathode after solidification, as obtained with the two starting materials, copper and stainless steel, are shown with the remaining aluminium. The complete alloy formation for the aluminium-copper

cathode is obvious, compared to the stainless steel plate with the aluminium metal. We assume that the copper is uniformly distributed in the metal phase.

Due to the dissolution of both iron and copper into the aluminium phase, the activity of aluminium will be lower than unity. This should result in a higher current efficiency. The change in CE is estimated in Appendix L.

Fig. 7-6: *Comparison of the remaining aluminium/cathode material after the experiment. To the right: aluminium and stainless steel; to the left: aluminium-copper alloy.*

The formation of an Al-Cu alloy and thereby a liquid cathode on top of the alumina cement, apparently led to additional metal losses. The liquid metal must have crept under the alumina cement and formed aluminium carbide, as presented in a sketch in Figure 7-7. A yellow layer and some aluminium metal between the bottom of the graphite crucible and the alumina cement was always found when dismantling the crucible after the end of an experiment. In some cases a yellow layer was found between the alumina side-lining and the graphite crucible wall. This indicates that the liquid alloy had penetrated this area and reacted with the graphite to form Al_4C_3 (see Appendix K, Figure K-2). This might also contribute to the much lower current efficiencies when using copper as cathode starting material instead of steel.

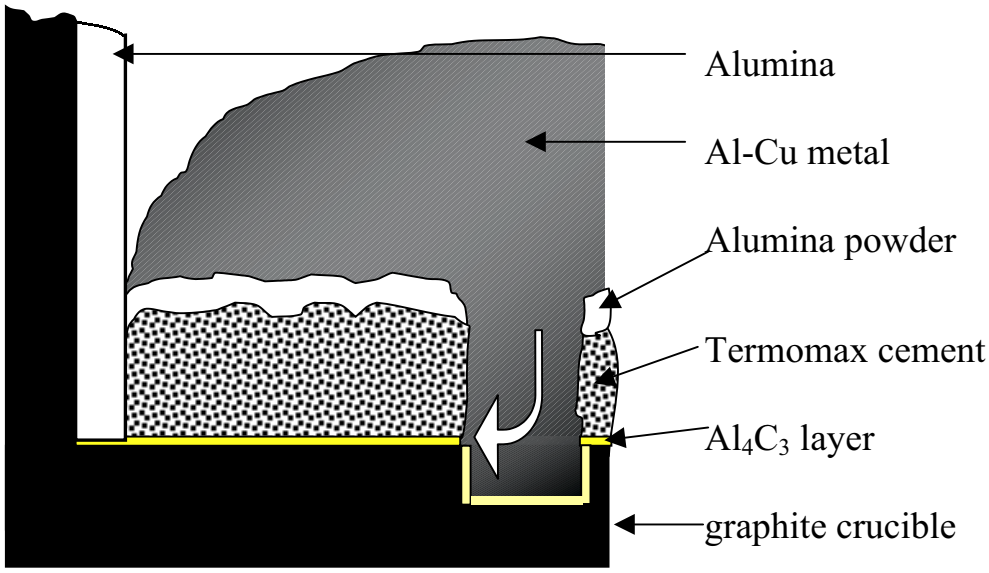

Fig. 7-7: *Sketch of the cell bottom showing the formation of aluminium carbide during the experiment. The arrow indicates how the metal moves between the cement layer and the bottom of the graphite crucible.*

Table 7-2: *Current efficiency as a function of added amount of phosphorus and temperature.*

Bath temperature [ºC ± 4 ºC]	ppm P added [± 10 ppm]	average ppm P in bath analysed	CE [%]	% CE loss / 100 ppm P in bath (analysed)
940	0	56 ± 18	82.6	-
-“-	1000	583 ± 106	77.1	1.04 ± 0.21
-“-	2000	902 ± 108	72.9	1.15 ± 0.15
960	0	11 ± 5	83.2	-
-“-	1000	880 ± 44	77.0	0.71 ± 0.04
-“-	2000	1060 ± 74	75.4	0.74 ± 0.05
980	0	24 ± 4	82.2	-
-“-	1000	344 ± 35	74.1	2.53 ± 0.28
-“-	2000	1148 ± 184	69.8	1.10 ± 0.18
1000	0	68 ± 13	80.9	-
-“-	1000	669 ± 62	73.6	1.21 ± 0.13
-“-	2000	830 ± 82	72.2	1.14 ± 0.12
1020	0	78 ± 15	83.5	-
-“-	1000	379 ± 62	81.7	0.60 ± 0.13
-“-	2000	687 ± 50	80.4	0.51 ± 0.04

The loss in current efficiency per 100 ppm P in the bath was found to be close to 1% for most of the experiments, as can be seen in Table 7-2. Exceptions are the experiment at 980 ºC when adding 1000 ppm P and the experimental series at 1020 ºC. However, the results are roughly in agreement with Solli [7] and the rule of thumb used in the industry (1% CE loss for each 100 ppm P in the bath).

7.5.2.2. Effect of carbon dust in the bath

As pointed out in Section 2.1.4.2., the presence of carbon particles (dust) in the electrolyte of industrial cells has an influence on the process impurities, especially phosphorus. It was assumed that due to the adsorption effect of carbon towards phosphorus and other impurities, e.g. iron or nickel, carbon particles in the bath phase might have a kind of purifying effect, transporting the impurities out of the bulk of the electrolyte towards the surface or even on top of the cell crust. Thereby it might be possible to reduce the phosphorus concentration in the bath by addition of carbon dust to the cell.

Carbon powder (see Table 7-1) was added during electrolysis with an electrolyte composition similar to the one described in Section 7.5.1. at 980 ºC, with additions of 1000, 2000 and 5000 ppm P. The results are presented in Figure 7-8.

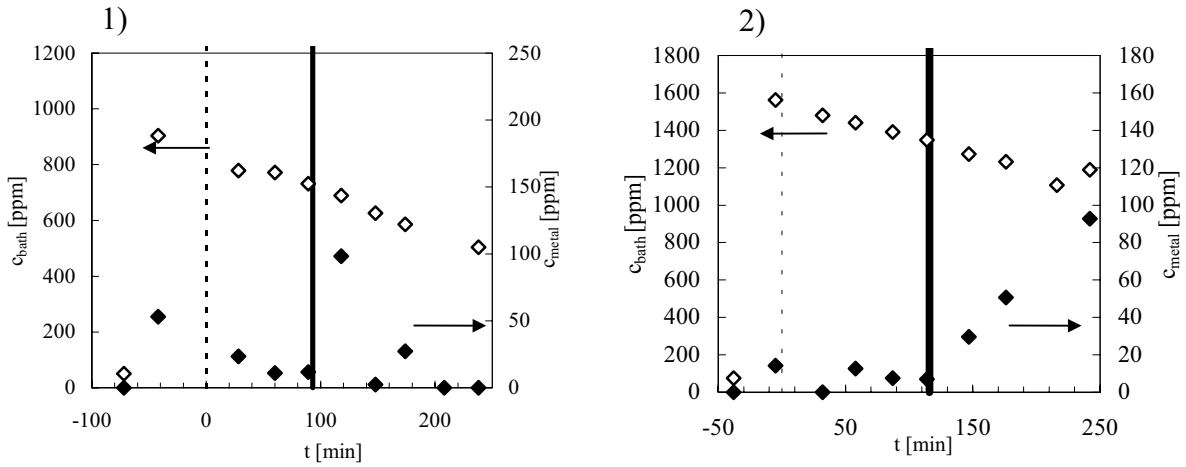

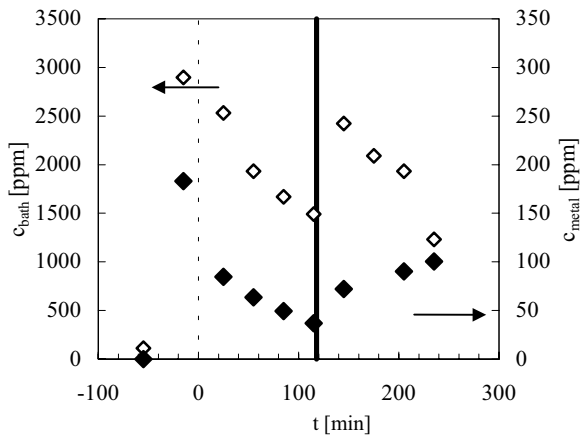

Fig. 7-8: *Effect of the presence of carbon powder in the electrolyte on phosphorus in bath and metal during electrolysis at 980 ºC for additions of 1) 1000 ppm P, 2) 2000 ppm P and 3) 5000 ppm P. The dotted line indicates the start of electrolysis. The thick full line indicates the time of addition of carbon. P in metal as full symbols, P in bath as open symbols.*

As can be seen from Figure 7-8, the addition of carbon powder to the bath during electrolysis does not lead to any obvious "cleaning" effect for phosphorus. For the measurement with 1000 ppm P added, the addition was rather complete, since the first bath sample shows 900 ppm P, in comparison to the measurement at 980 ºC (see Figure 7-4 3)). After addition both bath and metal show an increase of phosphorus which decays after starting electrolysis. When adding carbon powder, the phosphorus in the bath decayed steadily, contrary to the experiments concerning the effect of temperature, where the concentration of phosphorus was constant throughout the experiment. This can be seen for all experiments after addition of carbon.

The measurements where 2000 and 5000 ppm P were added, show a typical decrease of phosphorus in the bath, since the starting concentration after addition was higher than 1000 ppm. This becomes obvious by looking at Figure 7-8 3), where the phosphorus concentration in the bath decreases from 3000 to 1500 ppm P in a time span of 140 minutes, compared to Figure 7-8 2), where the phosphorus concentration in the bath decreases by 300 ppm in the approximately same time span. This behaviour indicates again that phosphorus at concentrations higher than 1000 ppm in the bath is not stable, as mentioned in Section 7.5.2.1.

The effect on the phosphorus concentration in the metal seems to depend on the amount added to the electrolyte. After an initial peak the concentration of phosphorus decreases up to the addition of carbon for both experiments with 1000 and 5000 ppm P added. For the experiment where 2000 ppm P was added, the metal does not show such behaviour. It seems like the transfer between bath and metal was different from the other experiments, so that most of the phosphorus remained in the bath phase. In Appendix K, Figure K-3, it is shown that for the experiment where 5000

ppm was added, the equipment used for sampling and adding phosphate or alumina was covered by a yellowish-reddish layer, most likely due to possible evaporation of a phosphorus compound.

However, carbon addition always leads to an increase of phosphorus in the metal phase, although it was only temporary for the experiment when 1000 ppm P was added. The experiments with higher additions of phosphorus show a steady increase of phosphorus in the aluminium. It should be mentioned that the amount of carbon added was varied. The exact amount and the current efficiencies obtained can be found in Table 7-3.

Table 7-3: *Amounts of carbon powder added and the current efficiencies obtained.*

ppm P added (± 10 ppm)	amount of Na_3PO_4 added [g]	amount of carbon powder added [g]	CE [%]
1000	1.8	7.1	66.1
2000	3.7	12.1	63.9
5000	9.3	9.8	61.8

As expected the current efficiencies obtained are lower than for the experiments with no carbon addition at 980 ºC (see Table 7-2). The carbon powder disturbs the normal performance of the cell, leading to a higher bath temperature due to a higher resistance in the electrolyte as found in industrial cells [13]. During the three experiments performed the temperature increased between 5 – 10 ºC as expected after the addition of carbon powder.

Concluding from the results obtained, increasing the amount of carbon powder added seems to increase the transfer between bath and metal, leading to a higher phosphorus concentration in the metal. The transfer also seems to be dependent on the amount of phosphorus added. However, the resulting concentrations of phosphorus added exceed the usual concentration of phosphorus in industrial cells.

7.5.2.3. Effect of current interruption during electrolysis

An accidental current interruption during a measurement in an industrial cell showed that the phosphorus concentrations in the bath and metal were affected (see Section 6.3.3.). Since long-lasting current interruptions for economic and operational reasons are not performed intentionally in

industrial cells, it was intended to see if this effect was just random, or if a current interruption really influences the behaviour of phosphorus in the cell.

The electrolyte composition was once again similar to the one used in Section 7.5.1., and the temperature was 980 ºC. The amounts of phosphorus added were 1000 and 2000 ppm. The current interruption lasted for one hour and was initiated about 90 minutes after starting electrolysis. During the current interruption, samples were taken every 15 minutes in order to get a better impression of what happens with phosphorus in both bath and metal. The results are presented in Figure 7-9.

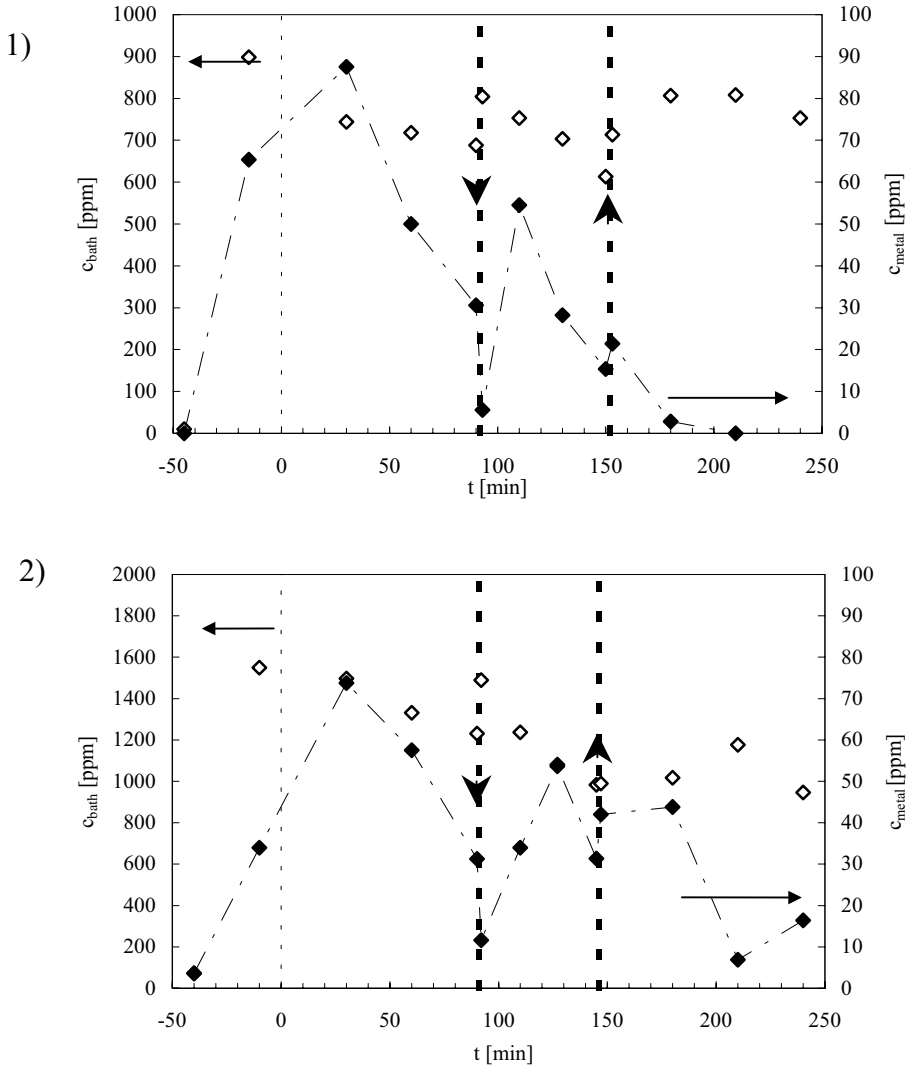

Fig. 7-9: *Effect of a one hour current interruption on the phosphorus content in bath and metal; dotted, vertical thin line marks electrolysis start, thick, dotted lines show times for current off and on. T = 980 ºC. P in metal as full symbols, P in bath as open symbols.*

Stopping the electrolysis for one hour clearly affects the phosphorus concentrations in bath and metal. For both experiments, where 1000 and 2000 ppm P were added respectively, the behaviour seems to be similar. In the metal phase the phosphorus level drops by 20-25 ppm, while the bath samples show an equivalent increase. This indicates that phosphorus released from the metal phase is transferred towards the electrolyte.

The decrease of phosphorus in the bath might be due to an increased concentration of dissolved aluminium in the electrolyte when the electrolysis was stopped. Even though it was expected to get more consistent results when using the laboratory cell to investigate this parameter, it became obvious that the occurrence of a current interruption affected the phosphorus in bath and metal.

7.5.3. Conclusions

The results obtained support the rule of thumb used in the industry, i. e. each 100 ppm P in the bath is related to a CE loss of 1%.

Even though the change in temperature did not show a clear effect on the phosphorus contents in bath and metal, it became clear that the presence of carbon in the bath and the interruption of current both influence the phosphorus. The phosphorus concentration in the bath seems to stabilise at a constant level, which is 1000 ppm P or lower. For higher phosphorus concentrations a decrease towards concentrations of around 1000 ppm P can be observed, supporting the findings by Monnier et al. [9] and by Deininger and Gerlach [10].

Copper was certainly not an ideal cathode material, due to alloy formation (see Appendix N). However, the low concentration of phosphorus in copper made it the best material available, when looking at the influence of phosphorus additions on bath and metal. In case of new experiments to investigate this matter, another cathode material, e.g. TiB_2 or Mo, should be considered. The main objectives in finding a better cathode material should be good wetting, a low phosphorus content and a material that does not form liquid alloys at the operating temperature.

To ensure that the addition of sodium orthophosphate is complete, for a new measurement series another way of adding should be considered. A separate feeding tube might be a solution, however, at larger additions the

powder may get stuck in the tube, as it occurred in preliminary experiments. The addition of tablets of sodium orthophosphate can be another solution, however, we could run the risk that the tablet plunges right through the electrolyte and into the metal.

References to Chapter 7:

[1] E. Haugland, G.M. Haarberg, E. Thisted, J. Thonstad, *The behaviour of phosphorus impurities in aluminium electrolysis cells*, Light Metals 2001, 549-553.

[2] J. Thonstad, *The behaviour of impurities in aluminium cells,* pp. 5-12, X. Slovak-Norwegian Symposium on Aluminium Smelting Technology, Stará Lesná-Ziar nad Hronom, Slovakia, Sep. 21-23, 1999.

[3] R. Oblakowski, S. Pietrzyk, *Superheating of Na_3AlF_6-AlF_3-Al_2O_3 electrolyte in the process of aluminium electrolysis*, Metallurgy and Foundry Engineering, **21**(3), 175-183, 1995.

[4] E.B. Frolova, V. B. Dobrokhotov, A.M. Tsyplakov, *Effect of phosphorus pentoxide on aluminium electrolysis,* Trudy VAMI, English translation, **89**, 1-6, 1974.

[5] P.A. Solli, T. Haarberg, T. Eggen, E. Skybakmoen, Å. Sterten, *A laboratory study of current efficiency in cryolite melts*, Light Metals 1994, 195-203.

[6] P.A. Solli, T. Eggen, S. Rolseth, E. Skybakmoen, Å. Sterten, *Design and performance of a laboratory cell for determination of current efficiency in the electrowinning of aluminium,* J. Appl. Electrochem., **26**(10), 1019-1025, 1996.

[7] P.A. Solli, *Current efficiency in aluminium electrolysis cells,* Dr. ing. thesis, NTNU Trondheim, Norway, 1993.

[8] Å. Sterten, *Current efficiency in aluminium reduction cells,* J. Appl. Electrochem., **18**, 473-483, 1988.

[9] R. Monnier, D. Tzanos, P. Tissot, *Obtention de phosphore élémentaire et de phosphures de nickel par électrolyse de solutions de pentoxyde de phosphore dans de bains à base de cryolithe*, Helv. Chim. Acta, **52**, 596-602, 1969.

[10] L. Deininger and J. Gerlach, *Stromausbeutemessungen bei der Aluminiumoxidreduktionselektrolyse in Laboratoriumszellen,* Metall, **33**, 131, 1979.

[11] J.J. del Campo, *La Electrolisis de la alumina en la criolita funda,* doctoral dissertation, Universidad de Oviedo, Escuela Tecnica Superior de Ingenieros de Minas, Oviedo, Spain, 1984.
[12] private communication with Christian J. Simensen, SINTEF Oslo, Norway; Results soon to be published.
[13] T. Foosnæs, T. Naterstad, M. Bruheim, K. Grjotheim, *Anode dusting in Hall-Héroult cells,* Light Metals 1986, 729-738.

8. Conclusion

Solubility studies showed that $AlPO_4$ is highly soluble in cryolite melts. The eutectic point was determined to be at (57.21 ± 0.02) mole% and (695.9 ± 1.0) ºC. The number of new species formed when adding $AlPO_4$ to Na_3AlF_6 was found to be between 1 and 2. Model calculations led to the conclusion that the orthophosphate ion is in equilibrium with a metaphosphate ion and an oxide ion:

$$PO_4^{34} \lozenge \quad PO_3^4 \; 2\, O^{24}$$

Since in industrial aluminium cells the amount of aluminium oxide is kept between 2 – 4 wt%, the prevailing phosphorus species in the electrolyte should be the orthophosphate, PO_4^{3-}. Local depletion of alumina might lead to a shift in the equilibrium between orthophosphate and metaphosphate favouring the PO_3^- ion.

Based on electrochemical measurements, the earlier finding that phosphorus in cryolite-based melts is reduced from its five-valent state to three-valent was confirmed. Further reduction to a lower valent species was observed, but since the deposition of aluminium occurred in the same potential range, further analysis of this reaction was difficult. The concentration of oxides, such as alumina, influences the reduction of the phosphorus species. The material of the working electrode seemed to influence the reduction behaviour of the phosphate as well. With a tungsten electrode a two-electron reduction step from P(V) to P(III) was found, while with a copper electrode the results indicated a three-electron step to a P(II) species.

Electrochemical studies of a sodium fluoride melt with addition of Na_3PO_4 showed that the orthophosphate dissociates into a metaphosphate and an oxide ion. This is supported by the results of the solubility studies. A reduction of a phosphorus species was observed and the number of electrons transferred was found to be two.

The diffusion coefficient for P(V) species was found to be in the range of (0.7 - 2.5)Ţ10^{-5} cm^2/s depending on if sodium or aluminium orthophosphate was added and which kind of method was chosen for the investigation.

Different impurities were added in the form of oxides to industrial cells to study their behaviour. These measurements showed that phosphorus has a longer retention time than metallic impurities, such as iron and silicon. Changes in ACD and interruption of the current effects the phosphorus concentration in the cell temporarily. Fitting the analysis data of the bath for various impurities to a double exponential function, showed that in larger industrial cells (30 anodes, 250 kA, SBS), the distribution time of the chemicals added was found to be about 2.5 to 3 hours. Data from industry showed that the phosphorus level in the bath and the metal phase decreases with increasing cell temperature.

Mass balances concerning phosphorus for both prebake and Søderberg lines were put up. It was found that a large portion of the phosphorus entering the cell, is transported with the off-gases to the dry-scrubber. However, since the secondary alumina is used as feed for the prebake cells, the phosphorus returns and approximately up to 80% will end up in the metal phase. For the Søderberg cells, which are fed with primary alumina, the phosphorus level in both bath and metal is lower than for the prebake cells. The mass balance of the Søderberg cells show that presumably 70% of the phosphorus leaves the cell via the off-gases. Since the fed to the cells consists of primary alumina, an accumulation of phosphorus in the cell as in the case of the prebake cell cannot occur. In addition is the working temperature of the Søderberg cells higher than for the prebake cells, which leads to a decrease in the total phosphorus in the cell. While the prebake cells (30 anodes, 250kA) show a relation of phosphorus between bath and metal in the order of 10, the Søderberg cells showed a much larger ratio with 27-28.

A laboratory study of phosphorus under electrolysis conditions confirmed that the change in ACD and the interruption of the current influenced the phosphorus concentration in the bath and metal. The amount of phosphorus analysed in the laboratory cell was less than the amount added. This was also observed in industrial cells. After calculations using the model in Section 6.3.6., only about 60 – 70 % of the added phosphorus reaches the electrolyte in the industrial cells. For investigations concerning the effect of temperature in the laboratory cell, the phosphorus present in the melt seemed to be at a stable level throughout the experiment.

A qualitative model for the behaviour of phosphorus in industrial cells was suggested:

- Phosphorus enters the process mainly with alumina, and is present in the bath as a P(V) or a P(III) species.

- Elemental phosphorus formed at the cathode will have a (strong) tendency to escape and dissolve in the electrolyte. Repetitive reduction and oxidation of phosphorus species cause a loss in current efficiency.

- Phosphorus species may also be reduced by impurities in the bath. Small carbon particles (carbon dust) may act as nucleation sites.

- Phosphorus is lost from the cells mainly attached to carbon particles and by possible evaporation, but reenters the cell through secondary alumina.

- Increased temperature leads to increased escape of phosphorus and reduced phosphorus in aluminium

Appendices

Appendix A

Bath compositions

The decomposition potential for alumina given in Table 2-11 from Bøe et al. [A1] seems to be lower than expected in the case of alumina. The composition of the melt and the temperature were different from experiment to experiment. Bøe et al. [A1] had five experimental series with different conditions:

(1) Na_3AlF_6 95wt%, SiO_2 5 wt%, graphite anode and cathode
(2) Na_3AlF_6, Al_2O_3 saturated, 1000ºC, graphite anode and cathode
(3) Na_3AlF_6 95wt%, SiO_2 5 wt%, graphite anode and aluminium cathode
(4) Na_3AlF_6, Al_2O_3 saturated, graphite anode and aluminium-silicon alloy as cathode (12.5wt% Si in Al)
(5) Na_3AlF_6, SiO_2 5 wt%, Al_2O_3 10 wt%, graphite anode and aluminium cathode

[A1] G. Bøe, K. Grjotheim, K. Matiašovsky, P. Fellner, *Electrolytic deposition of silicon and of silicon alloys Part II: Decomposition voltages of components and current efficiency in the electrolysis of the Na_3AlF_6-Al_2O_3-SiO_2 mixtures*, Can. Met. Quart., **10**(3), 179-183, 1972.

Appendix B

Effect on ohmic drop and double layer charging on cyclic voltammograms

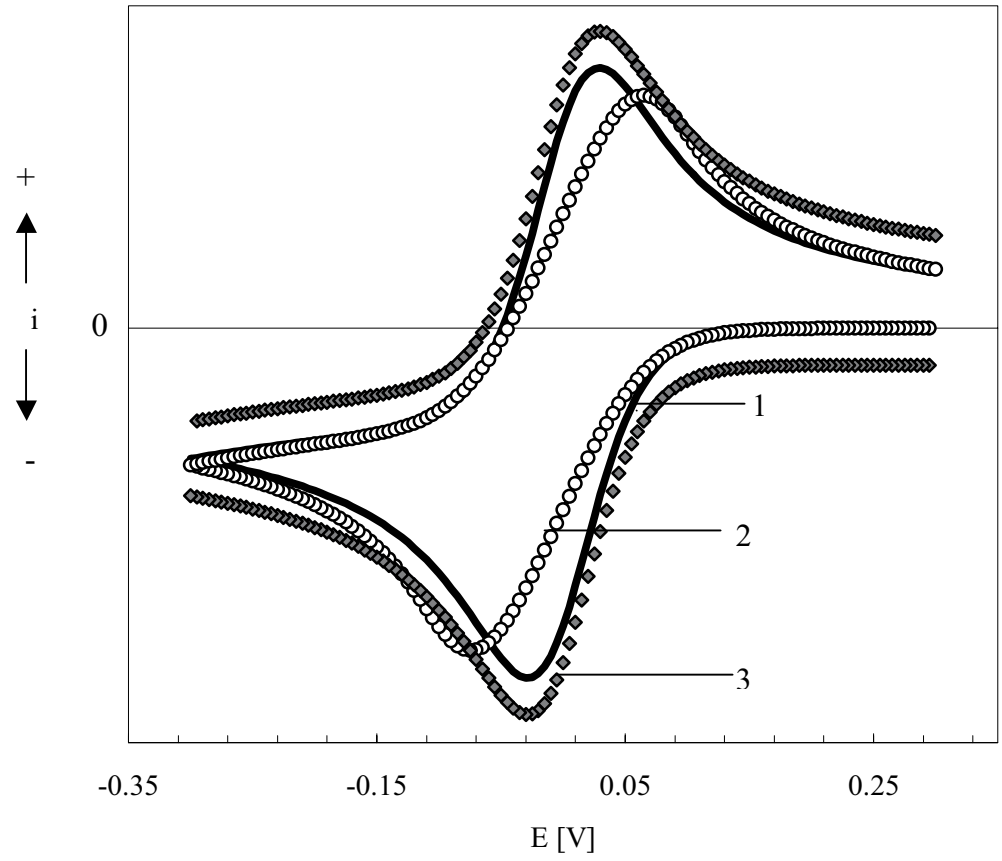

Fig. B-1: *Theoretical voltammograms at 0.2 V/s and 25 ∀C showing the effect of an uncompensated ohmic drop and double layer charging on the measurement; (1) full line – theoretical cyclic voltammogram without ohmic drop or double layer charging effects; (2) white circles – effect of ohmic drop on voltammogram (R = 0.1 q); (3) grey triangles – effect of double layer charging (C_d = 0.2 F/cm^2) [B1].*

In Figure B-1 the effect of an uncompensated ohmic drop (IR drop) in the electrolyte and the double layer charging at the electrode surface on the shape of the voltammogram can be seen.

The IR drop shifts the peak potentials towards larger values. The peak current decreases and an enlargement of the peak width can be observed. The effects of the ohmic drop are similar to kinetic effects and may give rise to draw wrong conclusions about the mechanism.
The current potential curves are distorted by the double layer charging, since the capacitance of the double layer varies with potential. The capacity of the double layer is chosen to be larger than usual to pronounce the effect on the measurement signal. The double layer charging current density, i_c, is given by:

$$i_c = 4C_d \frac{\in E}{\in t} \qquad \text{(B.1)}$$

C_d is the capacity of the double layer. The change of potential versus time is linear and can therefore be expressed as the sweep rate. Equation (B.1) can therefore be written:

$$i_c = 4C_d \qquad \text{(B.2)}$$

The contribution of the capacitive current to the voltammogram should therefore be constant at constant sweep rates and if the capacity of the double layer is assumed constant in the potential range scanned. The effect of the capacity current is more pronounced at higher sweep rates and lower initial concentrations of the electroactive specie under investigation.

[B1] M. Rudolph, S.W. Feldberg, *A cyclic voltammetric simulator for windows*, Digisim® 2.1 software, 1994-1996.

Appendix C

Concentration and current functions for square wave voltammetry

The change of concentration of species O at the electrode surface over time can be expressed as:

$$c_O(0,t) \mid c^* 2 (c_1 4 c^*) erfc \frac{x}{2 \lceil D_O^{1/2} \lceil t^{1/2}} 2 (c_2 4 c_1) erfc \frac{x}{2 \lceil D_O^{1/2} \lceil (t 4 \vartheta)^{1/2}} 2 ....$$

$$.....2 (c_j 4 c_{j41}) erfc \frac{x}{2 \lceil D_O^{1/2} \lceil (t 4 (j 4 1)\vartheta)^{1/2}}$$

The differential current, ι i, can be expressed as

$$\iota i \mid \frac{n \lceil F \lceil D_O^{1/2} \lceil c^o}{\phi^{1/2} \lceil \vartheta^{1/2}} \sum_{m\mid 1}^{j} \frac{/4 1 0^j / Q_m 4 2 Q_{m41} 2 Q_{m42} 0}{/\eta 2 j 4 m 0^{1/2}}$$

where Q_0 and Q_{-1} are both unity and ϧ is the fraction of the square wave half period at which the current is measured.

At the jth period of the staircase, the current measured at $ϧ_1$Ű during the forward pulse is

$$i_f \mid \frac{n \lceil F \lceil D_O^{1/2}}{\phi^{1/2} \lceil \vartheta^{1/2}} \left[\frac{c_2(j 4 1) 4 c_1(j)}{\eta_1^{1/2}} 2 \sum_{m\mid 0}^{j41} \frac{c_2(m 4 1) 4 c_1(m)}{/\eta_1 2 j 4 m 0^{1/2}} 2 \frac{c_1(m) 4 c_2(m)}{/\eta_1 2 j 4 m 4 \omega 0^{1/2}} \right]$$

The current measured at $ϧ_2$Ű during the reverse pulse is

$$i_b \mid \frac{n \lceil F \lceil D_O^{1/2}}{\phi^{1/2} \lceil \vartheta^{1/2}} \sum_{m\mid 0}^{j41} \left[\frac{c_2(m 4 1) 4 c_1(m)}{/\eta_2 2 j 4 m 0^{1/2}} 2 \frac{c_1(m) 4 c_2(m)}{/\eta_2 2 j 4 m 4 \omega 0^{1/2}} \right]$$

where ů, $ϧ_1$ and $ϧ_2$ are all fractions less than unity and $ϧ_1 < ů < ϧ_2$.

Appendix D.

Dissolution of samples for ICP-AES analysis

The bath samples were crushed and 3 g was extracted in 50 ml of a 30 % $AlCl_3 \cdot 6\ H_2O$ solution by heating it for 24 hours at 60 – 70 ºC. Thereafter the solution was decanted and the undissolved precipitate was again heated to the boiling point when 15 ml of 30% HCl was added. This procedure was carefully watched to avoid complete dryness of the solution. Whenever necessary, deionised water was added to keep the mixture liquid. The dissolved samples were diluted in deionsed water up to 100 ml and kept in a closed plastic container for analysis by ICP-AES.

From the metal samples 1g was dissolved in 15 ml of an acidic mixture of one part HNO_3 (65%) and 3 parts HCl (30%) while heating at 50 ºC. The dissolved samples were diluted in deionised water and kept in a plastic container for analysis by ICP-AES.

Appendix E

XRD spectrum of the Na_3AlF_6-$AlPO_4$ melt

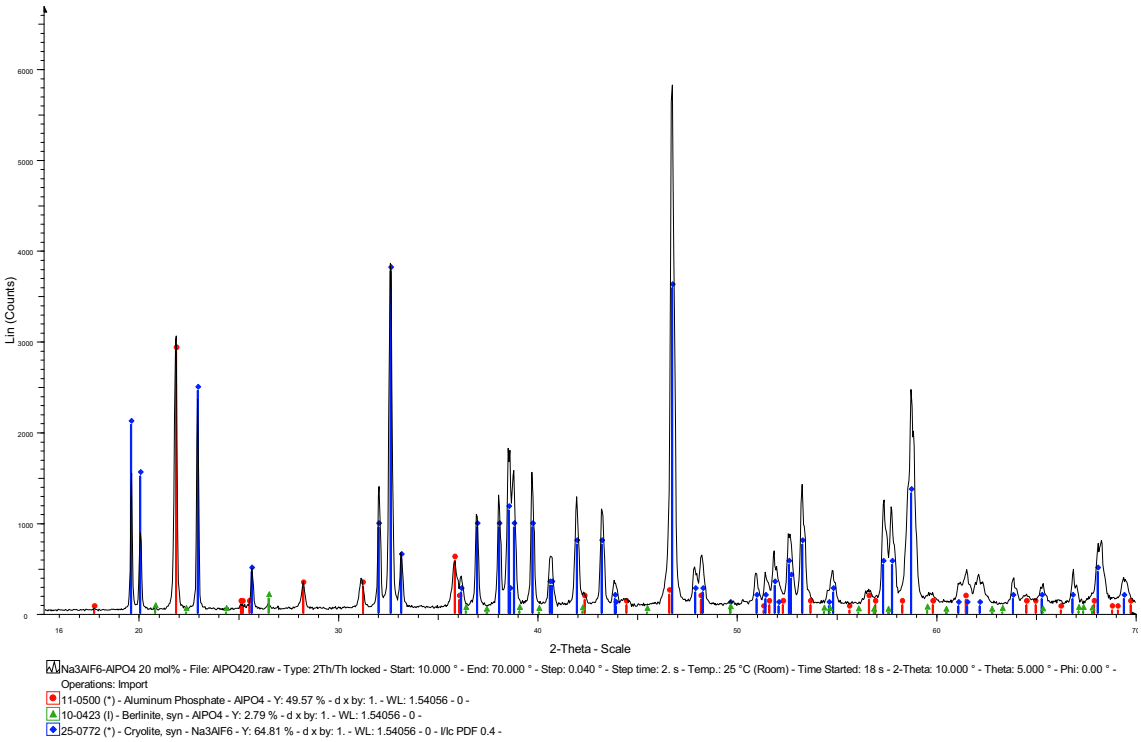

Fig. E-1: *XRD-spectrum from the solidified, crushed bath of Na_3AlF_6 – $AlPO_4$ (19.99 mole%)*

Appendix F

Determination of electrode area

By changing the immersion depths of the working electrode, the current of the peak under investigation varies.
Figure F-1 shows a peak couple (P3/P3' in the Na_3AlF_6-Al_2O_3-$AlPO_4$), for which the electrode wire was immersed further in the melt (+2 mm, + 4mm and +6 mm) and as well withdrawn (- 2mm).

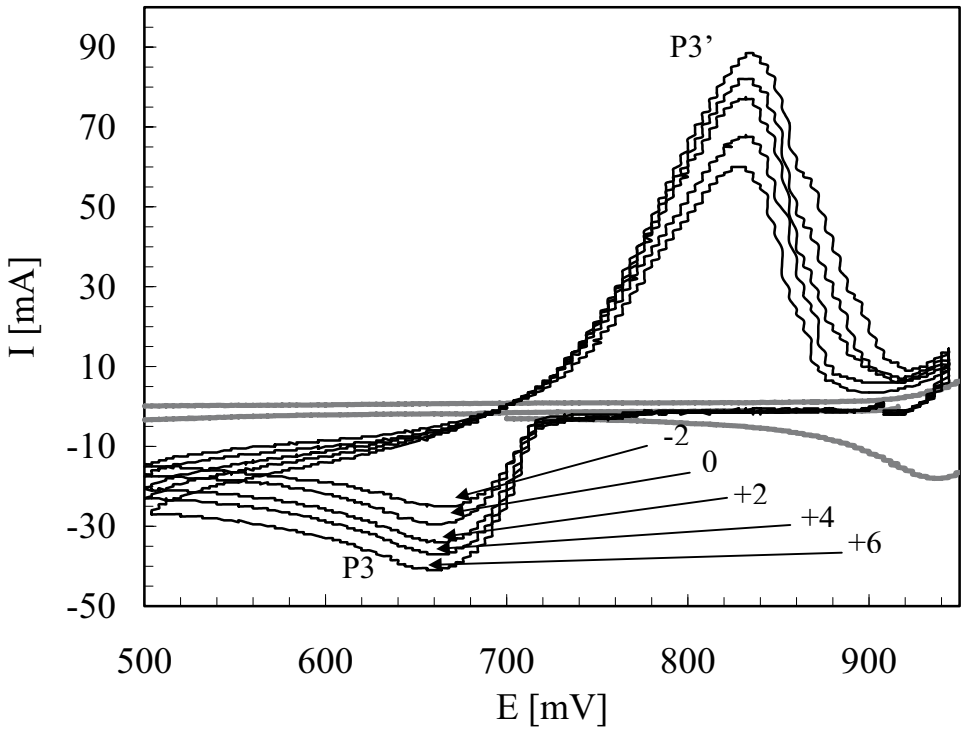

Fig. F-1: *Peak couple P3/P3' of the Na_3AlF_6-Al_2O_3-$AlPO_4$ melt at different immersion depths of the tungsten working electrode. Immersion depth changes given in the figure in mm. Concentration of $AlPO_4$, sweep rate and temperature kept constant.*

Throughout the experiment the electrode area was kept constant, which is given in Figure F-1 as the curve "0 mm". When recording the voltammograms to determine the electrode area, the only parameter changing should be the electrode area. The concentration of the diffusing species, the sweep rate and the temperature have to be kept constant. The peak current is thereby only depending on the electrode area (see equations

(3.14) and (3.22)). Reading the peak currents for each immersion depth and plotting the data, Figure F-2 results.

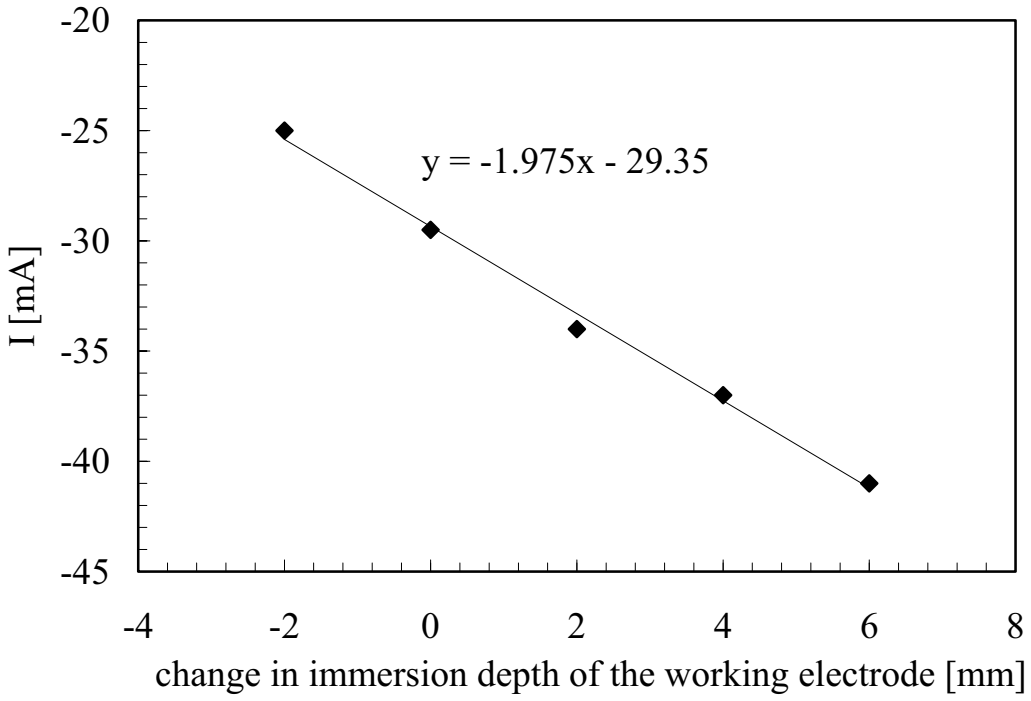

Fig. F-2: *Plot of the peak current of peak P3 in Figure F-1 versus the change in the immersion depth of the working electrode.*

From the slope of the regression line we can determine the real immersed length of the electrode named "0 mm". For a slope of –1.975 and a peak current of 29.35 mA at "0 mm", the real immersed length of the electrode is found to be 1.49 cm. Since the diameter of the wires used as electrode is known, the electrode area can be calculated.

Appendix G

Current fluctuations after addition of Na_3PO_4 to Na_3AlF_6

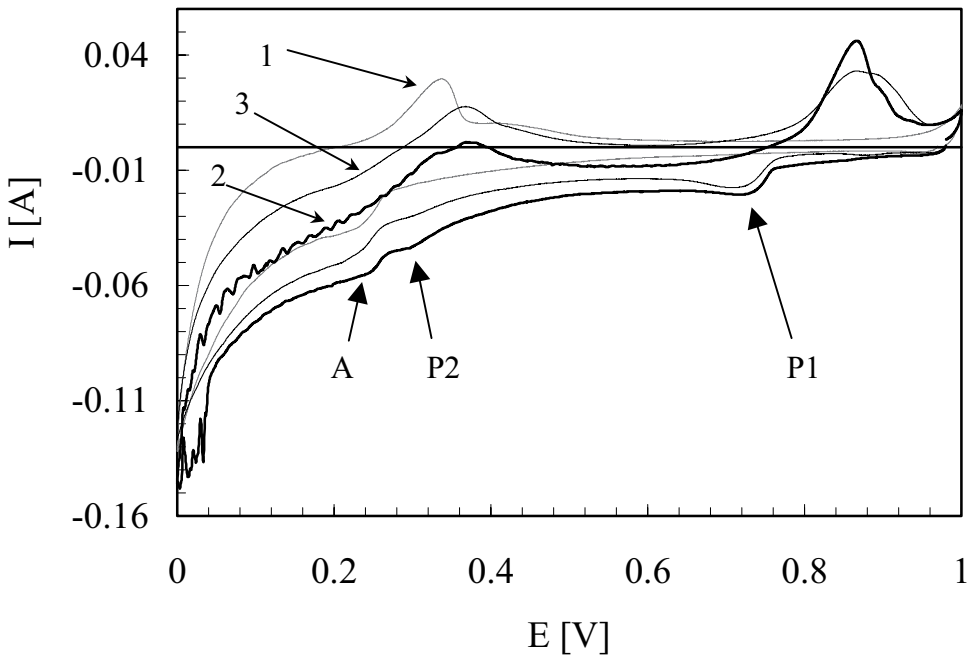

Fig. G-1: *Cyclic voltammograms before and shortly after the addition of 0.16 wt% Na_3PO_4 to a Na_3AlF_6-Al_2O_3 melt at 1000 ˚C. 1) no Na_3PO_4 added (grey curve), 2) 3 minutes after addition, 3) 20 minutes after addition; 0.2 V/s.*

The voltammograms in Figure G-1 show a variation over time when sodium orthophosphate was added to the melt. Curve 1 shows the voltammogram when no phosphate was present in the melt. Three minutes after the addition of 0.16 wt% Na_3PO_4 the scan showed a disturbance of the current signal in the vicinity of the cathodic vertex potential and after reversing the potential. It can be seen that curve 2 is shifted towards more negative currents. After reversing the potential in curve 2 the current signal remains negative for a much longer time than compared to curve 1. Twenty minutes after the addition the voltammogram does not show any disturbances.

In Figure G-2 the effect of the apparent gas evolution of phosphorus can be observed as well in a square wave voltammogram.

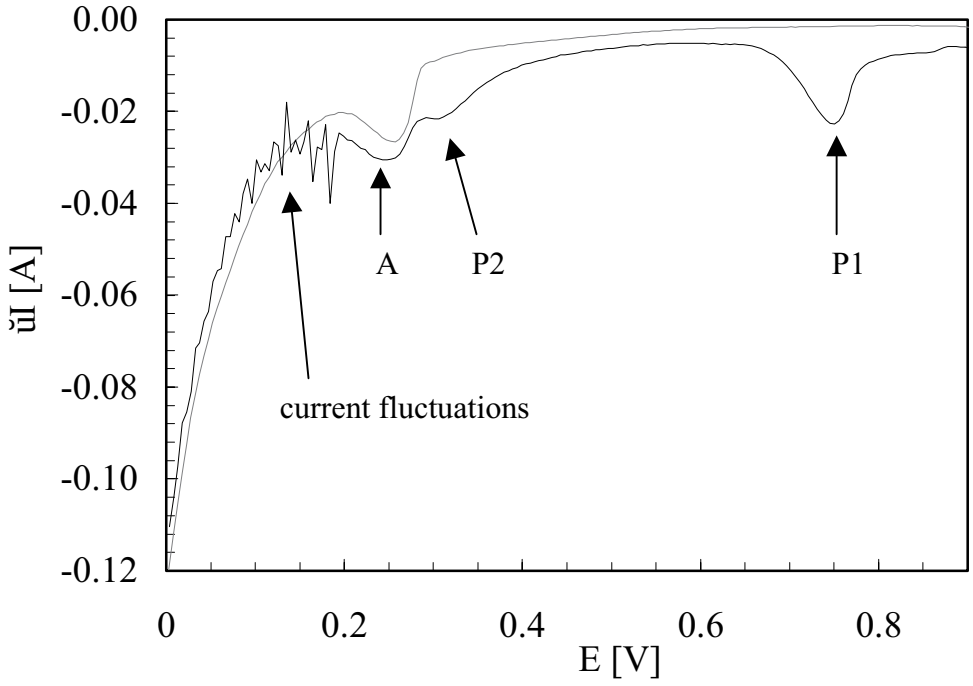

Fig. G-2: *Square wave voltammograms before (grey curve) and after addition (black curve) of 0.16 wt% Na_3PO_4 to an alumina-saturated cryolite melt at 1000 ˚C, f = 20 Hz. The current fluctuations are probably caused by gas evolution.*

In earlier experiments additions of 0.03 and 0.07 wt% Na_3PO_4 to the Na_3AlF_6-Al_2O_3 melt did not show these current disturbances. The phenomenon only occurred when 0.16 wt% sodium orthophosphate were added to the melt.

Appendix H

Data for industrial measurements

Table H-1 gives an overview over all measurements performed, including amounts of chemicals added to the prebake cell, extraordinary operational interventions and if gas/dust sampling was performed.

Table H-1:

Experiment	additions/chemicals	amount [kg]	extraordinary actions concerning cell operation	gas/dust sampling
Series 1	Fe_2O_3 SiO_2 TiO_2 Na_3PO_4 $AlPO_4$	7.609 1.498 1.000 1.250 1.158	none	no
Series 2	Fe_2O_3 SiO_2 TiO_2 Mn_2O_3 Na_3PO_4	10.150 5.001 2.010 1.985 4.786	current cut for 1 hour	no
Series 3	Fe_2O_3 SiO_2 TiO_2 Mn_2O_3 Na_3PO_4	10.571 5.195 2.029 1.986 5.194	ACD changed, decreased 1cm for 165 min.	no
Series 4	Fe_3O_4 SiO_2 TiO_2 Mn_2O_3 Na_3PO_4	10.105 5.492 2.011 2.005 5.386	20 kg carbon dust addition after 145 min. past addition of phosphorus	no
Series 5	Fe_3O_4 SiO_2 TiO_2 Mn_2O_3 Na_3PO_4	11.120 ? 2.062 2.101 5.388	40 kg carbon dust addition after 185 min. past addition of phosphorus	yes
Series 6	Na_3PO_4 $NiCO_3$	5.000 0.620	40 kg carbon dust addition after 165 min. past addition of phosphorus	yes
Series 7	LiCl Mn_2O_3 Na_3PO_4	5.002 2.003 4.969	none	yes
Series 8	LiCl MnO_2 Na_3PO_4	9.997 2.404 5.003	16.6 kg carbon dust addition after 229 min. past addition of phosphorus	yes

Experiment	additions/chemicals	amount [kg]	extraordinary actions concerning cell operation	gas/dust sampling
Series 9	MnO_2 Na_3PO_4 Fe_2O_3 TiO_2 Cu	2.013 5.018 10.870 3.093 1.953	none	no
Series 10	MnO Na_3PO_4 NiO	2.006 5.011 0.957	none	no

Appendix I

Model for the mass transport between bath and metal

According to this mechanism an impurity element will be reduced at the cathode at its limiting current density (i_l), which depends on the concentration of the element in the bath, c^o, and on the mass transfer coefficient, k_m:

$$i_l = n \cdot F \cdot k_m \cdot c^o \tag{I.1}$$

Assuming that step (1) in Figure 6-1 controls the mass transfer process, the flux of a species transported from the bulk to the bath/metal interface can be expressed as:

$$J = A \cdot k \cdot (c_{bath} - c_{boundary}) \tag{I.2}$$

where c_{bath} is the concentration in the bulk of the bath and A is the interface area. If step (2) and (3) in Figure 6-1 are comparably faster than step (1), we can make the assumption that $c_{boundary}$ is equal to zero. Thereby the expression for the flux (equation (I.2)) will be simplified:

$$J = A \cdot k \cdot c_{bath} \tag{I.3}$$

The flux can also be expressed as a partial current.

$$I = n \cdot F \cdot J = n \cdot F \cdot A \cdot k \cdot c_{bath} \tag{I.4}$$

The change of concentration in the electrolyte as a function of time can, therefore, be expressed as:

$$J = 4V \left(\frac{dc_{bath}}{dt} \right) = A \left(k_{bath} \right) c_{bath} \tag{I.5}$$

Integration of equation (I.5) results in

$$c_{bath} / t0 = c_{added} \left(e^{4 A V^{41} k_{bath} t} \right. \tag{I.6}$$

where c_{added} can either be expressed as the amount of impurity added or the difference between the concentration in the electrolyte immediately after

addition and the background concentration, c_{bc}, which basically should be the same, if the addition is complete. With a complete addition it is meant that the impurities added to the cell are completely dissolved in the bath and there are no losses due to the environment. Therefore the background concentration, c_{bc}, has to be added to equation (I.6).

$$c_{bath}(t) = c_{bc} + c_{added}\left(1 - e^{-\frac{A}{V}k_{bath}t}\right) \qquad \text{(I.7)}$$

Appendix J

Determination of the distribution function for impurities added

The mathematical calculations were done in cooperation with Ph.D. student Ulrik Thisted.

We are interested in how the distribution of phosphorus in the cell varies with time after the addition. For simplicity we assume that the convective patterns ensure immediate distribution in the vertical and "transverse" directions. Furthermore we assume that the transport in the "longitudinal" direction is diffusion-like. That means it can be described by Fick's 2. law, where D_t is the turbulent diffusion coefficient:

$$\frac{\partial c}{\partial t} = D_t \frac{\partial^2 c}{\partial t^2} \tag{J.1}$$

D is not necessarily the diffusion coefficient in the "usual" sense. To solve this equation we first write the concentration of phosphorus c(x,t) as a Fourier serie with time-dependent constants,

$$c(x,t) = \sum_{n=1}^{\infty} A_n(t) \cos\left(\frac{n\pi x}{L}\right) \tag{J.2}$$

After performing the derivations and inserting it in (N.1), we get,

$$\sum_{n=1}^{\infty} \frac{dA_n(t)}{dt} \cos\left(\frac{n\pi x}{L}\right) = D \sum_{n=1}^{\infty} \left(\frac{n\pi}{L}\right)^2 A_n(t) \cos\left(\frac{n\pi x}{L}\right) \tag{J.3}$$

which gives the following equation for the constants,

$$\frac{dA_n(t)}{dt} = D\left(\frac{n\pi}{L}\right)^2 A_n(t) \tag{J.4}$$

This leads to the following time dependence of the constants,

$$A_n(t) = A_n(0)e^{-\left(\frac{2\pi n}{L}\right)^2 Dt} \qquad \text{(J.5)}$$

If we assume that the initial distribution is a delta function in x = 0, we get that $A_n(0) = 1$ for all n. Using this and inserting (J.5) in (J.1), we find that the concentration at x = 0 is given by,

$$c(0,t) = \sum_{n=1}^{\infty} e^{-\left(\frac{2\pi n}{L}\right)^2 Dt} = Z_3(0, f(t)) \qquad \text{(J.6)}$$

where Z_3 is a Jacobi-Theta function. The variation with time of the logarithm to c(0,t) is shown in Fig. J.1, and we see that after an initial decrease c(0,t) decays exponentially.

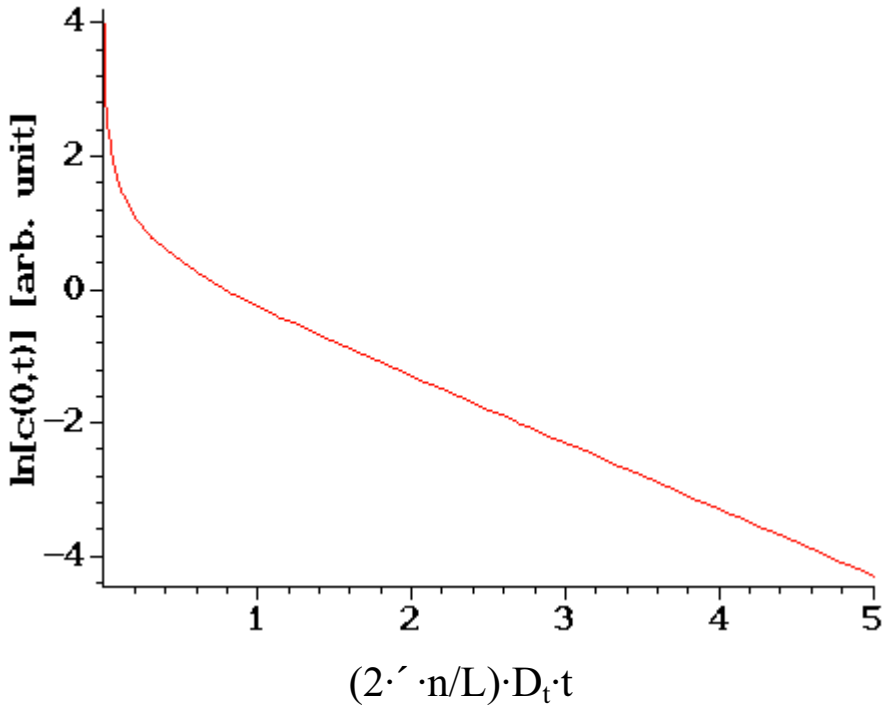

Fig. J-1: *The Jacobi-Theta function as ln c versus t.*

Since the plot of ln c versus time gives a straight line, excluding values at very short times, it is adequate to express the distribution of the impurities in the cell by an exponential function.

Appendix K

Pictures of the experimental equipment

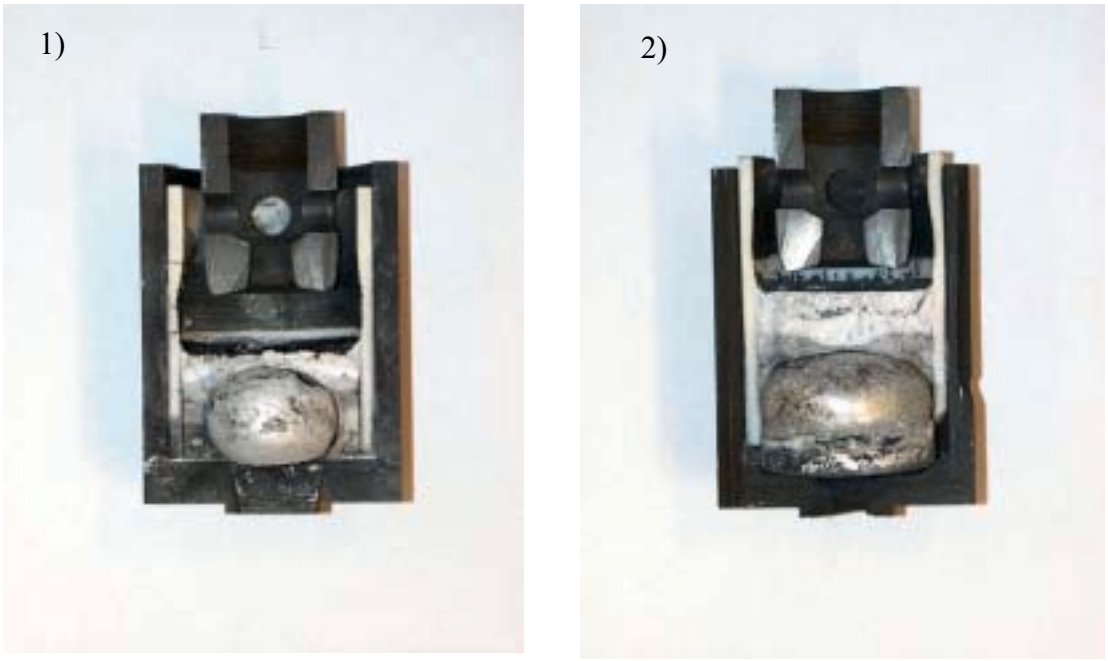

Fig. K-1: *Cross section of crucibles after the experiments; 1) Crucible without additional cathode material, 2) Crucible with iron as cathode material (covered in aluminium).*

Fig. K-2: *Cross section of empty crucibles after an experiment, showing the formation of Al_4C_3 (yellow colour) at the graphite bottom and partly on the side-walls (cathode material: copper).*

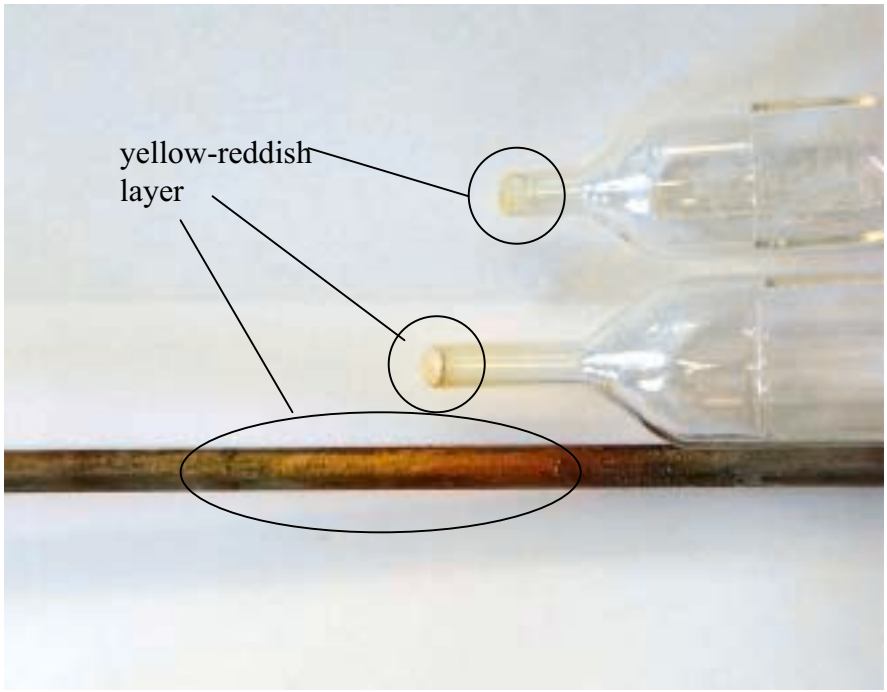

Fig. K-3: *Equipment from an experiment with carbon addition, where 5000 ppm P was added. Weighing ships after adding Na_3PO_4 and quartz sampling tube after first bath sample after phosphate addition. Powder-like, yellowish-reddish layer formed on equipment inserted into the anode steel tube.*

In Figure K-3 we clearly see that the addition of 5000 ppm P produces a gaseous phosphorus compound, which condenses on the colder sampling tube or weighing ships.

Appendix L

Influence of the alloy formation on the activity of aluminium and the current efficiency

1) Iron as cathode material

From ICP-AES analysis of metal samples from some experiments with respect to iron, it was found that the iron content varied from experiment to experiment. The values varied from 8 to 12 wt%. Looking at the phase diagram of the Al-Fe system, a solubility of 15 wt% Fe in Al can be found at 980 ºC (experimental temperature). Therefore, taking the worst case, we assume that 15 wt% of iron plus come chromium and nickel (usually 18% and 8% respectively in the steel) can be present in the aluminium metal. From Hultgren et al. [L1] it can be found that for the Al-Fe system the activity coefficient for aluminium lies between 0.954 and 0.841 when the weight fraction of aluminium varies from 0.9 to 0.8. The activity of aluminium can, therefore, be calculated as

$$a_{Al} = \nu_{Al} \left(1 - 4 \frac{\frac{wt\%Fe}{M_{Fe}}}{\frac{wt\%Fe}{M_{Fe}} + 2\frac{wt\%Al}{M_{Al}}} \right) \qquad \text{(L.1)}$$

when we disregard any contents of chromium and nickel. At 85 wt% Al the activity coefficient was assumed be 0.9. Hence, the activity of aluminium was calculated to be 0.83.

The change in aluminium activity influences the activity of sodium as well, due to the following relation [L2],

$$a_{Na} = K' \left(a_{Al} \right)^{1/3} \qquad \text{(L.2)}$$

where K' is a constant. The current loss during electrolysis can be expressed by the proportionality between i_{loss} and a_{Na} to be [L2],

$$i_{loss} = k \left(a_{Na}^{1/2} \right) = k \left(K'^{1/2} \right) \left(a_{Al}^{1/6} \right) \qquad \text{(L.3)}$$

The constant k can be calculated, since i_{loss} can be determined from the average current efficiency, 90.6 % (see Figure 6-1), and the applied cathodic current density, following the equation,

$$CE[\%] = 100 \left(\frac{i_{Al}}{i_{Al} + i_{loss}} \right) \qquad \text{where } i_{tot} = i_{Al} + i_{loss} \qquad \text{(L.4)}$$

The surface activity of sodium was determined by using equation (L.5). Following the procedure used by Solli [L2], the equilibrium activity of sodium was determined to be 0.0108. The surface activity of sodium was determined for 0.85 A/cm^2 and assuming a cathodic overvoltage, η, of 0.07 V,

$$\xi_{Al} = \frac{R \cdot T}{F} \left| \ln \left(\frac{a_{Na,eq}}{a^*_{Na}} \right) \right| \qquad \text{(L.5)}$$

for which a_{Na}^* was found to be 0.0057. According to equation (L.2) the surface activity of sodium equals the constant K', when the activity of aluminium is unity. Furthermore, we know the activity of aluminium in the presence of iron, and can, therefore, calculate the new surface activity of sodium, which was found to be 0.0054.

The constant k in equation (L.3) was found to be 1.059, for which the new i_{loss} was calculated to be 0.077 A/cm^2. Inserting the new values into equation (L.4), the current efficiency with a reduced aluminium activity is found to be

$$CE\ [\%] = 90.9$$

The increase of 0.3% shows that the decrease in aluminium activity in the metal phase raises the current efficiency as expected. However, the calculated increase in the case of iron as cathode material is within the limits of the error estimate.

2) Copper as cathode material

By ICP-AES analysis the content of copper in aluminium was found to be in the range 45 - 47 wt%. We can perform the same calculations when using copper as cathode material. From Hultgren et al. [L1] it can be found that the activity coefficient for aluminium in the Al-Cu system is 0.532 for a weight fraction of aluminium of 0.5.

$$a_{Al} = \nu_{Al} \left(1 - 4 \frac{\frac{wt\%Cu}{M_{Cu}}}{\frac{wt\%Cu}{M_{Cu}} + 2\frac{wt\%Al}{M_{Al}}} \right) \qquad \text{(L.6)}$$

The activity of aluminium was calculated to be 0.36. The activity of sodium has to be calculated according to equation (H.2). The current efficiency at 980 ºC is found to be 82.2 % (see Table 6-2). The cathodic current density applied was 0.833 A/cm^2, therefore, i_{loss} was found to be 0.148 A/cm^2, calculated according to equation (H.3). The constant k was, therefore, 1.96, and the new sodium activity was found to be 0.0041. The new i_{loss} was calculated to be 0.125 A/cm^2 and the new current efficiency determined to be,

CE [%] = 85.0.

Compared to the initial current efficiency of 82.2%, it can be concluded that the increase in CE by reducing the activity of aluminium is 2.8 %. Therefore, the calculated current efficiency in the case of copper as cathode material is even lower than given in Tables 6-2 and 6-3.

[L1] R. Hultgren, P.D. Desai, D.T. Hawkins, M. Gleiser, K.K. Kelley, *Selected values of the thermodynamic properties of binary alloys,* Am. Soc. Met., 1973.

[L2] P.A. Solli, *Current efficiency in aluminium electrolysis cells,* Dr. ing. thesis, NTNU Trondheim, Norway, 1993.

Appendix M

Typical raw data from electrolysis experiments

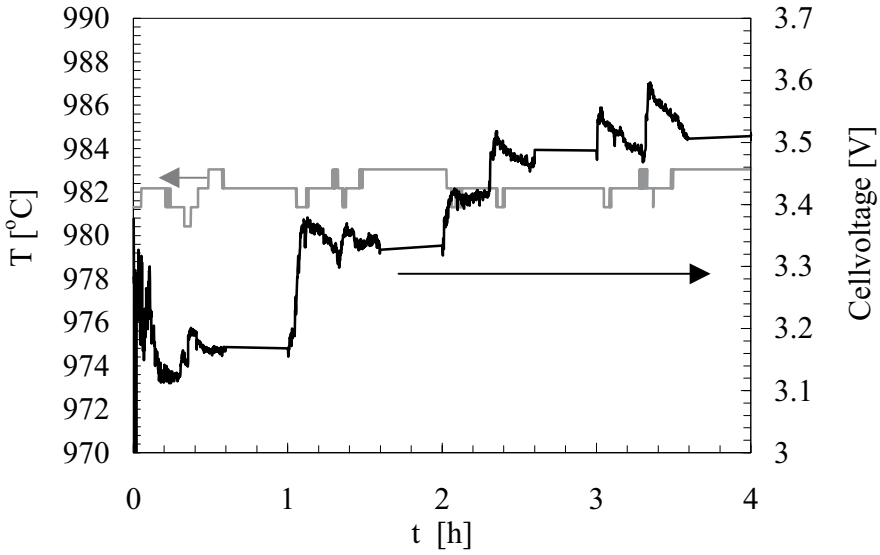

Fig. M-1: *Typical recorded data for temperature and cell voltage with time for measurements with steel as cathode material.*

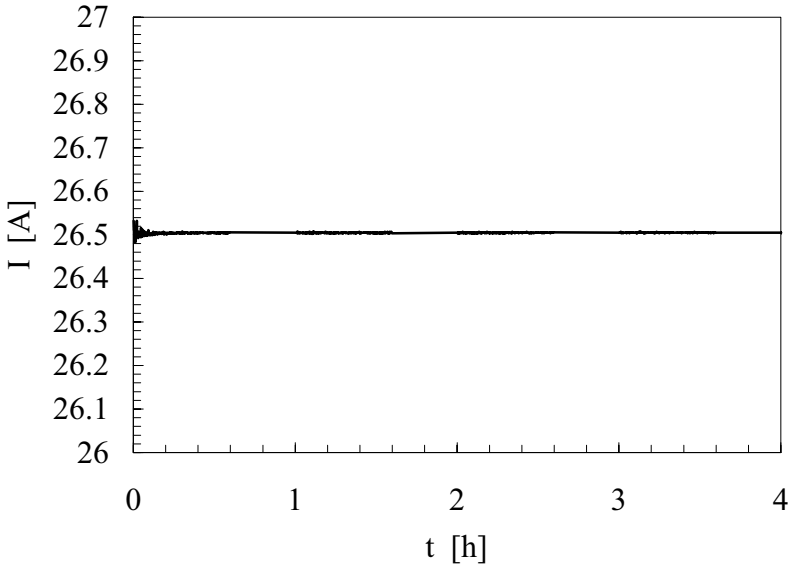

Fig. M-2: *Typical recorded data for current with time for measurements with steel as cathode material.*

Appendix N

Phase diagrams

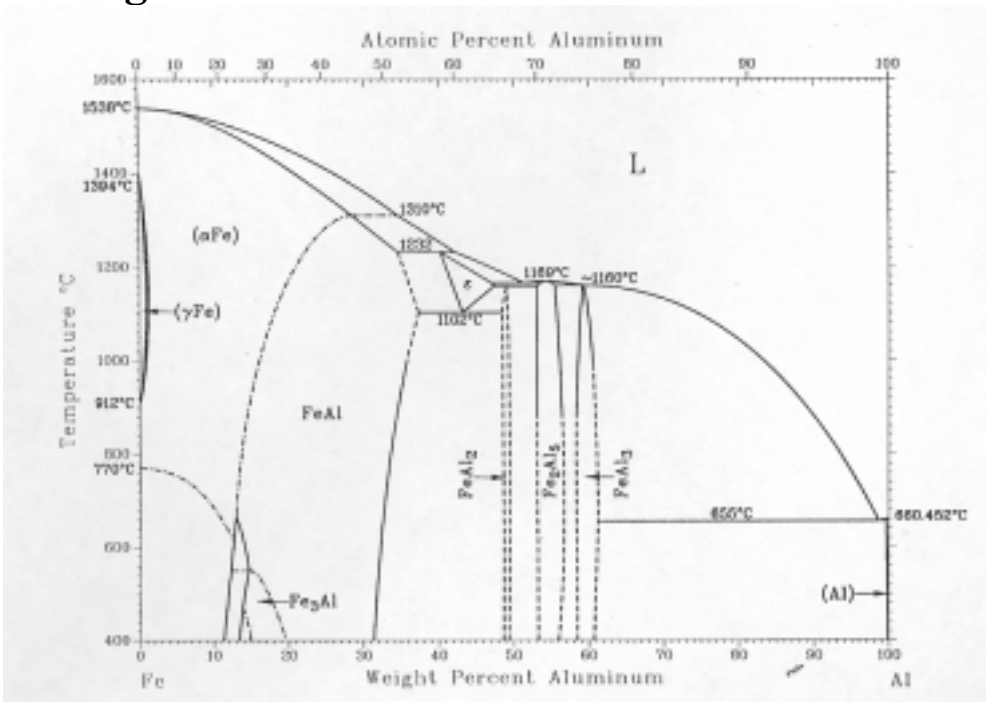

Fig. N-1: *Phase diagram of the binary system Al-Fe [N1].*

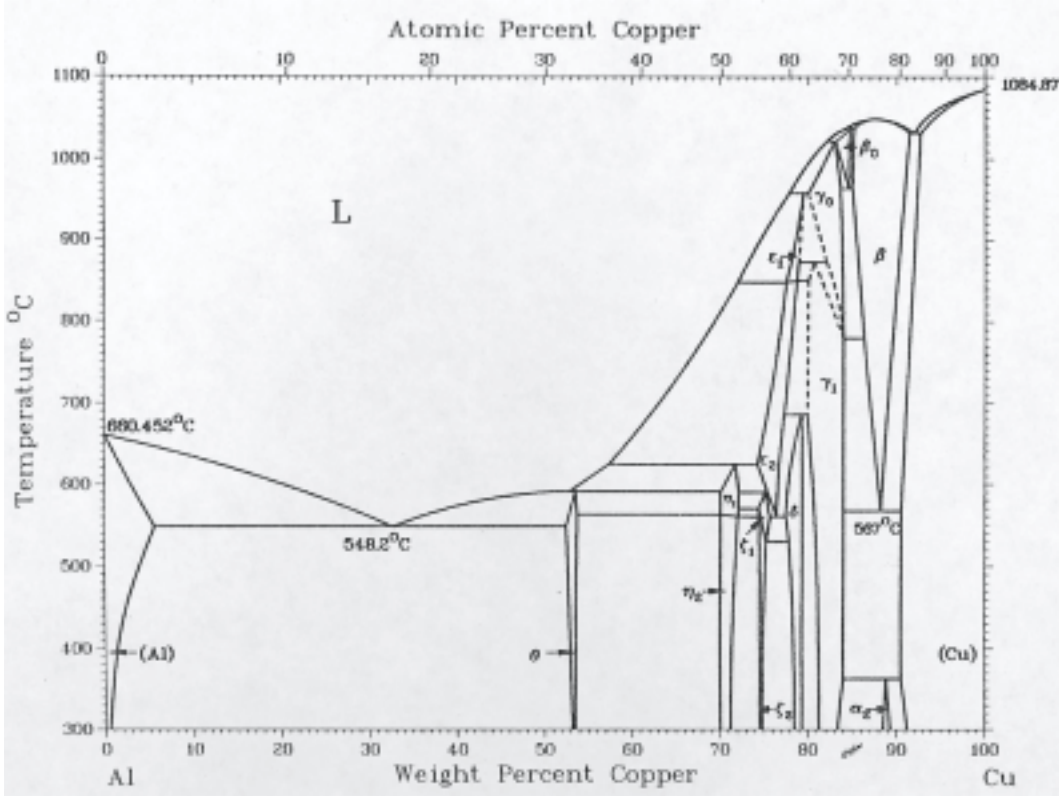

Fig. N-2: *Phase diagram of the binary system Al-Cu [N1].*

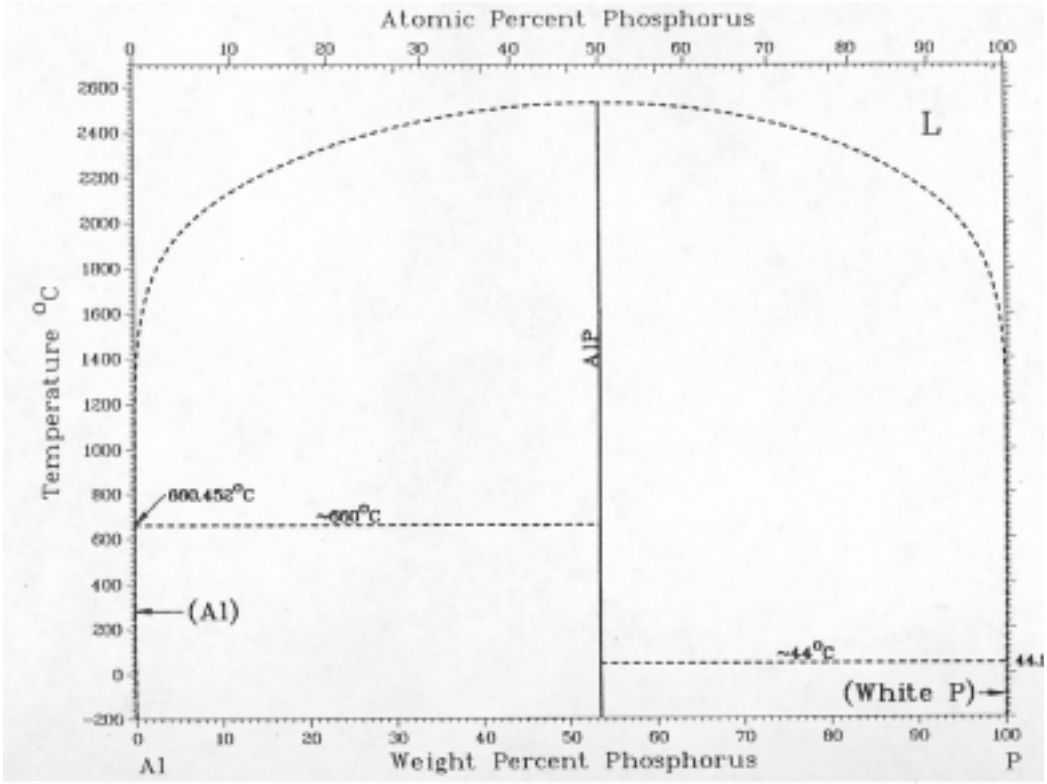

***Fig. N-3**: Phase diagram of the binary system Al-P [N1].*

[N1] T.B Massalski, *Binary alloy phase diagrams*, Material Parks Ohio: ASM International, 2nd ed., Vol. 1, 1990.

Appendix O

Error in analysis of bath and metal samples by ICP-AES

When using ICP-AES, the analytical method has to be fitted to the element of interest, which was phosphorus in this case.

The method was installed in the way that standard solutions prepared with known amounts of phosphorus should calibrate the instrument so that the height of the intensity signal measured corresponded to a certain concentration of phosphorus. No background correction was applied since it was presumed that the background was similar, because identical chemicals were used when preparing both the samples and the standards.

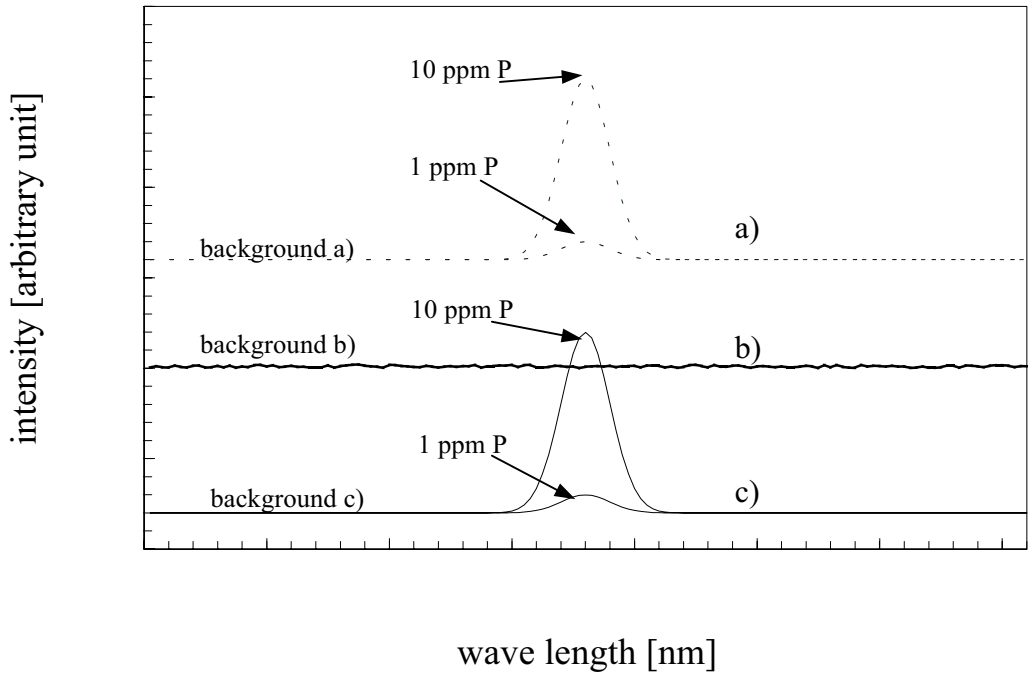

Fig. O-1: *Sketch of the intensity peaks for phosphorus; a) standards with phosphorus (1 and 10 ppm) in a solution containing 10000 ppm Al as well, b) sample without phosphorus, c) standard with phosphorus (1 and 10 ppm) in an acidic solution.*

As can be seen from Figure O-1, the difference in the background influences the total intensity of the signal. When calibrating the instrument with standards of 1 and 10 ppm P diluted in the same solution as the samples were dissolved in (HNO_3·3HCl plus water), the intensity levels are

set to the known concentration from the standards. Analysis of a sample without phosphorus (b) gives a higher background signal than the standards and the instrument will assume that the intensity at the wavelength chosen for phosphorus is equal to the concentration of P in the sample. Therefore, the instrument set the intensity of the peak equal to a concentration of 8-9 ppm P in sample (b), even though no phosphorus is present.

Since the matrix of the standard solution has to be similar to the solution of the samples, new standards were prepared containing 10000 ppm Al (~1 g Al in 100 g water). However, this did not work either (see Fig. O-1 a)), since the background signal was still different. This might be also due to the fact that each metal sample only contained about 0.5 g of aluminium. The rest was copper.

A third possible way to analyse the dissolved samples was considered by which the background was determined for each sample and substracted from the signal of the phosphorus peak. Thereby differences in the background height were avoided. This method was used for analysis for both bath and metal samples. The results are presented in Chapter 7.